

Aerostatic Journal Bearing based on an Orthotropic Layered Porous Structure

Vom Fachbereich Maschinenbau und Verfahrenstechnik
der Rheinland-Pfälzischen Technischen Universität
Kaiserslautern-Landau
zur Erlangung des akademischen Grades

Doktor-Ingenieur (Dr.-Ing.)
genehmigte
Dissertation

von
Herrn
Dipl.-Ing. Artur Schimpf
geb. in Kamyschin

Tag der mündlichen Prüfung: 03.04.2023
Dekan: Prof. Dr.-Ing. Tilmann Beck
Vorsitzender: Prof. Dr.-Ing. Jörg Seewig
Berichterstatter: Prof. Dr.-Ing. Martin Böhle
Prof. Dr.-Ing. Dieter Brillert

D 386

Vorwort

Diese Arbeit entstand im Rahmen meiner Beschäftigung als wissenschaftlicher Mitarbeiter am Lehrstuhl für Strömungsmechanik und Strömungsmaschinen (SAM) der Rheinland-Pfälzischen Technischen Universität Kaiserslautern-Landau (RPTU).

Mein besonderer Dank gilt Herrn Prof. Dr.-Ing. Martin Böhle für sein Vertrauen und seine wertvolle Unterstützung, die für die Erstellung dieser Arbeit grundlegend war. Ebenso möchte ich mich bei Herrn Prof. Dr.-Ing. Dieter Brillert bedanken, der das Koreferat übernommen und großes Interesse an dieser Arbeit gezeigt hat. Herrn Prof. Dr.-Ing. Jörg Seewig danke ich ferner für die Übernahme des Vorsitzes der Prüfungskommission sowie für hilfreiche Vorschläge für weiterführende Arbeiten.

Ich danke zudem den Kollegen am Deutschen Zentrum für Luft- und Raumfahrt (DLR), Herrn Markus Ortelt und Herrn Helge Seiler, für die Zusammenarbeit im Rahmen des Projekts zur Entwicklung von faserkeramischen Fluidfilmlagern (FKFL) zwischen dem SAM und dem DLR. Darüber hinaus danke ich Herrn Andrej Keksel vom Lehrstuhl für Messtechnik und Sensorik der RPTU für die wichtige Unterstützung bei der Oberflächenabtastung der porösen Hülsen. Ein weiterer Dank gebührt den Mitarbeitern der Metall- und Elektrowerkstatt für ihre Beratung und Realisierung des Luftlagerteststands.

Meinen Kolleginnen und Kollegen am SAM danke ich für anregende Diskussionen rund um Strömungsmechanik und Strömungsmaschinen. Besonderer Dank gilt Dr. Yandong Gu für unsere Diskussionen rund um Lager und für die Tischtennis-Matches. Auch meiner Bürokollegin Laura Sterle möchte ich meinen Dank aussprechen, sowohl für die bereichernden fachlichen Diskussionen als auch für ihre stetige Hilfsbereitschaft. Ich danke außerdem den Herren Watzmann, die mir vom ersten Tag mit Rat und Tat zur Seite standen.

Ein weiterer Dank geht an meine ehemaligen Studenten, die im Rahmen ihrer Abschlussarbeiten und als Hilfwissenschaftler maßgeblich zum Erfolg der Projekte beigetragen haben. Besonders Alexander Schwarzwälder und Dennis Gudi haben mit ihrer engagierten Arbeit einen wertvollen Beitrag zum Erfolg geleistet.

Nicht zuletzt danke ich meinen Eltern und meinem Bruder für ihre bedingungslose Unterstützung während meines gesamten Werdegangs. Ebenso gilt mein besonderer Dank meiner Frau und unseren beiden Töchtern für ihr außerordentliches Verständnis und ihre liebevolle Unterstützung während der Erstellung dieser Arbeit.

Abstract

The present thesis describes the experimental performance determination and numerical modeling of an aerostatic porous bearing made of an orthotropically layered ceramic composite material (CMC). The high temperature resistance, low thermal expansion and high reusability of this material makes it eminently suitable for use in highly stressed fluid-film bearing applications.

The work involves the development of an aerostatic journal bearing made of porous, orthotropically layered carbon fiber-reinforced carbon composite (C/C) and the design of a journal bearing test rig, which contained additional aerostatic support bearings and six optical laser triangulation sensors. The sensor system enabled the measurement of lubricant film thickness and shaft misalignment. As a result of the slight air lubrication clearance of 30 μm , the focus was on low concentricity and the determination of shaft misalignments.

The preliminary tests included the determination of the permeability of the porous material and the applicability of Darcy's law. A scan of the inner surface of the porous bushing revealed a characteristic grooved structure, which can be attributed to the layered structure of the material. Bearing tests were conducted up to a rotational speed of 8000 rpm and a pressure ratio of 5 to 7. No significant effect of rotational speed on load-carrying capacity and gas consumption was observed in this operating range. The examined operating points did not indicate any sign of the occurrence of the pneumatic hammer. A temporary load of below 90 N on the bearing and an eccentricity ratio below 0.8 did not cause any significant wear on the shaft.

Four numerical models, based on Reynolds' lubricant film equation and Darcy's law were developed. The models were gradually extended with consideration of shaft misalignment, the compressibility of the gas, the geometry of the pressure supply chamber and the embedding of the groove structure. The models were validated with external publications and the performed tests.

Numerous studies have investigated aerostatic porous bearings made of sintered metal and graphite. Current computational approaches to determine a fast preliminary design reached max. deviations of approximately 20 - 24 % compared to experimental tests. One of the central claims of this research was to extend this area of investigation by porous, orthotropically layered bearings made of C/C. The developed extended Full-Darcy model achieved a maximum deviation in the load-carrying capacity of 21.6 % and in the gas consumption of 23.5 %.

This study demonstrates the applicability of a resistant material from the aerospace field (reusable thrust chambers made of CMC) for highly stressed and durable fluid-film bearings. Furthermore, a numerical model for the computation and design of these bearings was developed and validated.

Kurzfassung

Die vorliegende Dissertation behandelt die Umsetzung, experimentelle Leistungsbestimmung und numerische Modellierung eines aerostatischen porösen Lagers aus einem orthotrop geschichteten keramischen Verbundwerkstoff (CMC). Die hohe Temperaturbeständigkeit, die niedrige thermische Ausdehnung und die hohe Wiederverwendbarkeit des Materials legen den Einsatz in hochbelasteten Fluid-Film-Lageranwendungen nahe.

Diese Arbeit umfasst die Entwicklung eines aerostatischen Lagers aus einem porösen, orthotrop geschichteten kohlenstofffaserverstärkten Kohlenstoff (C/C) und eines Prüfstands zur Bestimmung von statischen Leistungsparameter. Ein Gaslagerprüfstand bestehend aus zwei zusätzlichen aerostatischen Stützlagern und insgesamt sechs optischen Lasertriangulationssensoren wurde konzipiert und realisiert. Das Sensorsystem ermöglicht die Bestimmung der Schmierfilmdicke und des Wellenversatzes. Aufgrund des geringen Luftschmierspiels von $30\ \mu\text{m}$ lag der Fokus auf einem geringen Rundlauf und der Detektion von Wellenschiefstellungen.

Die Vorversuche umfassten die Bestimmung der Permeabilität des porösen Materials und dem Nachweis der Anwendbarkeit des Darcy'schen Gesetzes. Eine Analyse der Innenfläche des porösen Lagers ergab eine charakteristische Rillenstruktur, die auf den schichtweisen Aufbau des Materials zurückzuführen ist. Die Lagertests wurden mit einer Drehzahl von bis zu 8000 rpm und einem Druckverhältnis von 5 bis 7 durchgeführt. Im untersuchten Betriebsbereich wurde kein signifikanter Einfluss der Drehzahl auf die Tragfähigkeit und dem Gasverbrauch festgestellt. In den untersuchten Betriebspunkten wurde kein Auftreten des pneumatischen Hammers festgestellt. Eine temporäre Belastung des Lagers unter 90 N und ein Exzentrizitätsverhältnis unter 0.8 führten zu keinem signifikanten Verschleiß der Welle.

Zur Berechnung und Auslegung dieses Lagertyps wurden vier numerische Modelle auf der Grundlage der Reynolds'schen Schmierfilmgleichung und des Darcy'schen Gesetzes entwickelt. Die Modelle wurden schrittweise erweitert, indem die Wellenschiefstellung, die Kompressibilität des Gases, die Geometrie der Druckversorgung und die Einbettung der Rillenstruktur berücksichtigt wurden. Mithilfe externer Veröffentlichungen sowie der durchgeführten Tests wurden die Modelle validiert. In zahlreichen Studien wurden aerostatische poröse Lager aus gesintertem Metall und Graphit untersucht. Derzeitige Berechnungsansätze zur Ermittlung einer schnellen Vorauslegung erreichten im Vergleich zu experimentellen Versuchen maximale Abweichungen von etwa 20 - 24 %. Eine der zentralen Ziele dieser Arbeit war es, dieses Untersuchungsgebiet um poröse, orthotrop geschichtete Lager aus C/C zu erweitern. Das entwickelte erweiterte Full-Darcy-Modell erreichte eine maximale Abweichung in der Tragfähigkeit von 21.6 % und im Gasverbrauch von 23.5 %. Dieser Beitrag demonstriert die Anwendbarkeit eines widerstandsfähigen Werkstoffs für hochbelastete und langlebige Fluid-Film-Lager. Weiterhin wurde ein numerisches Modell zur Berechnung und Auslegung entsprechender Lager entwickelt und validiert.

Contents

Abstract	I
Kurzfassung	III
Nomenclature	VI
1 Introduction	1
1.1 Motivation	1
1.2 Classification	2
1.3 Objectives	4
1.4 Outline	5
2 Design of a Novel Journal Bearing made of Layered Porous C/C	6
2.1 Design of the Porous Liner and the Bearing Housing	6
2.2 Determination of Permeability	9
2.3 Surface Structure of the Porous Liner	17
2.4 Discussion of the Preliminary Tests	19
3 Experimental Determination of the Static Performance Parameters	21
3.1 Experimental Setup	21
3.2 Experimental Procedure	23
3.3 Experimental Results	24
3.3.1 Hysteresis Measurements	25
3.3.2 Load-Carrying Capacity and Vertical Misalignment	28
3.3.3 Gas Consumption	28
3.3.4 Orbit Measurements	31
3.3.5 Influence of Shaft Misalignment on Repeatability	32
3.4 Discussion of the Experimental Results	40
4 Numerical Models based on Reynolds' Lubricant Film Equation and Darcy's Law	42
4.1 Generalized Reynolds Equation for Fluid-Film Lubrication	43
4.2 Generalized Equation for Porous Liner Flow	47
4.3 Lubricant Film Width	48
4.3.1 Film Width with Shaft and Bushing Axis in Alignment	50
4.3.2 Film Width with Consideration of Shaft Misalignment	50
4.3.3 Film Width with Consideration of Shaft Misalignment and Surface Structure	51
4.4 Further Model Assumptions	55
4.4.1 Thermohydrodynamic Modelling	55

4.4.2	Turbulence in Lubricant Film	56
4.5	Developed models	59
4.5.1	Simple Model	59
4.5.2	Full Darcy	63
4.5.3	Full Darcy Compressible	67
4.5.4	Full Darcy Extended	72
5	Modeling with Computational Fluid Dynamics (CFD)	77
6	Analysis of Developed Numerical Models for Aerostatic Porous Journal Bearings	81
6.1	Mesh Independency and Computational Time	81
6.1.1	Simple	81
6.1.2	Full Darcy	84
6.1.3	Full Darcy Compressible	85
6.1.4	Full Darcy Plus	88
6.1.5	Computational Fluid Dynamics	92
6.2	External Validation	94
6.2.1	Hydrodynamic Porous Bearing	96
6.2.2	Aerostatic Porous Bearing made of Sintered Iron	99
6.2.3	Aerostatic Porous Bearing made of Sintered Graphite	101
6.3	Validation with Experimental Results of a Porous Orthotropic Layered Journal Bearing made of C/C	104
6.3.1	Load-Carrying Capacity	104
6.3.2	Gas Consumption	110
6.3.3	Analysis of the Pressure Distribution	115
6.4	Discussion regarding the Validity of the Models	121
6.4.1	Dynamic Bearing with Oil Lubrication	121
6.4.2	Aerostatic Bearing made of Sintered Metal	122
6.4.3	Aerostatic Bearing made of Sintered Graphite	122
6.4.4	Aerostatic Bearing made of Orthotropic Layered C/C	123
7	Conclusion	125
8	Perspectives	127
	Bibliography	128
	List of Figures	139
	List of Tables	142

Nomenclature

Symbols

α	Permeability	m^2
α_F	Forchheimer term	m
β	Misalignment angle	$^\circ$
δ	Deviation	-
Δ_B	Bearing number	-
\dot{m}	Mass flow rate	kg s^{-1}
γ	Vertical inclination angle of force transmission	$^\circ$
μ	Dynamic viscosity	Pa s
ϕ_a	Attitude angle	$^\circ$
Ψ	Permeability parameter	-
ρ	Density	kg m^{-3}
\tilde{u}_α	Combined standard uncertainty for the measurement of permeability	-
\tilde{u}_x	Standard uncertainty	-
ε_v	Vertical eccentricity ratio	-
ε_{vm}	Vertical misalignment ratio	-
φ	Circumferential direction	$^\circ$
φ_0	Angle of the smallest film width	$^\circ$
A	Cross area of cylindrical porous sample	m^2
C	Convergence criteria	-
c	Radial clearance	m
e'	Misaligned eccentricity	m
e	Eccentricity	m
F	Load-carrying capacity	N
F^*	Static load-carrying capacity	-

F^{\sim}	Dynamic load-carrying capacity	–
h	Lubricant film width	m
h_{tex}	Profile of inner bearing surface	m
Kn	Knudsen number	-
L	Length of porous bushing	m
l_c	Charecteristic length	m
N	Number of nodes	-
n	Rotational speed	min^{-1}
p	Absolute Pressure	Pa
p_1	Upstream pressure	Pa
p_2	Downstream pressure	Pa
p_a	Athmospheric pressure	Pa
p_s	Supply pressure	Pa
Q	Flow rate	m s^{-3}
q_n	Norm flow rate	$\text{l}_n \text{min}^{-1}$
r	Radius direction	m
R_1	Radius shaft	m
R_2	Inner radius bushing	m
R_a	Average roughness	m
R_s	Outer radius bushing	m
R_g	Specific gas constant	$\text{J kg}^{-1} \text{K}^{-1}$
Re	Reynolds number	-
T	Temperature	K
t	Thickness of porous bushing	m
T_n	Temperature at standard conditions	K
t_s	Thickness of cylindrical porous sample	m

Ta	Taylor number	-
U	Velocity	m s^{-1}
u	Velocity	m s^{-1}
V	Vertical displacement	m

Indices

4022 DIN EN ISO 4022:2018-12

φ Circumferential coordinate

a Parameter on shaft

b Parameter on inner bearing surface

r Radius coordinate

x x-coordinate

y y-coordinate

z Axial coordinate

Acronyms / Abbreviations

% FS Percentage of full scale

% RD Percentage of reading

Bc Boundary condition

C/C Carbon fibre-reinforced Carbon

CFD Computational fluid dynamics

CMC Ceramic matrix composite

Exp Experiment

FD Full Darcy

FD+ Full Darcy extended

FDc Full Darcy compressible

Ge Governing equation

GREL General Reynolds equation for lubricants

NS Navier-Stokes

Ref Reference

REL Reynolds equation for lubricants

RTD Resistance temperature detector

SEM Scanning electron microscope

Si Simple

STD Standard deviation

1 Introduction

1.1 Motivation

Low friction, high speeds, high-precision positioning and homogeneous pressure distribution are the advantages of aerostatic porous bearings in turbomachinery. The use of an air bearing obviates the need for oil or grease in the application, which provides an ecological advantage and simplifies the design [69]. In addition, lubricants such as oil and grease can cause contamination of the process medium and require costly and complex seals [100].

Air bearings are used in a wide variety of applications, for example, in medical applications, such as dental air turbines [42]; high precision applications [30, 86]; high speed propulsion systems [113]; or in clean room environments such as the microelectronics industry [53] and even in seismic isolation systems [51].

A summary of applications in turbomachinery was presented by Barnett and Silver in 1970 [8] and Agrawal in 1997 [1]. These included air-cycle applications in aircrafts, trucks, tractors and ships. Consequently, air bearings have been used in turbochargers and compressors.

Another application area is the use of air lubrication in micro gas turbines. Bearing investigations of foil air-bearings made of nickel-based superalloys at process temperatures of up to 650 °C have been conducted [35]. In particular, the high temperatures on the turbine side posed challenges to bearing development and led to the investigation of an additional cooling flow and its thermal influence on the performance [75, 96, 99, 107].

Fluid-film bearings made of ceramic matrix composites (CMC) are a promising alternative. The material has high temperature resistance and low thermal expansion [55]. In 2002, Leuchs and Mühlratzer [76] presented a brief overview of tests performed on CMC bearings. Hydrodynamic bearings made of wound silicon carbide fibers have demonstrated low wear in water pump applications, and the elastic material properties prevent the risk of brittle fracture under critical operating conditions [52, 71]. Furthermore, tests performed by Dogigli et al. [40, 76] at temperatures of up to 1600 °C have shown the potential for high temperature applications. Uhlmann and Neumann [116] performed experimental investigations of bearings made of wounded silicon carbide composites with external air pressurization. The porous material has positive properties, such as a uniform pressure distribution based on a large number of micropores. Measurements included the determination of the load-carrying capacity and stiffness.

New materials are being developed or transferred from other development areas due to the high demands on bearings. In this study, a bearing made of carbon fiber-reinforced carbon (C/C) developed by the German Aerospace Center is designed and investigated. This CMC material was originally developed for reusable thrust chambers in liquid rocket engines [59]. The developed CMC thrust chambers are subject to high temperature gradients due to combustion and transpirational cooling with cryogenic propellant [55]. The positive properties of the material have been determined experimentally in thrust chamber tests

[89] and simulated numerically [85]. These high temperature gradients cause high thermal and structural mechanical stresses on the material. The positive material properties of these composites, such as structural integrity, durability, thermal load capacity and manufacturing controlled adjustment of porous properties are compatible with the requirements of a porous bearing in turbomachinery.

In this study, an aerostatic journal bearing is designed, based on a porous bushing made of C/C, and the static performance characteristics are experimentally determined. Furthermore, software was developed to map the specific properties of the bearing and validate it with experimental data. The investigations serve to assess a material developed in the aerospace industry for use in bearing technology and to develop a suitable software for performance computation and preliminary design generation.

1.2 Classification

Air bearings can be divided into different categories. The classification in Figure 1.1 has been adapted to the divisions of Hamrock [60], Al-Bender [2] and Someya [109]. As a consequence of the large number of design possibilities for fluid-film bearings, only certain categories have been enumerated.

The first category for the classification of the bearings is the direction of the load. The

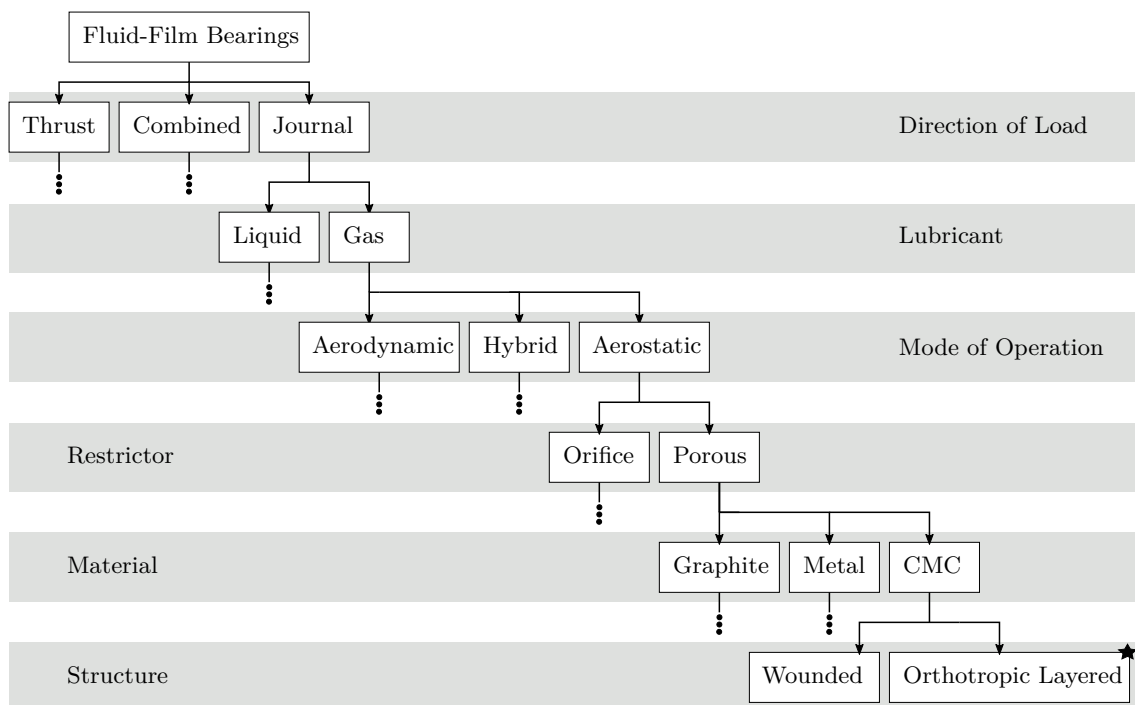


Figure 1.1: Types of fluid-film bearings

direction of load-carrying capacity of thrust bearings is oriented in an axial direction [101] and that of journal bearings in a radial direction [17]. Special designs that include both force components include trapezoidal bearings [73] and spherical bearings [31]. In this study, the focus is on journal bearings.

Depending on the application, liquid or gaseous fluids are used for fluid-film lubrication. The choice of fluid has an influence on the geometry of the bearing, such as on the film width and the numerical requirements. This study mainly focused on gas lubrication. In addition, two numerical models were validated with the experimental investigations of Mokhtar et al. [84]. Mokhtar et al. investigated dynamic, oil-lubricated porous bearings. The mode of operation can be divided into three types. Aerodynamic bearings, such as foil bearings [19] or spiral groove bearings [126] are mainly used in high-speed applications. These self-acting bearings generate the load-carrying capacity through the aerodynamic effect of a high circumferential speed. Hybrid bearings additionally use the aerostatic effect of an external feed [68, 110]. Aerostatic bearings generate a load-carrying capacity even with a stationary shaft, but require an external pressure supply and a restrictor. To establish a dependence of the pressure distribution on the lubrication gap height, aerostatic bearings use flow restrictors. The most common restrictors are micro-orifices and porous materials. Micro-orifices include annular orifices and simple orifices [12]. A porous material is basically a multitude of micro-nozzles that enables a uniform pressure distribution.

Furthermore, bearings can differ in the manufacturing processes and materials. The majority of studies have been conducted with sintered metal mixtures [25, 108] or graphite [61, 77]. Ceramic matrix composites produced by the gradient chemical vapor infiltration (CVI) processes were also successfully investigated experimentally by Uhlmann and Neumann [116] with a wound structure of a silicon carbide (SiC) fiber-reinforced composite. In the present study, the layers were applied two-dimensionally. The orthotropic layered material of carbon fiber-reinforced carbon (C/C) composite was produced by polymer impregnation and pyrolysis (PIP) [104].

The schematic structure of the orthotropic layered porous bushing is shown in Figure 1.2. A bushing is extracted from a composite plate consisting of $0^\circ/90^\circ$ and $\pm 45^\circ$ arranged layers. The ceramic called "Oetra" [39] consist of carbon and aramid fibers. Through the pyrolysis process, the aramid fibers dissolve and a multitude of micro channels are formed. The ratio of aramid and carbon allows the adjustment of the parameters of flow coefficients, such as permeability.

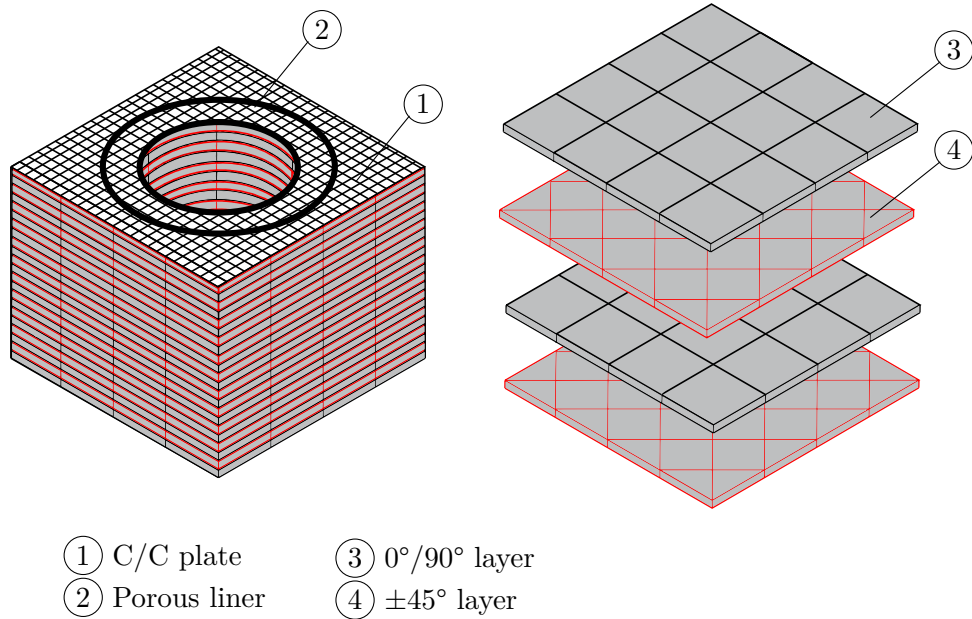


Figure 1.2: Schematic concept of the orthotropic layered structure [102]

1.3 Objectives

This study focuses on the implementation of a material originally developed for aerospace applications in bearing design. The positive material properties should result in resistant and durable new types of bearings. This study deals with the assessment of the suitability of the material for aerostatic air lubrication and the experimental determination of the static performance parameters. Numerical models based on the specific characteristics of the bearing are developed. The models are validated with experimental data and able to compute the performance of an aerostatic bearing made of an orthotropic layered material with minimal computational resources. The thesis focuses on the following three points:

- Design of a porous journal bearing made of orthotropic layered carbon fiber-reinforced carbon
- Design of a journal bearing test rig with low concentricity and experimental determination of static performance parameters under consideration of a minor misalignment
- Development of a numerical model for a pre-design of a pressurized porous journal bearing with an orthotropic layered texture

1.4 Outline

The outline of the manuscript is as follows:

- **Chapter 2** discusses the design of the bearing and the preliminary investigations of the CMC material. The preliminary investigations include the determination of the permeability coefficients and the classification of the flow through the porous material (laminar or turbulent). The texture of the inner surface of the bushing is captured with a stylus instrument and used in the procedure for the numerical modelling of the test specimen.
- **Chapter 3** concerns the design of an aerostatic journal bearing test rig and the subsequent experimental determination of the static performance parameters. Based on the low film width of air bearings, a test rig with low concentricity was engineered. Furthermore, the setup enables the determination of shaft misalignment. The tests include three supply pressures in the range of 5 to 7 bar and a rotational speed of 1000 to 8000 rpm. The measurements include the determination of the load-carrying capacity and the gas consumption with consideration of the shaft misalignment. Orbit plots indicate the concentricity of the shaft and identify possible instabilities. The repeatability of the measurements is investigated in terms of performance and shaft misalignment during hysteresis measurements.
- **Chapter 4** focuses on the derivation and development of numerical bearing models. The derivation of general equations for the computation of flows in the lubricant film and through porous bushings is included. The lubricant film thickness equation includes the approaches of an ideal shaft eccentricity without misalignment, with misalignment, and an approach to implement the structure of the bushing inner surface. The definition of the bushing structure is based on the experimental sampling of the bushing inner surface and the generation of an averaged groove pattern. This is followed by a description of four numerical models with increasing complexity for the computation of an aerostatic air bearing.
- **Chapter 5** describes the modeling of the aerostatic journal bearing using commercial CFD (computational fluid dynamics) software.
- **Chapter 6** discusses the evaluation of the numerical models. A mesh independence study of the developed models and the CFD model is performed. The developed models are validated and evaluated with external publications. Subsequently, the conducted experiments on the CMC bearing are used to validate the numerical models. An evaluation of the numerical models for the simulation of an aerostatic bearing made of a porous orthotopic layered structure is presented.

2 Design of a Novel Journal Bearing made of Layered Porous C/C

In this chapter, the design of the bearing specimen is presented and the properties of the porous liner are investigated experimentally. The permeability is determined using a sample of the porous material. In a further experimental investigation, the inner surface of the test bushing is measured with a stylus sensor, which results in a specification of the surface structure and the basis for the conversion of the texture into a numerical model.

2.1 Design of the Porous Liner and the Bearing Housing

The main component of the test housing is a porous liner made of carbon fiber-reinforced carbon (C/C), which is encased in an aluminum liner (see Figure 2.1). Compressed air is passed through 20 round openings of the aluminum liner. Twenty slots on the outer

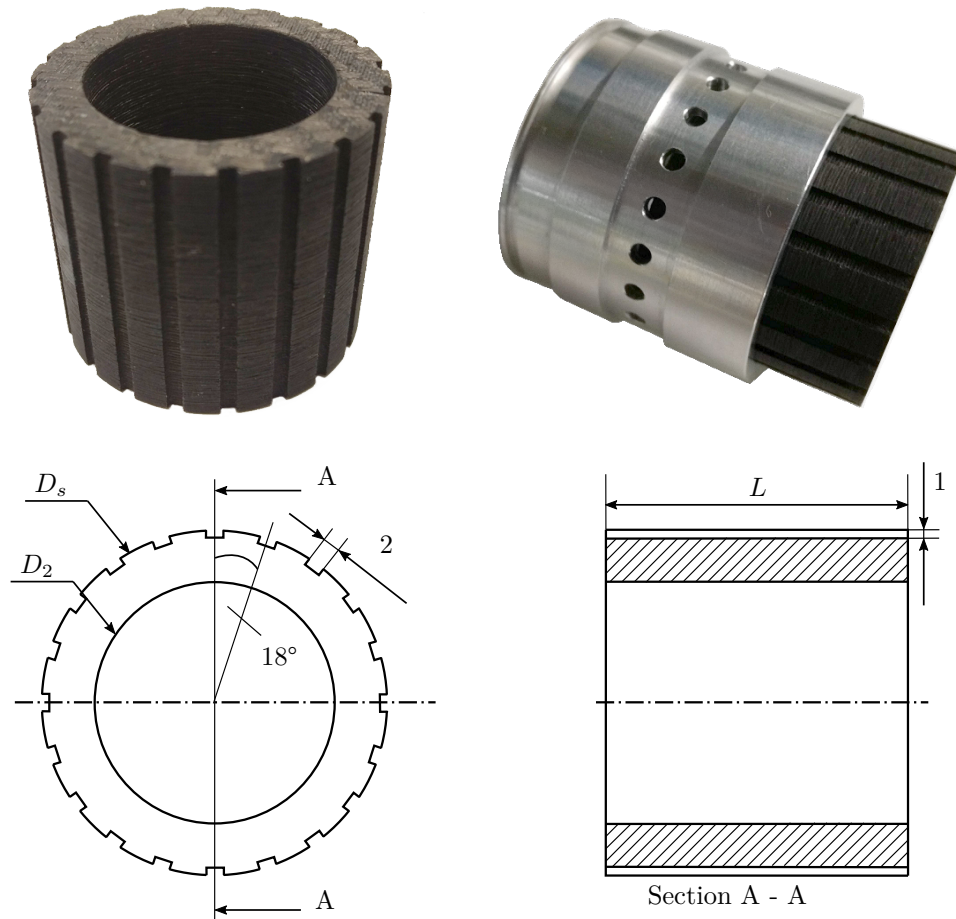


Figure 2.1: Top: C/C and aluminum liner, bottom: dimensions of the C/C liner [102]

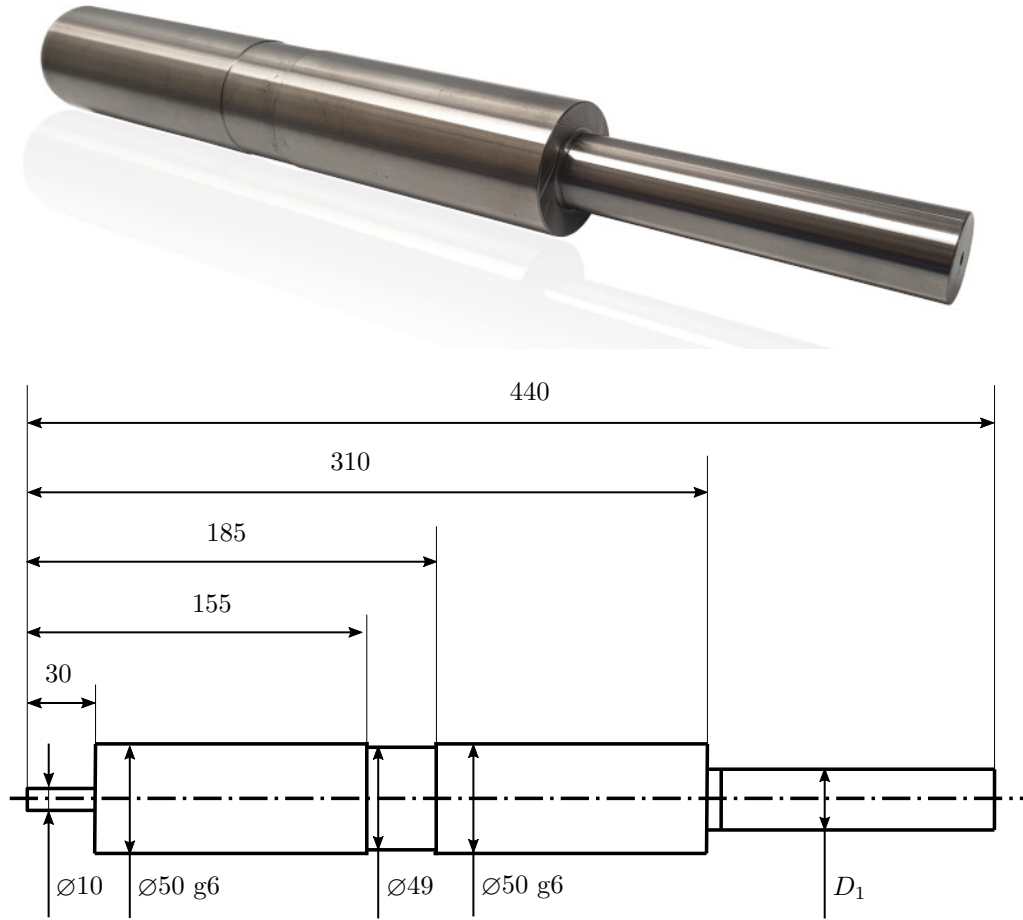


Figure 2.2: Top: shaft after the performed experiments, bottom: dimensions of the shaft [102]

diameter of the porous liner lead to a uniform distribution of the pressurized air. The length of the porous liner is $L = 35$ mm and has an outer diameter of $D_s = 40$ mm. The inside diameter of the porous liner was measured with an inside micrometer and is $D_2 = 28.120$ mm \pm 0.010 mm.

The shaft for the tests was made of 100Cr6 and the surface was machined in a multiple grinding process. The shaft is connected to the motor at the 10 mm shaft diameter with an elastomer coupling. The contact surfaces with a diameter of 50 mm g6 are used by two aerostatic support bearings. The outside diameter of the shaft at the shaft/bearing contact surface was measured with an outside micrometer and is $D_1 = 28.060$ mm \pm 0.001 mm. The radial clearance c of the C/C bearing is the difference between the inner radius of the porous bushing R_2 and the radius of the shaft R_1 :

$$c = \frac{D_2}{2} - \frac{D_1}{2} = R_2 - R_1 = 0.030 \text{ mm} \pm 0.006 \text{ mm} \quad (2.1)$$

The designed assembly of the housing and the shaft is shown in Figure 2.3. A pneumatic port is located on the underside of the housing. The compressed air is distributed through the described holes through the aluminum liner to the surface of the porous liner. The pressurized air is directed through the porous liner and serves as a lubricating film between the liner inner surface and the shaft surface. The air is released into the atmosphere at the axial ends of the housing. There are O-rings between the aluminum liner and the housing and between the aluminum liner and the porous liner to guide the medium through the housing and prevent leakage (see Figure 2.4).

A connection for a force sensor and the force transmission is located on top of the test housing. Horizontal and vertical displacement sensors are located at each axial end of the housing. Optical triangulation sensors were used to determine the lubrication film thickness. The assembly of the bearing housing mounted on the test stand is shown in Figure 2.5.

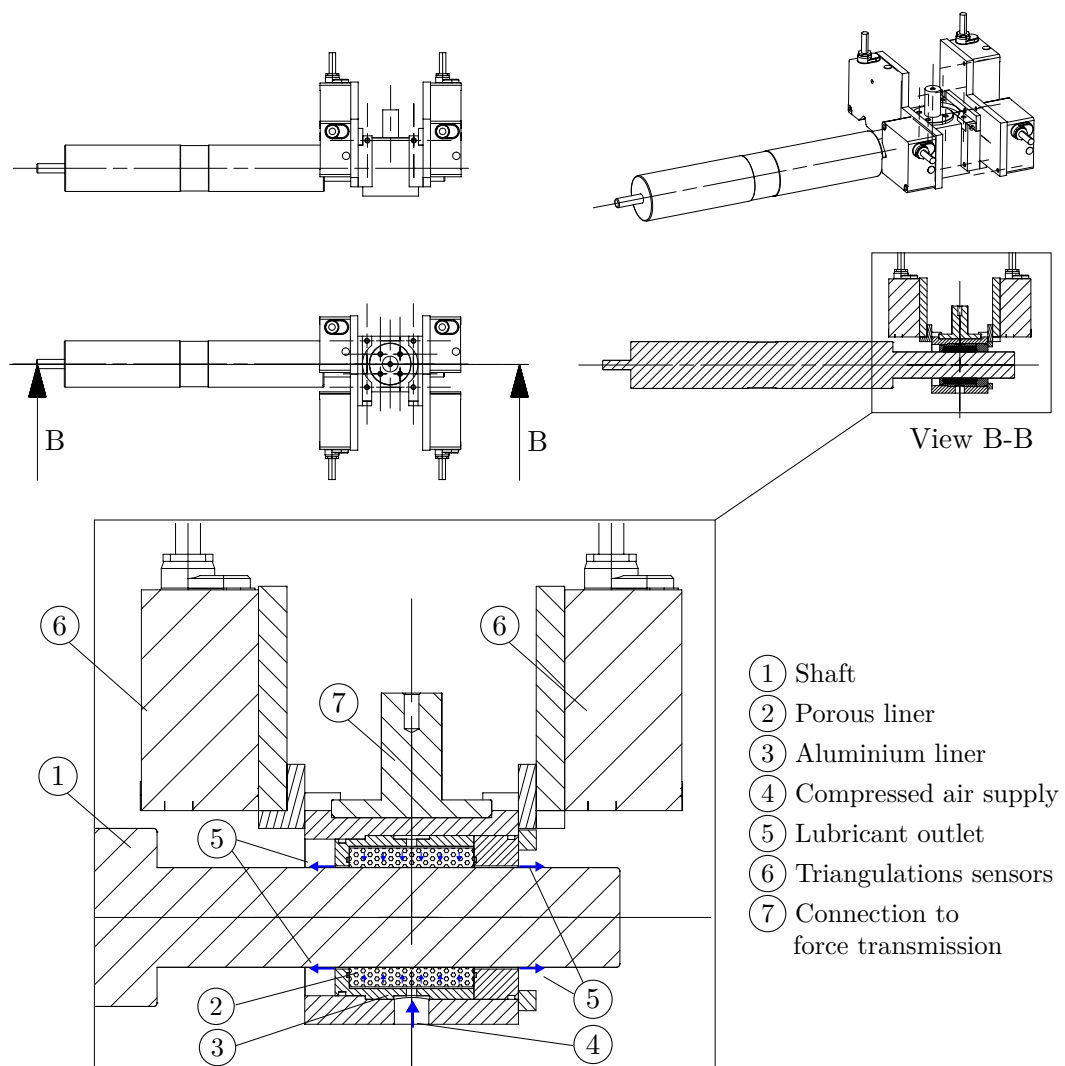


Figure 2.3: C/C bearing housing



Figure 2.4: Seals of the aluminium liner

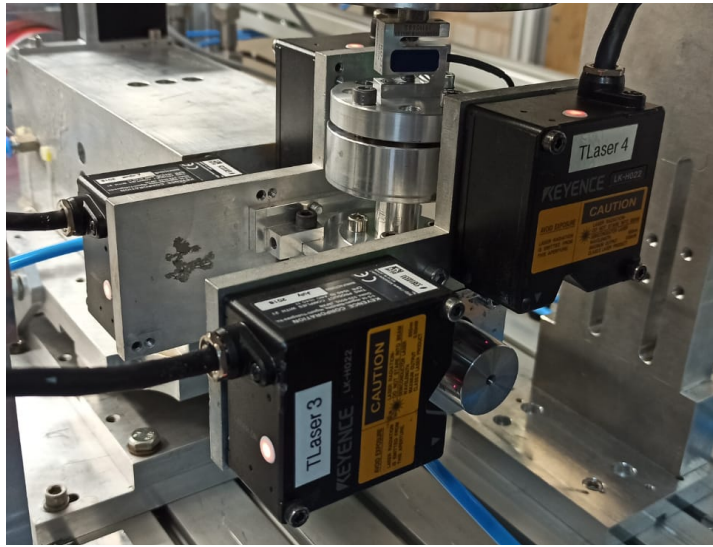


Figure 2.5: Assembly of the bearing test housing

2.2 Determination of Permeability

The following experimental examinations were performed to determine the flow coefficients of the C/C material. These material properties were used in the further procedure for numerical modeling.

Darcy's law (equation 2.2) states that the velocity u through a porous material is proportional to the pressure gradient through the porous sample $\partial p/\partial x$. The dynamic viscosity is defined as μ and the permeability as α .

$$\frac{\partial p}{\partial x} = -\frac{u \cdot \mu}{\alpha} \quad (2.2)$$

During the course of the investigation, the material dependent permeability term α was determined. Darcy's law is valid for laminar flow through porous materials [18]. Due to its restricted applicability, the validity of Darcy's law for this study is discussed. At higher Reynolds numbers the relationship between the velocity through the porous material and

the pressure gradient is no longer linear. The Forchheimer term provides a possibility to extend the validity of Darcy's law for higher Reynolds numbers [74, 120]. The Forchheimer constant α_F represents a second material constant and the influence of inertial forces.

$$\underbrace{-\frac{\partial p}{\partial x}}_{\text{Darcy law}} = \underbrace{\frac{u \cdot \mu}{\alpha}}_{\text{Darcy law}} + \underbrace{\frac{u^2 \cdot \rho}{\alpha_F}}_{\text{Forchheimer term}} \quad (2.3)$$

Experimental Setup und Results

To determine the material properties, a cylindrical C/C specimen was experimentally tested. The cylindrical sample, as well as the porous liner, are taken from a C/C plate with $0^\circ/90^\circ$ and $-45^\circ/45^\circ$ layers (see Figure 2.6). Permeability measurements are made by axial flow through the porous sample. As shown schematically in Figure 2.6, the experimentally determined permeability value of the cylindrical sample corresponds to the permeability of the liner in the radial α_r and circumferential α_φ directions.

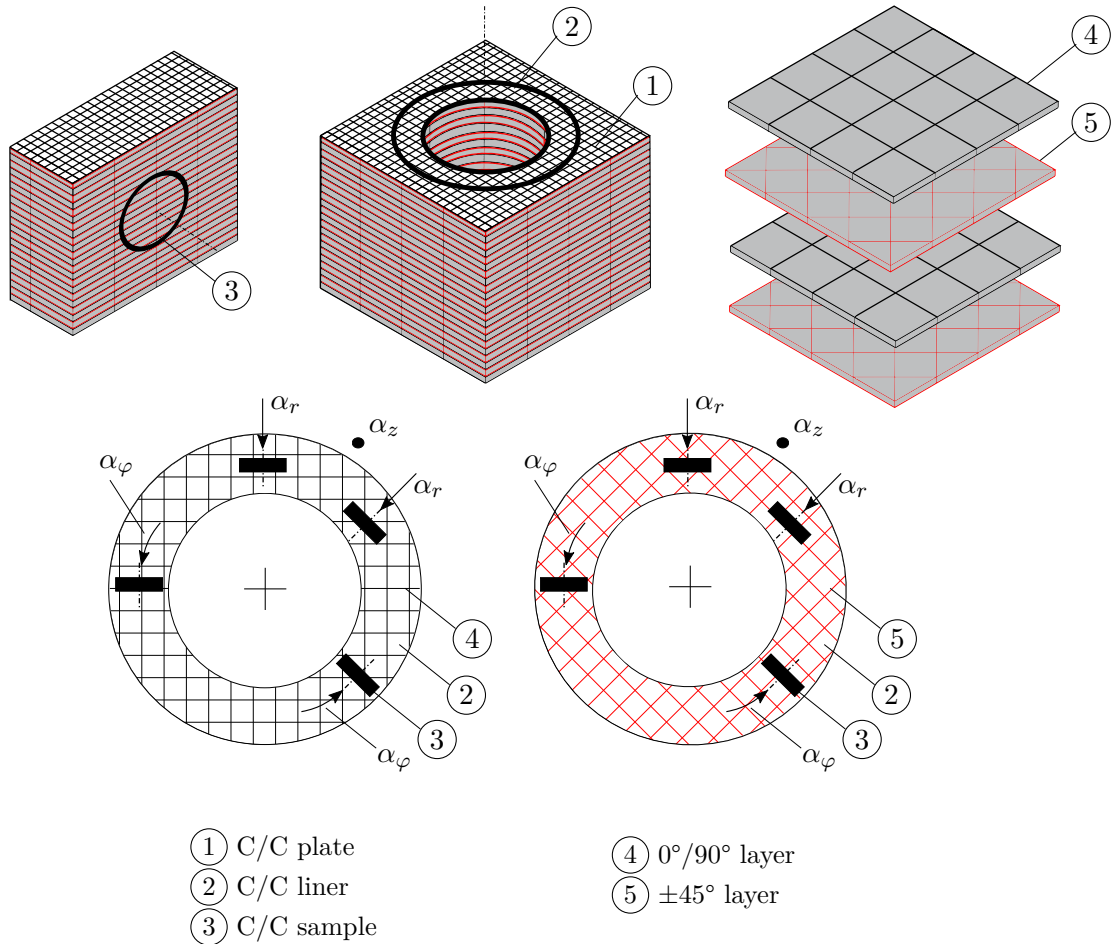


Figure 2.6: Porous C/C sample for permeability measurements

On the permeability test stand (see Figure 2.7 and Figure 2.8) the cylindrical C/C sample was clamped between two flanges and sealed with flat gaskets and hardened sealant. The sample was impinged with twice-filtered and dried compressed air. The specimen had a thickness of 6 mm and the contact area a radius of 13.8 mm (uncertainty of caliper: 0.02 mm). The flow rate was measured with a turbine flow meter (uncertainty: 1.5% RD + 0.5% FS) and adjusted with a control valve. The temperature is measured with a Pt100 resistance temperature detector (RTD) class A (uncertainty based on standard DIN EN 60751:2009-05: $1.5\text{ }^{\circ}\text{C} + 0.002\text{ }^{\circ}\text{C} \cdot T$ [37]). The pressure difference upstream and downstream of the C/C sample was determined with relative pressure sensors (uncertainty: 0.03% FS). In the following, the measured relative pressures are given as absolute pressures. To determine the flow coefficients, the differential pressure was increased up to 6 bar, and the flow rate was measured. This level of pressurization is representative and comparable with the following C/C bearing investigations. In the following, the formula for the determination of permeability is derived on the basis of Belforte et al. [13].

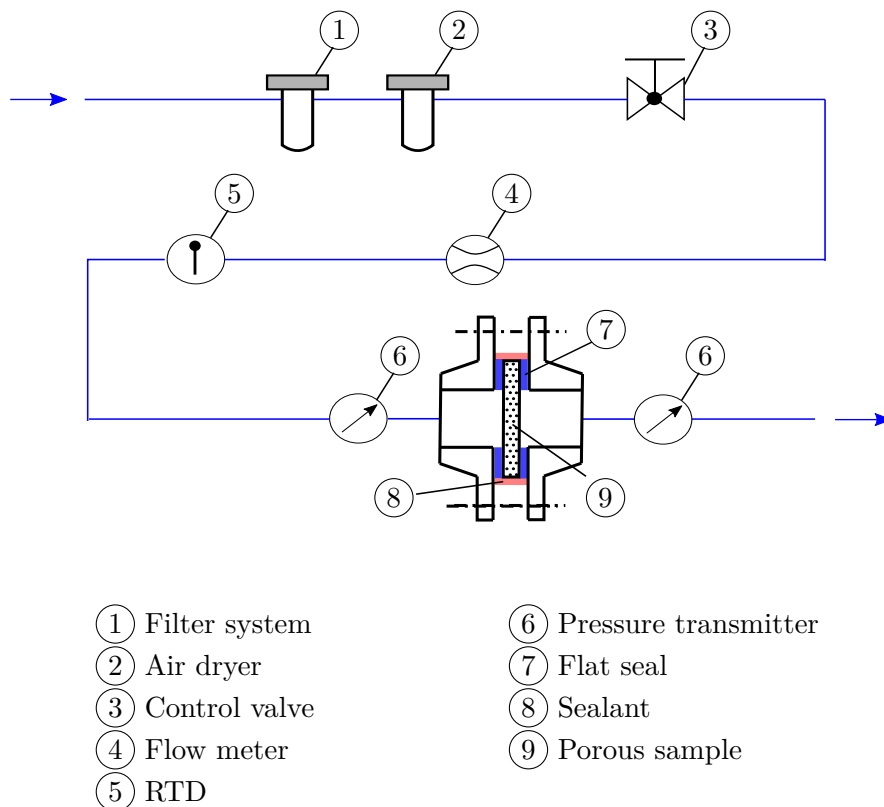


Figure 2.7: Concept of the permeability measurement



Figure 2.8: Instruments for determining the flow coefficients

For the experimental determination of the permeability, the flow rate Q through the porous medium was determined with a flow meter. The velocity u can be expressed by the density of air ρ , the cross-section of the sample A and the mass flow rate \dot{m} .

$$u = \frac{Q}{A} = \frac{\dot{m}}{\rho \cdot A} = \frac{\dot{m}}{\rho \cdot \pi \cdot r^2} \quad (2.4)$$

The pressure gradient in the flow direction was determined by measuring the pressure upstream of the sample p_1 and downstream of the sample p_2 . The thickness of the sample is t_s .

$$\frac{\Delta p}{\Delta x} = \frac{p_2 - p_1}{t_s} \quad (2.5)$$

ρ is the average density between pressure p_1 and p_2 . This value was determined with the use of the ideal gas equation. The specific gas constant of air is defined as R_g and the temperature as T .

$$\rho = \frac{p_1 + p_2}{2 \cdot R_g \cdot T} \quad (2.6)$$

Inserting the equations 2.4 to 2.6 into the equation 2.2 leads to the formula for the experimental determination of permeability.

$$\alpha = \frac{2 \cdot R_g \cdot T \cdot \dot{m} \cdot t_s \cdot \mu}{\pi \cdot r^2 \cdot (p_1^2 - p_2^2)} \quad (2.7)$$

The determined differential pressures $p_1 - p_2$ were plotted against the mass flow rate \dot{m} and the permeability in Figure 2.9. The differential pressures were between 3 and 6 bar. The subsequent bearing tests were performed with the supply pressures $p_s = 5, 6$ and 7 bar. The determined permeabilities for the three operating points were determined using equation 2.7. The values of the permeabilities in the operating range varied by 26.7%. The combined standard uncertainties \tilde{u}_α for the permeability values were determined by equation 2.8 based on standard JCGM 100:2008 [65]. The standard uncertainties \tilde{u}_{x_i} of the quantities were given on the basis of the calibration records (type B evaluation [65]).

$$\tilde{u}_\alpha = \sqrt{\sum_{i=1}^N \left(\frac{\partial \alpha}{\partial x_i} \cdot \tilde{u}_{x_i} \right)^2} \quad x_i = L, \dot{m}, T, A, p_1, p_2 \quad (2.8)$$

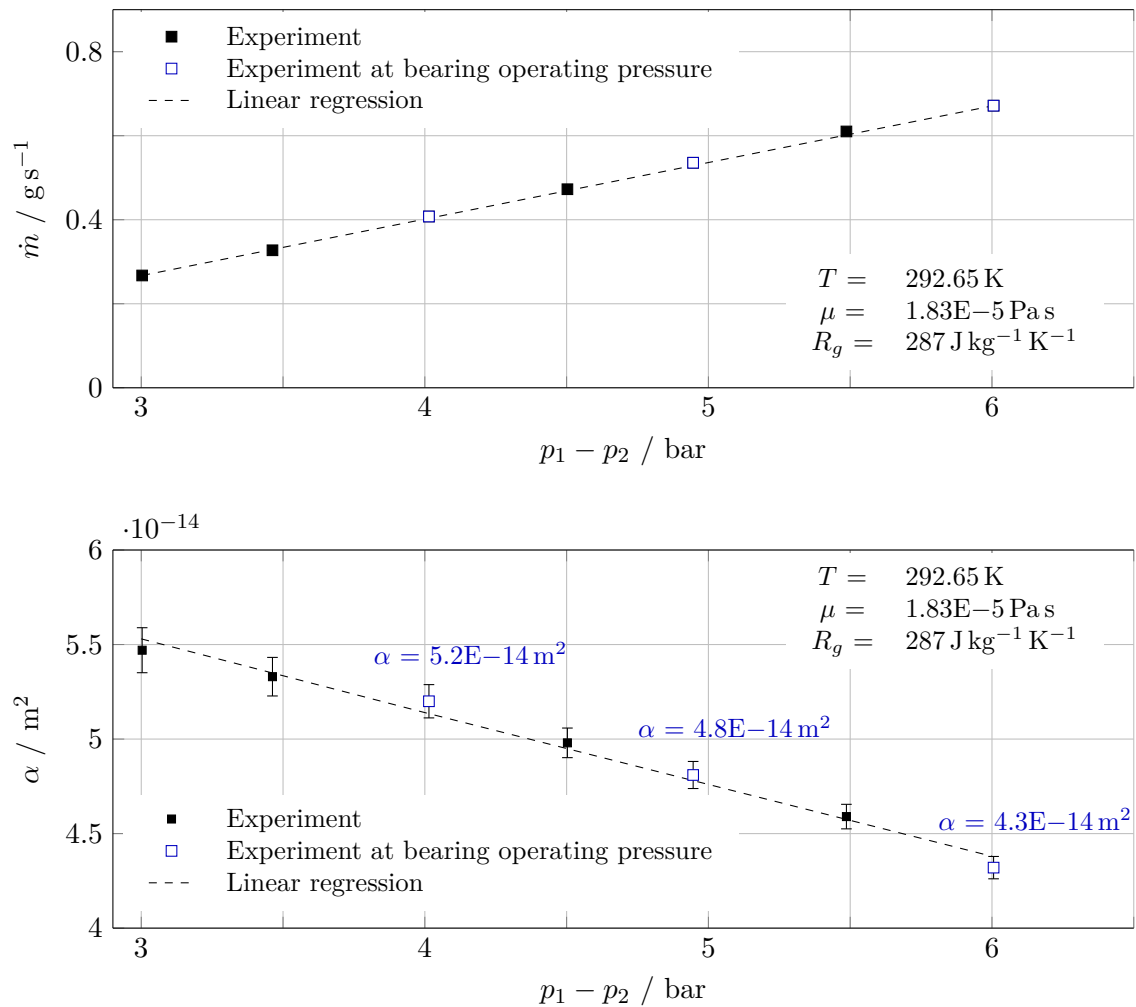


Figure 2.9: Experimental results of permeability measurements

Validity of Darcy's Law

To assess validity, three common approaches from the literature are described in the following. The approaches are the qualitative proportionality between the mass flow rate \dot{m} and the term $p_1^2 - p_2^2$, the Reynolds number based on the grain size of the porous material, and the coefficient of Taylor and Lewis [115], based on the ratio of the viscous and the inertial terms.

Sneck and Elwell [108] and Fleder et al. [48] have shown the applicability of Darcy's law by a comparison of the mass flow rate versus the difference in the squares of the upstream and downstream pressures. A linear plot shows proportionality. In our experiment, a linear curve and a second-order polynomial curve were plotted by the measuring points. Both curves sufficiently represent the course of the measuring points and, consequently, the viscous term is the dominating component.

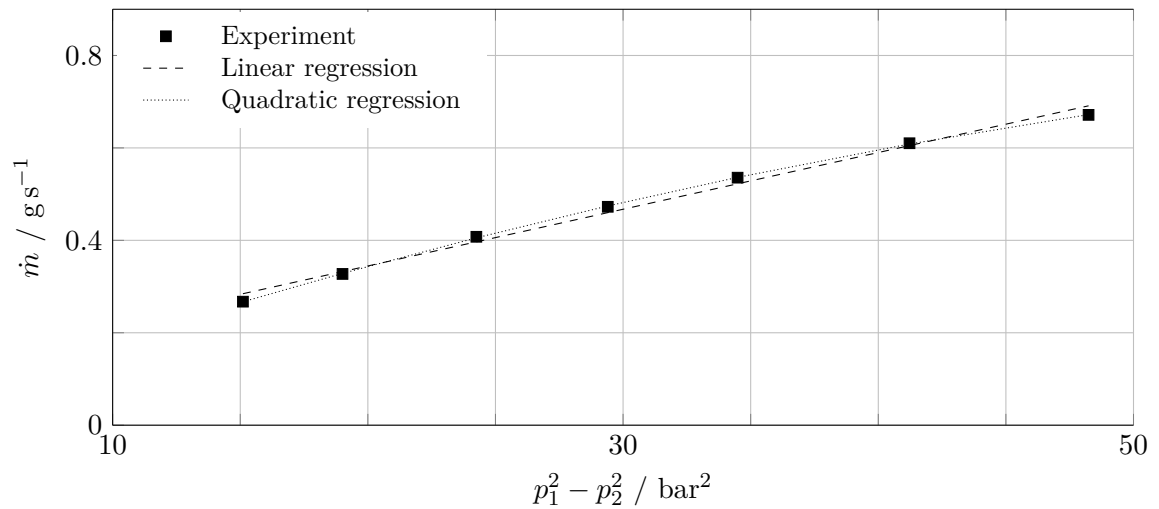


Figure 2.10: Applicability of Darcy's law

The dimensionless Reynolds number Re can be used to determine whether the flow is laminar or turbulent and therefore whether Darcy's Law applies. Depending on the application, empirical data is available and an associated characteristic length is selected. Re provides the ratio between the viscous and inertial forces of the flow [98]. The equation is formed with the dynamic viscosity of the fluid μ , the flow velocity u and the characteristic length l_c :

$$Re = \frac{\rho \cdot c \cdot l_c}{\mu} \quad (2.9)$$

Pipe flows represent a well-known application, and the transition process has been intensively studied [34, 43]. In the context of pipe flows, the pipe diameter was chosen as the characteristic length. Experiments and computationally intensive direct numerical simulations by Avila et al. [7] have shown that a Reynolds number of approximately 2040

represents the onset of a turbulent flow. The Reynolds number is commonly used to assess the type of flow through a porous body and has been widely used in investigations using sintered metal as a porous medium [13, 28, 54, 128]. The mean grain diameter is used as the characteristic length due to the structure. According to Bear [10], Darcy's law is valid, provided that the Reynolds number does not exceed a value of 10.

In contrast, the C/C probe and the tested C/C bushing were produced via the PIP method and has a layered structure. Figure 2.11 depicts a scanning electron microscope image (SEM) of a C/C sample. For comparison, corresponding SEM images of sintered metal samples can be found in the study by Zhong et al. [128]. The powder form of the raw material before the sintering process shows the recurring round grain size. During the pyrolysis of the C/C sample, aramid fibers were dissolved, forming fractures. Furthermore, it is clear that the directional sense of the fibers also affects the flow. The surface structures of a sintered material and a layered material are not comparable. Thus, the Reynolds number, which is based on the grain diameter as the characteristic length, provides an inadequate evaluation of whether the flow in the porous bushing is laminar or turbulent.

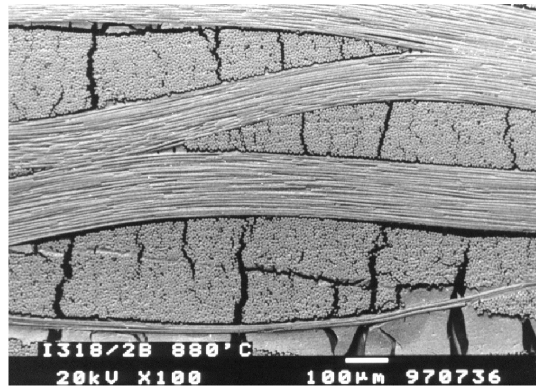


Figure 2.11: SEM image of a C/C sample made by PIP [59]

Taylor and Lewis used a different approach [115]. With equation 2.10, the authors address the basic idea of the Reynolds number, namely the ratio of the viscous and inertial forces. The viscous component corresponds to the permeability term α , and the inertia term corresponds to the inertial coefficient α_F . With the dynamic viscosity μ , the density ρ and the pressure drop in the flow direction, the ratio is de-dimensioned. The authors provide a range of less than 1 as a range for the use of the simple Darcy's law.

$$\left| \frac{\rho \cdot \alpha^2}{\mu^2 \cdot \alpha_F} \cdot \frac{\partial p}{\partial x} \right| \ll 1 \quad (2.10)$$

The permeability α_{4022} as well as the inertia coefficient $\alpha_{F,4022}$ were formed with equation 2.11, following standard DIN EN ISO 4022:2018-12 [38]. The obtained terms are presented in Figure 2.12. In the examined operating pressure range, coefficients of below 0.81 were obtained. Thus, the application of Darcy's law is valid.

$$\frac{(p_1 - p_2) \cdot A}{t_s \cdot Q \cdot \mu} = \frac{1}{\alpha_{4022}} \cdot \frac{Q \cdot \rho}{A \cdot \mu} + \frac{1}{\alpha_{F,4022}} \quad (2.11)$$

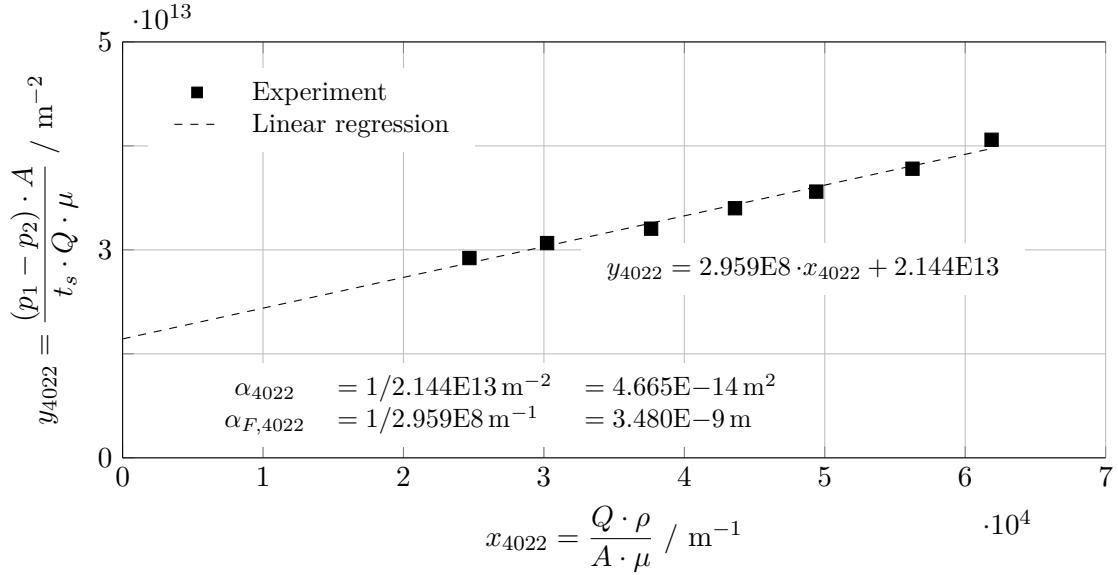


Figure 2.12: Determination of fluid permeability coefficients according standard DIN EN ISO 4022:2018 [38]

Klinkenberg Effect

The permeability coefficient depends on the material and is independent of pressure and flow rate [54]. However, deviations from the permeability constant were observed in the results of this experiment. These can be explained by Klinkenberg's gas slip theory [70]. The laminar gas flow through the porous channels can no longer be assumed to be Poiseuille flow. The molecules have a velocity component in the main flow direction near the wall before they collide with the wall. In this experiment, the velocity component in the main flow direction did not decrease to a value of zero after the impact. Consequently, the resulting slip led to a higher flow rate than a comparative Poiseuille flow.

The present results evidenced an nearly linear increase in the permeability over the reciprocal of the pressure difference (see Figure 2.13). According to Klinkenberg, this quasi-linear curve can be associated with slip [70].

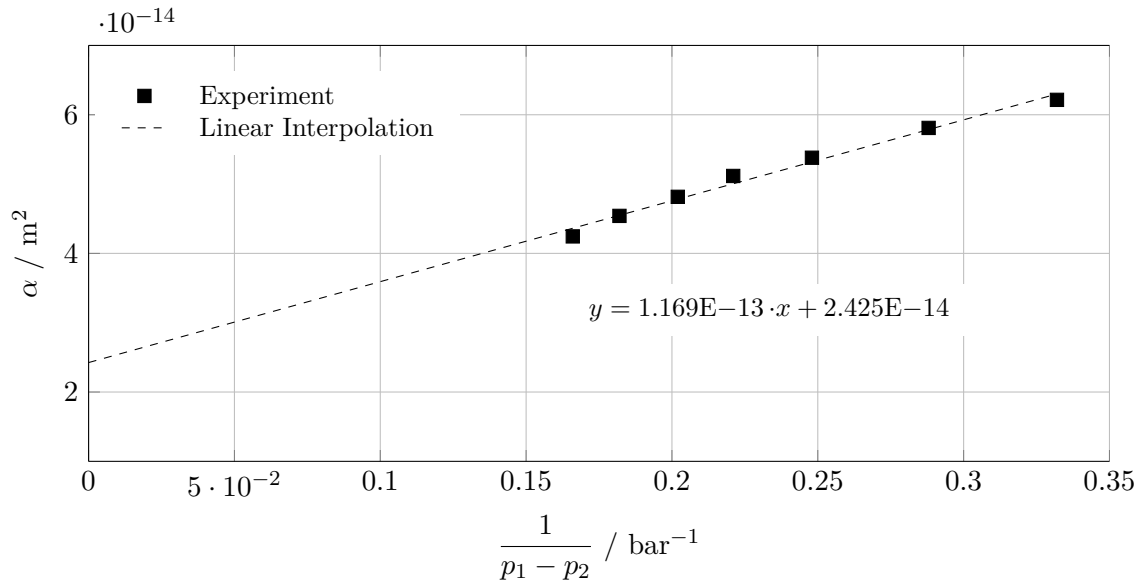


Figure 2.13: Klinkenberg effect

2.3 Surface Structure of the Porous Liner

The porous contact area was measured tactilely with a 0.5 mm measuring tip (see Figure 2.14). The measuring distance L was traversed axially with a step size of $0.5 \mu\text{m}$. Two measuring runs were performed at the positions $\varphi = 0^\circ$ and $\varphi = 180^\circ$.

Grooves of up to $130 \mu\text{m}$ were determined in the axial direction, which can be related to the layered structure of the porous composite material. The centerline of the diagrams corresponded to an equal ratio of surface areas on both sides (see Figure 2.15). In addition, a probability distribution was provided on each series of measurements. The highest distribution value, based on the Gauss interpolation, was marked as a reference line. This resulted in a reference line at $r = 6.231 \mu\text{m}$ for the measurement series $\varphi = 0^\circ$ and a value of $r = 8.643 \mu\text{m}$ for $\varphi = 180^\circ$.

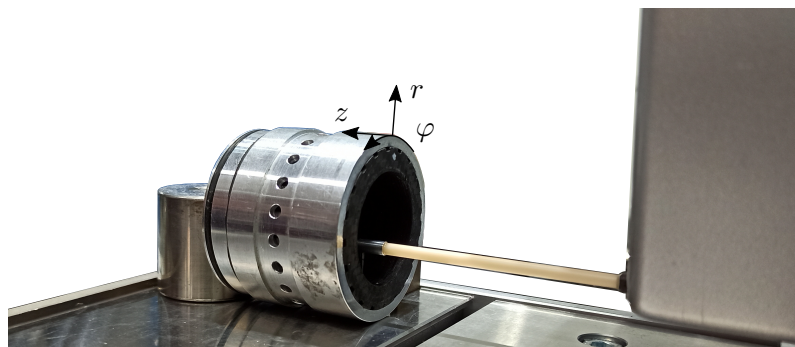


Figure 2.14: Experimental setup for determining the inner surface texture of the porous liner

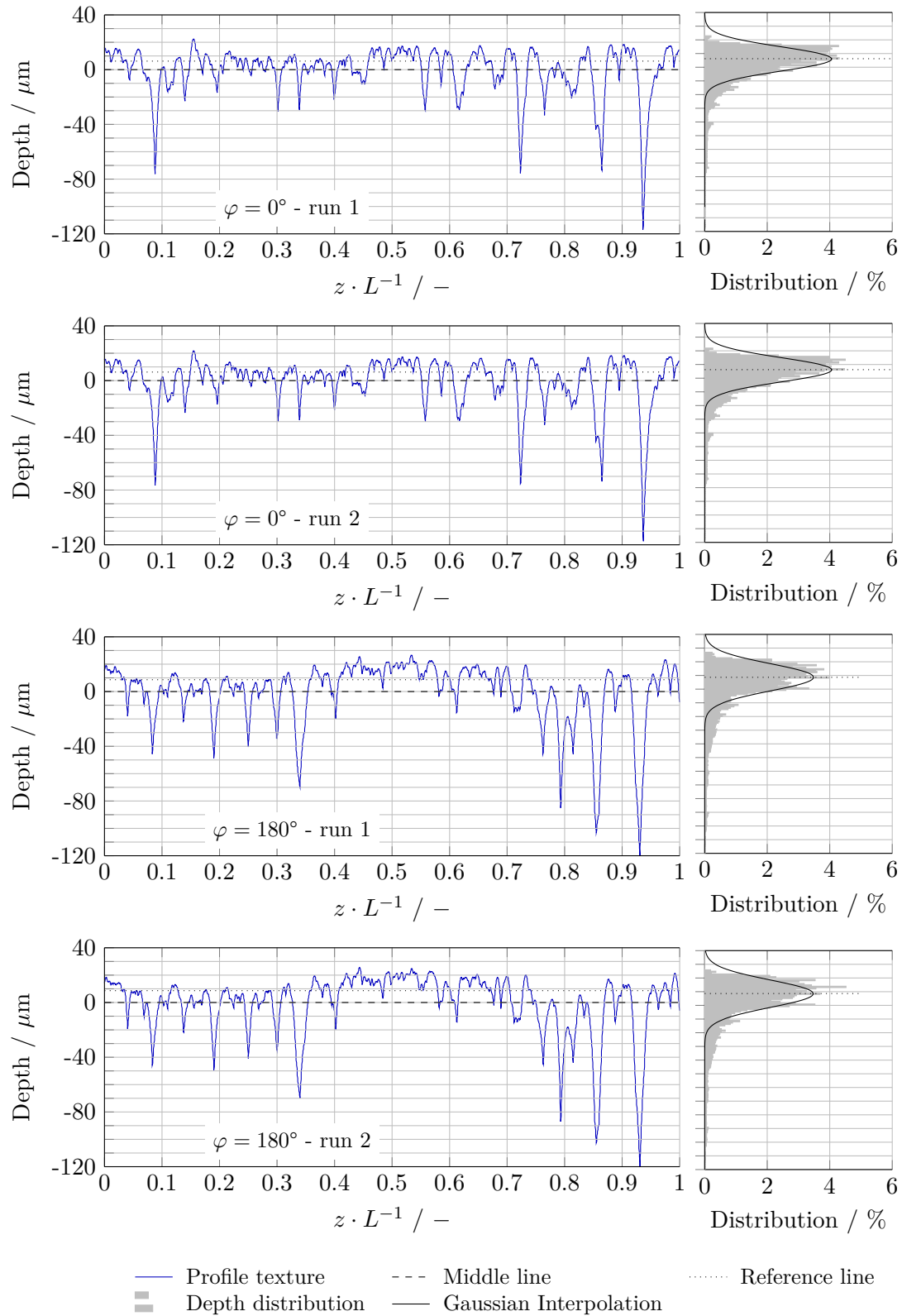


Figure 2.15: Inner surface texture of the porous liner

2.4 Discussion of the Preliminary Tests

The preliminary investigations of the bearing included the design of the bearing, the determination of the permeability and the mapping of the surface structure of the bushing. The flow coefficients were determined with material samples. Comparable measurement setups have been built by Zhong et al. [128] and Belforte et al. [13], who determined the permeabilities of sintered metals.

Three approaches are presented for the evaluation of the flow types:

- **Proportionality between \dot{m} to $p_1^2 - p_2^2$.** On the basis of the Darcy approach, there is a proportional relationship (see equation 2.7). This approach was used by, among others, Sneek and Elwell [108] and Fleder et al. [48]. A linear regression curve and a quadratic regression curve were generated for assessment. Both curves showed high agreement. Thus, the viscous term represents the dominant component. Therefore, the proportionality and use of Darcy's law was considered acceptable.
- **Reynolds number based on grain diameter as characteristic length.** Another evaluation criterion is the dimensionless Reynolds number. Bear [10] conducted investigations and determined the transition from laminar to turbulent flow. The grain diameter was chosen as the characteristic length. It is not possible to specify a grain size for a sample based on an orthotropically layered structure. During the pyrolysis process, the aramid fibers dissolve and individual channels interspersed with fractures are formed. Furthermore, the orientation of the fibers also affects the flow. The surface structure of a sintered material and a layered material are not comparable. Consequently, the Reynolds number that relies on the grain diameter as the characteristic length does not allow for an adequate evaluation of the flow type of the C/C sample.
- **Parameter of Taylor and Lewis [115].** Another possibility for the evaluation is the parameter of Taylor and Lewis. The de-dimensioned ratio represents the ratio between viscous and inertial forces. A value of less than 1 corresponds to the suitability of Darcy's law. Depending on the supply pressure, values between 0.20 to 0.81 were determined, and, since the characteristic value is slightly less than 1, the use of Darcy's law was considered acceptable.

As a result, the viscous forces are more dominant than the inertial forces. For the further procedure, the flow in the porous bushing is considered laminar and Darcy's law is applied. According to Klinkenberg [70], the almost linear permeability progression versus the reciprocal of $p_1 - p_2$ can be associated with slip. Xiao et al., who studied the permeability through sandstone fractures and the influence of the Klinkenberg effect, reported a similar curve progression [123]. As a result, the permeability values corresponding to the supply pressure were adopted for numerical simulations.

As part of the measurements, the radial and circumferential permeability values of the porous liner were determined using a porous sample. In the further procedure, the C/C material is assumed to be isotropic. The additional determination of axial permeability is a promising extension for further investigation.

Tactile scanning along the bushing revealed grooves up to $130\ \mu\text{m}$. Furthermore, investigations at the position $\varphi = 0$ and 180° revealed grooves of comparable size in circumferential direction.

The porous bushing was taken from a layered C/C plate. The groove structure is explained by the transition of the layers. Since the layers are arranged orthotropically, comparable amplitudes occur in the circumferential direction. The measurement was performed tactilely with a probe tip with a diameter of $0.5\ \text{mm}$. The determined grooves depend on the measuring tip diameter, whereby the tactile grooves can be even more extensive.

3 Experimental Determination of the Static Performance Parameters

Experimental tests were performed to verify the suitability of the porous material for aerostatic bearings and to validate the numerical models developed for this type of bearing. The experiments included the determination of the static performance parameters, such as the load-carrying capacity and gas consumption. Furthermore, by using several distance sensors, the shaft misalignment was determined. Orbit measurements enable conclusions regarding the occurrence of instability. For the sake of repeatability, the shaft misalignment in particular was analyzed.

3.1 Experimental Setup

The concept of the bearing test rig (Figure 3.1) was developed to determine the static performance parameters with the inclusion of a rotating shaft. The test stand was designed for the investigation of aerostatic journal bearings. A stationary load was applied to the test bearing in a radial direction. The resulting eccentricity and misalignment of the shaft were determined with a total of six displacement sensors. The hardware of the radial gas bearing test bench is presented in Figure 3.2.

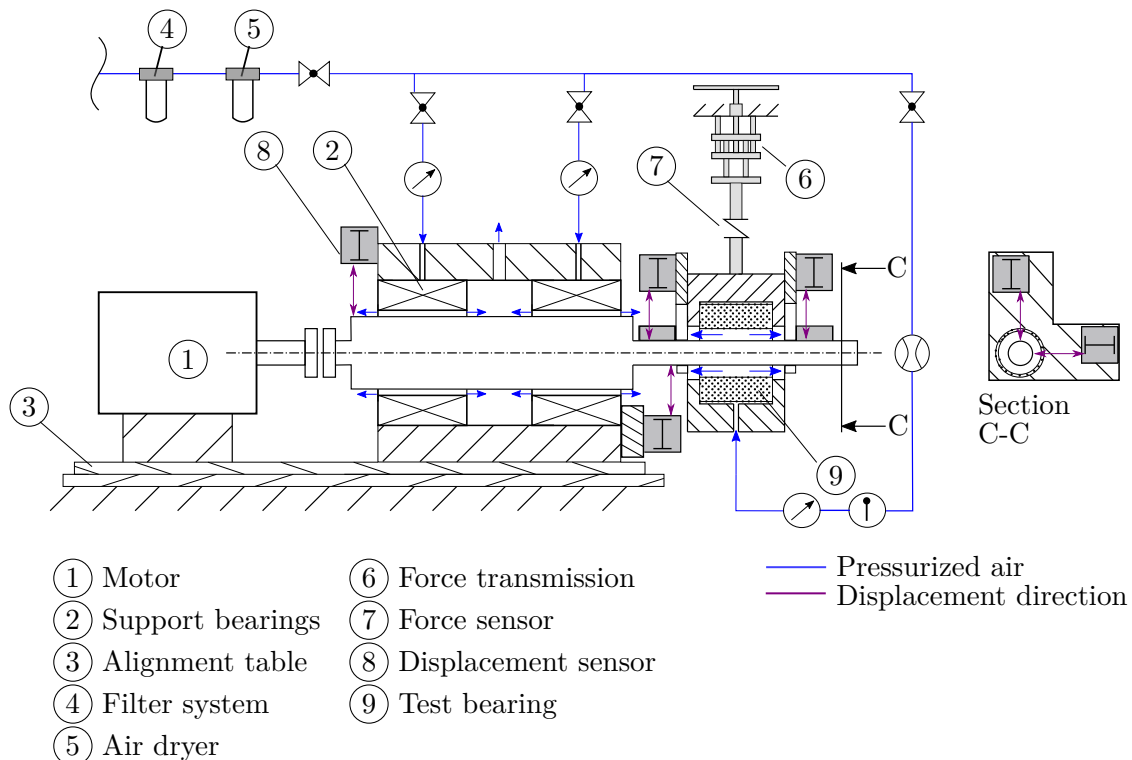


Figure 3.1: Concept of the test bench for journal gas bearings

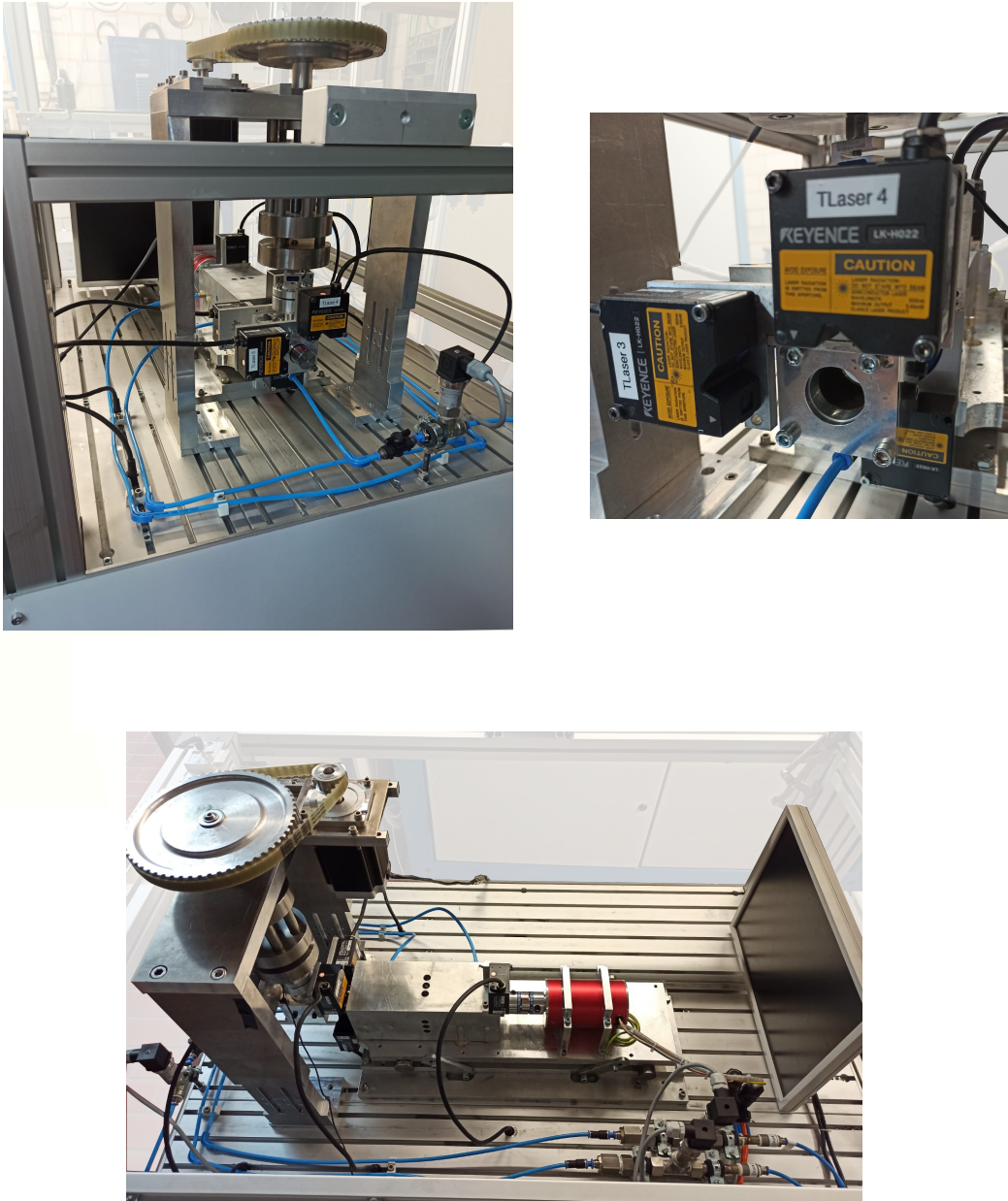


Figure 3.2: Test bench for journal gas bearings

The force was transmitted to the test housing via a stepper motor. The rotary motion is converted into a linear motion with a fine pitch thread and allows the force to be increased in small increments. The test bearing was rigidly connected to the linear traversing unit with an s-shaped sensor, which determined tensile and compressive forces in the vertical direction. A total of four laser-triangulation sensors (max. linearity error: $1.2 \mu\text{m}$) were mounted at both ends of the bearing in the direction of the shaft. The sensors were arranged horizontally and vertically and determined the relative position of the bearing to the shaft. Since the radial clearance of the tested air bearing was $30 \mu\text{m}$, a low radial

eccentricity of the shaft was targeted. The shaft was connected to the DC motor via a flexible elastomer coupling. The motor was aligned with the shaft with fine plates with a thickness of 5 to 20 μm . A continuous shaft was designed for the support bearings and the test housing to avoid the influences of another coupling.

Two additional aerostatic air bearings were used as support bearings. These bearings provided the advantage of low concentricity, but had the disadvantage of misalignment. Compared to the test bearing ($c = 30 \mu\text{m}$), the radial clearance of the support bearings was lower ($c = 16 \mu\text{m}$). The support bearings were larger in dimension (inner diameter: 50 mm, length: 89 mm) than the test bearing (inner diameter: 28 mm, length: 35 mm, see Figure 2.1) and were supplied with a higher pressure (see Figures 3.11 to 3.13) to cause a minimal inclination of the shaft. However, the shaft misalignment was determined with two vertically positioned laser triangulation sensors, which were mounted at both ends of the bearing support block in the direction of the shaft.

The test bearing and the support bearings were supplied with compressed air that had been processed with a two-stage filter system and a dryer. Any contamination could cause a closing of the pores and, thus, disadvantage the performance and the repeatability of the results. The compressed air supply to the support bearings was controlled with a manual valve in each case. For safety reasons, the compressed air to both support bearings was recorded by relative pressure sensors. In the event of a drop in pressure, the motor driving the shaft was shut off. The mass flow of compressed air to the test bearing was determined with a coriolis flow meter (uncertainty: 0.035 % FS). The temperature was determined with a Pt100 RTD (uncertainty: $1.5^\circ\text{C} + 0.002^\circ\text{C} \cdot T$). A further relative pressure sensor (uncertainty: 0.03 % FS) determined the pressure upstream of the compressed air connection of the test housing.

3.2 Experimental Procedure

Before the measurements, the test stand was adjusted in two steps. In the first step, the motor was aligned with the shaft. The shaft was positioned in the support bearing bushing under pressurization. As the test rig was not designed for axial loads, no thrust bearings were installed, which allowed axial movement of the shaft. The motor, including the elastomer coupling, were thus aligned with the shaft. Metal plates with a thickness of 5 to 20 μm were used for precise alignment. Laser triangulation sensors were used for the assessment to realize the highest possible concentricity.

In the second alignment step, the assembly, consisting of motor and shaft, was aligned with the test bearing housing. The motor and support bearing block were mounted on a movable alignment table, which allowed the alignment of the assembly with the test bearing. The test bearing was pulled over the shaft under active air supply. As soon as the test bearing had been positioned, the offsets of the distance sensors were set. To adjust the vertical sensors, the compressed air supply was turned off so that there was contact between the shaft and bushing. This vertical offset corresponded to $\varepsilon = 1$. Subsequently,

the offset of the horizontal sensors was set with an active compressed air supply. The position of the test bearing was adjusted with the force transmission to apply a force of approximately 0 N to the bearing (minus the weight of the housing).

After the preparation phase, the measurements to determine the static performance parameters could commence. The compressed air supply to all aerostatic bearings remained open, and the motor for driving the shaft was ramped up to the aimed for rotational speed. During hysteresis measurements, the radial force was increased and then decreased. The performance parameters were measured at each operating point. The measurement duration time was 2 s, and the sampling rate of the distance sensors was 10 kHz.

3.3 Experimental Results

Within the scope of the investigation, the influence of two operational parameters on the static performance parameters of the bearing were examined. The parameters were the rotational speed of the shaft n and the supply pressure p_s of the bearing. Three rotational speeds ($n = 1000, 4000$ and 8000 rpm) and three supply pressures ($p_s = 5, 6$ and 7 bar) were investigated. This resulted in a total of nine measurement series. Each series of measurements included the performance of a hysteresis measurement. Starting from a load of approximately 0 N, the load on the test bearing was increased stepwise to approximately 80 N to 100 N. The radial load was then reduced step by step, until a load of approximately 0 N was obtained. The vertical eccentricity ratio ε_v and the misalignment ratio ε_{vm} were used to evaluate the results. The vertical eccentricity ratio was determined by the mean value of the eccentricity, which was determined by two vertical displacement sensors and de-dimensioned by the two times radial clearance.

$$\varepsilon_v = \frac{V_1 + V_2}{2 \cdot c} \quad (3.1)$$

The vertical misalignment was determined by the differences in both eccentricities and divided by the radial clearance. The values V_1 and V_2 were formed by the linear interpolation of V_{B1} and V_{B2} . To calculate the characteristic values, eccentricities at the bushing ends V_1 and V_2 were determined.

$$\varepsilon_{vm} = \frac{V_1 - V_2}{c} \quad (3.2)$$

Figure 3.3 shows the nomenclature of the distance sensors and the position of the sensors. The lengths L_1 to L_6 define the axial distance between the sensors in relation to the shaft length. Sensors V_{S1} and V_{S2} were also vertically directed and mounted on the support bearing block to determine the shaft inclination. The distances V_{B1} and V_{B2} represent the data acquired by the vertically arranged sensors on the test bearing. With the application of the lengths L_4 to L_6 , the vertical measured data were interpolated for the distances at both ends of the bushings V_1 and V_2 .

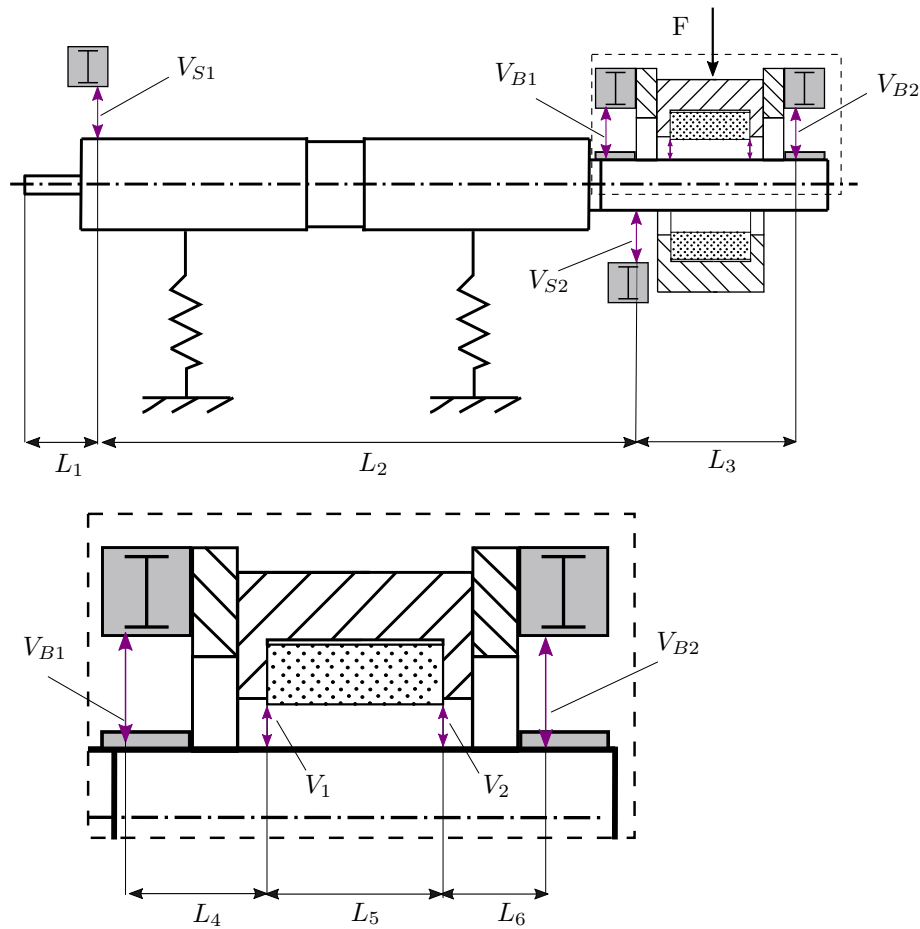


Figure 3.3: Nomenclature of the eccentricity measurement

3.3.1 Hysteresis Measurements

The determined measurement series for the rotational speed $n = 1000$ rpm is shown in Figure 3.4 and, for $n = 4000$ rpm to 8000 rpm, in Figure 3.5. The diagrams show the experimentally determined vertical eccentricity ratio ε_v and the vertical misalignment ratio ε_{vm} , depending on the radial load-carrying capacity F of the bearing. In addition, the attitude angle ϕ_a of the shaft relative to the vertical eccentricity ratio ε_v is shown. The course of the hysteresis measurement is indicated by arrows.

An increase in misalignment was consistently observed in the series of measurements due to an increase in the load. An increase in supply pressure tended to result in lower eccentricity and lower misalignment.

The vertical eccentricity ratio showed a consistent course during force loading and release. The greatest differences were observed in the transition from load to release. In the lower load range, both curves converge again.

This effect is also apparent with ε_{vm} values. There was a significant decrease at the saddle

point of max. F and the values converged again at lower loads.

The values of ε_v and ε_{vm} decreased after load peak had been attained. Thus, a clockwise characteristic curve can be observed.

The agreement of ε_v and ε_{vm} is high, depending on the rotational speed. No significant influence on the measurements were observed with an increase in the rotational speed from 1000 to 8000 rpm.

The deflections of the attitude angles ϕ_a were consistently less than 10° . A slight increase in deflection could be observed as the rotational speed increased and the supply pressure decreased. The highest attitude angles were thus determined at $n = 8000$ rpm and $p_s = 5$ bar. Moreover, the directional sense was not uniform. A clockwise trend could be observed for the supply pressures 5 and 7 bar. With a supply pressure of 5 bar, the measurements also resulted in positive attitude angles; however, a counterclockwise course was obtained in the hysteresis of the attitude angles.

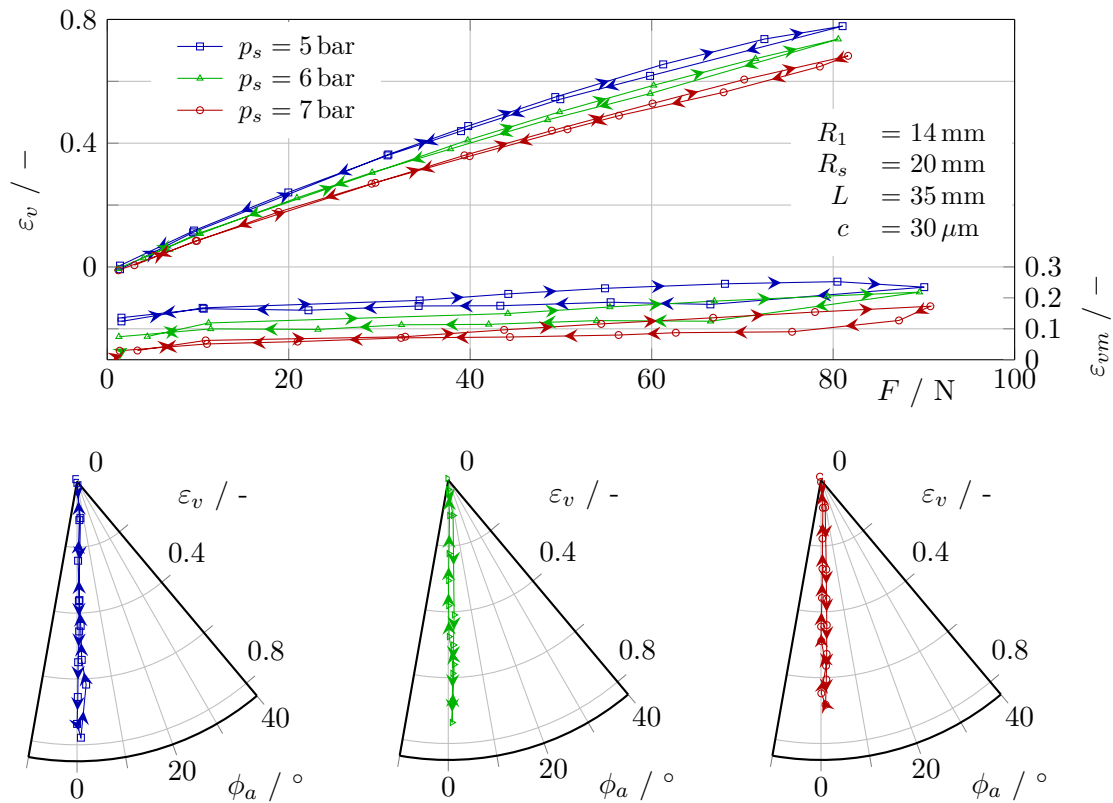


Figure 3.4: Hysteresis at $n = 1000$ rpm

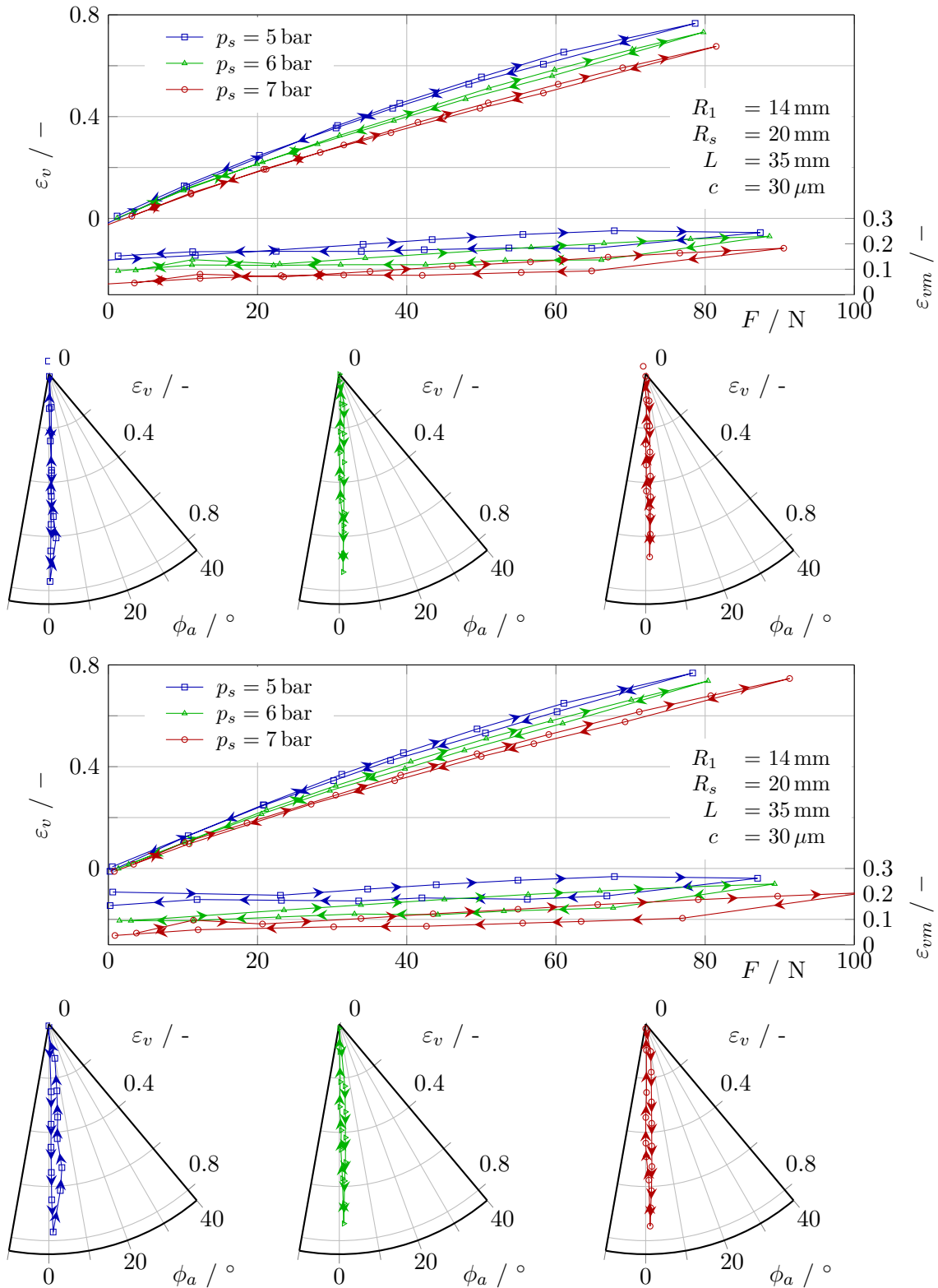


Figure 3.5: Hysteresis at $n = 4000$ (top) and 8000 rpm (bottom)

3.3.2 Load-Carrying Capacity and Vertical Misalignment

The load-carrying capacities of the bearing, depending on the vertical eccentricity ratio and including the standard deviations, are shown in Figure 3.6. The standard deviation were obtained by averaging the standard deviation of the values V_1 and V_2 . In addition, a second-order polynomial regression for the values of vertical eccentricity ratio and vertical misalignment was added for each series of measurements.

The regression lines show a steady increase in the load-carrying capacity with an increase in the supply pressure. No rotational speed dependence could be observed in the range up to 8000 rpm, and the differences were less than 1 %.

Differences are more significant in a comparison of the respective standard deviations. An increase in the rotational speed led to a decrease in the standard deviation. Especially in the comparison of the $n = 1000$ rpm and 8000 rpm, a clear decrease can be observed.

The standard deviations were at maximum in the low radial load range and decreased in the higher range of loads. The high standard deviations in the low-load range were particularly noticeable in combination with a low rotational speed of $n = 1000$ rpm.

The regression lines of the ε_{vm} values also show high agreement in the rotational speed comparison. The high agreement is valid for the three investigated supply pressures, 5 to 7 bar. For $p_s = 6$ and 7 bar, the regression lines show a progressive course of the curve. The characteristic curves for the value $p_s = 5$ bar are degressive.

3.3.3 Gas Consumption

The gas consumption of the bearings over the eccentricity range 0 to 0.8 is shown in Figure 3.7. Three diagrams were generated, depending on the rotational speed and including three investigated supply pressures.

The gas consumption increased with an increase in supply pressure. The insertion of a polynomial regression line of the second order led to a tendency for a slight reduction in the mass flow, with an increase in the eccentricity. Since the reduction in mass flow was well below 1 %, the mass flow curve remained mostly constant over the eccentricity range. The differences were well below 1 % in the comparison of the measurements related to rotational speed.

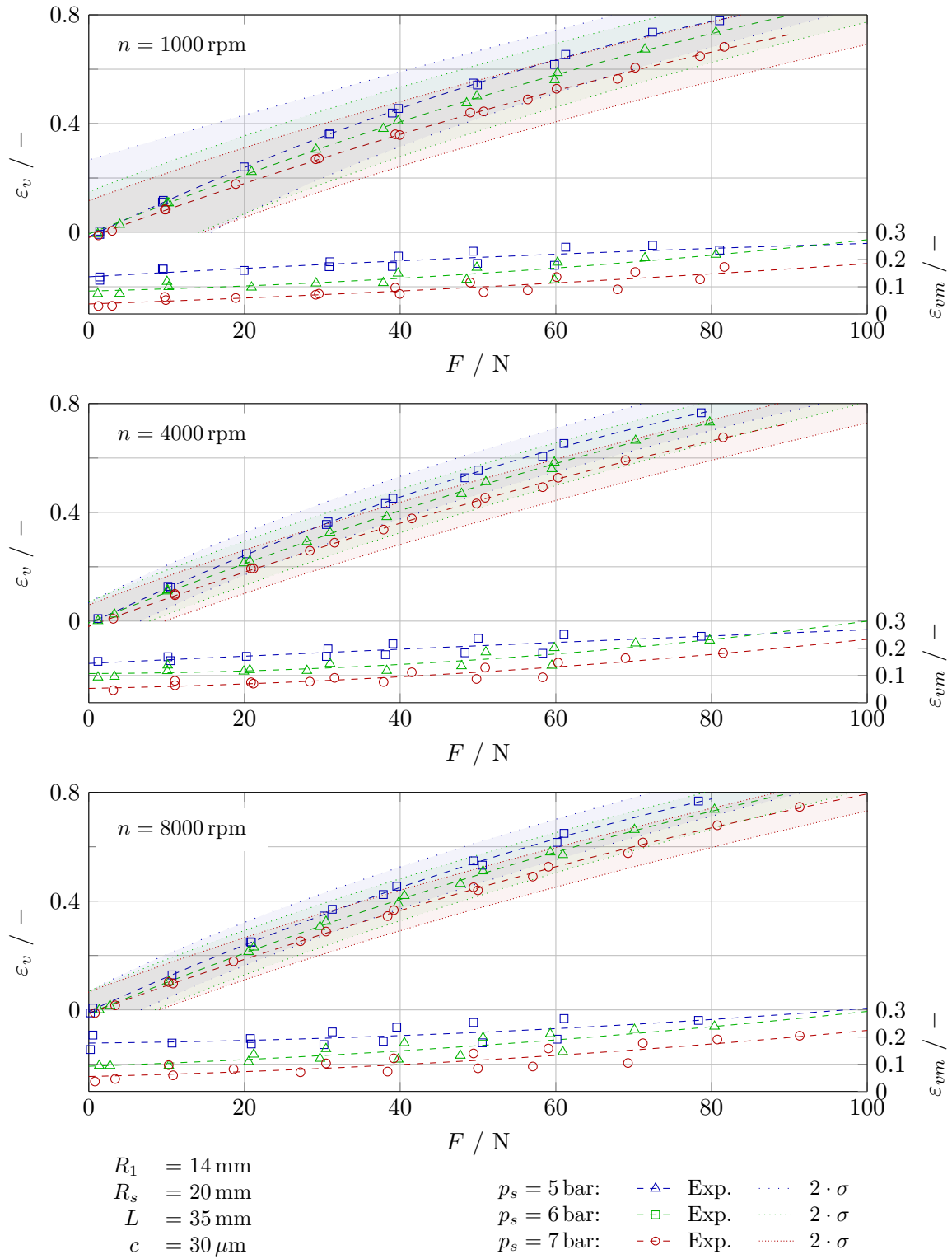


Figure 3.6: Experimental results: load-carrying capacity and vertical misalignment

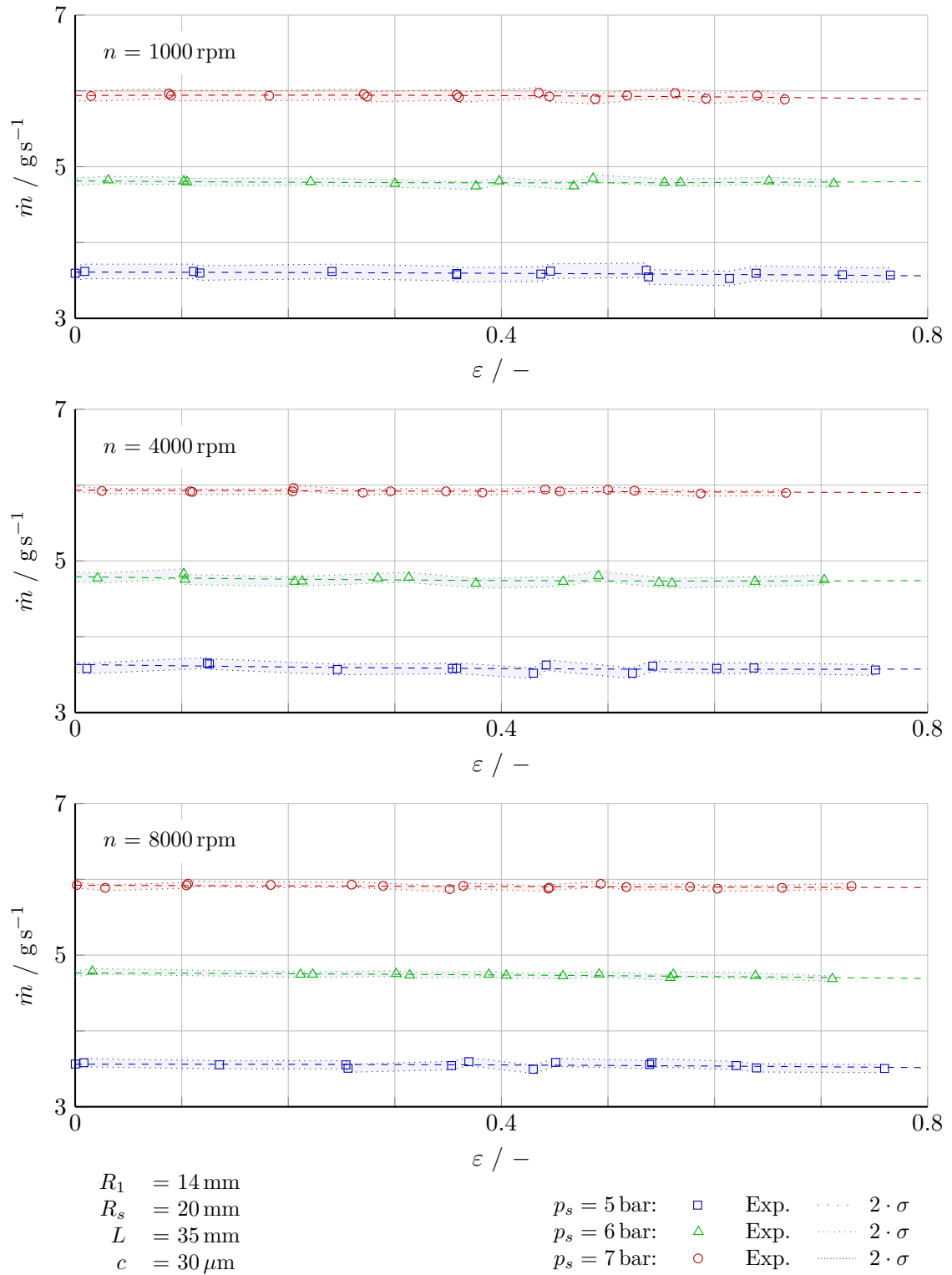


Figure 3.7: Experimental results: mass flow rate

3.3.4 Orbit Measurements

The orbit of the shaft under the influence of the supply pressure, the radial load and the rotational speed is shown in subfigures of Figure 3.8. The subfigures include the determined raw data, the filtered data at the lowest load (approximately 0 N) and the filtered data at the respective maximum loads of the characteristic curve (approximately 80 N to 100 N). The results show a dependence of the orbit on the rotational speed. Similar to the rotational speed, an increase in the supply pressure and the radial load led to a reduction in the deflections. Consequently, measurements at $n = 1000$ rpm, $p_s = 5$ bar and $F \approx 0$ N show the highest deflections.

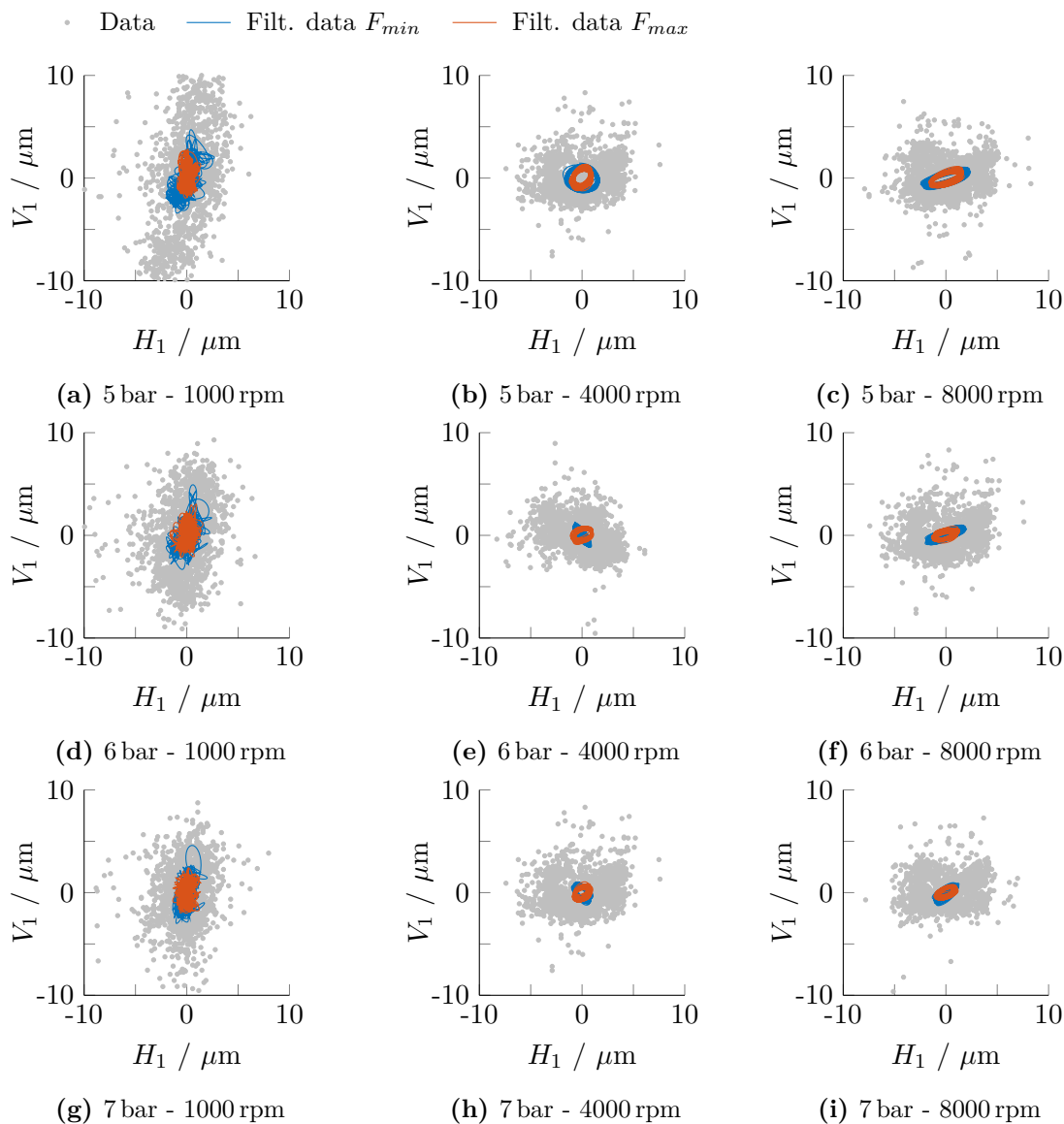


Figure 3.8: Orbit of the shaft

The results of the measurement at 1000 rpm had a chaotic course. No unambiguous shaft movement could be detected. Increasing the rotational speed to 4000 rpm resulted in an almost round or oval orbit. An increase to 8000 rpm enhanced the oval orbital pattern. Subsequently, the vertical component of the orbit decreased with an increase in rotational speed.

No pneumatic hammering was observed. The pneumatic hammer is a self-induced instability. The gas compresses and energy is stored in the pores of the porous body. This could result in self-excited oscillations, if the release of energy is in phase with the bearing system, and, thus, the pneumatic hammer is formed [2].

3.3.5 Influence of Shaft Misalignment on Repeatability

In the following, the influence of shaft misalignment on repeatability is investigated. In the hysteresis investigations, the largest hysteresis error was observed at the transition from load increase to load reduction. This error can be attributed to the angle β or the

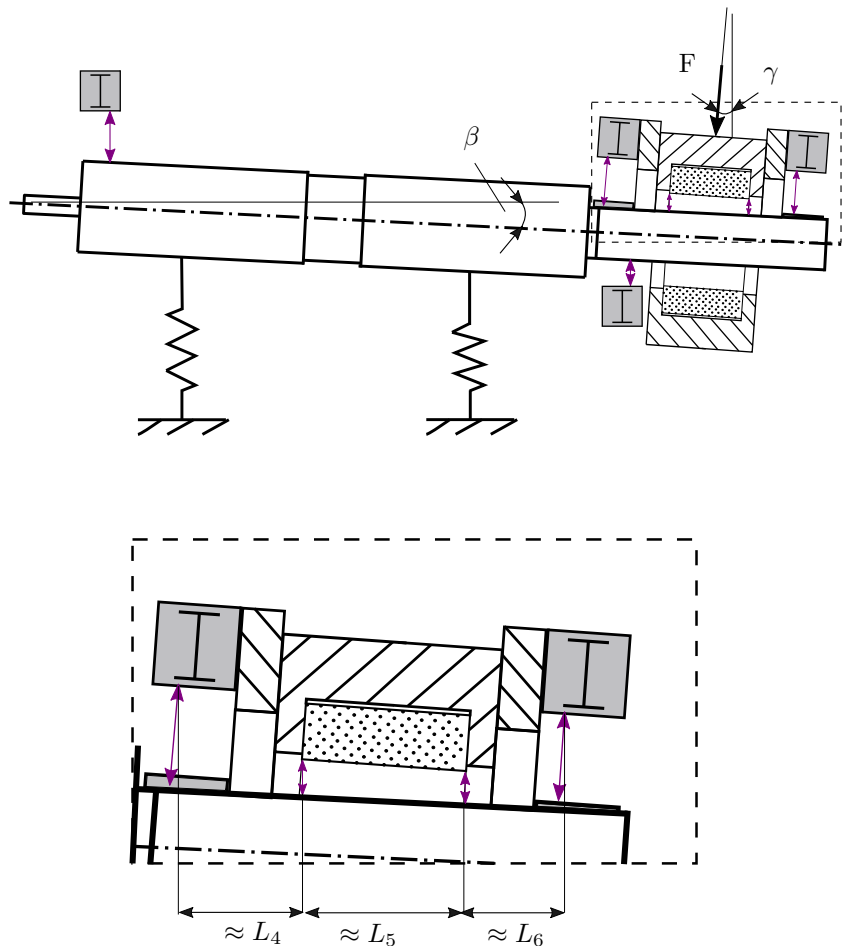


Figure 3.9: Nomenclature of a misaligned shaft

angle γ (see Figure 3.9). The angle β denotes the misalignment of the shaft in the vertical direction and γ is defined as the angle of linear force application. In the following analysis, the influence of β on repeatability is investigated.

The lengths L_1 to L_6 are considered to be constant in the event of misalignment. The inclination of the shaft is approximately five orders of magnitude smaller than the length of the shaft and can be ignored.

The aerostatic support bearings caused misalignment of the shaft as the radial load on the test bearing was increased. This inclination was determined by the triangulation sensors V_{S1} and V_{S2} . The vertical displacement of both sensors is graphed relative to the radial load on the test bearing in Figure 3.10. The figures contain specifications of the supply pressure of the support and the test bearing.

An increase in the bearing load showed a nearly linear displacement. The vertical displacement of the sensor V_{S2} increased to a maximum of approximately $6 \mu\text{m}$. The vertical displacement of the sensor V_{S1} was significantly lower and decreased to approximately $2 \mu\text{m}$. The radial clearance of the support bearings was $16 \mu\text{m}$. Thus, no vertical eccentricity ratio of greater than 0.38 was achieved at the support bearing across the measurement series.

The values of V_{S1} and V_{S2} were obtained with the hysteresis measurement. The data showed the largest deviations with low radial load. Sensor V_{S1} attained the highest deviation at a rotational speed of 8000 rpm and a supply pressure of 5 bar. The deviation was less than $1 \mu\text{m}$ and was, thus, within the linearity error ($1.2 \mu\text{m}$) of the triangulation sensors.

The agreement of the measurements with the increase of the rotational speed showed no significant changes in the range up to 8000 rpm. The deviations were within the error tolerances.

The supply pressures of the support bearings p_{S1} and p_{S2} were between 5.8 bar and 8.35 bar. The supply pressures of the support bearings were set higher than those of the test bearing. The vertical displacement of the shaft decreased due to the increase in the supply pressure. The influence of the shaft misalignment to the location of the test bearing housing for $n = 1000, 4000$ and 8000 rpm is shown in Figures 3.11 to Fig. 3.13. The vertical eccentricity determined by sensors V_{S1} and V_{S2} was linearly extrapolated over the shaft length in the z direction. A rigid shaft was assumed. The bushing ends of the bearing were marked at $z = 321$ mm and $z = 356$ mm, respectively.

The extrapolation of the inclination shows the vertical movement of the test bearing housing. The vertical displacement depended on the radial load of the test bearing and the supply pressure of the support bearings. The maximum displacement occurred at a load of 81 N and a supply pressure of 5.8 bar. The maximum displacement at the bushing end were $V_1 = 6.3 \mu\text{m}$ and $V_2 = 6.8 \mu\text{m}$.

The vertical displacement was compensated by the linear guidance of the test bearing, which is also vertical. Therefore, the decisive factor is the increase in the misalignment of the shaft with an increase in the bearing load. Thus, this would be the difference between V_{s1} to V_{s2} . Figure 3.14 includes the vertical misalignment ratio values based on the shaft misalignment. The increasing tilt due to the reduction in supply pressure is also evident

in the vertical misalignment ratio. The highest values of approximately $\varepsilon_{vms} = 0.01$ were obtained at $p_s = 5.8$ bar. Compared to the misalignment of the bearing by the sensors V_1 and V_2 mounted on the test housing, the values are one order smaller and negligible.

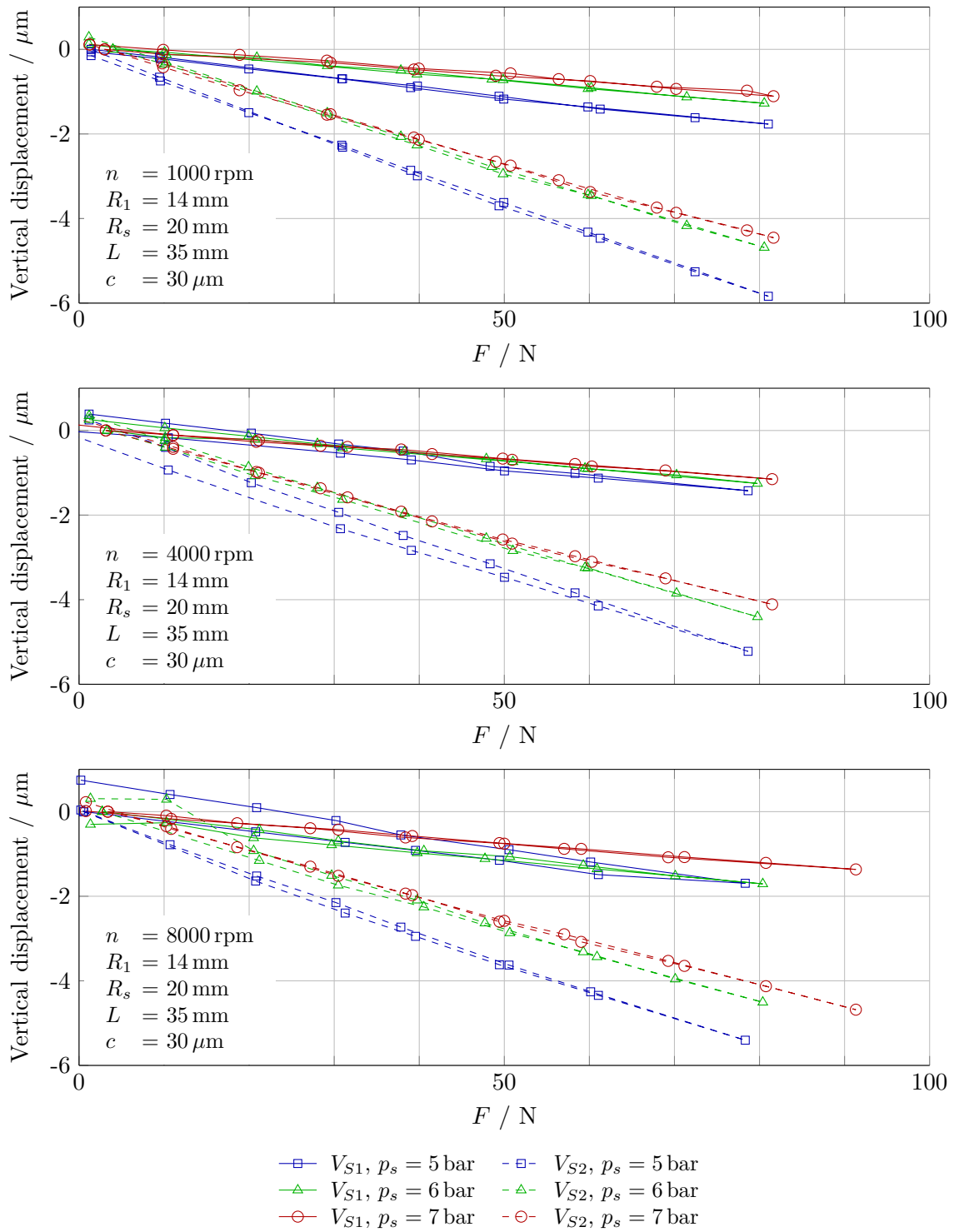
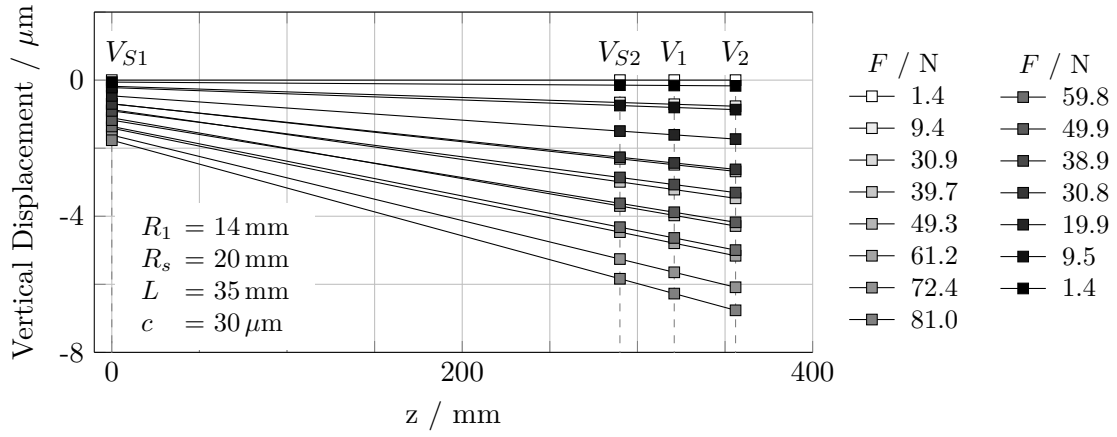
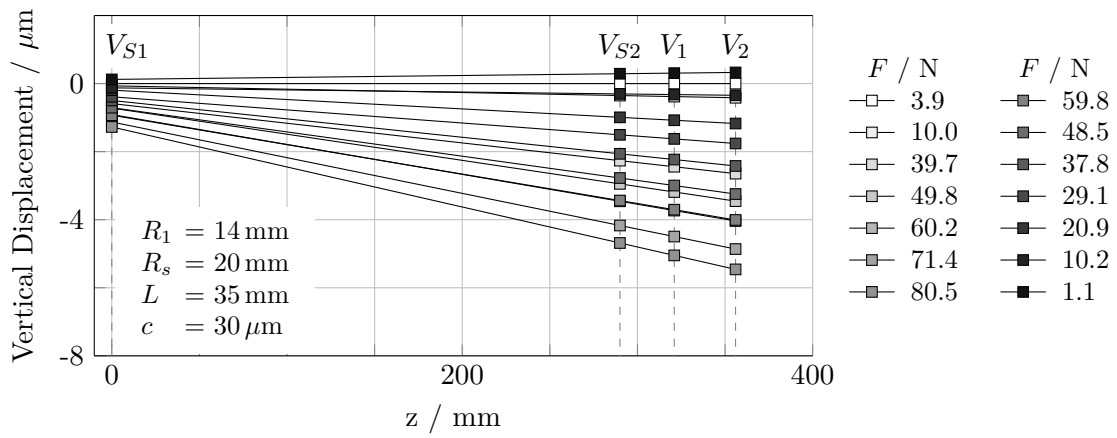


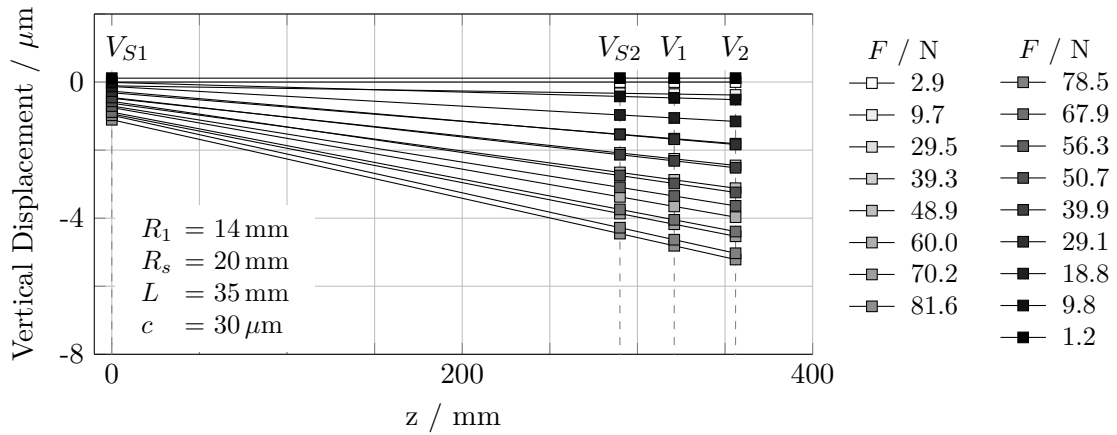
Figure 3.10: Absolute vertical displacement V_{S1} and V_{S2}



(a) $p_{s1} = 5.8 \text{ bar}$, $p_{s2} = 5.8 \text{ bar}$, $p_s = 5 \text{ bar}$

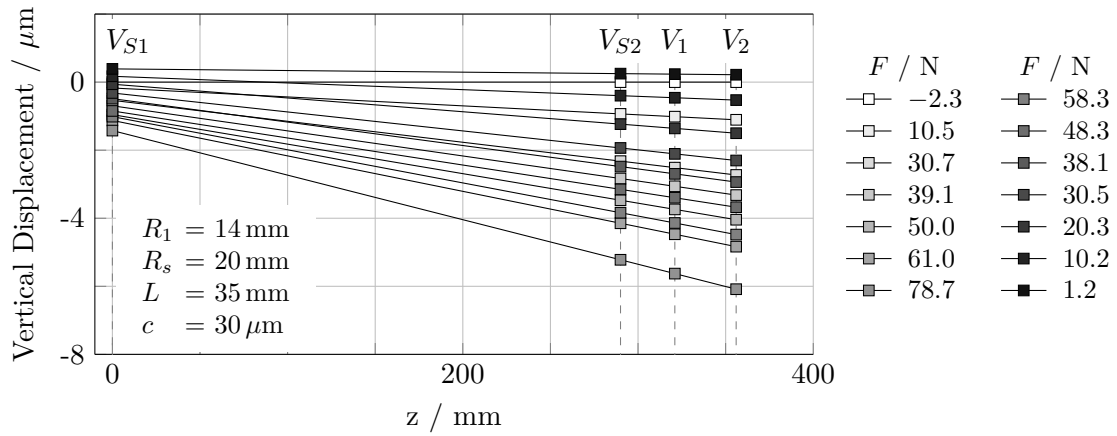


(b) $p_{s1} = 7.1 \text{ bar}$, $p_{s2} = 7.1 \text{ bar}$, $p_s = 6 \text{ bar}$

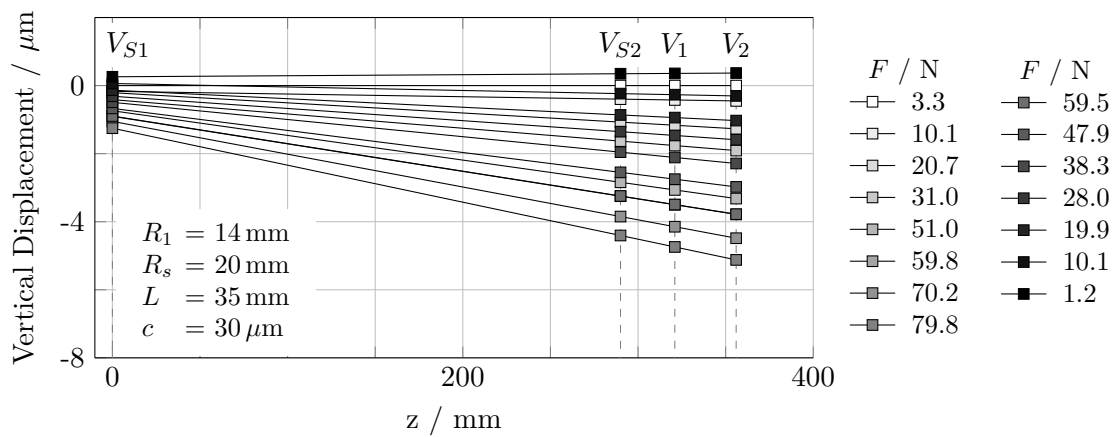


(c) $p_{s1} = 8.35 \text{ bar}$, $p_{s2} = 8.35 \text{ bar}$, $p_s = 7 \text{ bar}$

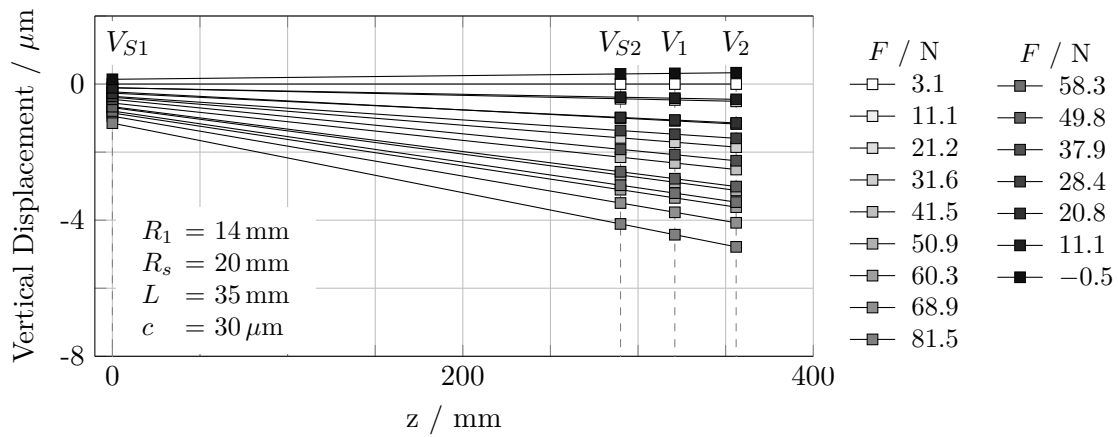
Figure 3.11: Absolute vertical displacement of shaft at 1000 rpm



(a) $p_{s1} = 5.8 \text{ bar}$, $p_{s2} = 5.8 \text{ bar}$, $p_s = 5 \text{ bar}$

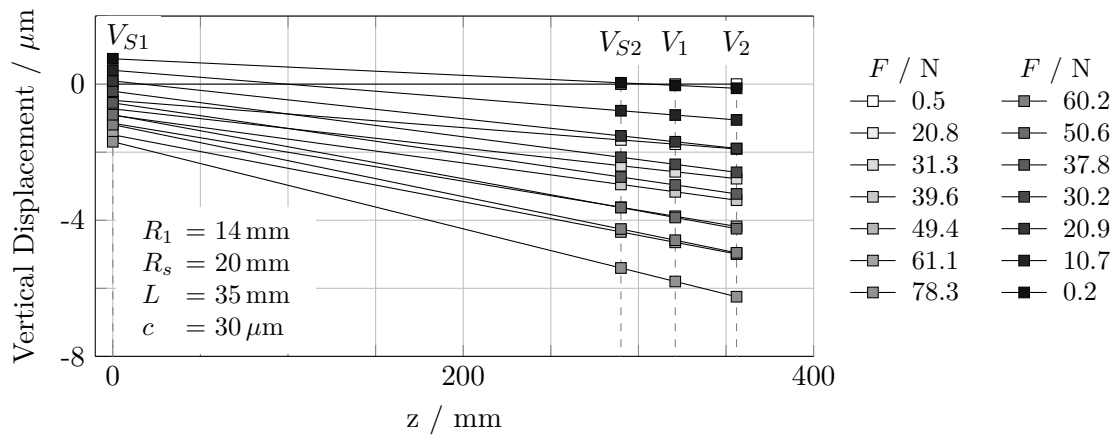
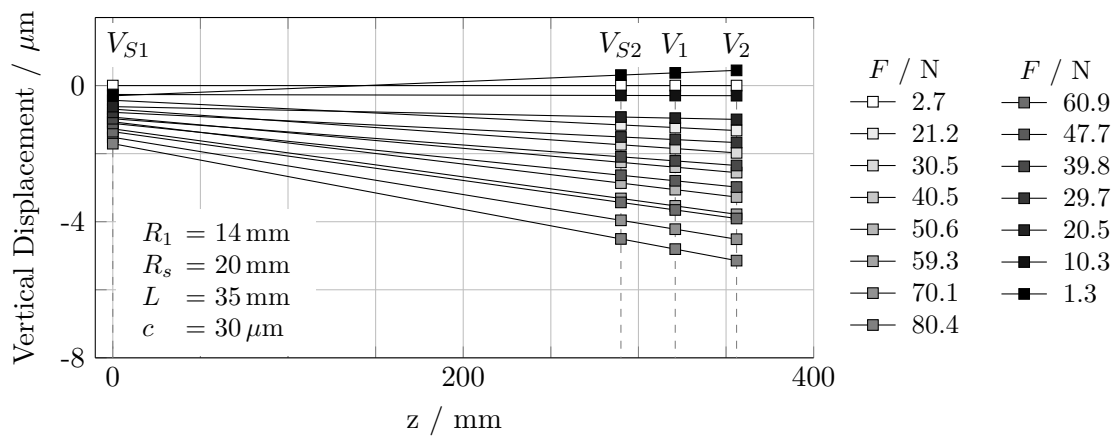
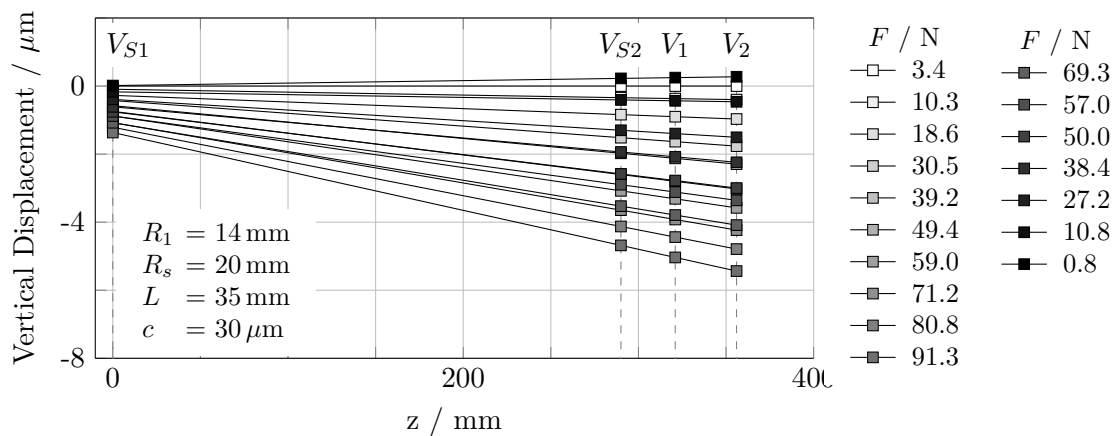


(b) $p_{s1} = 7.1 \text{ bar}$, $p_{s2} = 7.1 \text{ bar}$, $p_s = 6 \text{ bar}$



(c) $p_{s1} = 8.35 \text{ bar}$, $p_{s2} = 8.35 \text{ bar}$, $p_s = 7 \text{ bar}$

Figure 3.12: Absolute vertical displacement of shaft at 4000 rpm

(a) $p_{s1} = 5.8 \text{ bar}$, $p_{s2} = 5.8 \text{ bar}$, $p_s = 5 \text{ bar}$ (b) $p_{s1} = 7.1 \text{ bar}$, $p_{s2} = 7.1 \text{ bar}$, $p_s = 6 \text{ bar}$ (c) $p_{s1} = 8.35 \text{ bar}$, $p_{s2} = 8.35 \text{ bar}$, $p_s = 7 \text{ bar}$ **Figure 3.13:** Absolute vertical displacement of shaft at 8000 rpm

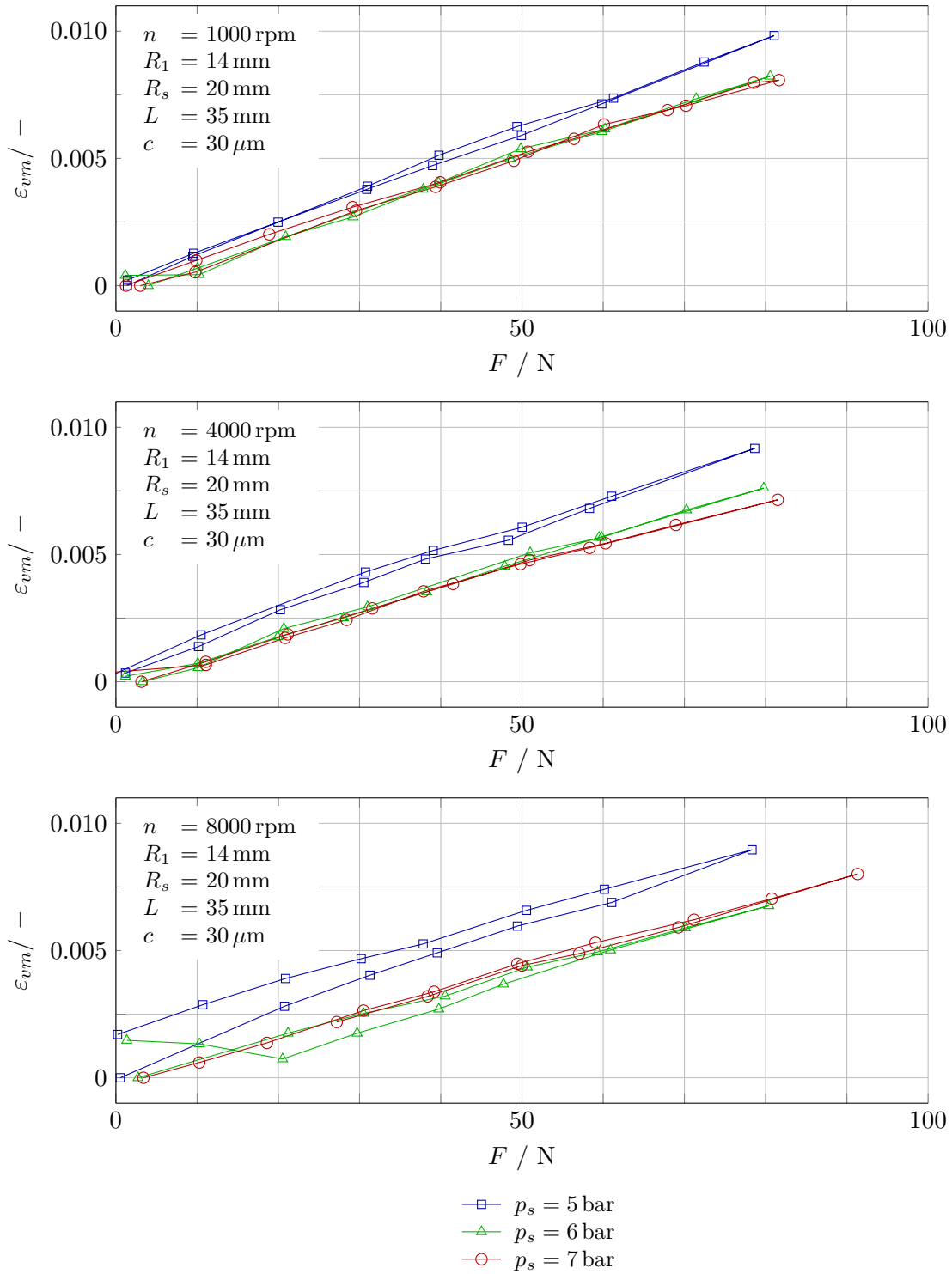


Figure 3.14: Vertical misalignment ratio based on shaft inclination

3.4 Discussion of the Experimental Results

The experimental investigations included a rotational speed of $n = 1000, 4000$ and 8000 rpm with a pressure ratio of $p_s/p_a = 5, 6$ and 7 , respectively. Measurements included the determination of the load-carrying capacity and the gas consumption of the bearing, up to an eccentricity ratio of approximately 0.8 . Furthermore, the attitude angle and the orbit of the shaft were determined.

The load-carrying capacities and the shaft misalignments were determined in the form of hysteresis measurements. The relatively highest deviations were obtained in the transition when the radial load is decreased. A hysteresis error of less than $\varepsilon_v = 0.04$ was obtained for the vertical displacement ratio, and, for the vertical misalignment ratio, the maximum hysteresis error was below $\varepsilon_{vm} = 0.08$. An increase in the load-carrying capacity resulted in a maximum increased misalignment ratio of $\varepsilon_{vm} = 0.27$.

The hysteresis error and the increase in the misalignment ratio were analyzed with consideration of the vertical inclination of the shaft in the absolute system of the test rig. The shaft was supported by two aerostatic air bearings. Thus, an increase in the load on the test specimen led to tilting. Two displacement sensors were mounted on the support bearing housing ends to determine the extent of the inclination. The evaluation showed a hysteresis error below $\varepsilon_{vm} = 0.002$ and a maximum of approximately $\varepsilon_{vm} = 0.01$.

The resulting influence of the inclination of the shaft led to a negligible misalignment of the test specimen. Consequently, the cause of the misalignment can be attributed to the inclination in the force transmission. By extending the force transmission, the misalignment could increase and vice versa. In addition, the inversion of the force transfer motion into the fibrous structure of the material is also a probable cause of the hysteresis error at the transition.

The determined load-carrying capacities and gas consumption showed a negligible influence of the rotational speed up to 8000 rpm (below 1%).

Furthermore, the determined attitude angle showed a mainly vertical component. The negligible influence of the rotational speed and the low attitude angle indicate the generation of the load-carrying capacity through the aerostatic effect. Self-acting (dynamic) bearings exhibit higher attitude angles and the characteristic Gumbel curve (see Ref. [109]). Corresponding air-lubricated dynamic bearings are operated at higher speeds (see Refs. [26, 122]).

The standard deviations of the load-carrying capacities and the orbit measurements allow conclusions about the operating behavior at the respective operating points. The measurements showed no occurrence of pneumatic hammering. The orbit diagrams show a course that was within the range of the lubricant film width.

The orbit course of the shaft showed a dependence on the rotational speed, the load and the supply pressure ratio. The highest deflections of the orbit were observed at the lowest rotational speed ($n = 1000$ rpm), the lowest load (approximately $F = 0$ N) and the lowest supply pressure ratio ($p_s/p_a = 5$). Conversely, an increase in the three parameters led to

lower amplitudes and a reduction in the standard deviations.

Especially the rotational speed of 1000 rpm had an unpredictable course. Comparable orbit courses are described in a publication by Czolczynski [4] and are classified as chaotic. On the C/C bearing measurements, an increase in supply pressure ratio and load at a rotational speed of 1000 rpm resulted in a reduction in amplitude but no significant improvement in unstable behavior. The course is attributed in particular to the unstable running behavior of the motor at low speeds.

The measurements at rotational speeds of 4000 and 8000 rpm indicate a significantly lower concentricity. The shape of the concentricity at $n = 4000$ rpm has a nearly circular trajectory, which becomes oval with an increase in the rotational speed to 8000 rpm. On the one hand, circular orbits can be observed particularly with static bearings (see Ref. [33]). Self-acting bearings, on the other hand, tend to exhibit an oval-shaped curve (see comparable measurements in Ref. [112]). The slight increase in the horizontal component could indicate the increasing dynamic component at $n = 8000$ rpm. This would also correlate with the slight attitude angle of approximately 2° . Nevertheless, the influence of the dynamic effect on the load-carrying capacity is negligible in this rotational speed range.

4 Numerical Models based on Reynolds' Lubricant Film Equation and Darcy's Law

Numerical models based on the Reynolds equation for lubricating films, coupled with Darcy's law, allow a rapid calculation of a bearing prototype through simplifications. Compared to commercial software based on computational fluid dynamics (CFD), fewer computing resources are required to create a pre-design of a bearing. In the following, the governing equations (Ge) are derived and the assumptions discussed.

In the following, the general equations for the flow calculation of the lubricant film, the flow through the porous journal bearing and the lubricant film thickness are derived, specifically for a porous journal bearing. The computation of the lubricant film thickness was conducted for three cases and described in the following. This includes the ideal scenario of a shaft without misalignment and cases with vertical misalignment and vertical misalignment with inclusion of the surface structure of the inner surface of the bushing. Furthermore, general and model-spanning assumptions are explained in this chapter. These include the approach to thermohydrodynamic modeling and the turbulence in the lubricant film.

The numerical models "simple model" (Si), "full Darcy model" (FD), "full Darcy compressible" (FDc) and "full Darcy extended" (FD+) are presented. The complexity of the models increases and are at different levels. Table 4.1 shows the assumptions that each model fulfills. The details are explained in the individual subchapters. The criteria are enumerated: discretization of the lubricant, discretization of the porous liner, misalignment of the shaft, compressibility, texture of the inner surface and the geometry of the pressure chambers. The complexity of the models increases from the Si to the FD+ model. For further verification, additional simulations were performed with commercial CFD software and included in the comparison. The numerical models were programmed with Matlab 2021a and used the bi-conjugate gradient stabilized method (BiCGSTAB) [17, 119].

Table 4.1: Assumptions underlying the models

	Si	FD	FDc	FD+	CFD
Discretization of the lubricant	✓	✓	✓	✓	✓
Discretization of the porous liner		✓	✓	✓	✓
Misalignment			✓	✓	
Compressibility			✓	✓	✓
Texture of the inner surface				✓	
Geometry of the pressure chambers				✓	✓

4.1 Generalized Reynolds Equation for Fluid-Film Lubrication

The origin of the equation dates back to one of the most-often cited publications in the field of tribology. Osborne Reynolds' 1886 [97] assumptions lead to the equation for the calculation of lubricating films and laid the foundation for a variety of developments in bearing and seal technology. The general form of Reynolds' lubricating film equation (GREL), based on the fundamental conservation equations, was derived by Dowson [41] and can also be found in the literature by Hamrock [60]. In this study, the generalized Reynolds equation for lubricants was derived according to the nomenclature and requirements of the tested and computed bearing. The general equation serves as a foundation for the derivation of the particular models.

A common derivation of the Reynolds lubricating film equation is based on the assumption that the bearing radii are significantly larger than the lubricating film width h . In the present bearing case, the shaft radius is $R_1 = 14.030$ mm, the inner bushing radius is $R_2 = 14.060$ mm and the radial clearance is $c = R_2 - R_1 = 0.030$ mm. This allows the surface curvature to be disregarded and the lubricant film to be unwound in the circumferential direction [60].

Figure 4.1 shows the concentric position of the shaft in the bushing and the resulting form in cartesian coordinates. The width of the lubricating film is overdimensioned for illustration purposes. As the bearing is concentric, the film width h is equal to the radial clearance c . The respective velocities in the x , y and z directions are denoted by U_x , U_y and U_z . In addition, the velocities on the shaft are indicated by indice a and, on the inner surface of the bushing, by the indice b .

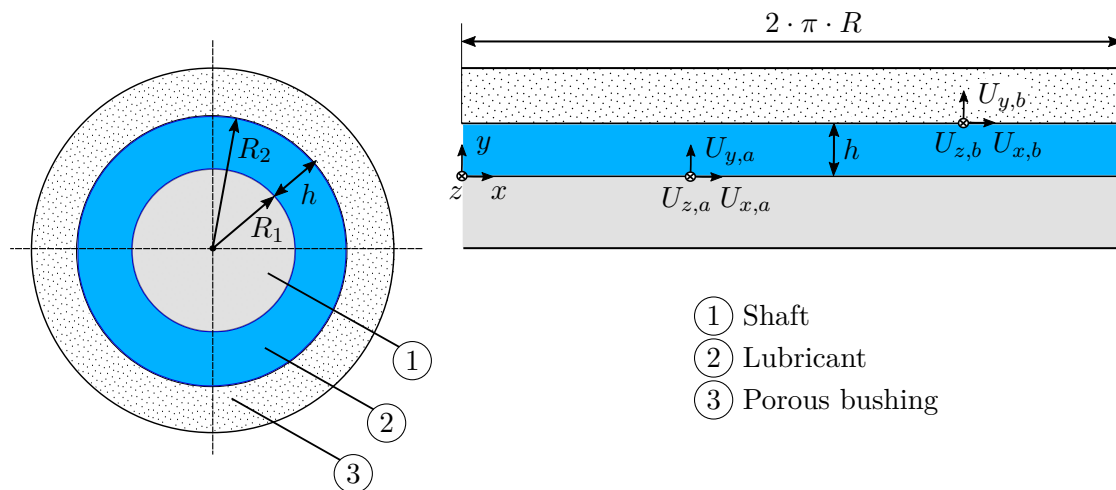


Figure 4.1: Nomenclature of a porous journal bearing (overscaled visualization of the lubricant film width)

The velocities on the shaft and the inside of the bushing are as follows:

$$\begin{aligned} u_x(y=0) &= U_{x,a} & u_y(y=0) &= U_{y,a} & u_z(y=0) &= U_{z,a} \\ u_x(y=h) &= U_{x,b} & u_y(y=h) &= U_{y,b} & u_z(y=h) &= U_{z,b} \end{aligned} \quad (4.1)$$

In the nomenclature of Figure 4.1, the lubricant film thickness h is given as a quantity, dependent on the circumferential direction. Chapters 4.3.2 and 4.3.3 additionally consider the influence of the shaft misalignment and the surface structure.

Depending on the design, the porous liner consists of porous ($\alpha > 0$) and nonporous ($\alpha = 0$) parts. The experiments and computations were performed with a continuous porous liner. In Böhle's study [16], for instance, an assembly of porous and non-porous parts was used for computations.

The following assumptions were made for the derivation of the GREL (see [60, 41, 9]):

- L, R_1 and $R_2 \gg h$
- Viscous and pressure terms $>$ inertial forces and body forces
- Laminar flow (no turbulence and no Taylor-vortex, see state of the art in Chapter 4.4.2)
- $\frac{\partial p}{\partial y} = 0, \frac{\partial \rho}{\partial y} = 0, \frac{\partial \mu}{\partial y} = 0,$
- $\frac{\partial u_x}{\partial y}$ and $\frac{\partial u_z}{\partial y} \gg \frac{\partial u_x}{\partial x}, \frac{\partial u_x}{\partial z}, \frac{\partial u_z}{\partial x}$ and $\frac{\partial u_z}{\partial z}$
- Newtonian fluid
- Steady state

The viscous and pressure forces were assumed to be significantly greater than the inertial and body forces due to the small gap width. This leads to an averaged assumption of pressure, density and dynamic viscosity in the y direction. In the following, a two-dimensional discretization in the lubrication film width and a reduction in the computational effort was obtained through this simplification. The velocity gradients in the radial direction were greater than in the other directions, due to the low film thickness. Air was used to lubricate the bearing, and this is classified as a Newtonian fluid. The derivation starts from the Navier-Stokes equations (NS equations) for transient, three-dimensional and compressible flows in the cartesian coordinate system. The derivation of the NS equations can be found in [88].

The aforementioned simplifications applied to the NS equations lead to the following equations in the x and z directions:

$$0 = -\frac{\partial p}{\partial x} + \frac{\partial u_x}{\partial y} \left(\mu \cdot \frac{\partial u_x}{\partial y} \right) \quad (4.2)$$

$$0 = -\frac{\partial p}{\partial z} + \frac{\partial u_z}{\partial y} \left(\mu \cdot \frac{\partial u_z}{\partial y} \right) \quad (4.3)$$

The equations 4.2 and 4.3 are integrated twice ($\mu = \text{const}$). B_y , C_y , B_{yy} and C_{yy} are integration constants.

$$\frac{\partial u_x}{\partial y} = \frac{\partial p}{\partial x} \cdot \frac{y}{\mu} + B_y \quad (4.4)$$

$$\frac{\partial u_z}{\partial y} = \frac{\partial p}{\partial z} \cdot \frac{y}{\mu} + C_y \quad (4.5)$$

$$u_x(y) = \frac{\partial p}{\partial x} \cdot \frac{y^2}{2 \cdot \mu} + B_y \cdot y + B_{yy} \quad (4.6)$$

$$u_z(y) = \frac{\partial p}{\partial z} \cdot \frac{y^2}{2 \cdot \mu} + C_y \cdot y + C_{yy} \quad (4.7)$$

The following formulae for the velocities $u_x(y)$ and $u_z(y)$ are given by the equations 4.4 to 4.7 and the boundary conditions from 4.1:

$$u_x(y) = -y \cdot \left(\frac{h-y}{2 \cdot \mu} \right) \cdot \frac{\partial p}{\partial x} + U_{x,b} \cdot \left(\frac{h-y}{h} \right) + U_{x,a} \cdot \frac{y}{h} \quad (4.8)$$

$$u_z(y) = -y \cdot \left(\frac{h-y}{2 \cdot \mu} \right) \cdot \frac{\partial p}{\partial z} + U_{z,b} \cdot \left(\frac{h-y}{h} \right) + U_{z,a} \cdot \frac{y}{h} \quad (4.9)$$

Integrating the velocities along the lubricant gap width gives the volume flow rates Q_x and Q_z in the x and z directions:

$$Q_x = \int_0^h u_x(y) \, dy = -\frac{h^3}{12 \cdot \mu} \cdot \frac{\partial p}{\partial x} + \frac{U_{x,a} + U_{x,b}}{2} \cdot h \quad (4.10)$$

$$Q_z = \int_0^h u_z(y) \, dy = -\frac{h^3}{12 \cdot \mu} \cdot \frac{\partial p}{\partial z} + \frac{U_{z,a} + U_{z,b}}{2} \cdot h \quad (4.11)$$

The velocity field of the fluid is $\mathbf{u} = (u_x, u_y, u_z)$ and is given in the vector notation of the stationary compressible continuity equation (see [88]):

$$\nabla \cdot (\rho \cdot \mathbf{u}) = 0 \quad (4.12)$$

The individual terms of the continuity equation are integrated along the width of the lubricant film:

$$\underbrace{\int_{y=0}^{y=h} \frac{\partial}{\partial x} (\rho \cdot u_x) dy}_{(4.15)} + \underbrace{\int_{y=0}^{y=h} \frac{\partial}{\partial z} (\rho \cdot u_z) dy}_{(4.16)} + \underbrace{\int_{y=0}^{y=h} \frac{\partial}{\partial y} (\rho \cdot u_y) dy}_{(4.17)} = 0 \quad (4.13)$$

The Leibniz integration rule (see equation 4.14 from [60, 15]) is used for the integration of the terms 4.15 and 4.16:

$$\int_0^h \frac{\partial}{\partial x} (f(x, y, z)) dy = -f(x, y, h) \cdot \frac{\partial h}{\partial x} + \frac{\partial}{\partial x} \left(\int_0^h f(x, y, z) dy \right) \quad (4.14)$$

The integration of the particular terms from equation 4.13 is as follows:

$$\int_{y=0}^{y=h} \left(\frac{\partial}{\partial x} (\rho \cdot u_x) \right) dy = -\rho \cdot u_{x(y=h)} \cdot \frac{\partial h}{\partial x} + \frac{\partial}{\partial x} \left(\rho \cdot \underbrace{\int_{y=0}^{y=h} u_x dy}_{Q_x} \right) \quad (4.15)$$

$$\int_{y=0}^{y=h} \left(\frac{\partial}{\partial z} (\rho \cdot u_z) \right) dy = -\rho \cdot u_{z(y=h)} \cdot \frac{\partial h}{\partial z} + \frac{\partial}{\partial z} \left(\rho \cdot \underbrace{\int_{y=0}^{y=h} u_z dy}_{Q_z} \right) \quad (4.16)$$

$$\int_{y=0}^{y=h} \left(\frac{\partial}{\partial y} (\rho \cdot u_y) \right) dy = \rho \cdot (u_{y(y=h)} - u_{y(y=0)}) \quad (4.17)$$

Inserting terms 4.15 to 4.17 into equation 4.13 leads to the following equation:

$$\begin{aligned} & -\rho \cdot u_{x(y=h)} \cdot \frac{\partial h}{\partial x} + \frac{\partial}{\partial x} (\rho \cdot Q_x) \\ & -\rho \cdot u_{z(y=h)} \cdot \frac{\partial h}{\partial z} + \frac{\partial}{\partial z} (\rho \cdot Q_z) + \rho \cdot (u_{y(y=h)} - u_{y(y=0)}) = 0 \end{aligned} \quad (4.18)$$

Substituting the boundary conditions 4.1 into equation 4.18 leads to equation 4.19, with the unknown variables $U_{x,a}$, $U_{z,a}$, Q_x , Q_z , $U_{y,a}$ and $U_{y,b}$.

$$\begin{aligned} & -\rho \cdot U_{x,a} \cdot \frac{\partial h}{\partial x} + \frac{\partial}{\partial x} (\rho \cdot Q_x) \\ & -\rho \cdot U_{z,a} \cdot \frac{\partial h}{\partial z} + \frac{\partial}{\partial z} (\rho \cdot Q_z) + \rho \cdot (U_{y,a} - U_{y,b}) = 0 \end{aligned} \quad (4.19)$$

The general Reynolds equation for liquid film lubrication is obtained by substituting the volume flows Q_x and Q_z (equations 4.10 and 4.11).

$$\begin{aligned} & \frac{\partial}{\partial x} \left(\frac{\rho \cdot h^3}{12 \cdot \mu} \cdot \frac{\partial p}{\partial x} \right) + \frac{\partial}{\partial z} \left(\frac{\rho \cdot h^3}{12 \cdot \mu} \cdot \frac{\partial p}{\partial z} \right) = \frac{\partial}{\partial x} \left(h \cdot \rho \cdot \left(\frac{U_{x,a} + U_{x,b}}{2} \right) \right) \\ & + \frac{\partial}{\partial z} \left(h \cdot \rho \cdot \left(\frac{U_{z,a} + U_{z,b}}{2} \right) \right) - U_{x,a} \cdot \rho \cdot \frac{\partial h}{\partial x} - U_{z,a} \cdot \rho \cdot \frac{\partial h}{\partial z} + \rho \cdot (U_{y,a} - U_{y,b}) \end{aligned} \quad (4.20)$$

The conversion from the cartesian to the cylindrical coordinate system is based on the following assumptions [2, 117]:

$$x = R_2 \cdot \varphi \quad y = r \quad z = z \quad (4.21)$$

$$\begin{aligned} & \frac{1}{R_2^2} \cdot \frac{\partial}{\partial \varphi} \left(\frac{\rho \cdot h^3}{12 \cdot \mu} \cdot \frac{\partial p}{\partial \varphi} \right) + \frac{\partial}{\partial z} \left(\frac{\rho \cdot h^3}{12 \cdot \mu} \cdot \frac{\partial p}{\partial z} \right) = \frac{1}{R_2} \cdot \frac{\partial}{\partial \varphi} \left(h \cdot \rho \cdot \left(\frac{U_{\varphi,a} + U_{\varphi,b}}{2} \right) \right) \\ & + \frac{\partial}{\partial z} \left(h \cdot \rho \cdot \left(\frac{U_{z,a} + U_{z,b}}{2} \right) \right) - U_{\varphi,a} \cdot \frac{\rho}{R_2} \cdot \frac{\partial h}{\partial \varphi} - U_{z,a} \cdot \rho \cdot \frac{\partial h}{\partial z} + \rho \cdot (U_{r,a} - U_{r,b}) \end{aligned} \quad (4.22)$$

4.2 Generalized Equation for Porous Liner Flow

Another general approach is adopted for the calculation of the porous bushing. The main equations for the FD, FDc and FD+ models for the computation of the porous bushing are derived based on this general equation. The discretization of the porous liner enables the computation of a three-dimensional flow pattern in the bushing.

The general main equation is derived from the continuity equation and Darcy's law. The equation's application range is, therefore, restricted by Darcy's law. The flow in the porous body must fulfill the following assumptions [10]:

- Laminar flow
- Adiabatic walls
- Steady state solution

The approach in the general equation is based on an anisotropic assumption of permeability. The material's permeability (α_φ , α_z and α_r) and velocity components (u_φ , u_z and u_r) are provided in the φ , z and r directions. Therefore, the velocity components in the cylindrical coordinates within the porous body can be determined using the following equations:

$$u_\varphi = \frac{\alpha_\varphi}{\mu \cdot r} \cdot \frac{\partial p}{\partial \varphi} \quad u_z = \frac{\alpha_z}{\mu} \cdot \frac{\partial p}{\partial z} \quad u_r = \frac{\alpha_r}{\mu} \cdot \frac{\partial p}{\partial r} \quad (4.23)$$

The equation for mass conservation in cylindrical coordinates for a compressible and transient flow is as follows (refer to equivalent equation 4.12 in the Cartesian coordinate system):

$$\frac{\partial \rho}{\partial t} + \frac{1}{r} \cdot \frac{\partial}{\partial r} (\rho \cdot r \cdot u_r) + \frac{1}{r} \cdot \frac{\partial}{\partial \varphi} (\rho \cdot u_\varphi) + \frac{\partial}{\partial z} (\rho \cdot u_z) = 0 \quad (4.24)$$

The assumption of a steady-state solution simplifies the equation to:

$$\frac{1}{r} \cdot \frac{\partial}{\partial r} (\rho \cdot r \cdot u_r) + \frac{1}{r} \cdot \frac{\partial}{\partial \varphi} (\rho \cdot u_\varphi) + \frac{\partial}{\partial z} (\rho \cdot u_z) = 0 \quad (4.25)$$

Substituting the three velocity equations 4.23 into the continuity equation 4.25 leads to the derivation of the general equation for compressible modeling of the porous bushing:

$$\frac{\alpha_r}{r} \cdot \frac{\partial}{\partial r} \left(\frac{\rho \cdot r}{\mu} \cdot \frac{\partial p}{\partial r} \right) + \frac{\alpha_\varphi}{r^2} \cdot \frac{\partial}{\partial \varphi} \left(\frac{\rho}{\mu} \cdot \frac{\partial p}{\partial \varphi} \right) + \alpha_z \cdot \frac{\partial}{\partial z} \left(\frac{\rho}{\mu} \cdot \frac{\partial p}{\partial z} \right) = 0 \quad (4.26)$$

4.3 Lubricant Film Width

The third important formula for the computation of the porous bearing is the equation of the lubricating film thickness (1st equation: computation of lubricating film flow, 2nd equation: computation of flow in the porous bushing). Three approaches of increasing complexity are presented. Starting from an ideal parallel position of the shaft to the bushing, further approaches consider the vertical misalignment of the shaft and, subsequently, the texture of the inner surface of the bushing.

Investigations into the shaft misalignment have already been conducted in the past with different lubrication media. As a result of the low film thickness of the fluid-film bearings, even a slight misalignment can cause contact between the bush and the shaft. This results in friction and wear leading to a deterioration in performance and damage. This issue has been examined, especially in hydrodynamic bearings with oil lubrication. The investigations of Pierre et al. [92] and Bouyer et al. [20] have shown that in oil lubricated bearings eccentricity and misalignment influence deformation and temperature distribution [92, 20]. Experiments by Prabhu [94] have demonstrated that high amplitudes of oscillations can occur from certain misalignments. Investigations into oil lubrication can only be compared to a limited extent to air lubrication. Aerostatic bearings have low heat generation due to low friction. Furthermore, the external pressure supply is comparable to a cooling flow

and counteracts the heating of the lubricating film. Based on the low heat generation, Shi et al. [106] and Li et al. [79] assumed an isothermal flow in the numerical investigations of aerostatic orifice bearings. Their studies numerically demonstrated the dependence of stiffness and damping coefficients on misalignment. The misalignment affects the rotordynamic properties of the system and can even lead to instabilities. A study by Markho et al. [81] investigated the influence of the misalignment on the static performance parameters of an aerostatic orifice bearing. The effect of misalignment on the load-carrying capacity was rarely more than 10 % over the entire eccentricity ratio range studied, and no more than 5 % on the gas consumption.

Another essential aspect to be considered for the computation of the lubricant film thickness is the roughness and texture of the surfaces. Gropper et al. [56] wrote a review paper on the numerical modelling of roughness and textures. They separate direct/deterministic and indirect/stochastic methods. The deterministic methods aim at a fine discretization to resolve the topography. This method is disadvantageous for the resolution of fine structures or roughness and requires a high resolution, which leads to a disproportionately high requirement for computing power. Stochastic methods based on flow factors, such as by Patir and Cheng [90] or Elrod [44], can lead to physically implausible flows due to the averaging [63].

Furthermore, the grooves of the tested bearing are considerably more significant than the usual roughness of plain bearings. The aerostatic bearings examined by Castelli [25] had an average roughness of $1.3 \mu\text{m}$ to $1.8 \mu\text{m}$. The C/C bearings examined in this experiment have deflections of up to $120 \mu\text{m}$ (mean depth of $30.6 \mu\text{m}$). The grooves are, thus, more comparable to textured bearings. For instance, Korenaga et al. [72] performed experiments with dimple journal bearings with a depth of $60 \mu\text{m}$, and Song et al. [110] examined spiral-grooved air journal bearings with a groove depth of $10 \mu\text{m}$. Different assumptions regarding the lubricant film geometry are applied for the models for the computation of the gap width. The assumption of a uniform lubricant film width in the axial direction was adopted for the Si and FD models (see Table 4.1). The assumption was extended for the FDc and FD+ models by including the shaft misalignment. In addition, the texture of the inner surface of the porous material was implemented in the FD+ model.

4.3.1 Film Width with Shaft and Bushing Axis in Alignment

The Si and FD models assume a uniform width distribution of the lubricant film in the axial direction, as illustrated in Figure 4.2. These models assume an ideal position of the shaft to the bushing without misalignment, resulting in a constant eccentricity e in the axial direction. The location of the narrowest lubrication gap is determined by φ_0 . The lubricant film width $h(\varphi)$ is constant in the z direction and depends on the radial clearance c and the eccentricity e :

$$h(\varphi) \approx c + e \cdot \cos(\varphi - \varphi_0) \quad (4.27)$$

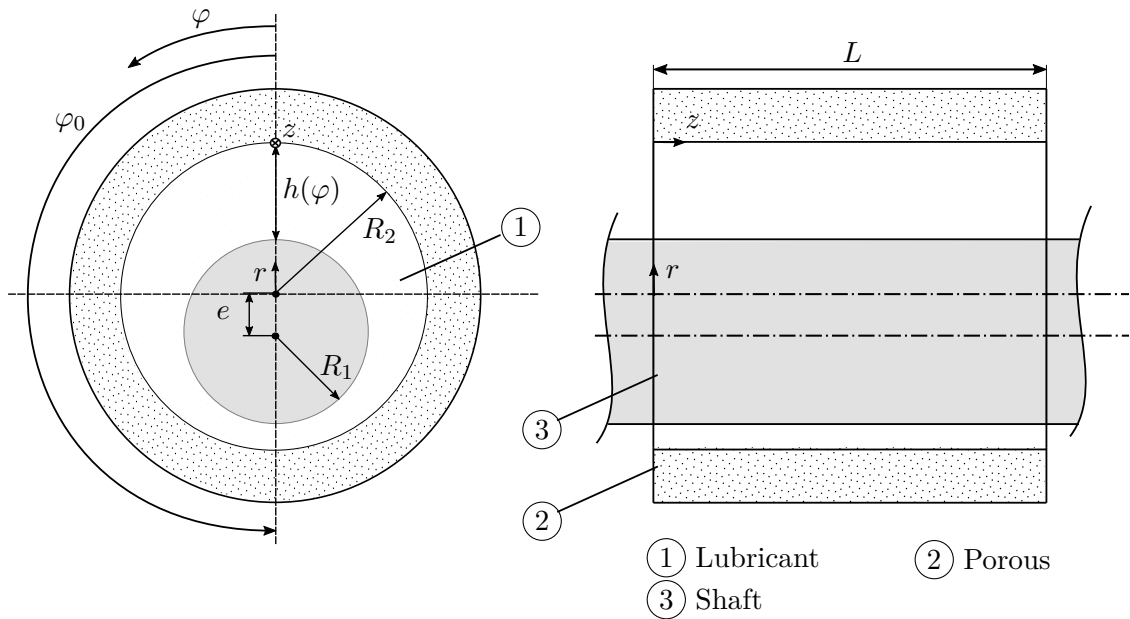


Figure 4.2: Schematic representation of an axially uniform lubricant film thickness in cylindrical coordinates (overscaled visualization of the lubricant film width)

4.3.2 Film Width with Consideration of Shaft Misalignment

Incorporating the shaft misalignment into the calculation of the lubricant film width is achieved by adding a new term to Equation 4.27, as presented by Xu et al. [124], and used in this study for the FDc model. Figure 4.3 depicts the lubricant film geometry that accounts for the shaft misalignment.

A rigid shaft without deformation is assumed in this study, which results in a linear progression of eccentricity from e_1 to e_2 due to shaft misalignment. The average eccentricity is determined at the position $z = L/2$ and denoted by e_m . The difference in eccentricities at the liner endings is denoted by e' . This assumption of misalignment introduces an

additional dependence of the lubrication gap width on the axial direction along the bushing length L . The equation used to calculate the lubricant film width, taking into account the misalignment, is as follows:

$$h(\varphi, z) \approx c + e \cdot \cos(\varphi - \varphi_0) + e' \cdot \left(\frac{z}{L} - \frac{1}{2}\right) \cdot \cos(\varphi - \varphi_0) \quad (4.28)$$

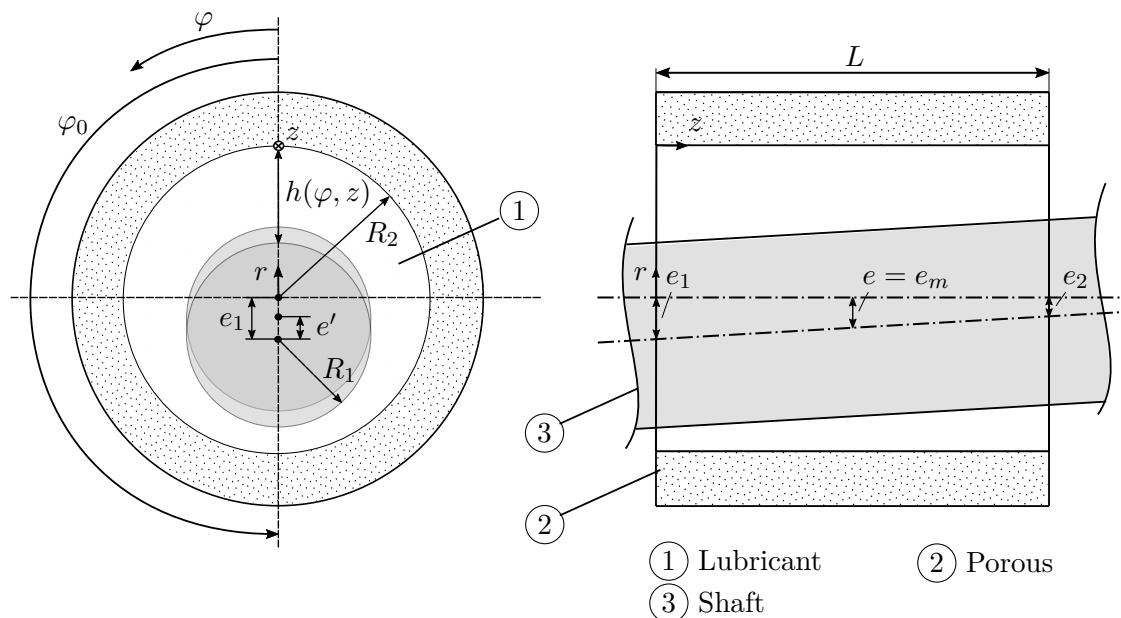


Figure 4.3: Schematic representation of the lubricant film width under consideration of the shaft misalignment in cylindrical coordinates (overscaled visualization of the lubricant film width)

4.3.3 Film Width with Consideration of Shaft Misalignment and Surface Structure

In the previous two equations of the lubrication gap width, an ideal smooth surface of the shaft and the inner surface of the bushing was assumed. On the one hand, the shaft surface was assumed to be smooth due to the multiple grinding processes, leading to an average roughness R_a far below $1 \mu\text{m}$. The structure of the inner surface of the bushing, on the other hand, exhibited distinct grooves, as determined by the measurements with a contact-type probe described in Chapter 2.3. The measurements showed a pattern of repeating grooves. The grooves formed in particular in the z direction and showed an approximately rotation-symmetrical course. This structure can be attributed to the layered structure of the porous C/C material. Thus, the following assumptions were made for the formulation of the lubricant film equation.

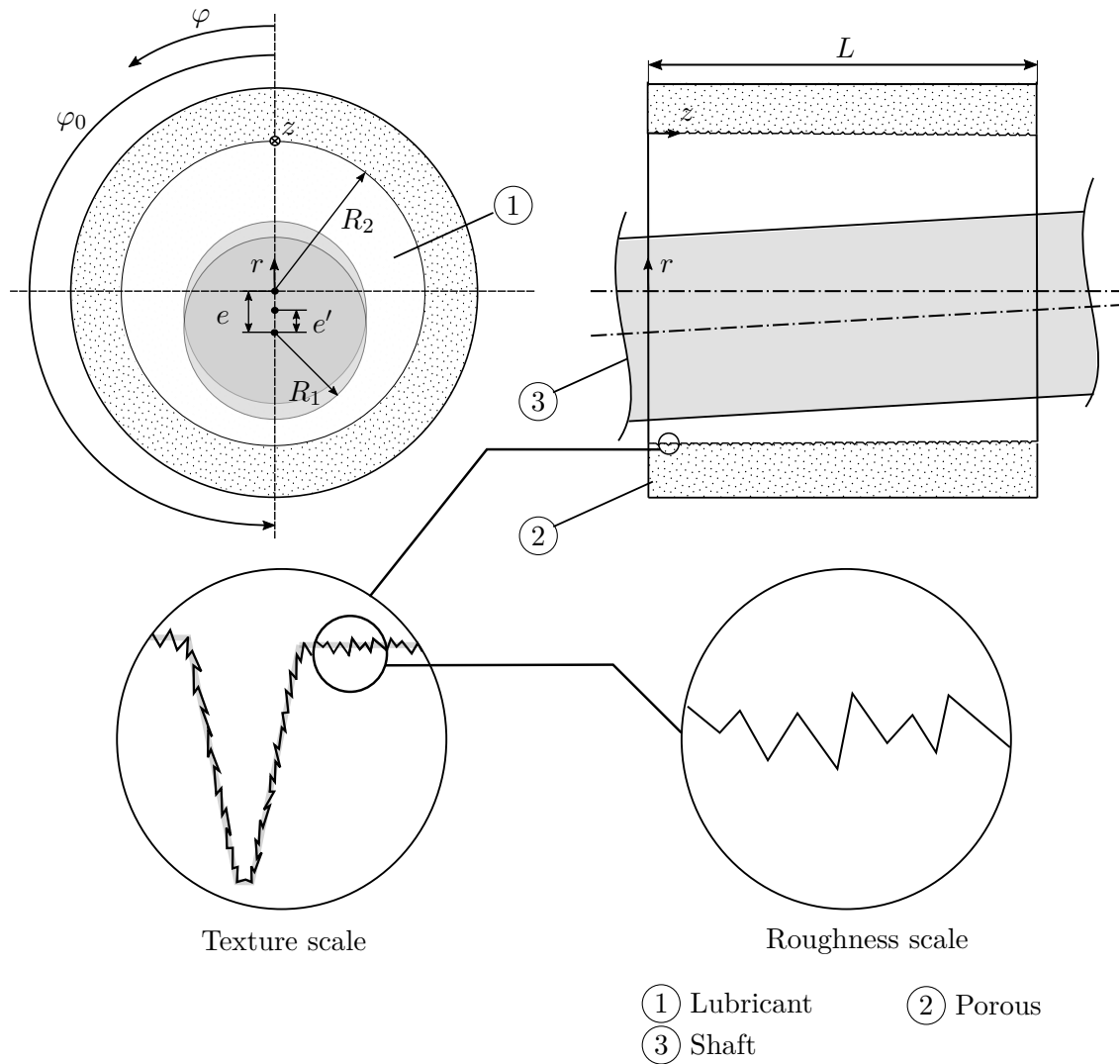


Figure 4.4: Schematic representation of the lubricant film width under consideration of the shaft misalignment and surface structure in cylindrical coordinates (overscaled visualization of the lubricant film width)

- $R_{a,bushing} \gg R_{a,shaft}$
- $h_{tex}(z)$, nearly rotationally symmetric groove structure

The separation of a bearing into contact, texture and roughness scales done by Gropper et al. [56] was used for the C/C liner inner surface (see Figure 4.4). The contact scale represents two non-parallel contact surfaces of a journal bearing. The texture scale applies to machined structures, such as spiral grooves or dimples. For this particular C/C bushing, the grooves were also classified as texture. Some of the deepest grooves in the C/C bushing were deeper than the radial clearance of $30 \mu\text{m}$. The roughness scale correlated to an order of magnitude of approximately $1 \mu\text{m}$. As a consequence of the distinctive groove

contour, the focus was on the modeling of the grooves. The lubricant film width equation with consideration of the shaft misalignment and the structure of the inner surface of the bushing is as follows:

$$h(\varphi, z) \approx c + e \cdot \cos(\varphi - \varphi_0) + e' \cdot \left(\frac{z}{L} - \frac{1}{2}\right) \cdot \cos(\varphi - \varphi_0) + h_{tex} \quad (4.29)$$

The formula is based on equation 4.28 and is extended by the term $h_{tex}(z)$. A simplified periodic groove structure is determined based on the measured inner surface of the bushing. This groove pattern is imposed on the lubricant film thickness equation and implemented in the FD+ model.

Procedure for Generating the Average Groove Profile

The objective of this study is to implement the characteristic surface structure of the bushing in order to reproduce the influence of the orthotropically layered material. The surface structure is characterised by frequently occurring, distinctive grooves. This implementation of the surface structure is expected to improve the accuracy of the lubrication analysis by accounting for the effects of the grooves on the lubricant film thickness and overall fluid flow.

The deterministic approach involves the direct transfer of the texture into the modeling, which admittedly has significant disadvantages. However, this approach has significant disadvantages, including the need for extensive surface measurements of the bushing and subsequent computer-intensive simulations due to the high discretisation effort required. On the other hand, the stochastic approach reduces computation time but has the disadvantage of not modeling the characteristic recurring groove structure of the bearing. [56]

In the present study, a semi-deterministic approach is adopted. Specifically, an averaged groove is determined from the captured surface data of the test specimen and repeatedly projected across the inner surface. The simplification of rotationally symmetrical grooves is chosen on the basis of the layered structure of the bushing material. Additionally, it is assumed that the influence of the grooves is more dominant than that of the roughness. Therefore, the focus is on the implementation of the grooves. The process for determining the average groove contour involves measuring the inner surfaces of the bush along the z-direction at positions $\varphi = 0^\circ$ and 180° . From the measurement data, a distribution of contour depths for each measurement series is generated. The statistically most frequent depth t_0 is then used to generate reference lines in each series, as shown in Figure 2.15. The measurement data is offset by t_0 so that the most frequent distribution of the structure at the radius is at depth zero. The initial and processed data with offset are shown for the measurement series at positions $\varphi = 0^\circ$ and 180° along the liner in Figure 4.5 i).

The standard deviation (STD) is determined from the processed data and plotted as an auxiliary line in Figure 4.5 ii). The STD-line is used to classify the profile into grooves. Values below the std-line are identified as grooves, and the subsequent groove width is

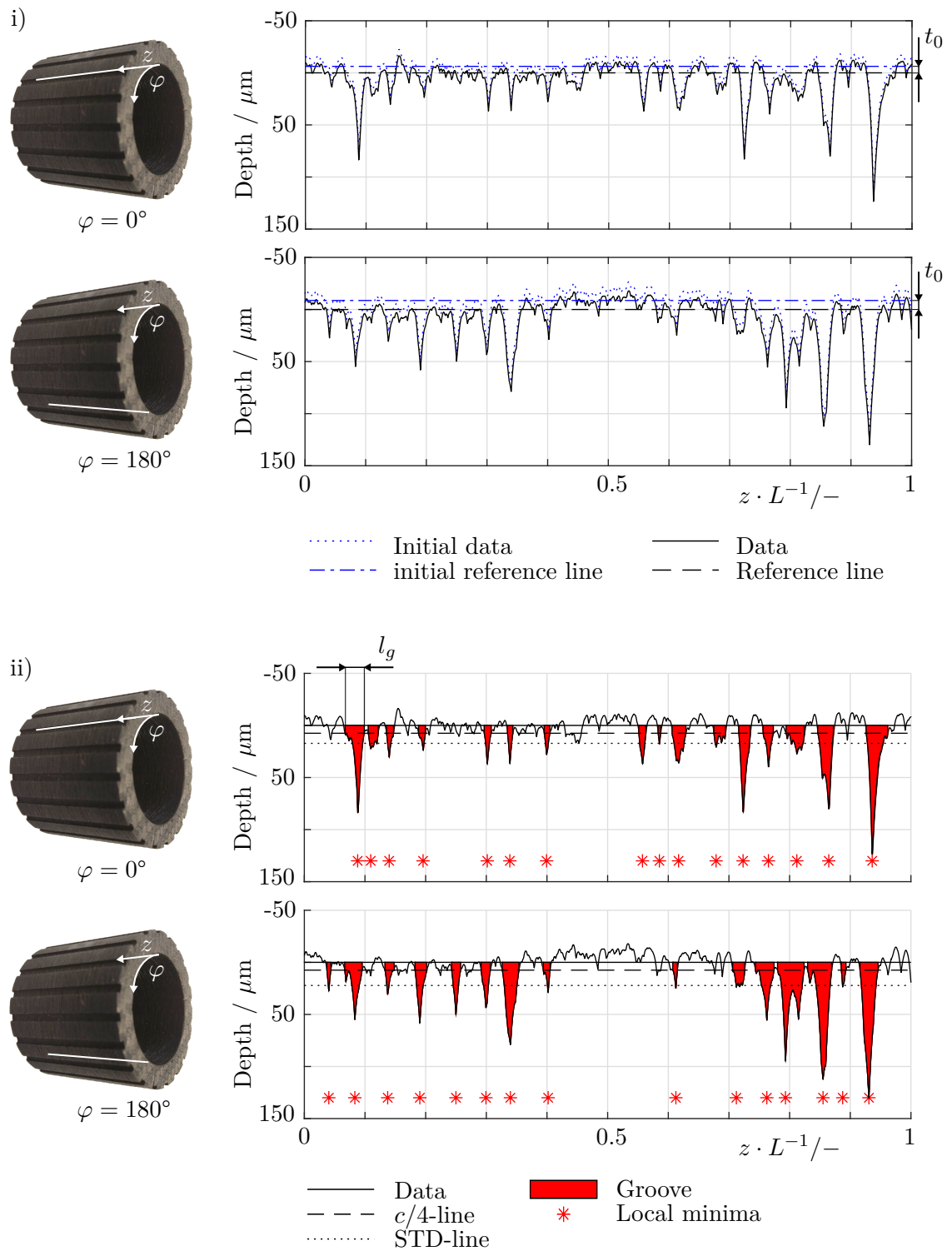


Figure 4.5: Generating the average groove profile:

i) Set offset, ii) Detection of grooves

determined by the $c/4$ -line. The $c/4$ -line is located at a depth of one-quarter of the radial clearance. The mean groove width is determined by taking the arithmetic mean of the identified groove widths l_g , and the average groove depth is determined as the arithmetic mean of the data associated with the grooves, denoted as \bar{t}_g . The number of grooves along the measured distance is given by the value x_g .

Using the determined values \bar{l}_g and \bar{t}_g , an average groove is generated, which is then multiplied by the number of grooves x_g along the z -axis to create the characteristic texture profile h_{tex} . Figure 4.6 shows the resulting profile.

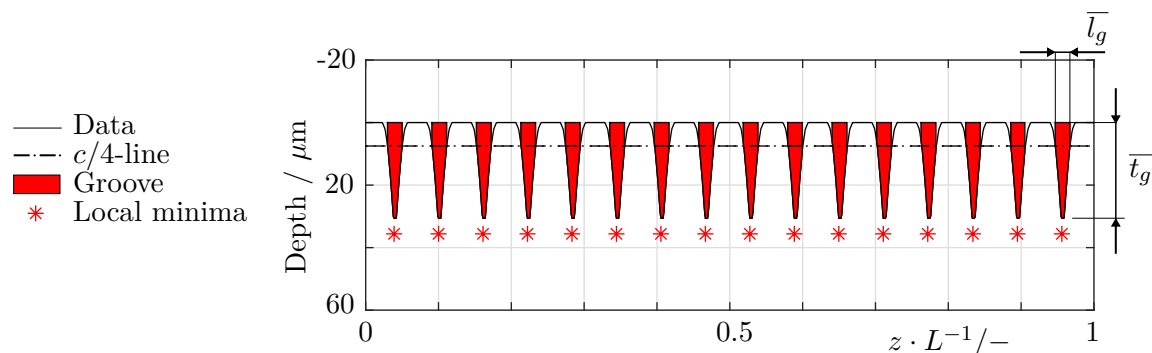


Figure 4.6: Groove profile h_{tex}

4.4 Further Model Assumptions

4.4.1 Thermohydrodynamic Modelling

The calculation of the lubricating film for gas bearings is largely assumed to be isothermal. The low viscosity of air (compared to oil) causes low viscous forces and, thus, low heat generation [32]. Castelli and Pirvics [24] state in their review paper on gas film bearings that, for most gases, the lubricating film is essentially isothermal, and the viscosity can be assumed to be constant. Numerical publications with comparable justifications and the assumption of isothermal flow are widely available and were adopted in the publications of Castelli and McCabe [23].

Paulsen and Santos [91] numerically compared the use of an isothermal model with a thermohydrodynamic model of a dynamic journal bearing (see equation 4.30). The investigations support the widely used isothermal assumption in the range of small bearing numbers Δ_B . The bearing number Δ_B is a dimensionless parameter that is based on the dynamic viscosity of the fluid μ , the circumferential speed of the shaft $U_{\varphi,a}$, the radius of the shaft R_1 , the pressure p_a and the radial clearance c :

$$\Delta_B = \frac{6 \cdot \mu \cdot U_{\varphi,a} \cdot R_1}{p_a \cdot c^2} \quad (4.30)$$

In the investigation of Paulsen and Santos, the load on the bearing was increased up to 80 N. The influence on the stiffness and damping coefficients were rated small. In a direct comparison with the bearing examined in this study, the bearing loads are comparable. However, the rotational speed in this study was significantly lower, resulting in a lower number of bearings (see table 4.2). Zhang et al. [127] investigated aerostatic orifice sliding bearings under purely static and hybrid conditions. The calculations were performed under isothermal conditions. For comparability, the parameters of the hybrid measurement and the bearing numbers are listed in Table 4.2. The bearing number of Zhang et al., with a value of $\Delta_B = 2.2$, is within the values of the measurement series done in this study, $\Delta_B = 0.2$, and the experiments of Paulsen and Santos, $\Delta_B = 15.4$. The assumption of isothermal flow for aerostatic bearings is supported by Shi et al. [106]. The investigation by Shi et al. included air bearings with aerostatic orifice and also considered the isothermal assumption with regard to low friction and low heat generation. Based on the findings, it is assumed that the lubricant flow is isothermal.

Table 4.2: Parameters of the studies by Paulsen and Santos [91] and Zhang et al. [127]

	Mode	p_a	T	R_1	c	n	Δ_B
	/ -	/ bar	/ K	/ mm	/ μm	/ rpm	/ -
Paulsen and Santos	Dynamic	1	293.15	20.000	25	30000	15.4
Zhang et al.	Hybrid	1	293.15	12.500	15	25000	2.2
Exp. C/C	Static	1	292.65	14.030	30	8000	0.2

4.4.2 Turbulence in Lubricant Film

Evidence from external publications are used to argue whether lubricant flow is laminar or turbulent. Taylor contributed pioneering work on the transition from a laminar flow to a laminar vortex flow [114]. In 1923, he published his theory and experimental investigations on the stability of a viscous flow between two rotating cylinders. His linear instability theory and experiments showed high agreement with a rotating concentric inner cylinder and a stationary outer cylinder.

The journal bearing involves a stationary bushing and a shaft rotating at a constant speed, creating an analogy to a Taylor-Couette system. A Taylor-Couette system includes a rotating inner cylinder and a stationary outer cylinder. Based on external reports of Taylor Couette systems, the Taylor number is used to assess the flow characteristics in investigations of the bearing.

The Taylor number Ta is obtained from the Reynolds number Re , the square root of the quotient of the radial clearance c and the radius of the shaft R_1 . The Reynolds number is determined from the circumferential velocity of the shaft $U_{\varphi,a}$, the density ρ and the dynamic viscosity μ of the fluid. The radial clearance c is used as the characteristic length.

$$Ta = Re \cdot \sqrt{\frac{c}{R_1}} = \frac{U_{\varphi,a} \cdot \rho \cdot c}{\mu} \cdot \sqrt{\frac{c}{R_1}} \quad (4.31)$$

In this experiment the Taylor number was determined for two cases (see Table 4.3). Case (i) refers to the minimum Taylor value. It was assumed that the rotational speed is 1000 rpm. The calculation of density and viscosity was determined by the lowest supply pressure 5 bar and a temperature of 292.65 K. Case (ii) represents the highest possible Taylor number obtained during the series of measurements at a rotational speed of 8000 rpm and a supply pressure of 7 bar. The actual pressure in the lubricating film is between the supply pressure and the discharge pressure (atmospheric pressure). Consequently, the Taylor numbers for the bearing experiments are in a range between 0.9 and 7.5.

Two critical Taylor numbers can be determined for the mentioned bearing with a rotating inner cylinder and stationary outer cylinder. The first critical Taylor number, $Ta_{crit,1}$, describes the transition from a laminar flow to a laminar flow with a vortex flow (Taylor vortex). The second critical Taylor number, $Ta_{crit,2}$, characterizes the subsequent transition to a turbulent flow. Taylor [114] derived a theoretical value of $Ta_{crit,1} = 41.3$. A study on the determination of the second critical Taylor number was carried out by Sha et al. [105] using commercial CFD software and resulted in a transition at $Ta_{crit,2} \approx 400$.

Since the Taylor numbers of this study are below the first critical Taylor number, the transition of a laminar flow to a laminar flow with Taylor vortex is considered in more detail. Considerable research attention has been devoted to the transition in terms of Taylor number Ta , eccentricity ratio ε , and $c \cdot R_1^{-1}$. In the following, the parameters of these studies are compared with the C/C experiments to evaluate the lubricant flow.

The experiments of Cole [29] and Vohr [118] have proved that an increase in eccentricity stabilizes the flow. Similarly, it has been shown that a higher c/R_1 ratio also has a stabilizing effect. Figure 4.7 shows the results of [105, 114, 29, 118, 50]. The data from these studies represent the transition from a laminar flow to a laminar flow with Taylor vortices. The corresponding area of this C/C bearing study has also been added to the diagrams and is in the laminar region.

This study assumes that the rotating shaft does not generate Taylor vortices and that no turbulence forms in the lubricating film. Therefore, it is assumed that the lubricant flow is laminar.

Table 4.3: Ta of the C/C experiments: $R_1 = 14.03$ mm, $c = 0.03$ mm, $c \cdot R_1^{-1} = 0.0021$

	n / rpm	p_s / bar	T / K	$U_{\varphi,a}$ / m s ⁻¹	Re / -	Ta / -
Exp. i)	1000	5	292.7	1.5	20.2	0.9
Exp. ii)	8000	7	292.7	11.8	161.2	7.5

However, the assumption of a rotating inner cylinder and a stationary outer cylinder represents a simplified assumption of the bearing. There are supplementary boundary conditions with a pressurized porous journal bearing. In particular, the flow pattern is influenced by the radial inflow at the outer porous cylinder and an axial outflow at each axial end of the bearing. The additional flow components affect the Couette flow and, hence, the critical Taylor numbers [66].

Investigations have been performed into the Couette flow with additional flow components, for instance, for dynamic filter devices, such as for blood filtration. For this purpose, the medium is fed into the annular space. The rotating porous inner cylinder separates the filtrate and concentrate [66, 93, 11, 64, 83, 82].

Theoretical and experimental studies have been conducted in this area, and the assumptions of these studies are shown in Figure 4.8. The mentioned cases involve the rotating component of the inner cylinder and a stationary outer cylinder. The investigations of [114, 66, 93, 3] involved a porous outer cylinder and an additional porous inner cylinder. As a result, a radial flow is established through both cylinders. The model of Johnson and Lueptow [66] also includes an axial flow component, and the model of Altmeyer [3] used an additional magnetic field to investigate a ferrofluid that exerts an influence on the flow. The aforementioned studies included additional flow components, which precludes a proper comparison with the current bearing. In fact, there are no studies that have investigated the laminar transition for the specific case of a pressurized porous bearing.

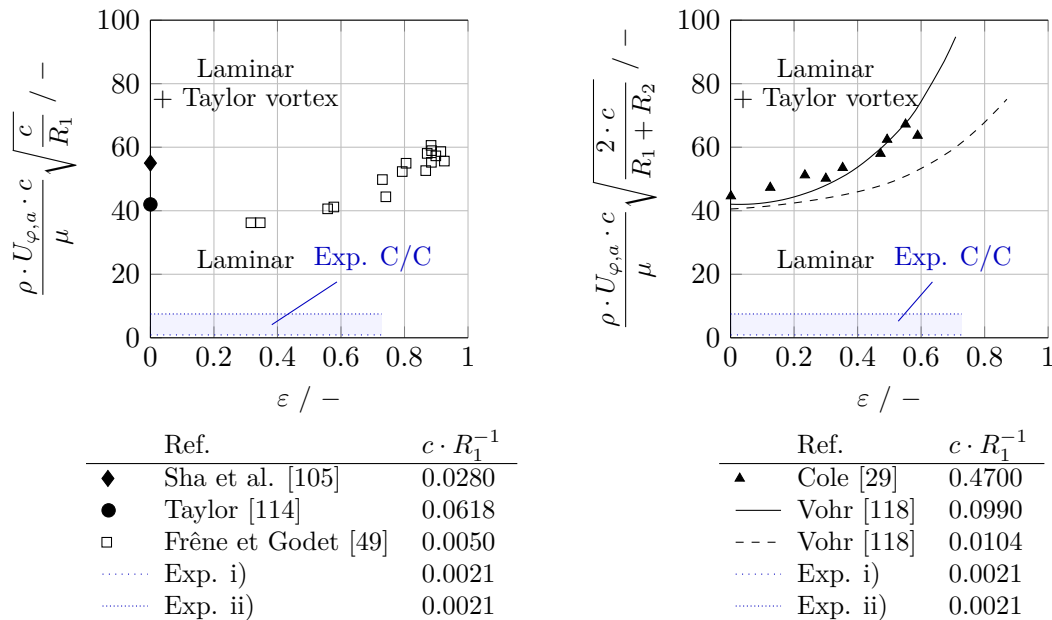


Figure 4.7: External experiments and calculations to determine the transition of a laminar flow to a laminar flow with Taylor vortices

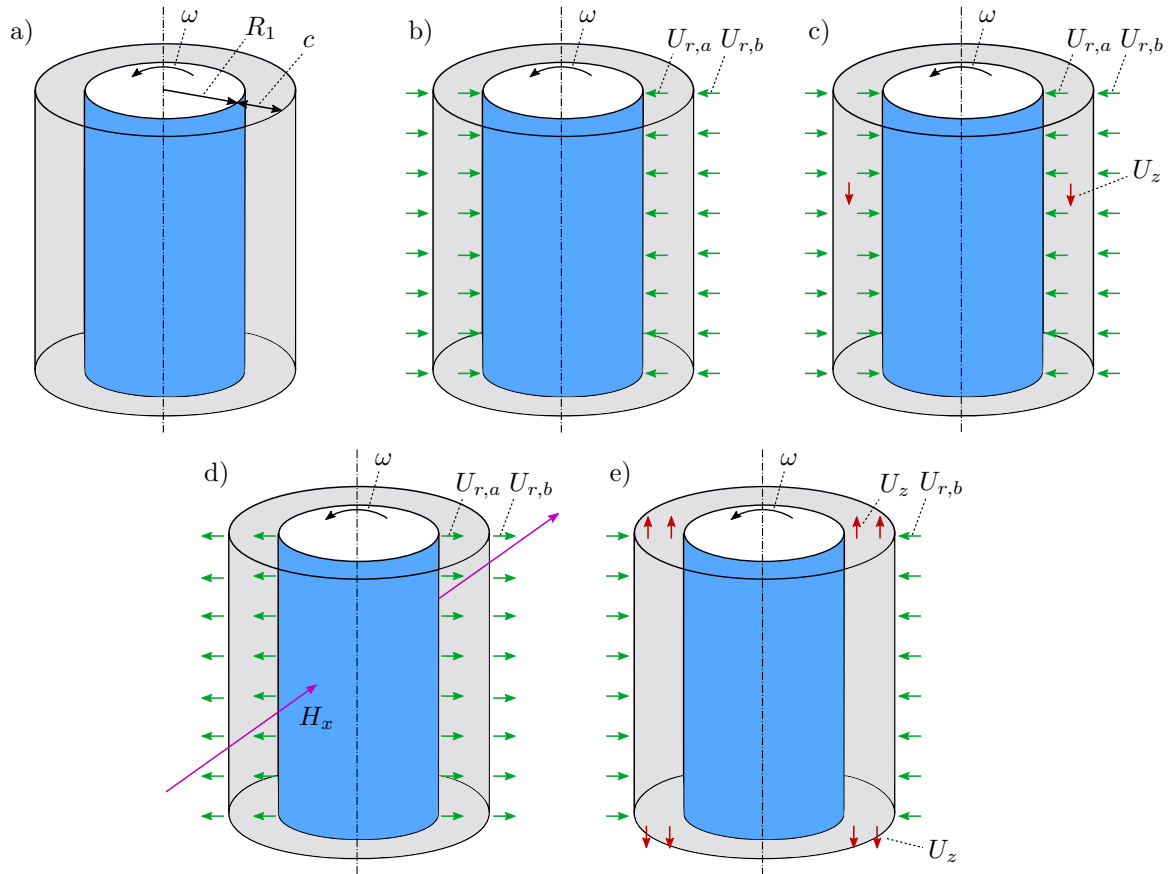


Figure 4.8: Schematic concepts of flow configurations - a) Taylor-Couette flow [114]: Rotating inner cylinder, b) Pourjafar et al. [93]: Rotating inner cylinder, radial throughflow c) Johnson and Lueptow [66]: Rotating inner cylinder, radial throughflow, axial flow, d) Altmeyer [3]: Rotating inner cylinder, radial throughflow, magnetic field, e) external pressurized porous journal bearing: Rotating inner cylinder, radial inflow at outer cylinder, axial outflow at annulus

4.5 Developed models

4.5.1 Simple Model

The Si model is used as the most elementary model for bearing simulation in this study. The porous bushing is not discretized, which significantly reduces the computation time. The following assumptions are made:

- $\left(\frac{\partial p}{\partial r}\right)_{bushing} \gg \left(\frac{\partial p}{\partial \varphi}\right)_{bushing}, \left(\frac{\partial p}{\partial z}\right)_{bushing}$
→ One-dimensional flow through the porous bushing
- $\rho = \text{const.}$

- $\mu = \text{const.}$
- Film width: $h(\varphi)$
- $\alpha = \alpha_\varphi = \alpha_z = \alpha_r$

The Si model assumes a one-dimensional radial flow through the porous body, based on the assumption that the pressure gradient in the radial direction is significantly greater than in the axial and circumferential directions. The computation of the lubricating film assumes a constant density and viscosity of the fluid. The lubricant film width $h(\varphi)$ is assumed to be uniform in the axial direction in the absence of misalignment (equation 4.27). The porous C/C bushing is assumed to be isotropic. Consequently, the experimentally determined permeability of the material α is assumed to be constant in the φ , z , and r directions.

Porous Liner

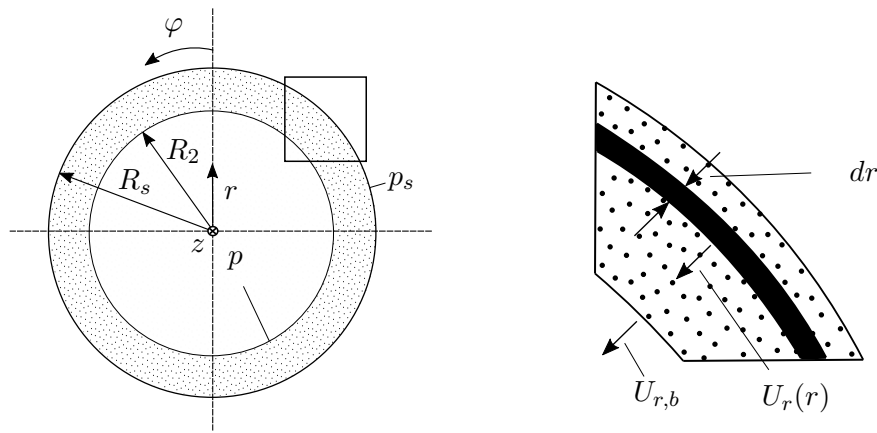


Figure 4.9: A schematic representation of a porous liner

To obtain the radial outflow velocity of the bushing $U_{r,b}$, the model assumes a pure radial flow through the porous structure, computed based on Darcy's law in the radial direction (see equation 4.32). The pressure drop dp is determined by the dynamic viscosity μ , the permeability α , and the radial velocity $U_r(r)$:

$$dp = \frac{\mu}{\alpha} \cdot U_r(r) \cdot dr \quad (4.32)$$

The porous liner can be analyzed using the continuity equation, which leads to equation (4.33). Figure 4.9 shows a schematic representation of the liner. The outer bushing radius R_s is imposed to the supply pressure p_s , while R_2 represents the inner bushing radius and the transition to the lubricant film.

$$U_r(r) \cdot r \cdot d\varphi = U_{r,b} \cdot R_2 \cdot d\varphi \quad \rightarrow \quad U_r(r) = U_{r,b} \cdot \frac{R_2}{r} \quad (4.33)$$

The substitution of equation 4.33 into equation 4.32 leads to the following equation:

$$dp = \frac{\mu}{\alpha} \cdot U_{r,b} \cdot R_2 \cdot \frac{dr}{r} \quad (4.34)$$

Subsequent integration and transformation of the equation yields the velocity $U_{r,b}$:

$$\int_p^{p_s} dp = \frac{\mu}{\alpha} \cdot U_{r,b} \cdot R_2 \cdot \int_{R_2}^{R_s} \frac{dr}{r} \quad (4.35)$$

$$p_s - p = \frac{\mu}{\alpha} \cdot U_{r,b} \cdot R_2 \cdot \ln\left(\frac{R_s}{R_2}\right) \quad (4.36)$$

$$U_{r,b} = \frac{\alpha}{\mu \cdot R_2 \cdot \ln\left(\frac{R_s}{R_2}\right) \cdot (p_s - p)} \quad (4.37)$$

Lubricant

The general lubricant film equation 4.22 is used to derive the lubricant film equation. The velocity $U_{r,b}$ is determined with a one-dimensional radial flow assumption. The circumferential velocity of the shaft, $U_{\varphi,a}$, is taken into account, while $U_{r,a}$ depends on $U_{x,a}$ and the derivative of the gap width in the φ direction (as described in the literature by Hamrock [60]). The remaining velocities, $U_{\varphi,b}$, $U_{z,a}$ and $U_{z,b}$ are assumed to be zero.

$$U_{\varphi,a} = 2 \cdot \pi \cdot n \cdot R_1 \quad (4.38)$$

$$U_{r,a} = U_{\varphi,a} \cdot \frac{1}{R_1} \cdot \frac{\partial h}{\partial \varphi} \quad (4.39)$$

$$U_{\varphi,b} = U_{z,a} = U_{z,b} = 0 \quad (4.40)$$

Substituting the velocity equations 4.37 to 4.40 into the GREL equation 4.22 results in the following equation:

$$\begin{aligned} & \frac{\partial}{\partial z} \left(h^3 \cdot \frac{\partial}{\partial z} \right) + \frac{1}{R_2^2} \cdot \frac{\partial}{\partial \varphi} \left(h^3 \cdot \frac{\partial}{\partial \varphi} \right) \\ & = 6 \cdot U_{\varphi,a} \cdot \frac{1}{R_2} \cdot \mu \cdot \frac{\partial h}{\partial \varphi} - (p_s - p) \cdot \frac{12 \cdot \alpha}{R_2 \cdot \ln\left(\frac{R_s}{R_2}\right)} \end{aligned} \quad (4.41)$$

By differentiating equation 4.41, the governing equation for computing the pressure distribution in the lubricant film is obtained.:

$$\begin{aligned} & \frac{\partial p}{\partial z} \cdot \left(3 \cdot h^2 \cdot \frac{\partial h}{\partial z} \right) + \frac{\partial^2 p}{\partial z^2} \cdot \left(h^3 \right) + \frac{\partial p}{\partial \varphi} \cdot \left(3 \cdot h^2 \cdot \frac{1}{R_2^2} \cdot \frac{\partial h}{\partial \varphi} \right) + \frac{\partial^2 p}{\partial \varphi^2} \cdot \left(h^3 \cdot \frac{1}{R_2^2} \right) \\ & = 6 \cdot U_{\varphi,a} \cdot \mu \cdot \frac{1}{R_2} \cdot \frac{\partial h}{\partial \varphi} - \left(p_s - p \right) \cdot \frac{12 \cdot \alpha}{R_2 \cdot \ln \left(\frac{R_s}{R_2} \right)} \end{aligned} \quad (4.42)$$

A two-dimensional equidistant computational mesh is used to discretize the lubricant (as shown in Figure 4.10). A periodic boundary condition is adopted at $\varphi = 0$ and $\varphi = 2 \cdot \pi$. At the axial bearing ends $z = 0$ and $z = L$, Dirichlet boundary conditions with the output pressure p_a (atmospheric pressure) are imposed. The number of nodes in the circumferential and axial directions are N_φ and N_z , respectively, and the distance between the nodes is provided by the variables $\Delta\varphi$ and Δz .

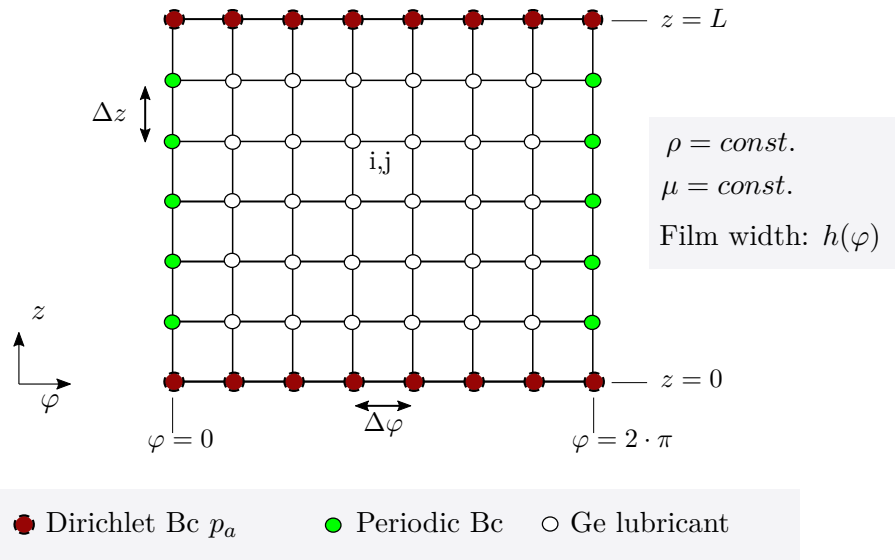


Figure 4.10: Si: numerical grid of the lubricant film

Solver

The Si model (see flowchart in Figure 4.11) requires minimal computing power due to its low complexity. A matrix is generated by inserting the geometrical data of the bushing, the parameters of the desired operating points, the material data of the lubricating film, and the numerical data. The pressure distribution of the lubricating film is determined within an iterative loop based on the governing equation 4.42, and the loop is stopped once the convergence criterion C_i is reached. A maximum residual criterion with a value of $1E - 8$ is selected. The static performance parameters, such as the load-carrying capacity and gas consumption, are determined based on the pressure distribution.

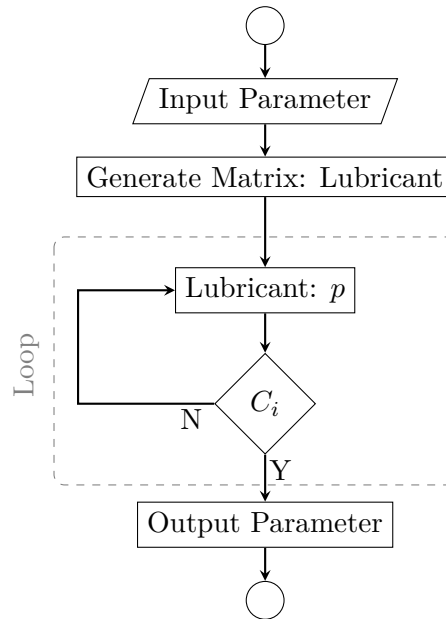


Figure 4.11: Si: flowchart

4.5.2 Full Darcy

The FD model extends the Si model by discretizing the porous bushing, which enables a three-dimensional analysis of the flow within the restrictor. The model is based on the following assumptions:

- Three-dimensional flow through the porous bushing
- $\rho = \text{const.}$
- $\mu = \text{const.}$
- Film width: $h(\varphi)$
- $\alpha = \alpha_\varphi = \alpha_z = \alpha_r$

Density and dynamic viscosity are assumed to be constant within the lubricant film and the porous body. The lubricant film thickness is calculated assuming a parallel position of the shaft axis and the bushing axis using equation 4.29. Additionally, the porous bushing material is considered to be isotropic. The FD model further assumes incompressible flow.

Porous Liner

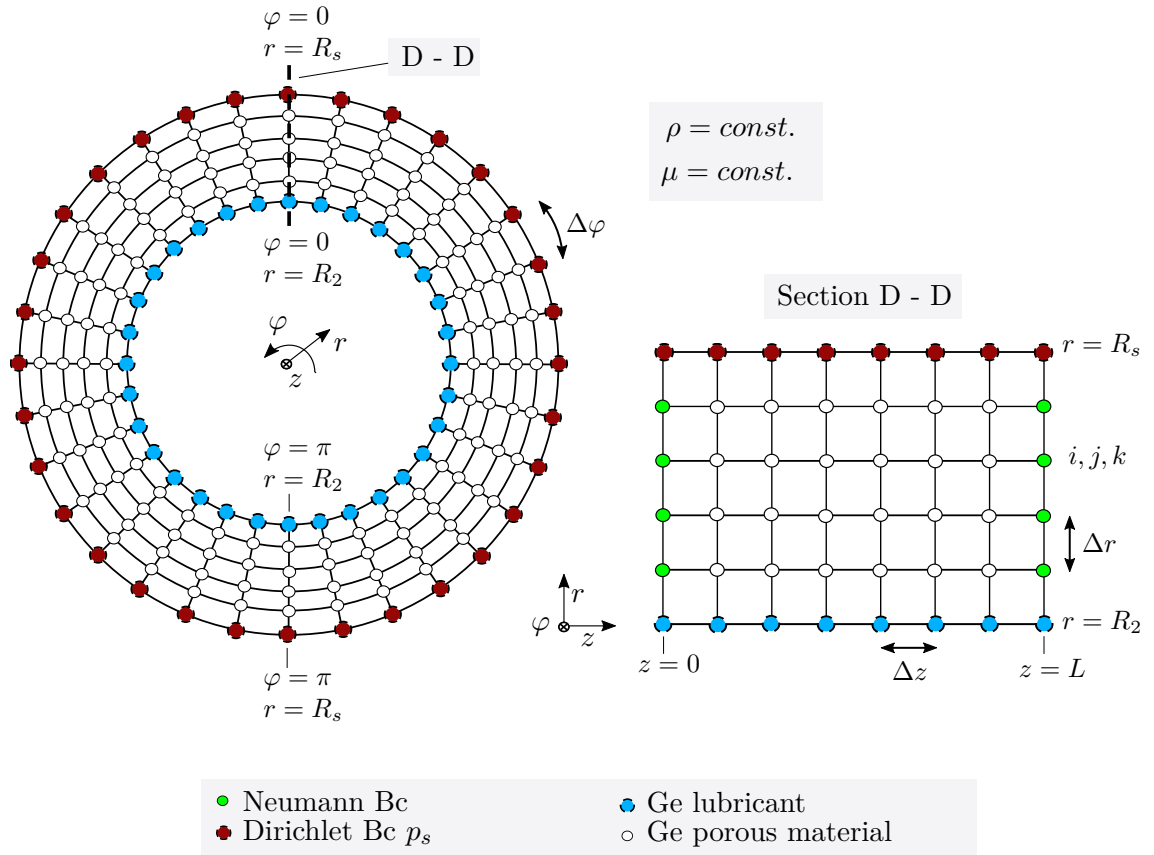


Figure 4.12: FD: numerical mesh for the porous bushing

The governing equation for the calculation of the porous liner is based on the derivation of the general equation for flow in porous liners. The assumptions of the FD model simplify equation 4.26 as follows:

$$\frac{\alpha \cdot \rho}{r \cdot \mu} \cdot \frac{\partial}{\partial r} \left(r \cdot \frac{\partial p}{\partial r} \right) + \frac{\alpha \cdot \rho}{r^2 \cdot \mu} \cdot \frac{\partial}{\partial \varphi} \left(\frac{\partial p}{\partial \varphi} \right) + \frac{\alpha \cdot \rho}{\mu} \cdot \frac{\partial}{\partial z} \left(\frac{\partial p}{\partial z} \right) = 0 \quad (4.43)$$

Assuming constant density, constant dynamic viscosity, and uniform permeability, the equation is simplified to the following:

$$\frac{1}{r} \cdot \frac{\partial}{\partial r} \left(r \cdot \frac{\partial p}{\partial r} \right) + \frac{1}{r^2} \cdot \frac{\partial}{\partial \varphi} \left(\frac{\partial p}{\partial \varphi} \right) + \frac{\partial}{\partial z} \left(\frac{\partial p}{\partial z} \right) = 0 \quad (4.44)$$

The equation governing the flow in the porous liner (Eq. 4.45) is obtained by differentiating equation 4.44:

$$\frac{1}{r} \cdot \frac{\partial p}{\partial r} + \frac{\partial^2 p}{\partial r^2} + \frac{1}{r^2} \cdot \frac{\partial^2 p}{\partial \varphi^2} + \frac{\partial^2 p}{\partial z^2} = 0 \quad (4.45)$$

Figure 4.12 shows a schematic numerical grid used for solving the main equation for porous

liner flow. The mesh used is equidistant, with node spacings of $\Delta\varphi$, Δz , and Δr . The porous material has Dirichlet boundary condition on its outer diameter R_s , where an imposed supply pressure p_s is applied. The sidewalls of the bushing, $z = 0$ and $z = L$, have second-order Neumann boundary conditions. The approximations for the derivations can be found in Ferziger's book [47]. The Neumann boundary conditions at the ends of the bushing are given as follows:

$$\left(\frac{\partial p}{\partial z}\right)_{z=0} = 0 = -3 \cdot p_{(\varphi,z=0,r)} + 4 \cdot p_{(\varphi,z=\Delta z,r)} - p_{(\varphi,z=2\cdot\Delta z,r)} \quad (4.46)$$

$$\left(\frac{\partial p}{\partial z}\right)_{z=L} = 0 = -3 \cdot p_{(\varphi,z=L,r)} + 4 \cdot p_{(\varphi,z=L-\Delta z,r)} - p_{(\varphi,z=L-2\cdot\Delta z,r)} \quad (4.47)$$

Lubricant

The computational grid for the calculation of the lubricant film is equivalent to the grid of the Si model shown in Figure 4.10. Periodic and Dirichlet boundary conditions are used at the edges of the mesh. The following velocity assignments are made for the flow at the level of the shaft. The circumferential velocity of shaft $U_{\varphi,a}$ are imposed on the flow. The curvature between the bushing and the shaft lead to the velocity component $U_{r,a}$. The shaft is assumed to be solid and the radial velocity component is zero.

$$U_{\varphi,a} = 2 \cdot \pi \cdot n \cdot R_1 \quad U_{z,a} = 0 \quad U_{r,a} = U_{\varphi,a} \cdot \frac{1}{R_2} \cdot \frac{\partial h}{\partial \varphi} \quad (4.48)$$

A three-dimensional flow in the porous body was assumed. A slip boundary condition is applied at the transition of the porous bushing to the lubricating film. The imposed velocities at the height of the inner bushing radius $r = R_2$ are thus determined on the basis of Darcy's law.

$$U_{\varphi,b} = -\frac{\alpha}{\mu} \cdot \frac{1}{R_2} \cdot \left(\frac{\partial p}{\partial \varphi}\right)_{r=R_2} \quad U_{z,b} = -\frac{\alpha}{\mu} \cdot \left(\frac{\partial p}{\partial z}\right)_{r=R_2} \quad U_{r,b} = \frac{\alpha}{\mu} \cdot \left(\frac{\partial p}{\partial r}\right)_{r=R_2} \quad (4.49)$$

Substituting the velocities 4.49 and 4.48 into the GREL equation 4.22 results in the following equation:

$$\begin{aligned} \frac{1}{R_2^2} \cdot \frac{\partial}{\partial \varphi} \left(h^3 \cdot \frac{\partial p}{\partial \varphi} \right) + \frac{\partial}{\partial z} \left(h^3 \cdot \frac{\partial p}{\partial z} \right) &= 6 \cdot \frac{1}{R_2^2} \cdot U_{\varphi,a} \cdot \frac{\partial h}{\partial z} \\ - 6 \cdot \frac{1}{R_2^2} \cdot \alpha \cdot \frac{\partial}{\partial \varphi} \left(h \cdot \frac{\partial p}{\partial \varphi} \right) - 6 \cdot \alpha \cdot \frac{\partial}{\partial z} \left(h \cdot \frac{\partial p}{\partial z} \right) - 12 \cdot \alpha \cdot \frac{\partial p}{\partial r} & \end{aligned} \quad (4.50)$$

The governing equation for the FD model used to compute the pressure distribution of the lubricant film is derived through differentiation:

$$\begin{aligned}
& \frac{\partial p}{\partial z} \cdot \left(3 \cdot h^3 \cdot \frac{\partial h}{\partial z} + 6 \cdot \alpha \cdot \frac{\partial h}{\partial z} \right) + \frac{\partial^2 p}{\partial z^2} \cdot \left(h^3 + 6 \cdot \alpha \right) \\
& + \frac{\partial p}{\partial \varphi} \cdot \left(3 \cdot h^3 \cdot \frac{\partial h}{\partial \varphi} + 6 \cdot \alpha \cdot \frac{\partial h}{\partial \varphi} \right) + \frac{\partial^2 p}{\partial \varphi^2} \cdot \left(h^3 + 6 \cdot \alpha \right) \\
& = 6 \cdot \frac{1}{R_2} \cdot U_{\varphi,a} \cdot \frac{\partial h}{\partial \varphi} - 12 \cdot \alpha \cdot \left(\frac{\partial p}{\partial r} \right)_{r=R_2}
\end{aligned} \tag{4.51}$$

The pressure derivative in the radial direction from equation 4.51 is determined using a second order approximation for equidistant grids. A boundary point representing the pressure in the lubricating film and two additional points representing neighboring nodes in the porous body are utilized, as described by Ferziger [47]. The pressures p_{por1} and p_{por2} are determined based on the pressure distribution within the porous body at radii $r = R_2$ and $r = R_2 + \Delta r$, respectively. The pressure p_{lub} represents the imposed lubricant pressure.

$$\left(\frac{\partial p}{\partial r} \right)_{r=R_2} \approx \frac{-p_{por2} + 4 \cdot p_{por1} - 3 \cdot p_{Lub}}{2 \cdot \Delta r} \tag{4.52}$$

Solver

The flowchart of the FD method (see Figure 4.13) begins with the input of the geometrical quantities, material properties of the bushing and lubricant, as well as information about the operating point and numerical specifications. Based on the inputs, a matrix is created for the porous bushing and lubricant film. The bearing is computed in a double-nested loop. In the inner loop, the pressure profile in the porous body is determined using the governing equation 4.45. As soon as the convergence criterion $C_i = 1E - 5$ (maximum residual convergence criterion) is reached, the outer loop starts to iterate. Beginning with the pressure distribution in the porous body, the pressure distribution in the lubricating film is determined according to equation 4.50. During the iteration steps of the outer loop, the pressure profile of the lubricant film is computed based on the pressure profile in the bushing. Once the convergence criterion of the outer loop $C_o = 1E - 8$ (maximum residual convergence criterion) is satisfied, the static performance parameters such as load-carrying capacity and gas consumption are returned.

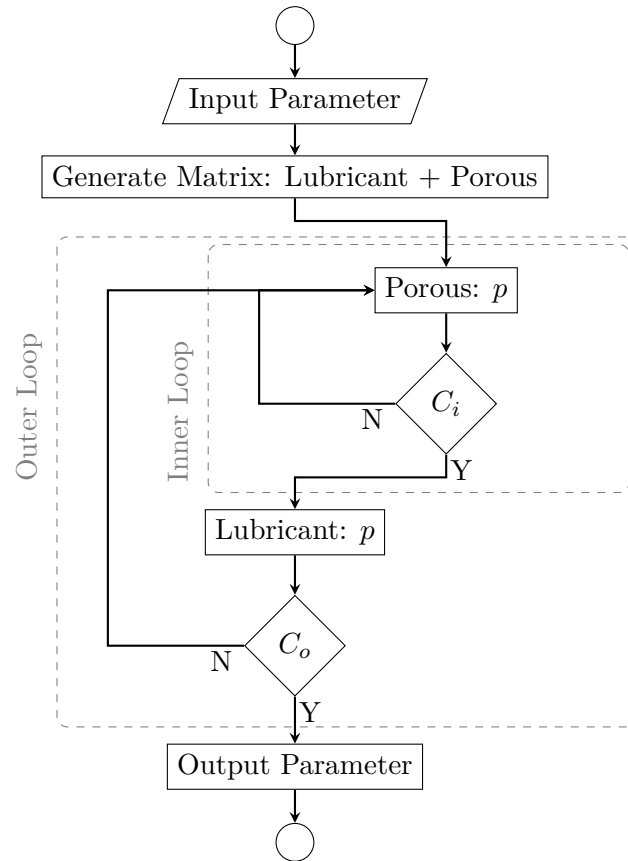


Figure 4.13: FD: flowchart

4.5.3 Full Darcy Compressible

The FDc model extends the FD method and includes the assumption that the lubricant is compressible. The density ρ and viscosity μ of the fluid are determined using the CoolProp substance database [14] as a function of pressure and temperature (isotherm). The calculation of ρ and μ are based on the use of Helmholtz energy-explicit equations of state. Further explanations of the equations of state and empirical correlations can be found in the literature by Span [111]. In addition, the FDc model incorporates vertical shaft misalignment. The lubricant gap width is computed using equation 4.28. The permeability of the porous material is assumed to be isotropic. In summary, the assumptions of the FDc model are:

- Three-dimensional flow through the porous bushing
- $\rho \neq \text{const.}$
- $\mu \neq \text{const.}$
- Film width: $h(\varphi, z)$
- $\alpha = \alpha_\varphi = \alpha_z = \alpha_r$

Porous Liner

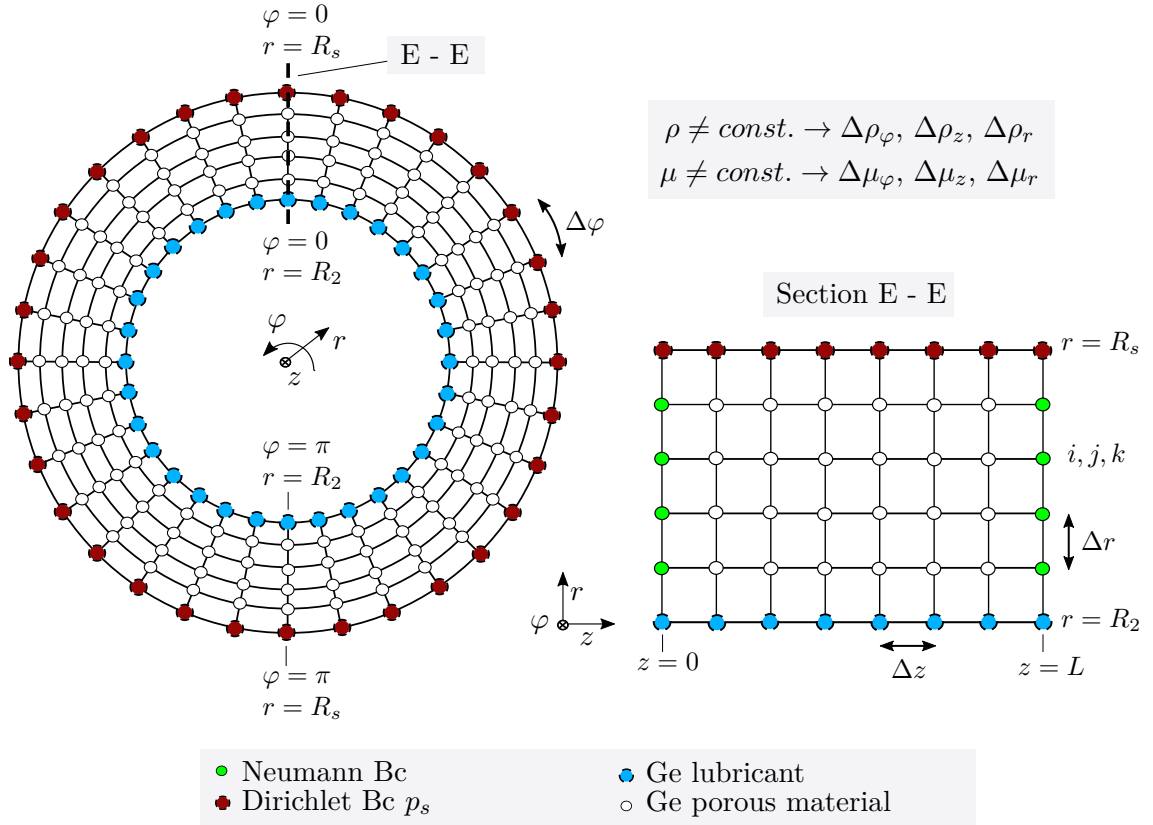


Figure 4.14: FDC - numerical mesh for the porous bushing

The assumptions of the FDC model simplify the general equation for porous flow, as given in equation 4.26, to:

$$\frac{1}{r} \cdot \frac{\partial}{\partial r} \left(\frac{\rho \cdot r}{\mu} \cdot \frac{\partial p}{\partial r} \right) + \frac{1}{r^2} \cdot \frac{\partial}{\partial \varphi} \left(\frac{\rho}{\mu} \cdot \frac{\partial p}{\partial \varphi} \right) + \frac{\partial}{\partial z} \left(\frac{\rho}{\mu} \cdot \frac{\partial p}{\partial z} \right) = 0 \quad (4.53)$$

Differentiation of equation 4.53 results in the governing equation of the FDC model for compressible flows in porous bushings:

$$\begin{aligned} & \frac{\partial p}{\partial z} \cdot \left(\frac{1}{\mu} \cdot \frac{\partial \rho}{\partial z} - \frac{\rho}{\mu^2} \cdot \frac{\partial \mu}{\partial z} \right) + \frac{\partial^2 p}{\partial z^2} \cdot \left(\frac{\rho}{\mu} \right) \\ & + \frac{\partial p}{\partial \varphi} \cdot \left(\frac{1}{r^2 \cdot \mu} \cdot \frac{\partial \rho}{\partial \varphi} - \frac{\rho}{r^2 \cdot \mu^2} \cdot \frac{\partial \mu}{\partial \varphi} \right) + \frac{\partial^2 p}{\partial \varphi^2} \cdot \left(\frac{\rho}{r^2 \cdot \mu} \right) \\ & + \frac{\partial p}{\partial r} \cdot \left(\frac{1}{\mu} \cdot \frac{\partial \rho}{\partial r} - \frac{\rho}{\mu^2} \cdot \frac{\partial \mu}{\partial r} + \frac{1}{r} \cdot \frac{\rho}{\mu} \right) + \frac{\partial^2 p}{\partial r^2} \cdot \left(\frac{\rho}{\mu} \right) = 0 \end{aligned} \quad (4.54)$$

Figure 4.14 displays a schematic representation of a numerical grid. An equidistant mesh with node spacings of Δz , Δr , and $\Delta \varphi$ is used. A Dirichlet boundary condition is set at the outer diameter R_s with supply pressure p_s , and Neumann boundary conditions are

applied at the walls $z = 0$ and $z = L$, as given in equation 4.47. The density and dynamic viscosity are obtained based on the substance database, which depend on the pressure and temperature at each node. The differential quotients of density and dynamic viscosity between nodes in cylinder coordinates are represented by $\Delta\rho_\varphi$, $\Delta\rho_z$, $\Delta\rho_r$, $\Delta\mu_\varphi$, $\Delta\mu_z$, and $\Delta\mu_r$.

Lubricant

The governing equation is based on the GREL, as given in equation 4.22. The assumptions of the fluid velocities at the level of the shaft and the inner surface of the bushing are similar to those of the FD model, and are as follows:

$$U_{\varphi,a} = 2 \cdot \pi \cdot n \cdot R_1 \quad U_{z,a} = 0 \quad U_{r,a} = U_{\varphi,a} \cdot \frac{1}{R_2} \cdot \frac{\partial h}{\partial \varphi} \quad (4.55)$$

A slip condition is applied at the interface between the lubricating film and the porous bushing. Assuming isotropic material, the velocities at the level of the inner surface of the bushing, $r = R_2$, are as follows:

$$U_{\varphi,b} = -\frac{\alpha}{\mu} \cdot \frac{1}{R_2} \cdot \left(\frac{\partial p}{\partial \varphi} \right)_{r=R_2} \quad U_{z,b} = -\frac{\alpha}{\mu} \cdot \left(\frac{\partial p}{\partial z} \right)_{r=R_2} \quad U_{r,b} = \frac{\alpha}{\mu} \cdot \left(\frac{\partial p}{\partial r} \right)_{r=R_2} \quad (4.56)$$

Substituting the velocities of the lubricant film at the level of the shaft (equation 4.55) and the inner surface of the bushing (equation 4.56) into GREL (equation 4.22) leads to the governing equation for the calculation of the lubricant film of the FDC model:

$$\begin{aligned} & \frac{1}{R_2^2} \cdot \frac{\partial}{\partial \varphi} \left(\frac{\rho \cdot h^3}{\mu} \cdot \frac{\partial p}{\partial \varphi} \right) + \frac{\partial}{\partial z} \left(\frac{\rho \cdot h^3}{\mu} \cdot \frac{\partial p}{\partial z} \right) = 6 \cdot \frac{1}{R_2^2} \cdot U_{\varphi,a} \cdot \frac{\partial}{\partial z} (\rho \cdot h) \\ & - 6 \cdot \frac{1}{R_2^2} \cdot \alpha \cdot \frac{\partial}{\partial \varphi} \left(\frac{\rho \cdot h}{\mu} \cdot \frac{\partial p}{\partial \varphi} \right) - 6 \cdot \alpha \cdot \frac{\partial}{\partial z} \left(\frac{\rho \cdot h}{\mu} \cdot \frac{\partial p}{\partial z} \right) - 12 \cdot \alpha \cdot \frac{\rho}{\mu} \cdot \frac{\partial p}{\partial r} \end{aligned} \quad (4.57)$$

Differentiation yields the following governing equation for computing the pressure distribution in the lubricant film:

$$\begin{aligned} & \frac{\partial p}{\partial z} \cdot \left(\frac{3 \cdot h^2 \cdot \rho}{\mu} \cdot \frac{\partial h}{\partial z} + \frac{h^3}{\mu} \cdot \frac{\partial \rho}{\partial z} - \frac{\rho \cdot h^3}{\mu} \cdot \frac{\partial \mu}{\partial z} + \frac{6 \cdot \alpha \cdot \rho}{\mu} \cdot \frac{\partial h}{\partial z} + \frac{6 \cdot \alpha \cdot h}{\mu} \cdot \frac{\partial \rho}{\partial z} \right. \\ & \left. - \frac{6 \cdot \alpha \cdot \rho \cdot h}{\mu^2} \right) + \frac{\partial^2 p}{\partial z^2} \cdot \left(\frac{\rho \cdot h^3}{\mu} + 6 \cdot \alpha \cdot \frac{\rho \cdot h}{\mu} \right) \\ & + \frac{\partial p}{\partial \varphi} \cdot \left(\frac{3 \cdot h^2 \cdot \rho}{\mu} \cdot \frac{\partial h}{\partial \varphi} + \frac{h^3}{\mu} \cdot \frac{\partial \rho}{\partial \varphi} - \frac{\rho \cdot h^3}{\mu} \cdot \frac{\partial \mu}{\partial \varphi} + \frac{6 \cdot \alpha \cdot \rho}{\mu} \cdot \frac{\partial h}{\partial \varphi} + \frac{6 \cdot \alpha \cdot h}{\mu} \cdot \frac{\partial \rho}{\partial \varphi} \right. \\ & \left. - \frac{6 \cdot \alpha \cdot \rho \cdot h}{\mu^2} \right) + \frac{\partial^2 p}{\partial \varphi^2} \cdot \left(\frac{\rho \cdot h^3}{\mu} + 6 \cdot \alpha \cdot \frac{\rho \cdot h}{\mu} \right) \\ & = 6 \cdot U_{\varphi,a} \cdot \left(\rho \cdot \frac{\partial h}{\partial \varphi} + h \cdot \frac{\partial \rho}{\partial \varphi} \right) - 12 \cdot \alpha \cdot \frac{\rho}{\mu} \cdot \left(\frac{\partial p}{\partial r} \right)_{r=R_2} \end{aligned} \quad (4.58)$$

Figure 4.15 shows the computational grid for the lubricant film in the FDc model. Periodic and Dirichlet boundary conditions are applied at the edges of the grid. The density and dynamic viscosity are assumed to be non-constant at both ends of the lubricant film, and the differential quotients of density and viscosity are determined using the three cylindrical coordinates φ , z , and r . Moreover, the model includes vertical misalignment of the shaft, resulting in the lubricant film equation $h(\varphi, z)$ being additionally dependent on the axial direction. The pressure derivative in the radius direction is determined using a second-order

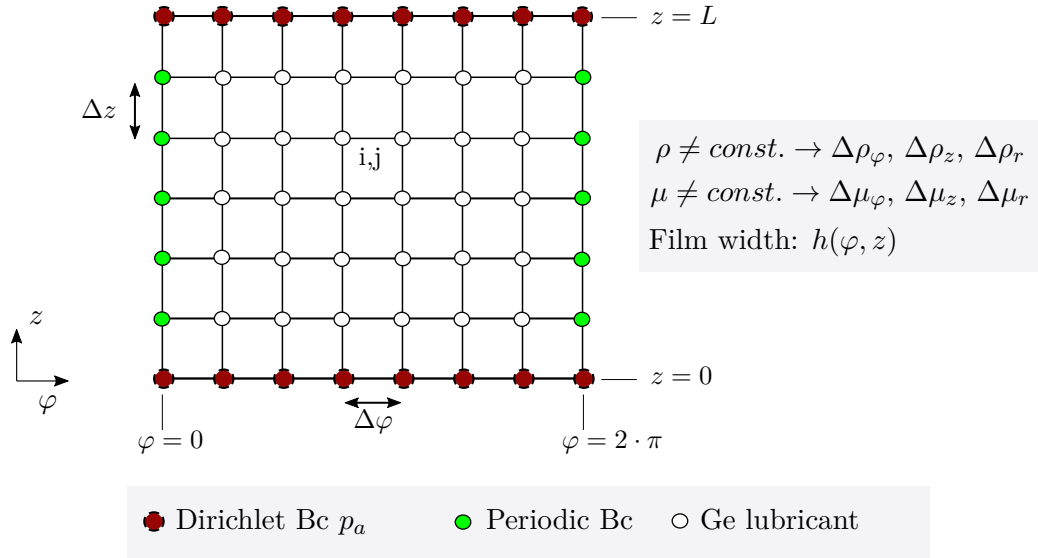


Figure 4.15: FDc: numerical grid of the lubricating film

approximation for equidistant grids. For more details, see the literature of Ferziger [47] and the derivation of the FD model in Section 4.5.2.

$$\left(\frac{\partial p}{\partial r}\right)_{r=R_2} \approx \frac{-p_{por2} + 4 \cdot p_{por1} - 3 \cdot p_{Lub}}{2 \cdot \Delta r} \quad (4.59)$$

Solver

The flowchart of the FDc model, as shown in Figure 4.16, begins with the input of geometrical quantities, material properties of the bushing and lubricant, and information about the operating points and numerical specifications. Based on the inputs, a matrix for the porous bushing and lubricant film is generated.

The bearing is computed using a double-nested loop and the BicGstab algorithm. In the first step of the inner loop, the density and dynamic viscosity distribution in the porous body is determined using the CoolProp substance database [14]. This is done by using the pressure and temperature distribution in the bushing, and an isothermal temperature distribution is assumed. Based on the data obtained, equation 4.54 is used to determine the pressure distribution in the porous bushing.

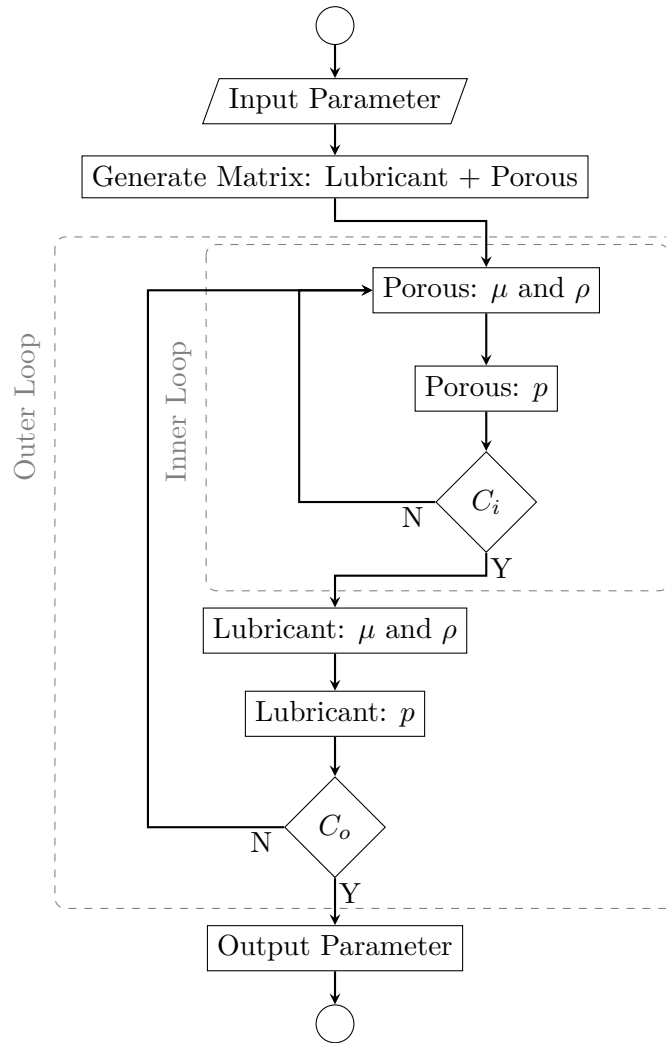


Figure 4.16: FDc: flowchart

Upon reaching the convergence criterion $C_i = 1E - 5$ (max. residual convergence criterion), the outer loop begins iterating, and the density and dynamic viscosity in the lubricating film are determined. The density and dynamic viscosity are determined again based on the pressure and temperature profile (isotherm) using the CoolProp substance database. Based on the pressure distribution in the porous body, the pressure distribution in the lubricating film is determined using equation 4.58. During the outer loop iteration steps, the pressure profile in the bushing is used to determine the lubricant film pressure. Once the convergence criterion of the outer loop $C_o = 1E - 8$ (max. residual convergence criterion) is satisfied, the static performance parameters are returned.

4.5.4 Full Darcy Extended

The FD+ model is the final expansion of the studied models, and includes specific details of the bearing, such as the number and geometry of the inlet chambers, as well as an average texture defined based on a texture measurement of the inner profile of the bearing. This model adds an additional texture term h_{tex} to the equation of the lubricant film thickness.

- Three-dimensional flow through the porous bushing
- $\rho \neq \text{const.}$
- $\mu \neq \text{const.}$
- Film width: $h(\varphi, z, texture)$
- $\alpha = \alpha_\varphi = \alpha_z = \alpha_r$

Porous Liner

The derivation of the main equation for the porous bushing coincides with the equation of the FDc model (see equation 4.54). The main governing equation of the FD+ model for the porous bushing is as follows:

$$\begin{aligned} & \frac{\partial p}{\partial z} \cdot \left(\frac{1}{\mu} \cdot \frac{\partial \rho}{\partial z} - \frac{\rho}{\mu^2} \cdot \frac{\partial \mu}{\partial z} \right) + \frac{\partial^2 p}{\partial z^2} \cdot \left(\frac{\rho}{\mu} \right) \\ & + \frac{\partial p}{\partial \varphi} \cdot \left(\frac{1}{r^2 \cdot \mu} \cdot \frac{\partial \rho}{\partial \varphi} - \frac{\rho}{r^2 \cdot \mu^2} \cdot \frac{\partial \mu}{\partial \varphi} \right) + \frac{\partial^2 p}{\partial \varphi^2} \cdot \left(\frac{\rho}{r^2 \cdot \mu} \right) \\ & + \frac{\partial p}{\partial r} \cdot \left(\frac{1}{\mu} \cdot \frac{\partial \rho}{\partial r} - \frac{\rho}{\mu^2} \cdot \frac{\partial \mu}{\partial r} + \frac{1}{r} \cdot \frac{\rho}{\mu} \right) + \frac{\partial^2 p}{\partial r^2} \cdot \left(\frac{\rho}{\mu} \right) = 0 \end{aligned} \quad (4.60)$$

The choice of boundary conditions distinguishes the FD+ from the previous models. Under realistic conditions, the porous bushing is supplied with compressed air through single pressure channels at the outer radius R_s (see Figure 4.17). The design of the channels thus influences the flow distribution in the porous body. Therefore, a Dirichlet boundary condition with pressure p_s is set along the channels (see Figure 4.18).

And a second-order Neumann boundary condition is set at the wall:

$$\left(\frac{\partial p}{\partial r} \right)_{r=R_s} = 0 = -3 \cdot p_{(\varphi, z, r=R_s)} + 4 \cdot p_{(\varphi, z, r=R_s-\Delta r)} - p_{(\varphi, z, r=R_s-2 \cdot \Delta r)} \quad (4.61)$$

Second-order Neumann boundary conditions are used on the sidewalls of the bushing at $z = 0$ and $z = L$:

$$\left(\frac{\partial p}{\partial z} \right)_{z=0} = 0 = -3 \cdot p_{(\varphi, z=0, r)} + 4 \cdot p_{(\varphi, z=\Delta z, r)} - p_{(\varphi, z=2 \cdot \Delta z, r)} \quad (4.62)$$

$$\left(\frac{\partial p}{\partial z} \right)_{z=L} = 0 = -3 \cdot p_{(\varphi, z=L, r)} + 4 \cdot p_{(\varphi, z=L-\Delta z, r)} - p_{(\varphi, z=L-2 \cdot \Delta z, r)} \quad (4.63)$$

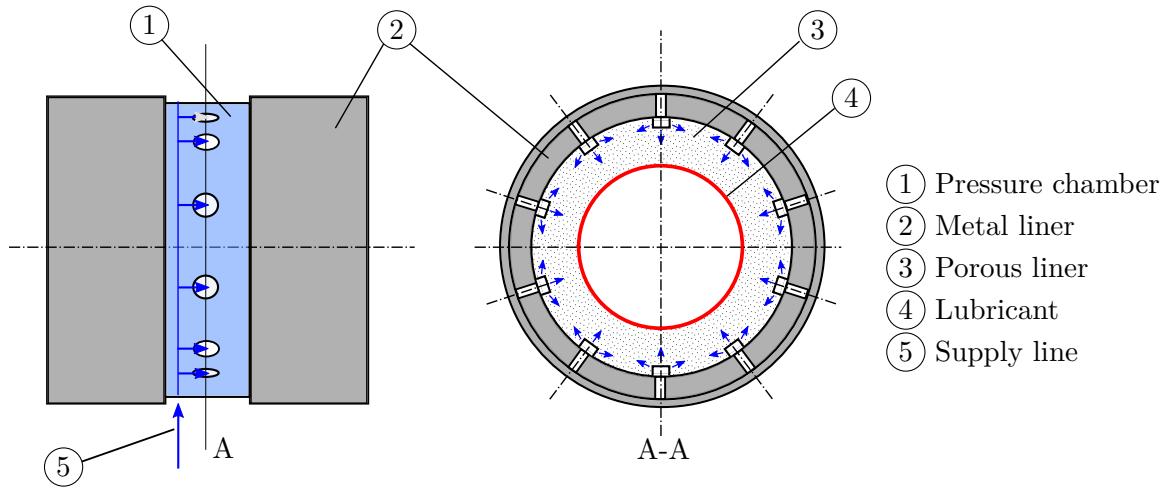


Figure 4.17: FD+: schematic concept of the inlet flow

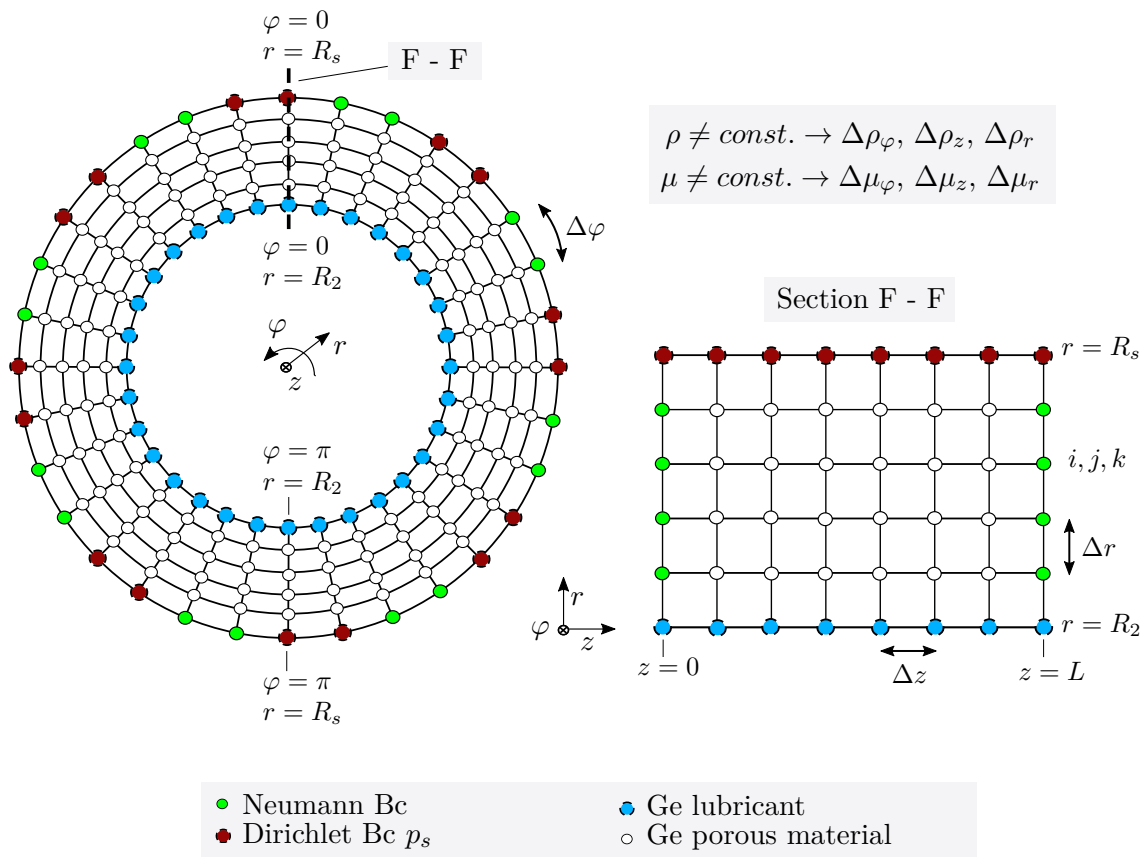


Figure 4.18: FD+: numerical mesh for the porous bushing

Lubricant

The governing equation of the FD+ model for the calculation of the lubricant film pressure is based on the GREL (equation 4.22). The assumptions for the fluid velocities at the level of the shaft and the inner surface are similar to those of the FDc model, and are as follows:

$$U_{\varphi,a} = 2 \cdot \pi \cdot n \cdot R_1 \quad U_{z,a} = 0 \quad U_{r,a} = U_{\varphi,a} \cdot \frac{1}{R_2} \cdot \frac{\partial h}{\partial \varphi} \quad (4.64)$$

$$U_{\varphi,b} = -\frac{\alpha}{\mu} \cdot \frac{1}{R_2} \cdot \left(\frac{\partial p}{\partial \varphi} \right)_{r=R_2} \quad U_{z,b} = -\frac{\alpha}{\mu} \cdot \left(\frac{\partial p}{\partial z} \right)_{r=R_2} \quad U_{r,b} = \frac{\alpha}{\mu} \cdot \left(\frac{\partial p}{\partial r} \right)_{r=R_2} \quad (4.65)$$

The governing equation of the FD+ model for computing the pressure profile in the lubricant film is based on the assumptions of the model and is derived from the main equation of the FDc model (equation 4.58). The key difference between the FD+ and FDc models is the inclusion of the texture h_{tex} on the bearing surface. This texture is represented by the groove profile h_{tex} in Figure 4.6. To calculate the lubricant film thickness, the FD+ model uses equation 4.29. The governing equation of the FD+ model for computing the pressure profile in the lubricant film is given by equation 4.66.

$$\begin{aligned} & \frac{\partial p}{\partial z} \cdot \left(\frac{3 \cdot h^2 \cdot \rho}{\mu} \cdot \frac{\partial h}{\partial z} + \frac{h^3}{\mu} \cdot \frac{\partial \rho}{\partial z} - \frac{\rho \cdot h^3}{\mu} \cdot \frac{\partial \mu}{\partial z} + \frac{6 \cdot \alpha \cdot \rho}{\mu} \cdot \frac{\partial h}{\partial z} + \frac{6 \cdot \alpha \cdot h}{\mu} \cdot \frac{\partial \rho}{\partial z} \right. \\ & \left. - \frac{6 \cdot \alpha \cdot \rho \cdot h}{\mu^2} \right) + \frac{\partial^2 p}{\partial z^2} \cdot \left(\frac{\rho \cdot h^3}{\mu} + 6 \cdot \alpha \cdot \frac{\rho \cdot h}{\mu} \right) \\ & + \frac{\partial p}{\partial \varphi} \cdot \left(\frac{3 \cdot h^2 \cdot \rho}{\mu} \cdot \frac{\partial h}{\partial \varphi} + \frac{h^3}{\mu} \cdot \frac{\partial \rho}{\partial \varphi} - \frac{\rho \cdot h^3}{\mu} \cdot \frac{\partial \mu}{\partial \varphi} + \frac{6 \cdot \alpha \cdot \rho}{\mu} \cdot \frac{\partial h}{\partial \varphi} + \frac{6 \cdot \alpha \cdot h}{\mu} \cdot \frac{\partial \rho}{\partial \varphi} \right. \\ & \left. - \frac{6 \cdot \alpha \cdot \rho \cdot h}{\mu^2} \right) + \frac{\partial^2 p}{\partial \varphi^2} \cdot \left(\frac{\rho \cdot h^3}{\mu} + 6 \cdot \alpha \cdot \frac{\rho \cdot h}{\mu} \right) \\ & = 6 \cdot U_{\varphi,a} \cdot \left(\rho \cdot \frac{\partial h}{\partial \varphi} + h \cdot \frac{\partial \rho}{\partial \varphi} \right) - 12 \cdot \alpha \cdot \frac{\rho}{\mu} \cdot \left(\frac{\partial p}{\partial r} \right)_{r=R_2} \end{aligned} \quad (4.66)$$

A schematic representation of the numerical grid for the lubricant film is shown in Figure 4.19. Periodic and Dirichlet boundary conditions are used at the edges of the grid. The density and dynamic viscosity are determined at all nodes. The differential quotients of ρ and μ are formed in the cylindrical coordinates. The equation for the lubricant film thickness includes the influence of a shaft misalignment and the texture of the inner surface of the bushing. The pressure derivation in the radius direction is determined with a second-order approximation for equidistant grids (see details in Section 4.5.2 and in [47]):

$$\left(\frac{\partial p}{\partial r} \right)_{r=R_2} \approx \frac{-p_{por2} + 4 \cdot p_{por1} - 3 \cdot p_{Lub}}{2 \cdot \Delta r} \quad (4.67)$$

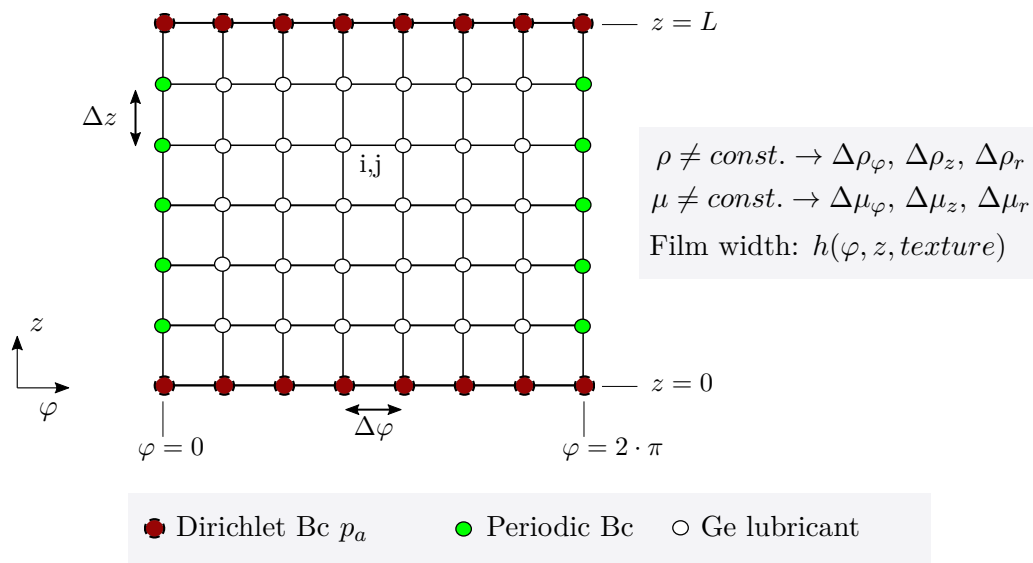


Figure 4.19: FD+: numerical grid of the lubricating film

Solver

The flowchart of the FD+ model (depicted in Figure 4.20) starts with the input of geometrical quantities and material properties of the bushing and lubricant, as well as information about operating points and numerical specifications, including the number and width of pressure supply channels. Additionally, an average texture is determined based on the texture measurement of the bushing's inner surface. Based on this input, a matrix for the porous bushing and lubricant film is created.

The bearing computation is performed in a double-nested loop. In the first step of the inner loop, the density and dynamic viscosity distribution in the porous body are determined using the CoolProp substance database [14] as well as the pressure and temperature (isotherm) distribution in the bushing. Based on this data, the main equation 4.54 is utilized to determine the pressure distribution in the porous bushing.

Once the convergence criterion $C_i = 1E-5$ (max. residual convergence criterion) is reached, the outer loop begins iterating and determines the density and dynamic viscosity in the lubricant film. The CoolProp substance database is utilized to determine the density and dynamic viscosity based on the pressure and temperature profile (isotherm). Using equation 4.58 and the pressure distribution in the porous body, the pressure distribution in the lubricating film is determined. The static performance parameters, such as load-carrying capacity and gas consumption, are returned once the convergence criterion of the outer loop $C_o = 1E-8$ (max. residual convergence criterion) is reached.

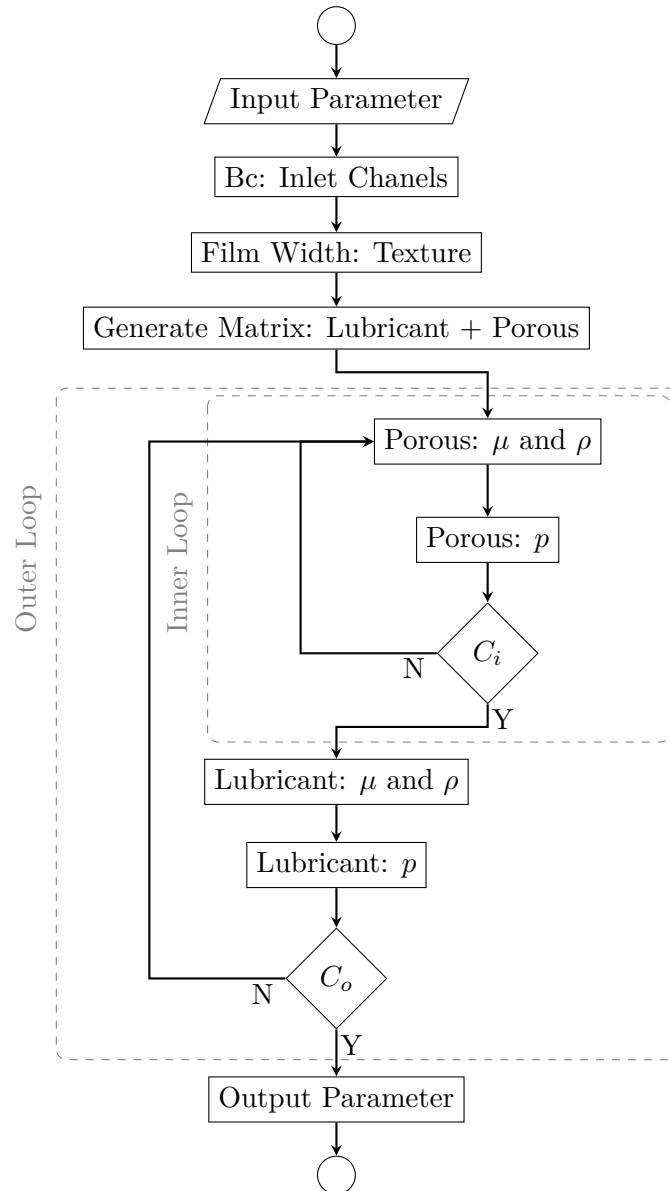


Figure 4.20: FD+: flowchart

5 Modeling with Computational Fluid Dynamics (CFD)

In addition, numerical simulations were performed with the commercial CFD software from Ansys. The simulation model included a supply line with 20 pressure channels, a porous bushing, the lubricant film and an outflow area to the atmosphere (see Figure 5.1).

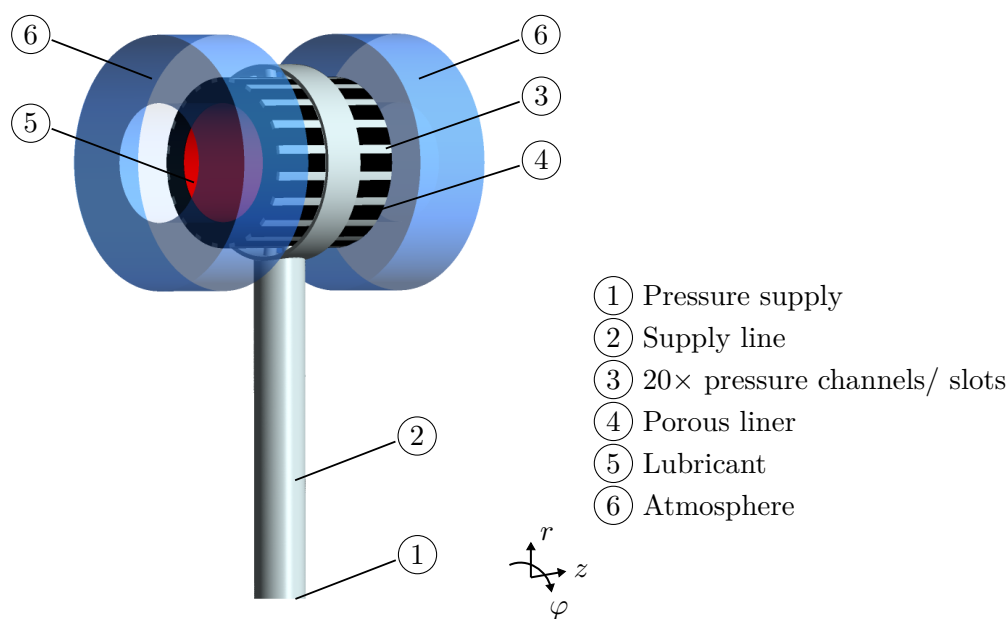
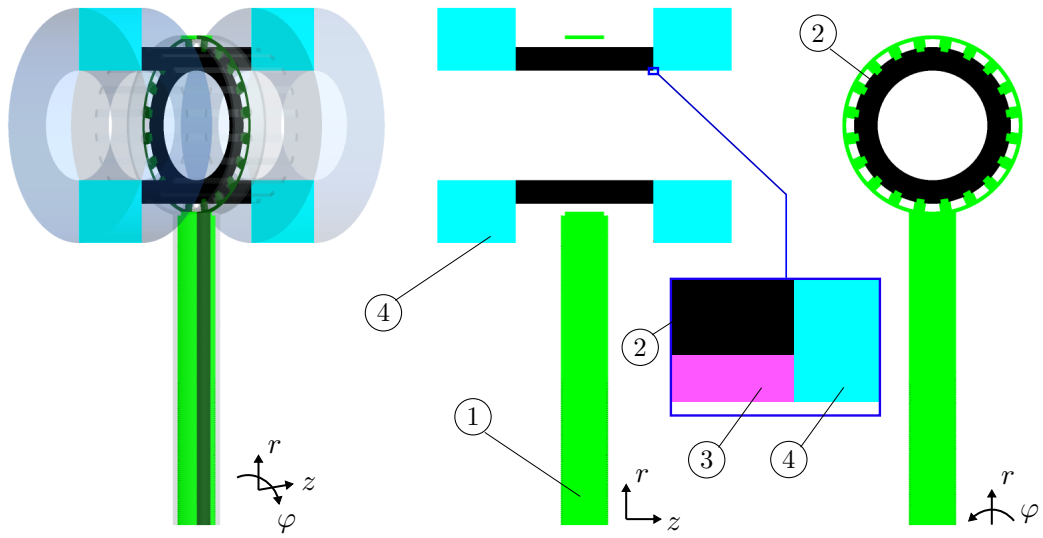


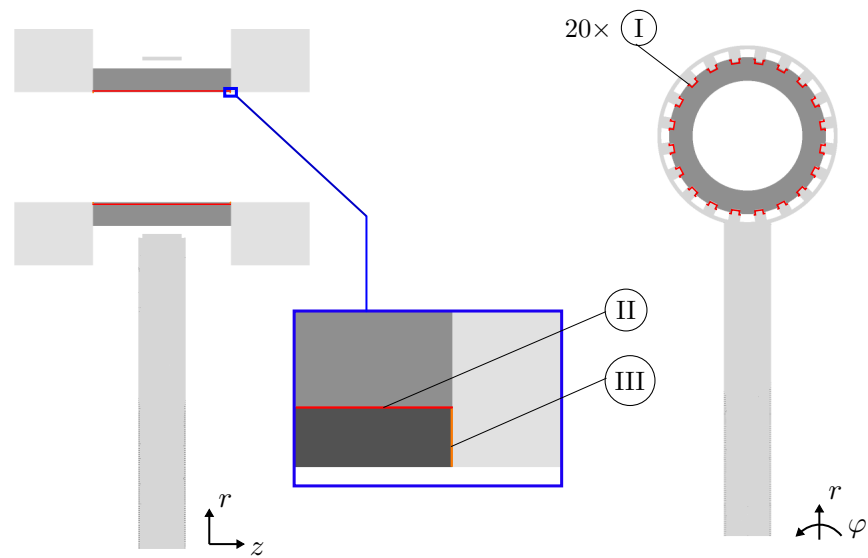
Figure 5.1: Overview of the CFD bearing model

An overview of the domains and interfaces of the CFD model is shown in Figure 5.2. The inlet chamber domain represents the channeling of the medium through the bearing housing and the metal liner. At the inlet, a pressure boundary condition was imposed with the supply pressure p_s . Wall boundary conditions (no slip) were set in the supply line to the porous bushing. The model was simplified in the supply channel region by not considering the sealing spaces in front of the O-rings. The porous liner was coupled at the 20 ports with 20 general porous-fluid interfaces. Wall boundary conditions were selected at the lateral ends of the porous liner. The porous area of the liner was connected to the lubricant film by an additional porous-fluid interface. The fluid region of the lubricating film had a rotating wall boundary condition and was coupled to the atmospheric region by two general fluid-fluid interfaces. The outflow of the fluid in the atmosphere region proceeded at the open boundary conditions, which were subjected to an atmospheric pressure p_a . Sections of the discretized bearing model are shown in Figure 5.3. The inlet chamber was meshed unstructured with the use of the Ansys Workbench Meshing 2020 [6]. The porous bushing and the atmosphere domain were meshed block structured with Ansys ICEM 2020



- | | |
|--------------------------------|----------------------|
| ① Domain inlet chamber (fluid) | ③ Lubricant (fluid) |
| ② Domain porous liner (porous) | ④ Atmosphere (fluid) |

(a) Domains



- | |
|---|
| ① Interface: inlet chamber ↔ porous liner |
| ② Interface: porous liner ↔ lubricant |
| ③ Interface: lubricant ↔ atmosphere |

(b) Interfaces

Figure 5.2: CFD setup

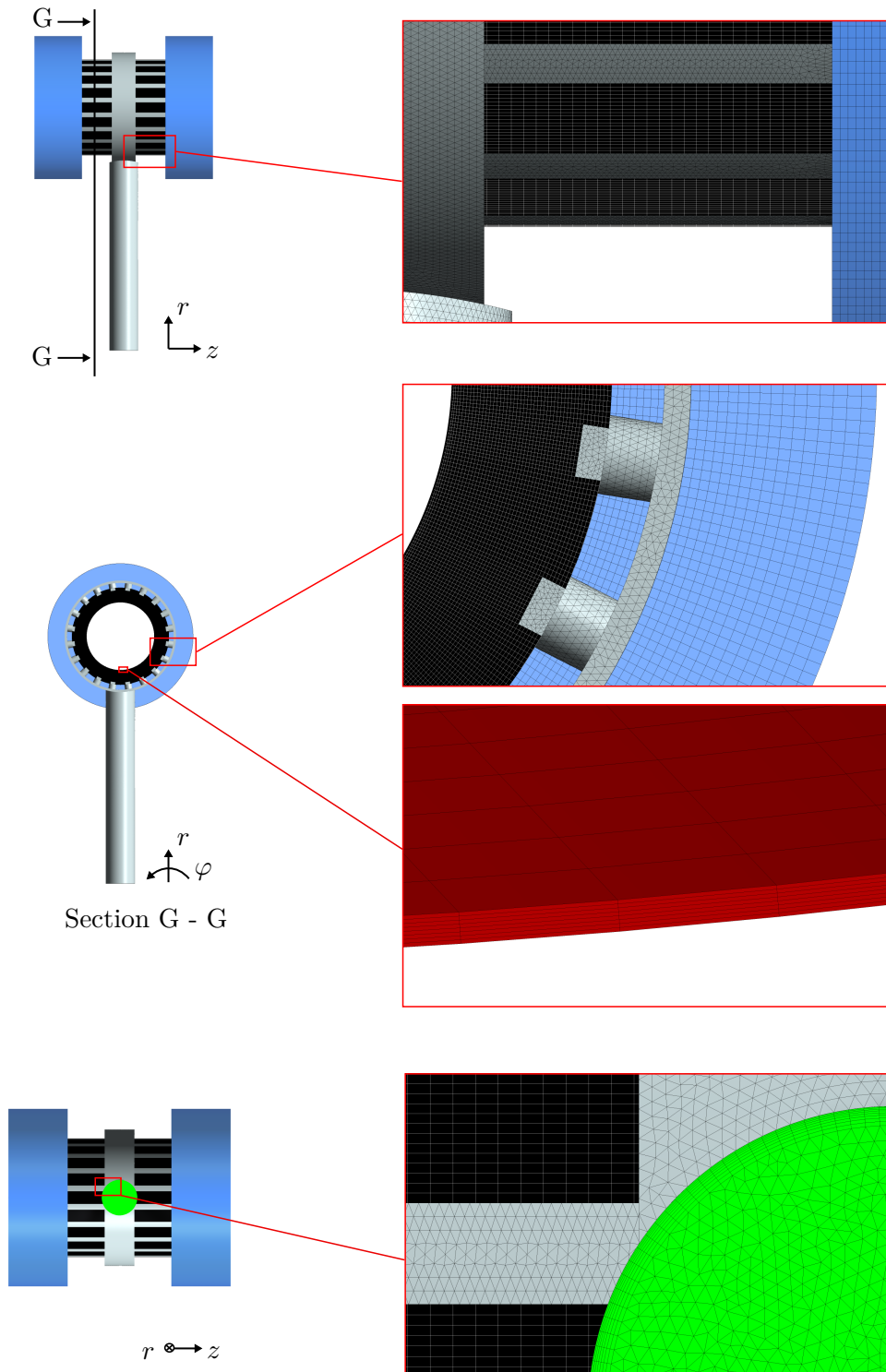


Figure 5.3: CFD: numerical grid

[5]. The porous domain had a mesh refinement in the direction of the lubricating film. The lubricating film had 8 layers in the radial direction, 140 in the axial direction and 400 layers in the circumferential direction. Due to the high ratio between the lubricant film width and the geometric dimensions of the bushing, a maximum eccentricity ratio of only 0.47 could be mapped. Higher eccentricity ratios caused difficulties with dissolving the lubricating film or the overlapping between the meshes of the lubricating film and the porous liner. The simulations were performed with the solver Ansys CFX 2020 [4]. A steady and laminar flow was used for the modeling. The lubricating medium air was calculated with the ideal gas equation and assumed to be isothermal with a temperature of 20 °C. The calculation of the porous body was based on Darcy's law. The porous body was designed with an isotropic loss with the specification of permeability α . A high-resolution advection scheme and single-precision resolution were chosen.

6 Analysis of Developed Numerical Models for Aerostatic Porous Journal Bearings

6.1 Mesh Independency and Computational Time

The study of mesh independence is intended to analyze whether there is a dependence of the result on the number of nodes. This includes the discretization of the lubricating film and the porous bushing. The mesh-independent analysis was performed for the Si, FD, FDc, FD+ and CFD models. Load-carrying capacity F and gas consumption as mass flow rate \dot{m} were used for evaluation.

$$F = \sqrt{\int_0^L \int_0^{2\pi} p \cdot R_1 \cdot \sin(\varphi) d\varphi dz + \int_0^L \int_0^{2\pi} p \cdot R_1 \cdot \cos(\varphi) d\varphi dz} \quad (6.1)$$

$$\dot{m} = \frac{1}{12} \left(\int_0^{2\pi} \frac{\rho \cdot h^3}{\mu} \cdot \left| \frac{\partial p}{\partial z} \right|_{z=0} d\varphi + \int_0^{2\pi} \frac{\rho \cdot h^3}{\mu} \cdot \left| \frac{\partial p}{\partial z} \right|_{z=L} d\varphi \right) \quad (6.2)$$

The deviations from the finest mesh in each case were determined for the evaluation. The deviation formulas for the radial load δ_F and mass flow rate $\delta_{\dot{m}}$ are as follows:

$$\delta_F = \frac{|F - F_{fine}|}{F_{fine}} \quad (6.3)$$

$$\delta_{\dot{m}} = \frac{|\dot{m} - \dot{m}_{fine}|}{\dot{m}_{fine}} \quad (6.4)$$

In addition, CPU time was recorded to evaluate the required computational resources. The computation was consistently performed on a single core of an Intel Xeon 6126, 2.6 GHz processor.

For this study, a representative operating point was chosen based on the following eccentricity ratio ε , supply pressure p_s , atmospheric pressure p_a , rotational speed n , shaft radius R_1 , length L and liner thickness t :

$$\begin{array}{llll} R = 14 \text{ mm} & L = 35 \text{ mm} & t = 6 \text{ mm} & \varepsilon = 0.1 \\ p_s = 5 \text{ bar} & p_a = 1 \text{ bar} & n = 4000 \text{ rpm} & \end{array}$$

6.1.1 Simple

The Si model computed the lubricating film with a two-dimensional approach. To determine the mesh dependence, the number of nodes in the z and in φ directions were increased, as shown in Figure 6.1. The total number of nodes was increased by a factor between 1.4 and

2. In this study, the number of nodes in the circumferential direction was always higher by a value of one than in the axial direction (see Figure 6.1). As a result of the periodic boundary condition at $\varphi = 0^\circ$ and $\varphi = 360^\circ$, the nodes at both positions used the same computed value.

Figure 6.1 shows the deviations of the load-carrying capacity and the gas consumption at the lubricating film to the respective finest mesh. Furthermore, the CPU time was plotted on a second ordinate. As the number of nodes increased, the deviation values converged towards a value of zero. The deviation of the evaluation criteria corresponded to approximately 1% with a total of 2550 nodes of ($N_\varphi = 51$, $N_z = 50$).

The deviation continued to decrease with a further increase in the number of nodes, but there was a significant increase in computation time. The CPU time was 0.375 s for 2550 nodes. However, as the number of nodes increased, the deviation of the result decreased below 1% and led to a significant increase in the computation time. For example, for 27060 nodes, the computation time increased 13 times to 5.17s. A node count of 2550 was, therefore, deemed to be sufficient and a further increase in the number of nodes to be unreasonable.

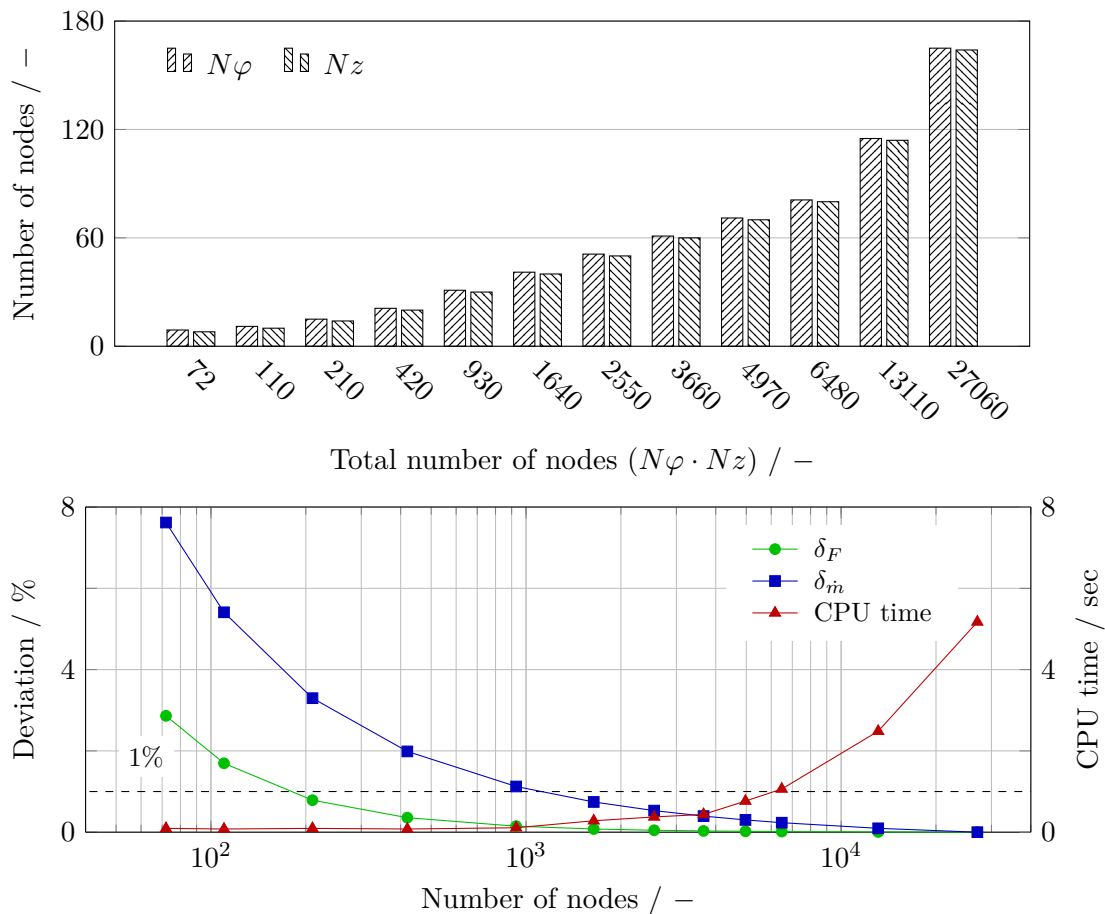


Figure 6.1: Mesh independency - Si

The absolute values are noted in Table 6.1. The influence of the mesh is below 0.1 N for a node number of more than 2550. The gas consumption converged towards a value of 0.6 g s^{-1} . The influence of the grid was below 0.01 g s^{-1} for a node number of 2550. For further investigation, a resolution of $N_\varphi = 51$ nodes and $N_z = 51$ nodes in φ and z directions was used. The pressure profile for the selected mesh and, additionally, a pressure profile with a coarser and a finer mesh, are shown in Figure 6.2. The diagrams show the high agreement of the pressure distributions qualitatively.

Table 6.1: Absolute values - Si

Total nodes / -	F / N	$\dot{m} / \text{g s}^{-1}$	Total nodes / -	F / N	$\dot{m} / \text{g s}^{-1}$
72	25.580	0.553	2550	26.321	0.596
110	25.887	0.566	4970	26.328	0.597
210	26.126	0.579	6480	26.330	0.597
420	26.240	0.587	13110	26.332	0.598
930	26.295	0.592	27060	26.334	0.599
1640	26.313	0.594			

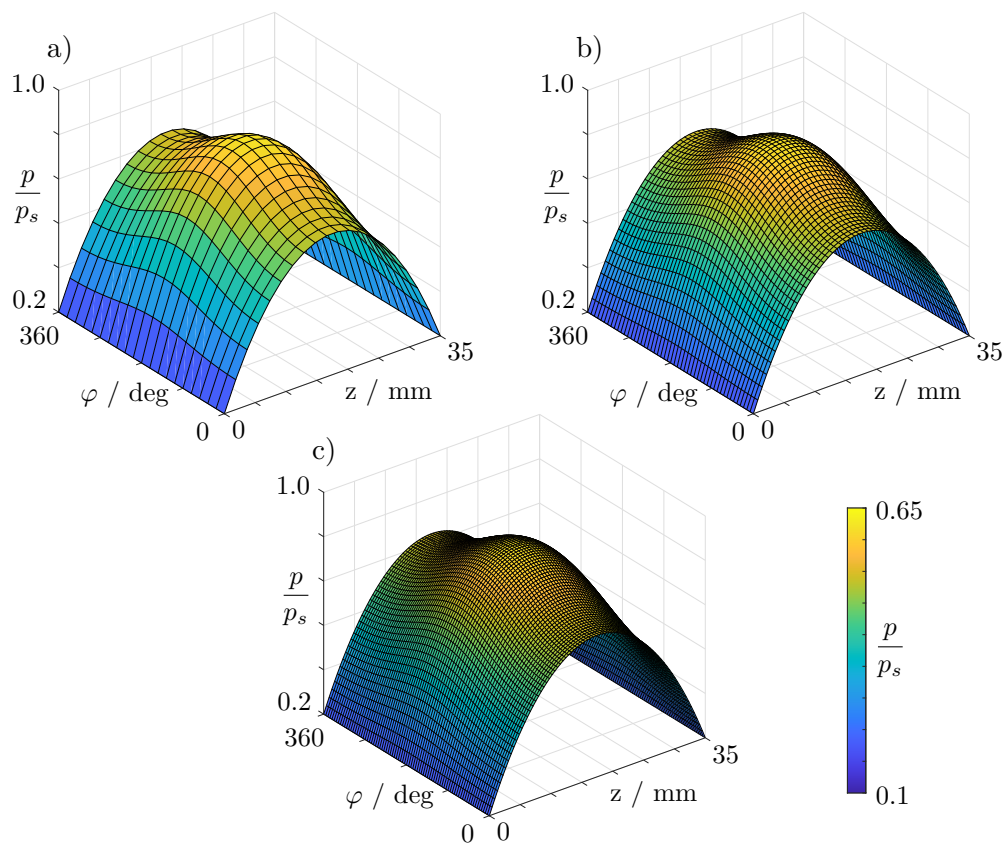


Figure 6.2: Pressure distribution - Si ($N_\varphi \times N_z$): a) 21 x 20, b) 51 x 50, c) 81 x 80

6.1.2 Full Darcy

The FD model included a two-dimensional resolution of the lubricating film and a three-dimensional resolution of the porous body. The mesh independence study of the Si model represented the required two-dimensional resolution of the lubricant film. Based on the results of the Si model mesh study, a distribution of nodes in the φ and in z directions ($N_\varphi = 51$, $N_z = 50$) was assumed for the mesh study of the FD and FDc models. Thus, for the three-dimensional discretization of the porous body, the influence of the number of nodes in the radius direction was investigated. The number of nodes was increased by 10 nodes per step (see Figure 6.3a).

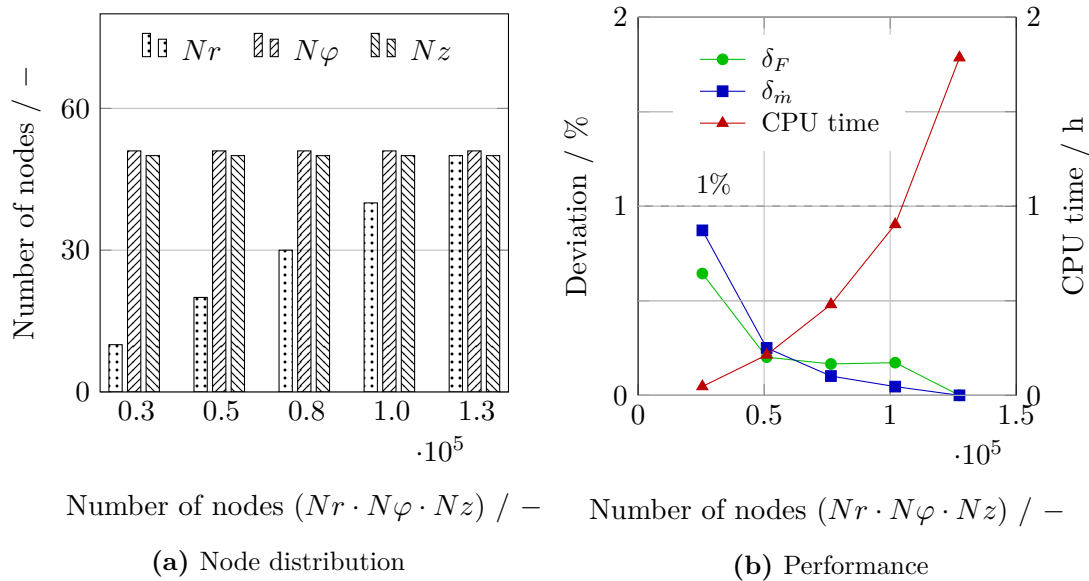


Figure 6.3: Mesh independency - FD

The deviation in the load-carrying capacities and the mass flow rates, depending on the number of nodes and the required computation time, are shown in Figure 6.8b. The deviations were consistently less than 1% in the range between 25500 to 127500. The CPU time ranged between 0.04 h and 1.78 h.

The absolute values of the mesh study of the FD model varied between approximately 25.0 N and 25.2 N for the load-carrying capacity and between approximately 0.60 g s^{-1} and 0.61 g s^{-1} for the mass flow rate (see Table 6.2). The pressure distribution in the porous liner showed a high agreement with an increase in the number of nodes (see Figure 6.4). The relatively highest deviations occurred at the transition to the lubricant film at $r = 14 \text{ mm}$. Nevertheless, the resulting quantitative values showed a high correlation.

A fine mesh with a node count of $1.02 \text{ E}5$ nodes ($N_r = 40$, $N_\varphi = 51$, $N_z = 50$) was adopted for the further studies. The calculation time was less than one CPU hour and allowed a high resolution of the pressure distribution in the porous liner.

Table 6.2: Absolute values - FD

Total nodes / -	F / N	$\dot{m} / g s^{-1}$
25500	25.048	0.602
51000	25.160	0.606
76500	25.169	0.607
102000	25.167	0.607
127500	25.211	0.608

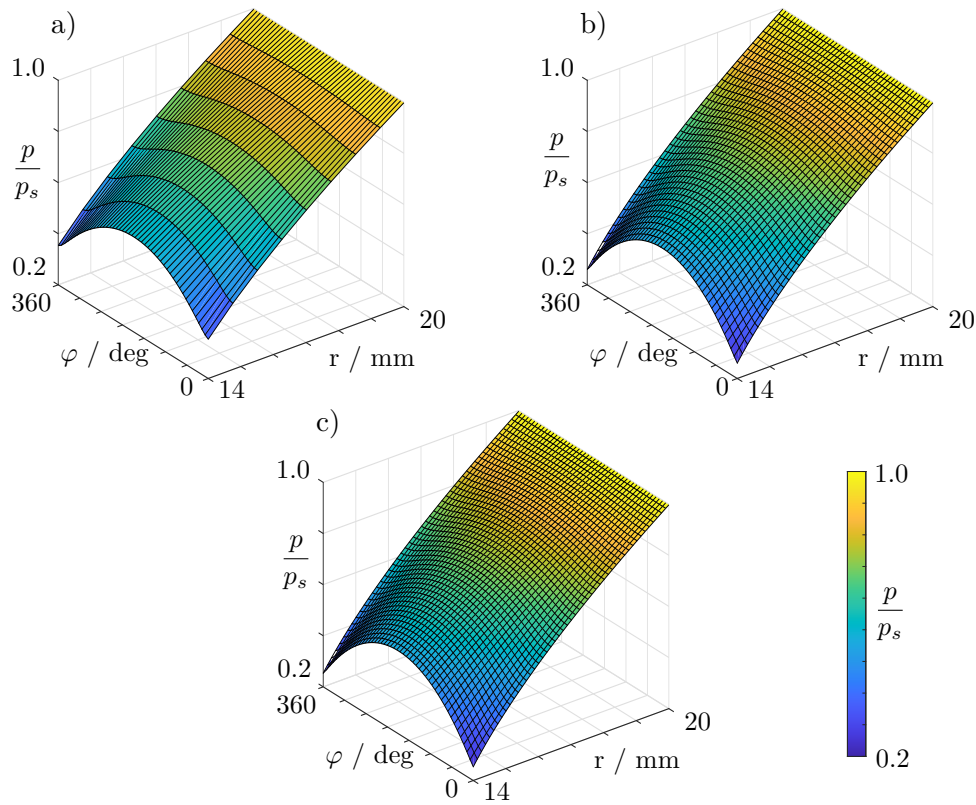


Figure 6.4: Pressure distribution on FD grids at $z = 17.5$ mm ($N_r \times N_\varphi \times N_z$):
a) 51 x 50 x 10, b) 51 x 50 x 40, c) 51 x 50 x 50

6.1.3 Full Darcy Compressible

The FDc model extended the FD model through the assumption of a non-constant density and non-constant dynamic viscosity. Furthermore, a vertical shaft misalignment in the z direction was implied. A vertical inclination of 0.0045 mm from one bushing end to the next was assumed.

The mesh independence study was based on the previously performed studies of the Si and FD model. The number of nodes in the φ and z directions were initially chosen based on the Si model study with the two-dimensional lubricant film ($N_\varphi = 51$, $N_z = 50$). These quantities were first set, and, similar to the FD study, the number of nodes in the radial

direction was examined. The number of nodes in the r direction was analyzed in the range of $Nr = 10$ to 50 nodes. Since shaft misalignment was involved, two additional analyses with an increase in the number of nodes in the z direction were performed ($Nz = 60$). Figure 6.5 represents the node distributions of each case and the quantitative deviation of the load-carrying capacity and gas consumption, as well as the CPU time. The total node count of the coarsest mesh was 25500 and, of the finest mesh, 153000. For a total node count upwards of 51000, the deviation of δ_F and $\delta_{\dot{m}}$ of the finest mesh already decreased to less than 1%. A refinement in the r and in z directions did not influence the result significantly. However, the computing time increased from 0.03 to 3.34 CPU h.

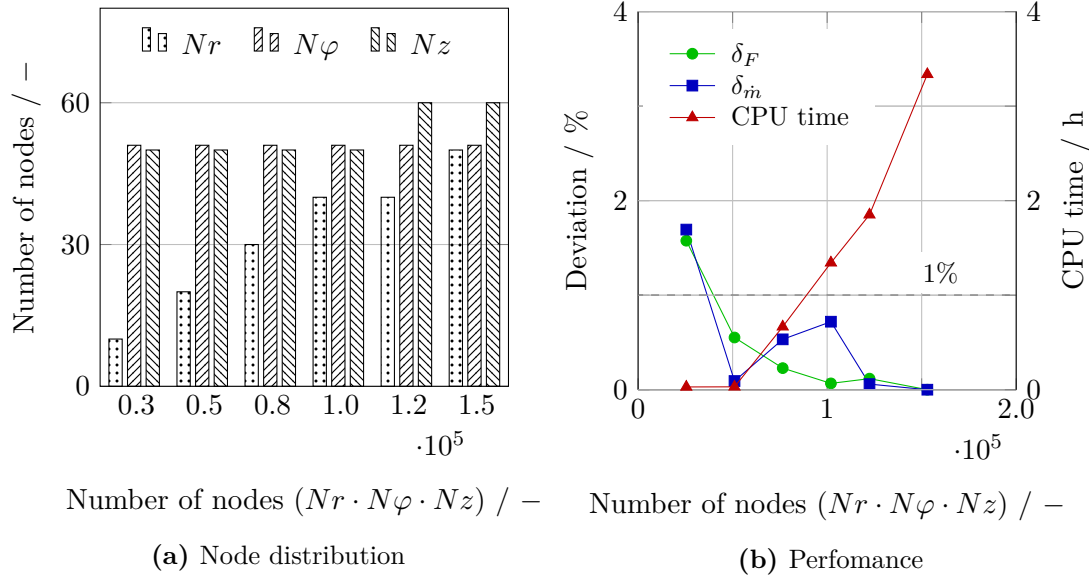


Figure 6.5: Mesh independency - FDC

The absolute values of each case are shown in Table 6.3. The difference between the grids was less than 0.5 N for load-carrying capacity and less than 0.05 g s^{-1} for gas consumption.

Table 6.3: Absolute values - FDC

Total nodes / -	F / N	\dot{m} / g s^{-1}
25500	25.777	1.954
51000	25.517	1.990
76500	25.435	1.999
102000	25.394	2.002
122400	25.407	1.987
153000	25.377	1.988

The pressure distribution in the lubricating film and the porous body ($r - \varphi$ plane at $z = 15 \text{ mm}$) are shown for three grids with increasing refinement in Figure 6.6. The coarsest mesh had a resolution of only 10 nodes in the radial direction. In contrast, the medium mesh with 40 nodes in the r direction had a smoother pressure progression from the outer

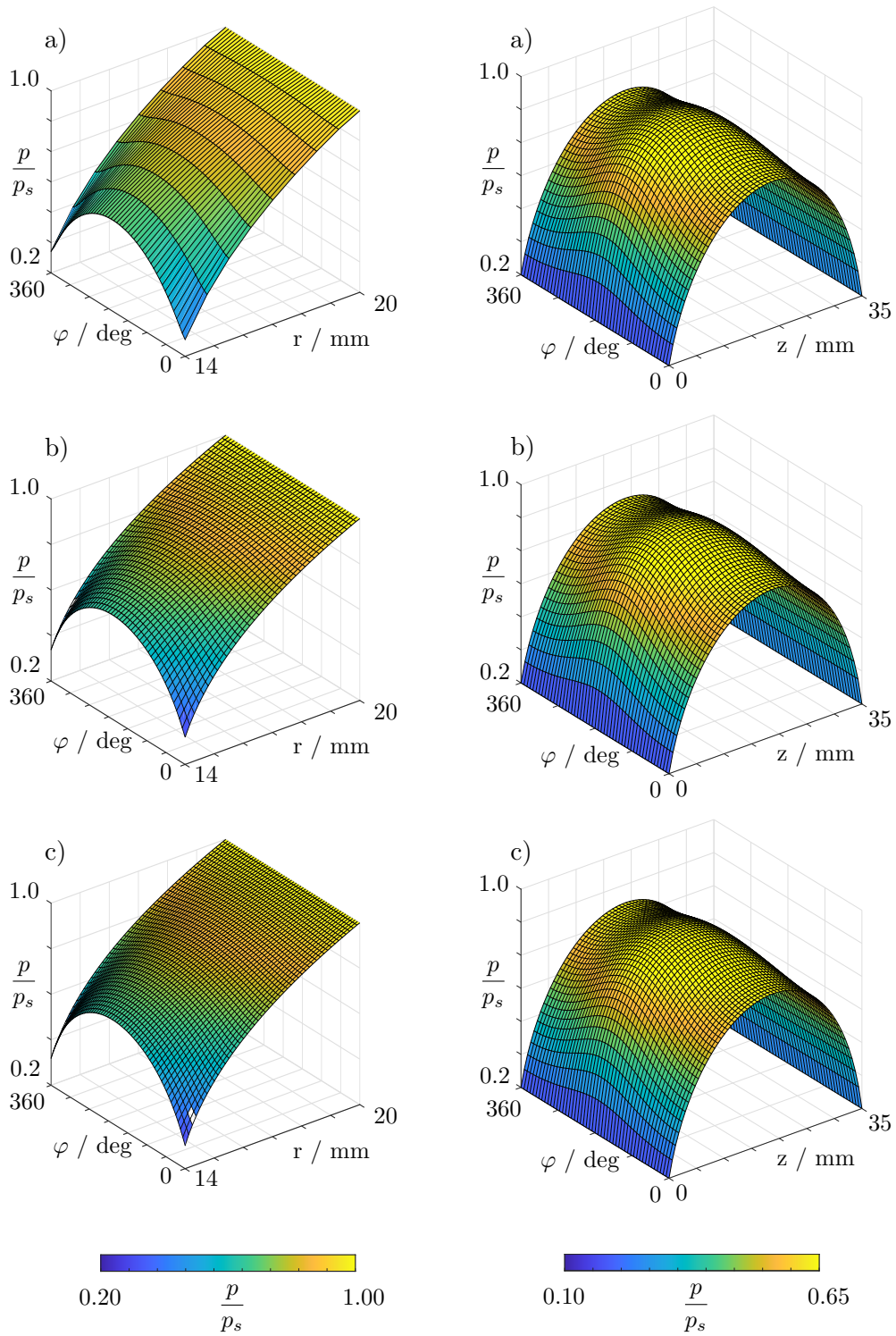


Figure 6.6: Pressure distribution on FDC grids ($Nr \times N\varphi \times Nz$):
 a) 10 x 51 x 50, b) 40 x 51 x 50, c) 51 x 50 x 60

to the inner radius of the porous liner. The finest mesh with 50 nodes in the radial direction and a likewise increased number of nodes in the z direction showed considerable similarities to the medium mesh. The resulting pressure distributions in the lubricant film did not show any significant differences across the meshes and were consistent with the high agreement of the quantitative values.

In the further study, a node count of ($N_r = 40$, $N_\varphi = 51$, $N_z = 50$) was adopted. Quantitatively, high agreement was already achieved at a lower resolution. The higher computational effort was justified by a smoother representation of the pressure gradient in the porous body. Furthermore, in the event of higher pressure differences, such as high pressure ratios p_s/p_a or high eccentricity ratios e/c , a higher number of nodes in the r direction was advantageous.

6.1.4 Full Darcy Plus

The FD+ model extended the FDc model through the addition of the pressure channels on the outer radius and the texture of the inner surface of the bushing.

As in the experiments, 20 pressure channels were considered. A Dirichlet boundary condition with pressure p_s was imposed at the edges of the pressure channels and Neumann boundary conditions were selected at the solid walls. In this study, each pressure channel was modeled with one to four nodes in the circumferential direction. This resulted in a number of nodes in the φ direction from $N_\varphi = 61$ to 241 (see pressure profile in the sectional view of a porous bushing with $N_\varphi = 61$ and 181 in Figure 6.9).

The experimental determination of the surface contour was described in Chapter 2.3. The generation of a mean groove contour is presented in Section 4.3.3. The required discretization of the groove contour to ensure mesh independence is investigated in the following. Since rotationally symmetric grooves were assumed, the number of nodes in the axial direction was crucial to the groove resolution. The resolution of a groove was

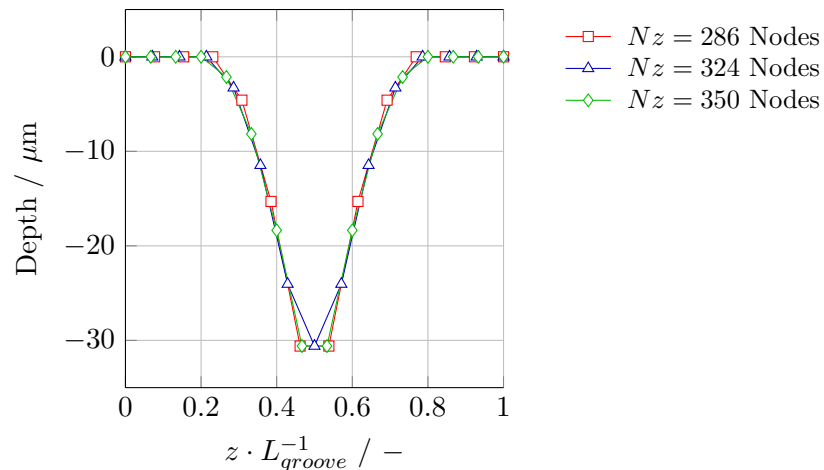


Figure 6.7: Average groove pattern

periodically repeated in the axial direction, according to the number of grooves. Thus, 17 grooves result in a total number of $Nz = 286$, 324 and 350 nodes. The discretizations of the groove (see Figure 6.7) showed high coincidence. However, contrary to the other two cases, in the resolution with $Nz = 324$, only one node with the smallest groove depth of $30.6 \mu\text{m}$ was used. Two nodes each were used for the meshes with $Nz = 286$ and 350. Based on the previous mesh studies, the number of nodes in the radius direction was assumed to be $Nr = 40$. Refinements of the mesh in the axial and circumferential directions resulted in a significantly (Figure 6.8a) higher number of nodes relative to the previous mesh studies. The number of nodes in the coarsest mesh was approximately $0.7\text{E}6$ and those of the finest mesh approximately $3.4\text{E}6$. The deviation in load-carrying capacity and gas consumption dropped below 1% with a number of nodes above $2.5\text{E}6$. The mesh with a node number of $2.5\text{E}6$ required a computation time of 94.8 CPU h. A further increase in the number of nodes led to an insignificant change in the quantitative values and a further increase in computation time. The computation time required for the finest mesh with a number of $3.4\text{E}6$ nodes was 140 CPU h.

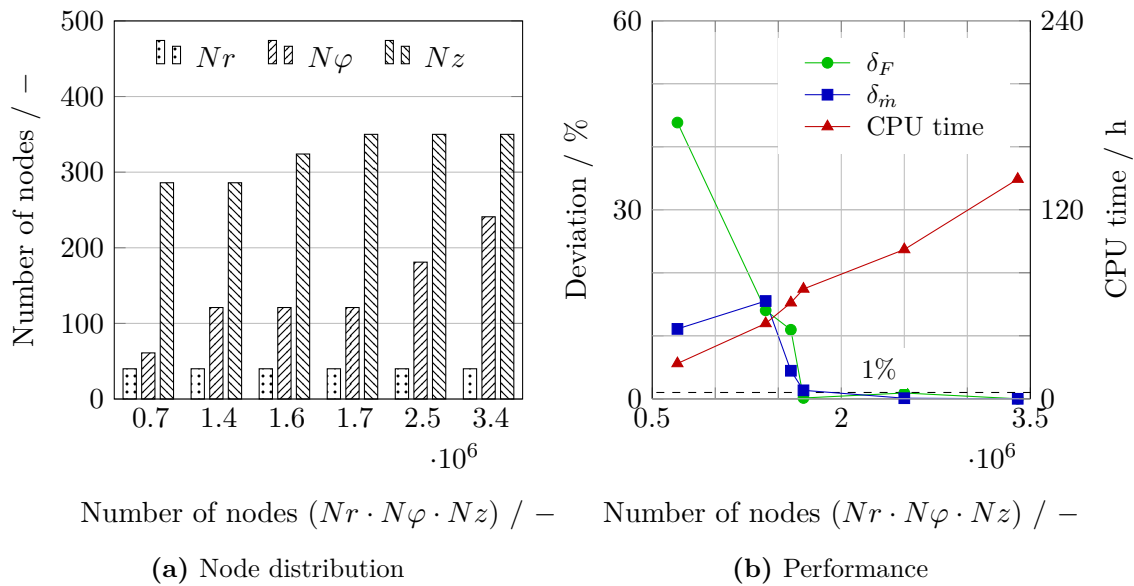


Figure 6.8: Mesh independency - FD+

The pressure distribution of the mesh with a node count of $2.5\text{E}6$ and the coarsest mesh with $0.7\text{E}6$ nodes are shown in the sectional view through the porous bushing in Figure 6.9. The coarser mesh applied one node with a Dirichlet boundary condition to map a pressure channel. The finer mesh used three nodes to discretize each of the 20 pressure channels. Especially at the outer radius, a more uniform pressure profile can be observed in the circumferential direction due to the higher number of nodes.

Pressure distribution in the lubricating film of both meshes are shown in Figure 6.10. Compared to the previous mesh independency studies, both meshes had a high resolution in the axial direction. The finer mesh showed a more continuous course at the axial ends.

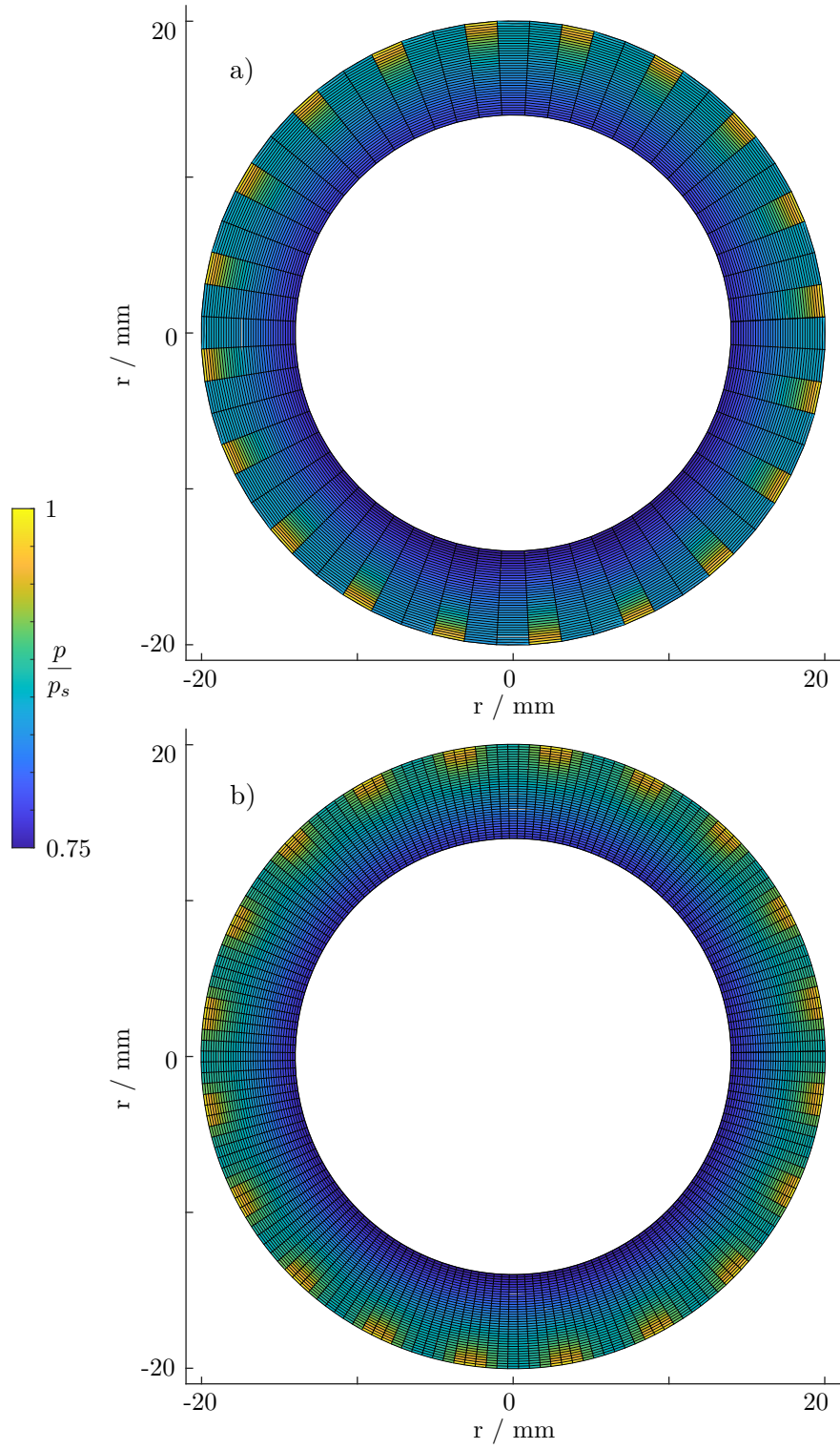


Figure 6.9: Pressure distribution on FD+ (sectional view through the porous bushing, $Nr \times N\varphi \times Nz$): a) 40 x 61 x 286, b) 40 x 181 x 350

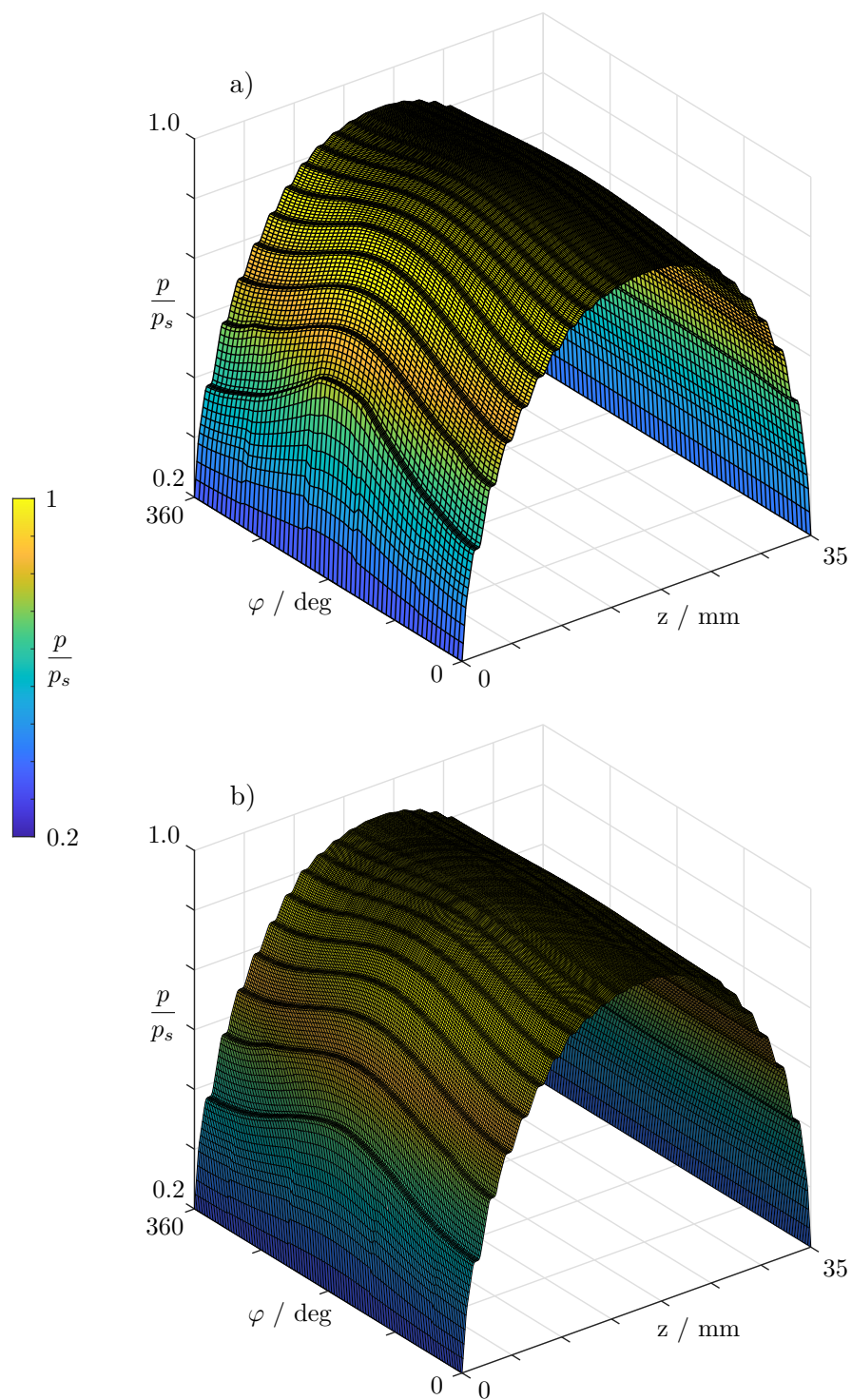


Figure 6.10: Lubricant pressure distribution on FD+ grids ($N_r \times N_\varphi \times N_z$):

a) $40 \times 61 \times 286$, b) $40 \times 181 \times 350$

This can be attributed to the high pressure drop (to atmospheric pressure) at the axial ends $z = 0$ and $z = L$.

The absolute values of the FD+ model mesh independency study showed that a minimum node number of 1.7E nodes is required. Beyond this number of nodes, the calculated difference in the characteristic values of the load-carrying capacity was below approximately 0.2 N and, for the gas consumption, below 0.06 g s^{-1} . The mesh with 2.5E6 nodes was used for further computations.

Table 6.4: Absolute values - FD+

Total nodes / -	F / N	$\dot{m} / \text{g s}^{-1}$
697840	18.539	4.551
1384240	14.698	4.732
1568160	14.301	4.279
1694000	12.905	4.042
2534000	12.771	4.093
3374000	12.889	4.097

6.1.5 Computational Fluid Dynamics

The mesh study of the CFD model included three levels of refinement. Figure 6.11 shows a section of the coarse and the fine mesh. The deviation in the load-carrying capacity and the gas consumption are shown in Figure 6.12. The number of nodes ranged from 6.8 million to 17.6 million. The deviation of F was less than 1% between the medium and fine mesh, and, for the gas consumption, the deviation was approximately 1%. The absolute values of the calculations are provided in Table 6.5. The difference in the absolute values of load-carrying capacity between the two fine meshes was below 0.1 N and, in the gas consumption, below 0.02 g s^{-1} . Based on the mesh study, the medium mesh was used for further numerical computations.

Table 6.5: Absolute values - CFD

	Total nodes / -	F / N	$\dot{m} / \text{g s}^{-1}$
Coarse mesh	6254605	16.360	1.712
Medium mesh	10311978	16.534	1.702
Fine mesh	17615058	16.542	1.683

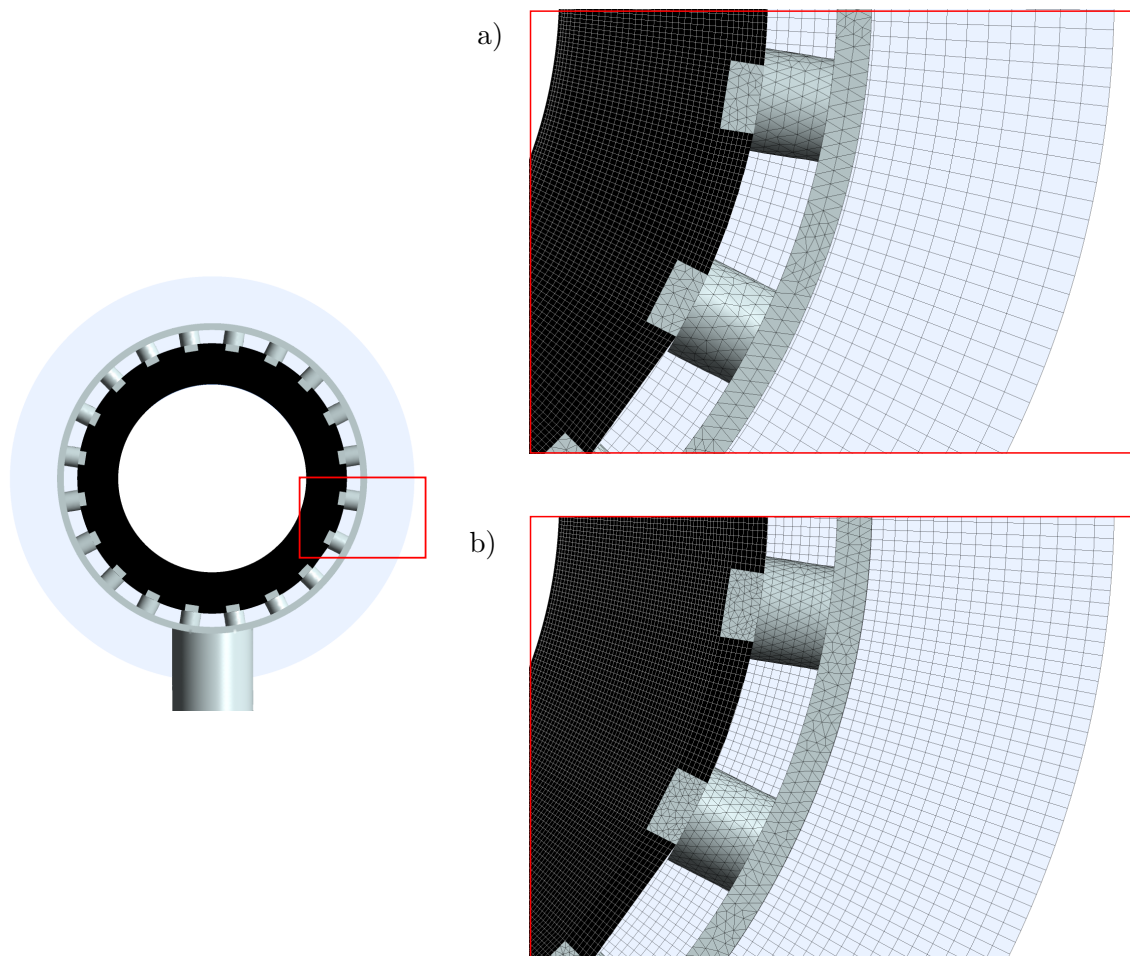


Figure 6.11: Numerical meshes of the CFD: a) Coarse mesh, b) Fine mesh

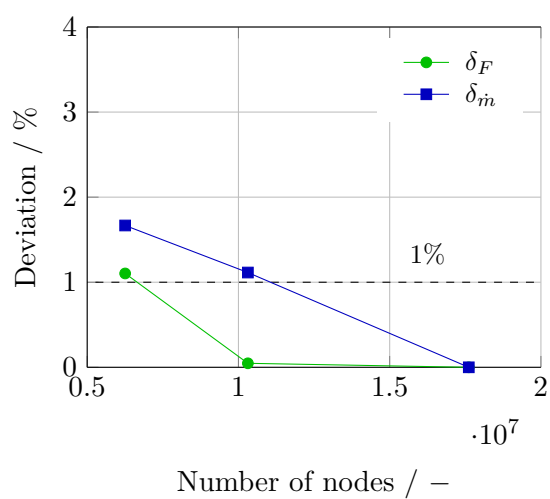


Figure 6.12: Mesh independency - CFD

6.2 External Validation

To verify their plausibility, the presented models were validated with external experiments and simulations. Since the common characteristics of bearings differ, this comparison showed further possible applications of the software as well as restrictions in the applicability. A direct comparison with already developed models allows conclusions regarding the model assumptions and the potential for case-related improvements.

The load-carrying capacity of the bushing versus the eccentricity ratio ε was used as the validation parameter. The load-carrying capacity of dynamic bearings is evaluated with the dynamic load parameter F^\sim (equation 6.5) and for externally pressurized bearings with the static load parameter F^* (equation 6.6). F^\sim was formed by the radial load-carrying capacity F and the radial clearance c , length of the bushing L and radius of the bushing R_1 . In addition, the dynamic viscosity μ of the lubricant and the circumferential speed of the shaft U_a were included. F^* was formed by radial load-carrying capacity F , length of the bushing L , radius of the shaft R_1 and difference of supply pressure p_s and atmospheric pressure p_a .

$$F^\sim = \frac{F}{\mu \cdot U_{\varphi,a}} \cdot \left(\frac{c}{R}\right)^2 \quad (6.5)$$

$$F^* = \frac{F}{(p_s - p_a) \cdot L \cdot 2 \cdot R} \quad (6.6)$$

Conformity with external publications was rated by the deviations δ_{F^\sim} and δ_{F^*} . The deviations in the results of the numerical models to the reference values of the external publications were defined as follows:

$$\delta_{F^\sim} = \frac{\left| F_{Model}^\sim - F_{Ref}^\sim \right|}{F_{Ref,max}^\sim} \quad (6.7)$$

$$\delta_{F^*} = \frac{\left| F_{Model}^* - F_{Ref}^* \right|}{F_{Ref,max}^*} \quad (6.8)$$

The validation included the measurements and simulations of porous sintered bearings by Mokhtar et al. [84], Elsharkawy et al. [46], Castelli [25] and Heidler [61]. Table 6.6 lists the parameters of these external publications. These investigations were conducted with sintered bushings made of graphite or metal. The material of the C/C bearings was manufactured through the pyrolysis process. The tests of Mokhtar et al. differ from those of the other authors due to the significant differences in the bearing characteristics. Mokhtar et al.'s experiments were based on a porous radial bearing, which differs in mode

Table 6.6: Overview of the external studies for the validation of the numerical models

		Mokhtar et al.	Castelli	Heidler	Exp.
Year		1984	1979	2016	2022
Mode		Hydrodynamic	Aerostatic	Aerostatic	Aerostatic
Production method		Sintering	Sintering	Sintering	Pyrolysis
Material liner		Metal mixture	Iron	Graphite	C/C
Lubricant		SAE 30 oil	Air	Air	Air
Parameter	Unit				
μ	Pa s	0.026 (0.025*)	1.85E-5	1.85E-5	1.85E-5
c	μm	85.5 (82.5*) & 32	20.5 (22.1**)	14.5	30
L	mm	33	40	76.2	35
R_1	mm	9.5	20	20.02	14
LD^{-1}	–	1.74	1	1.68	1.25
h_p	mm	3	5	3.5	6
α	m	1.5E-13	7.9E-15	1.52E-15	5.2E-14 - 4.3E-14
n	rpm	380-870 (720*)	0 - 6000	0	1000 - 8000
$\frac{p_s}{p_a}$	-	-	2 - 7	3 - 5 ***	5 - 7

* Assumption: Elsharkawy et al. [46]

** Hydraulic clearance

*** Vacuum experiments ($p_a < 1$ bar) are not included

of operation (hydrodynamic) and lubricating medium (SAE 30 oil). The experiments of Mokhtar et al. were also used by Elsharkawy et al. to validate their model, and, thus, this provides another numerical comparison. Since the parameters of Elsharkawy et al. differed slightly in some instances, the data were marked for completeness in Table 6.6. Castelli and Heidler's test series were pressurized with air. Castelli, on the one hand, investigated aerostatic bearings made of sintered metal experimentally and numerically. Heidler, on the other hand, studied aerostatic bearings made of sintered graphite. Likewise, these investigations included experiments and numerical simulations. As previously mentioned, the dynamic viscosity in Mokhtar et al.'s tests is higher due to the use of SAE 30 oil. With the use of the known lubricant temperature of $T = 60^\circ\text{C}$ from Mokhtar et al.'s publication, the dynamic viscosity was determined on the basis of a substance table [80]. A higher viscosity lubricant tends to result in a design with a larger radial clearance of $c = 85.5 \mu\text{m}$. The measurements also included lower radial clearances of $c = 32.0 \mu\text{m}$.

The air bearing tests in the studies of Castelli and Heidler and in this study were performed with radial clearances between $14.5 \mu\text{m}$ and $30 \mu\text{m}$. Castelli introduced hydraulic internal clearance, which is the sum of the arithmetic average roughness R_a and the radial clearance

c. For consistency, this validation study used radial clearance for the simulations.

The dimensions of the bearings in Castelli's study bear the closest resemblance to the C/C prototype. Castelli's bearings had a length of $L = 40$ mm, an inner radius of $R_1 = 20$ mm and a porous liner thickness of $t = 5$ mm. The dimensions of the C/C bearing correspond to $L = 35$ mm, $R_1 = 14$ mm, $t = 6$ mm. The agreement is also evident in the ratio $L/D = 1.0$ for Castelli and $L/D = 1.25$ for the C/C bearing. There are correspondingly larger dimensional deviations with the bearing from Heidler. The Heidler air bearing was slightly more than twice as long as the C/C bearing and had a smaller porous wall thickness with $t = 3.5$ mm.

The permeabilities of air bearings range between $\alpha = 5.39\text{E}-14\text{ m}^2$ and $1.52\text{E}-15\text{ m}^2$. Mokhtar et al.'s dynamic oil-lubricated bearing has higher permeability with $\alpha = 1.5\text{E}-13\text{ m}^2$. A comparison of the rotational speed and supply pressure of the bearings of Castelli and Heidler is in the main reasonable due to the compressible gaseous lubricant and the aerostatic mode. Heidler's tests were conducted with a stationary shaft. Castelli also included tests with a stationary shaft and, additionally, tests with a rotational speed of $n = 6000$ rpm. The pressure ratios in the air bearing investigations are comparable with values between $p_s/p_a = 2$ to 7 .

6.2.1 Hydrodynamic Porous Bearing

The experiments by Mokhtar et al. [84] involved an oil-lubricated dynamic journal bearing. SAE 30 oil at a temperature of 60°C was used as lubricant. The metal bushings were made by sintering. The metal powder used included 89 % copper, 10 % tin and 1 % graphite. Two inductive transducers were used to determine the vertical and horizontal eccentricity of the bearing. The use of differing shafts resulted in radial clearances of $c = 85.5\ \mu\text{m}$ and $32\ \mu\text{m}$. The tests were classified by the permeability parameter Ψ , which is composed by the permeability α , the radius R_1 and the radial clearance c . Consequently, a radial clearance of $c = 85.5\ \mu\text{m}$ resulted in a value of approximately $\Psi = 2.54\text{E}-3$ and, for $c = 32.0\ \mu\text{m}$, approximately $\Psi = 4.35\text{E}-2$.

$$\Psi = \alpha \cdot \frac{R_1}{c^3} \quad (6.9)$$

The Si and FD models were validated with the measurement results of Mokhtar et al. and the simulation results of Elsharkawy et al.

The Si and FD models were extended with the Gumbel solution to calculate the oil lubricant film. This approach uses only the positive pressure distribution for the simulation [21] and has been used by, among others, Buuren [21] and Childs et al. [27] for the calculation of hydrodynamic bearings. Elsharkawy et al. used the more advanced cavitation model of Elrod [45], which can be used to model cavitation while considering the conservation of mass. There is an additional difference in the computation of the porous/fluid interface. Elsharkawy

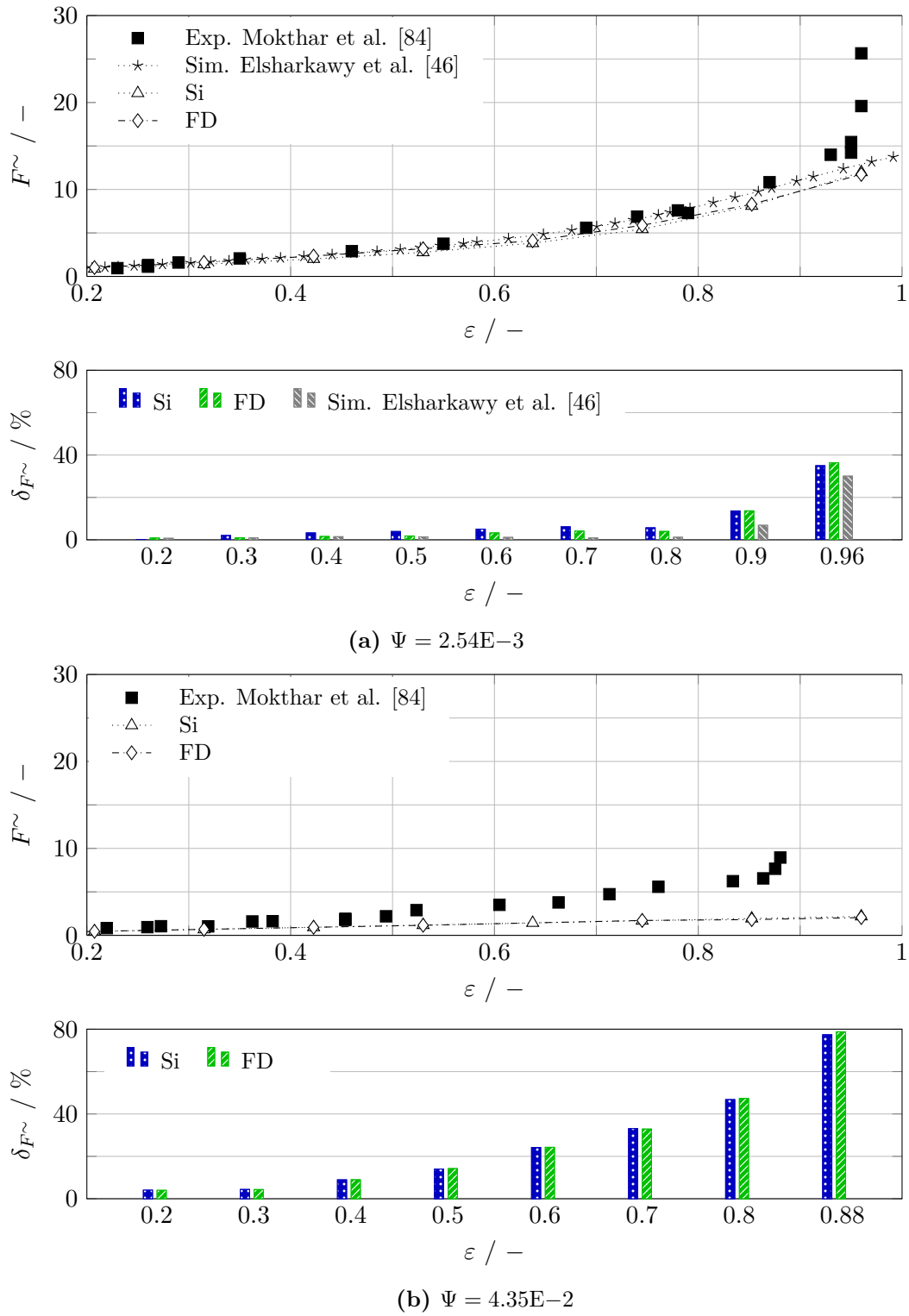


Figure 6.13: Validation and deviation of Si and FD with a hydrodynamic porous bearing

et al. used the extended Darcy-Brinkman model [78], where a stress-jump boundary condition is set at the interface between porous liner and fluid. This takes into account the effect of viscous shear stress forces and corrects the velocity at the interface with an adjustable coefficient. As already discussed by Buuren [21], the correction factors of those models have to be determined for each application. Furthermore, the implementation of further terms increases the complexity of the model, although the influence can be negligible [21]. The slip boundary conditions of the relevant models of this study are explained in Chapter 4.5.

The dimensionless dynamic load capacities F^{\sim} versus eccentricity ratio ε for $\Psi = 2.54\text{E-}3$ is shown in Figure 6.13. This includes Mokthar et al.'s experiments, Elsharkawy et al.'s simulations and the results of the Si and FD models. In addition, Mokthar et al.'s experiments with a value of $\Psi = 4.35\text{E-}2$ were recalculated with the Si and FD models. The simulation results of Elsharkawy et al, the SI and the FD show high agreement in the results to $\Psi = 2.54\text{E-}3$, with the measured results in the range of $\varepsilon < 0.96$. The high increase in load from 0.96 was not captured by either model. The agreement between the Si and FD models are high in the entire operating range. Tendentially, the Si and FD indicate lower load-carrying capacity than Elsharkawy et al.'s model above an eccentricity ratio of 0.5.

No external simulations for the results of $\Psi = 4.35\text{E-}3$ could be found. Simulation results of the Si and FD models again showed a high agreement with each other. At $\varepsilon > 0.32$, the difference between the calculations and the experiments increased, and both models significantly underestimated the external measurement results. The deviations in the numerical models to the experimental tests are shown via the eccentricity ratio in Figure 6.13. The experimental data of Mokthar et al. was used as reference values. The significant increase in the deviations in the high eccentricity range is evident in both measurement series. In comparison, there is significantly higher agreement with the measurements with $\Psi = 2.54\text{E-}3$ than with $\Psi = 4.35\text{E-}3$.

This is also reflected in the quantitative evaluation of the numerical models in Table 6.7.

Table 6.7: Maximum deviation for calculating a hydrodynamic bearing with respect to the radial clearance c and permeability parameter Ψ

	Si	FD	Elsharkawy et al.
<hr/>			
$\Psi = 2.54\text{E-}3$			
$c = 85.5 \mu\text{m}$			
<hr/>			
max. $\delta_{F^{\sim}}$	5.7 %	4.1 %	1.2 %
<hr/>			
$\Psi = 4.35\text{E-}3$			
$c = 32.0 \mu\text{m}$			
<hr/>			
max. $\delta_{F^{\sim}}$	46.8 %	47.3 %	-
<hr/>			

The maximum deviations in the range $\varepsilon < 0.8$ were used for validation. The measurement series with the lower radial clearance $c = 32.0 \mu\text{m}$ led to significantly higher deviations. The results of the SI and FD models differ by only one percentage point in both series of measurements. The highest agreement was achieved by the model of Elsharkawy et al. for the higher radial clearance ($c = 85.5 \mu\text{m}$), with a deviation of 1.2%.

6.2.2 Aerostatic Porous Bearing made of Sintered Iron

Castelli [25] performed measurements and calculations with aerostatic porous journal bearings made of a sintered metal mixture. The dimensions of the bushing and the test conditions are provided in Table 6.6. The measurements were performed with a stationary shaft and a rotational speed of 6000 rpm. The bearings were externally pressurized with a pressure ratio $p_s/p_a = 2$ to 7. For validation purposes, the measurement results of $p_s/p_a = 6$ are presented.

The dimensionless static load capacity F^* versus the eccentricity ratio ε is presented in Figure 6.14. As already stated by Sneek [108], the roughness $R_a = 1.6 \mu\text{m}$ of the inner bushing surface was determined and integrated with consideration of the lubricant film thickness. Castelli used the hydraulic clearance c_v to determine the lubricant film thickness. This was formed from the radial clearance (mechanical clearance) c and the arithmetic average roughness R_a :

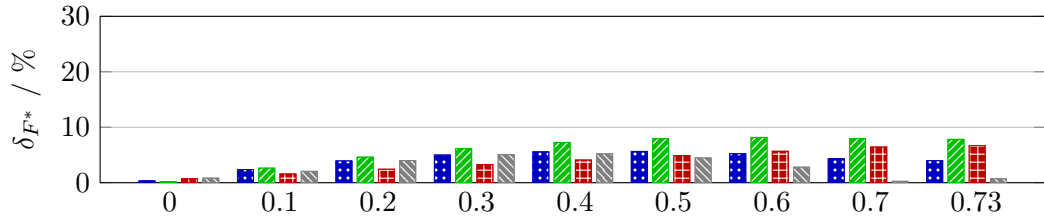
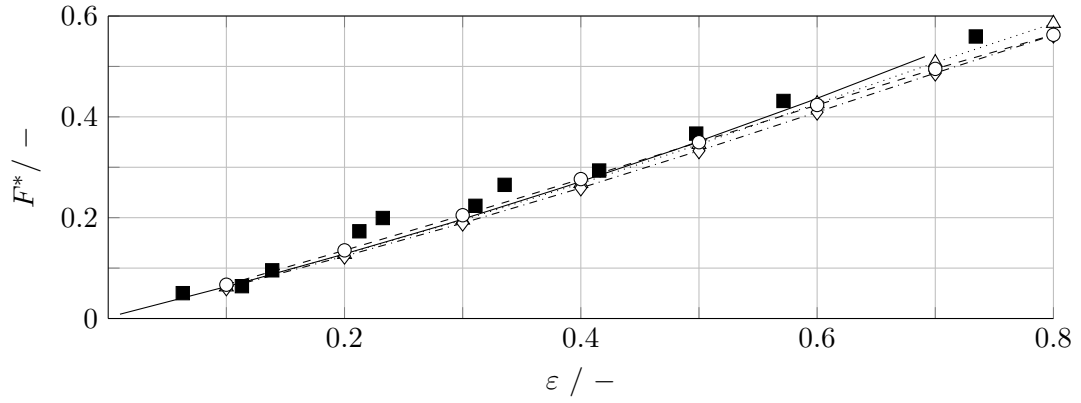
$$c_v = (R_2 - R_1) + R_a = c + R_a \quad (6.10)$$

Castelli's investigations were recalculated by the Si and FD models. Since air lubrication is involved, the FDc model was also used. For consistency in the models, the radial clearance c (mechanical clearance) was used for the calculation of the film thickness. The measured data corresponding to $p_s/p_a = 6$ for $n = 0$ rpm and 6000 rpm were used for validation (see Figure 6.14).

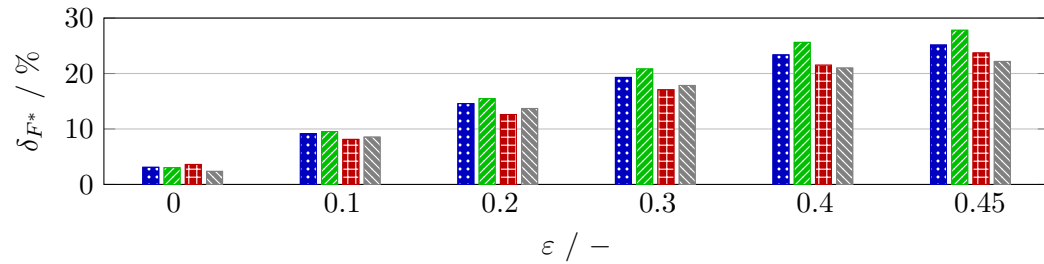
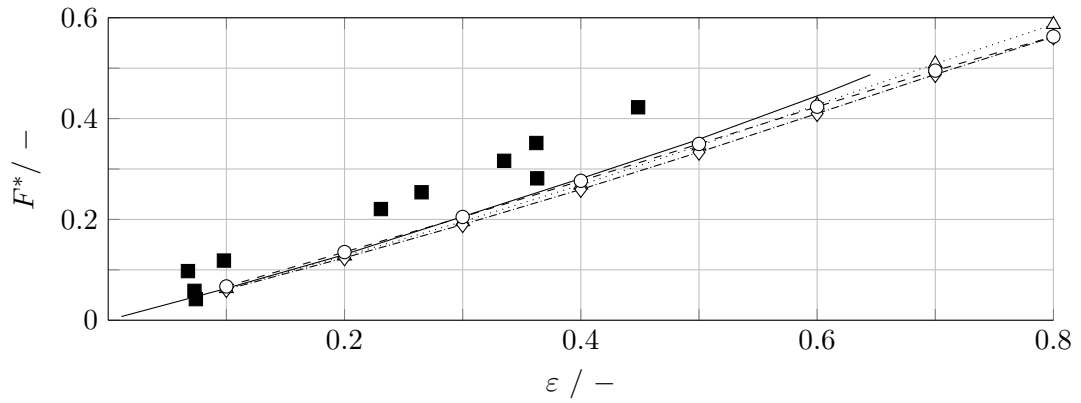
Overall, the numerical models Si, FD, FDc and the model of Castelli show a high agreement with each other. As the eccentricity increases, the difference between Castelli's

Table 6.8: Maximum deviation for calculating an aerostatic porous bearing made of sintered iron with respect to the rotational speed n

	Si	FD	FDc	Sim. Castelli
<hr/> $n = 0$ rpm <hr/>				
max. δ_{F^*}	5.6 %	8.2 %	6.6 %	5.2 %
<hr/> $n = 6000$ rpm <hr/>				
max. δ_{F^*}	25.1 %	27.8 %	23.7 %	22.2 %



(a) $n = 0$ rpm, $p_s/p_a = 6$



(b) $n = 6000$ rpm, $p_s/p_a = 6$

$\dots\triangle\dots$ Si $\dots\diamond\dots$ FD $\dots\circ\dots$ FDc \blacksquare Exp. Castelli — Sim. Castelli
 \blacksquare Si \blacksquare FD \blacksquare FDc \blacksquare Sim. Castelli

Figure 6.14: Validation of Si, FD and FDc with an aerostatic porous bearing made of sintered iron

simulations and the models of this study tended to increase slightly.

A higher agreement was observed in a comparison of the simulation models with the experiments with a stationary shaft than with a rotating shaft. The maximum deviations were between 5.6 % and 8.2 % for the first case ($p_s/p_a = 6$, $n = 0$ rpm) and approximately 22.2 % to 25.1 % for the second case ($p_s/p_a = 6$, $n = 6000$ rpm).

The increase in the rotational speed to 6000 rpm also led to a significant fluctuation in the experimental values of Castelli. The fluctuation in the measured parameters are in part larger than the deviation of the measured to the numerical results. No information about the standard deviations of the measured values could be sourced.

6.2.3 Aerostatic Porous Bearing made of Sintered Graphite

The research of Heidler [61] includes an experimental and numerical investigation of aerostatic porous bearings. This involves a sintered bushing made of graphite. The diameter, length, and diameter-to-length ratio are larger than that of the C/C bearing. However, the thickness and the permeability of the porous bushing is lower. The tests were performed with a stationary shaft. Two vertically positioned capacitive distance sensors were used to determine the eccentricity. Furthermore, the measurements include a determination of the gas consumption with a thermal flow sensor. The surface roughness was measured tactilely and was found to be $R_a = 0.045 \mu\text{m}$ in the axial direction and $R_a = 0.085 \mu\text{m}$ in the circumferential direction.

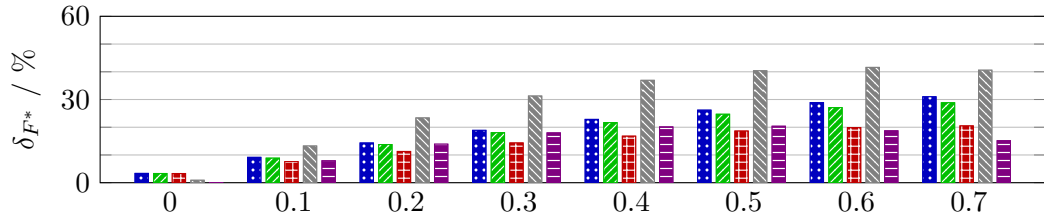
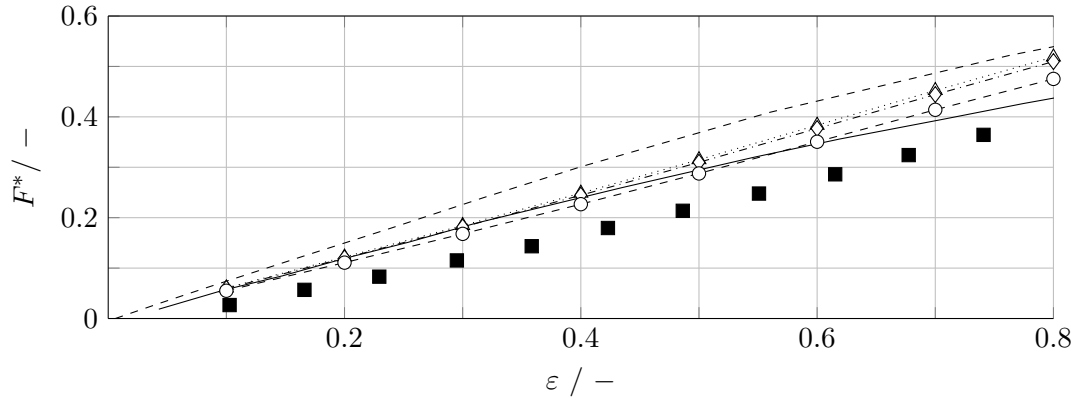
Heidler developed a numerical model to calculate the bearings. His "Vereinfachtes Modell" (English: simplified model) discretized the lubricant film into volume elements. The following assumptions were made: air is an ideal gas, viscosity is constant, flow is laminar and volume and inertia forces are negligible. Furthermore, Heidler used the commercial software COMSOL Multiphysics 4.4 based on the finite element method to calculate the load-carrying capacity.

Figure 6.15 shows the static load-carrying capacity F^* and the max. deviations δ_{F^*} for the pressure ratios $p_s/p_a = 3$ to 5 versus an eccentricity ratio up to 0.8. Atmospheric pressure was used as the output pressure. Heidler's vacuum tests with an initial pressure below $p_a < 1$ bar were not considered for this validation.

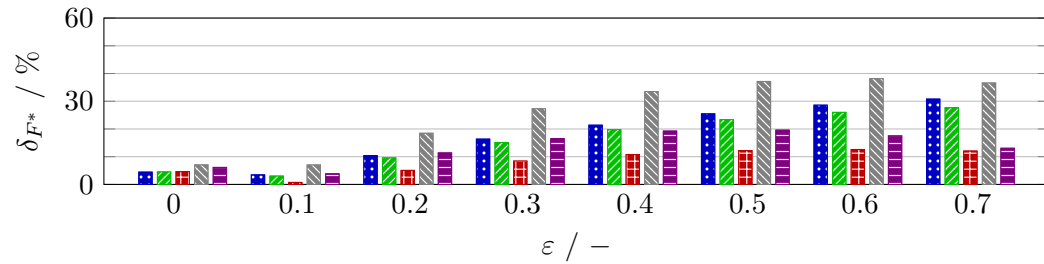
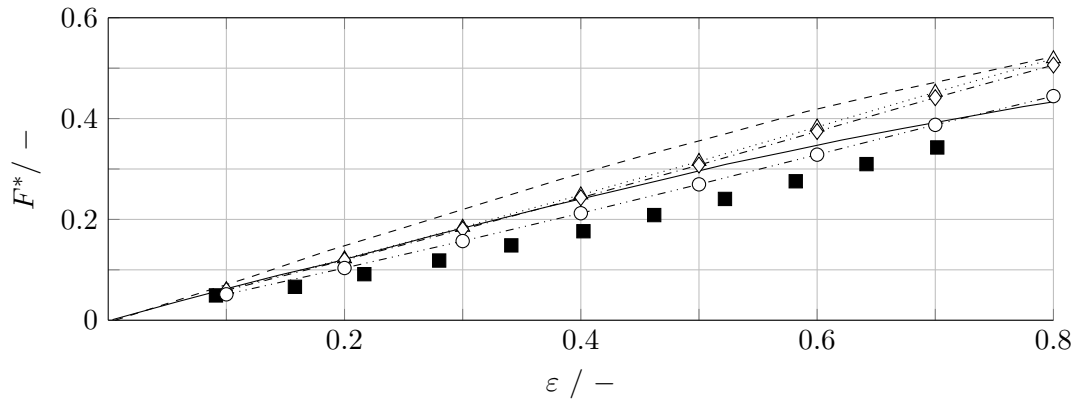
All the numerical models (simplified Heidler, FEM Heidler, Si, FD and FDc) overestimated the experimental values of F^* for $\varepsilon < 0.8$. The highest agreement with the experiments was achieved with the FDc and FEM models. The experiments indicated a nearly linear increase in F^* , consistent with what the FDc model showed. In contrast, the results of the FEM model showed a degressive course.

For evaluation of the models, the maximum deviation from the experiments for $\varepsilon < 0.8$ are listed in Table 6.9. The models were rated based on the load-carrying capacity.

The FDc and FEM models achieved the highest agreement in terms of load-carrying capacity at approximately 20 %. At $p_s/p_a = 5$, the highest deviation of the FDc model was 12.6 %.



(a) $n = 0 \text{ rpm}, p_s/p_a = 3$



(b) $n = 0 \text{ rpm}, p_s/p_a = 5$

$\cdots\triangle\cdots$ Si $-\diamond-$ FD $-\circ-$ FDC \blacksquare Exp. Heidler $---$ Simp. Heidler $---$ FEM Heidler
 \blacksquare Si \blacksquare FD \blacksquare FDC \blacksquare Simp. Heidler \blacksquare FEM Heidler

Figure 6.15: Validation and deviation of Si, FD and FDC with an aerostatic porous bearing made of sintered graphite based on F^*

Table 6.9: Maximum deviation for calculating an aerostatic porous bearing made of sintered graphite with respect to the pressure ratio p_s/p_a

	Si	FD	FDc	Simplified Heidler	FEM Heidler
<hr/>					
$p_s/p_a = 3$					
max. δ_{F^*}	31.6 %	29.3 %	20.6 %	41.6 %	20.4 %
<hr/>					
$p_s/p_a = 5$					
max. δ_{F^*}	30.8 %	27.7 %	12.6 %	38.1 %	19.6 %

6.3 Validation with Experimental Results of a Porous Orthotropic Layered Journal Bearing made of C/C

Based on the experimental tests described in Chapter 3, the Si, FD, FDc, FD+ and CFD models were validated. The static load-carrying capacity F^* , gas consumption q_n and attitude angle ϕ_a were used for quantitative evaluation. Furthermore, qualitative pressure profiles were used to analyze the models in a comparison with each other.

6.3.1 Load-Carrying Capacity

The static load-carrying capacities F^* of the numerical models and the experimental results of the C/C bushings were plotted relative to the eccentricity ratio ε . The data also includes bar graphs that show the deviations from the obtained test results. The validation included a pressure ratio $p_s/p_a = 5$ to 7 and an eccentricity ratio of maximum $\varepsilon = 0.8$.

The FD+ was calculated to an eccentricity ratio of $\varepsilon = 0.6$ and the CFD to a value of $\varepsilon = 0.47$. Compared to the simplified models, the FD+ experienced convergence problems as ε increased. The CFD model experienced additional discretization problems due to an increase in eccentricity. In the region of the lowest film width, the lubrication film could no longer be resolved with eight layers. The results for a rotational speed of $n = 1000$ rpm are shown in Figure 6.16, and the results for $n = 4000$ rpm and $n = 8000$ rpm are shown in Figure 6.17 and Figure 6.18.

The numerical models consistently overestimated the experimental results.

The Si model showed the largest discrepancy (see Table 7.2). With an increase in the eccentricity ratio and in the pressure ratio, the deviation in the measured results increased. The highest deviation, 229.9%, occurred at $\varepsilon = 0.8$ and $p_s/p_a = 7$.

Compared to the FD model, the FDc model tended to show a similar progression of the static load-carrying capacity with an increase in the eccentricity ratio and the pressure ratio. Indeed, with a $\varepsilon = 0.8$ and $p_s/p_a = 7$, the FD model yielded a maximum deviation of 212.9% and the FDc 218.3%.

The CFD model demonstrated a nearly linear trend as well and, thus, an increase in the deviation with an increase in the eccentricity ratio. A clear increase in the deviation with an increase of the pressure ratio was not identified. At $\varepsilon = 0.8$ and $p_s/p_a = 6$, the deviation was 52.7%. The FD+ model values were tendentially degressive and an increase in the pressure ratio led to an increase of the deviation between numerical and experimental values. The highest deviation of 21.6% was determined with $\varepsilon = 0.4$ and a $p_s/p_a = 7$.

The investigations included a rotational speed range from $n = 1000$ rpm to 8000 rpm. The influence of the rotational speed on the static load capacity is shown in Figure 6.19. The deviation in the results of $n = 1000$ rpm and $n = 8000$ rpm was determined. The respective deviations were determined for the numerical models and the experiments, depending on the eccentricity ratio, and presented as bar graphs. Except for one FD+ model outlier (0.63% at $p_s/p_a = 5$, $\varepsilon = 0.5$), the numerical models Si, FD, FDC and FD+ showed

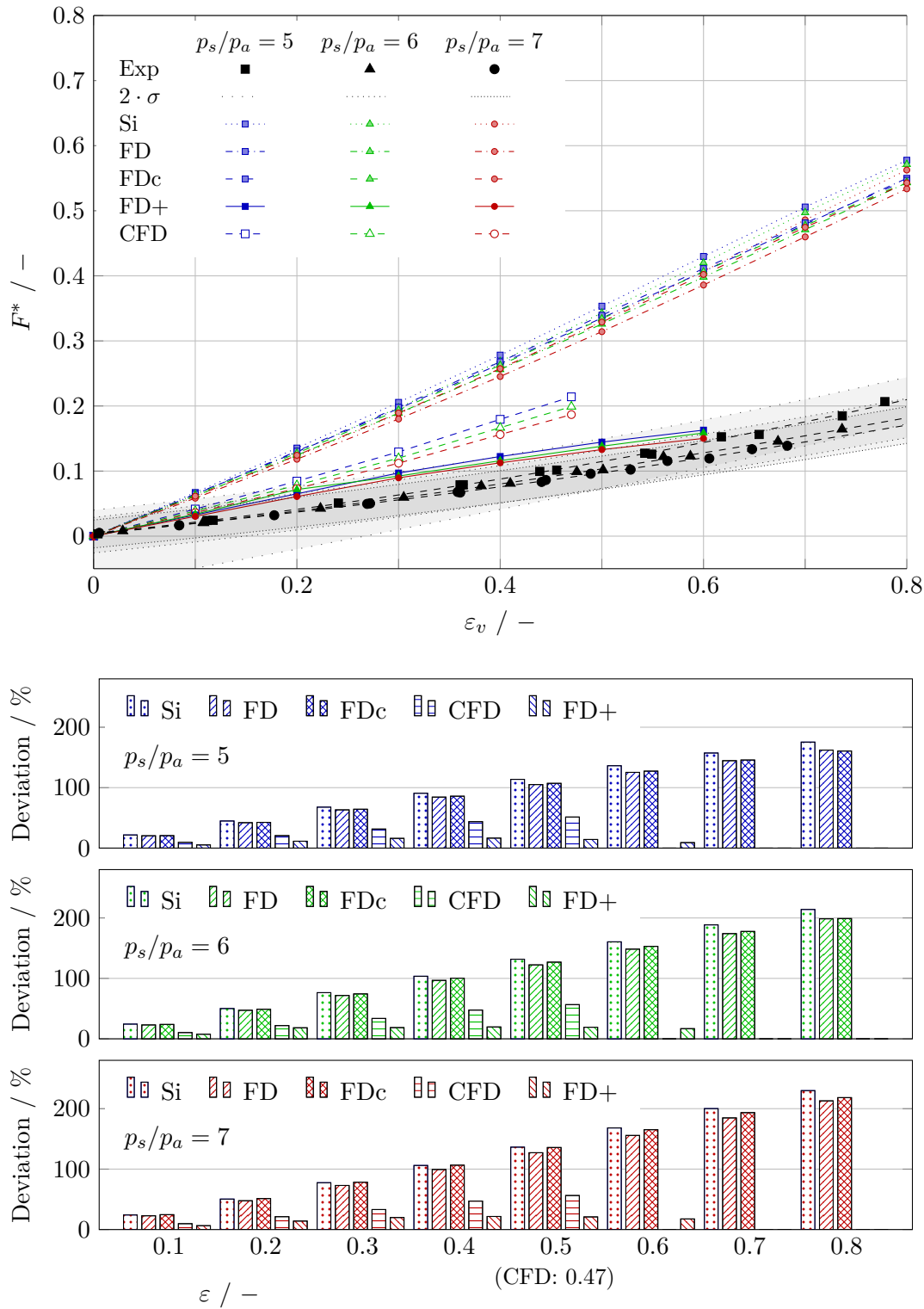


Figure 6.16: Validation of numerical results on the basis of static load-carrying capacity at $n = 1000$ rpm

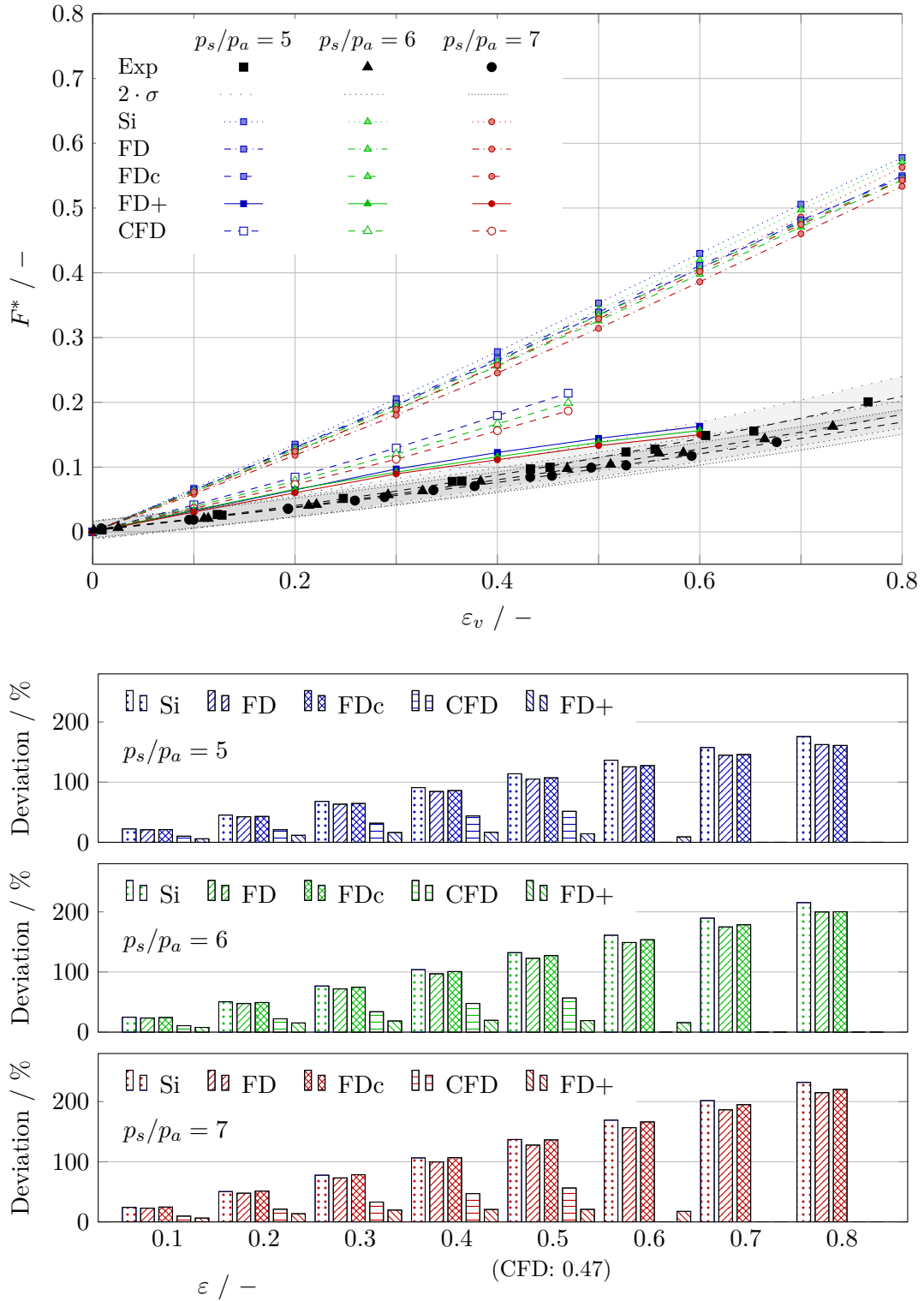


Figure 6.17: Validation of numerical results on the basis of static load-carrying capacity at $n = 4000$ rpm

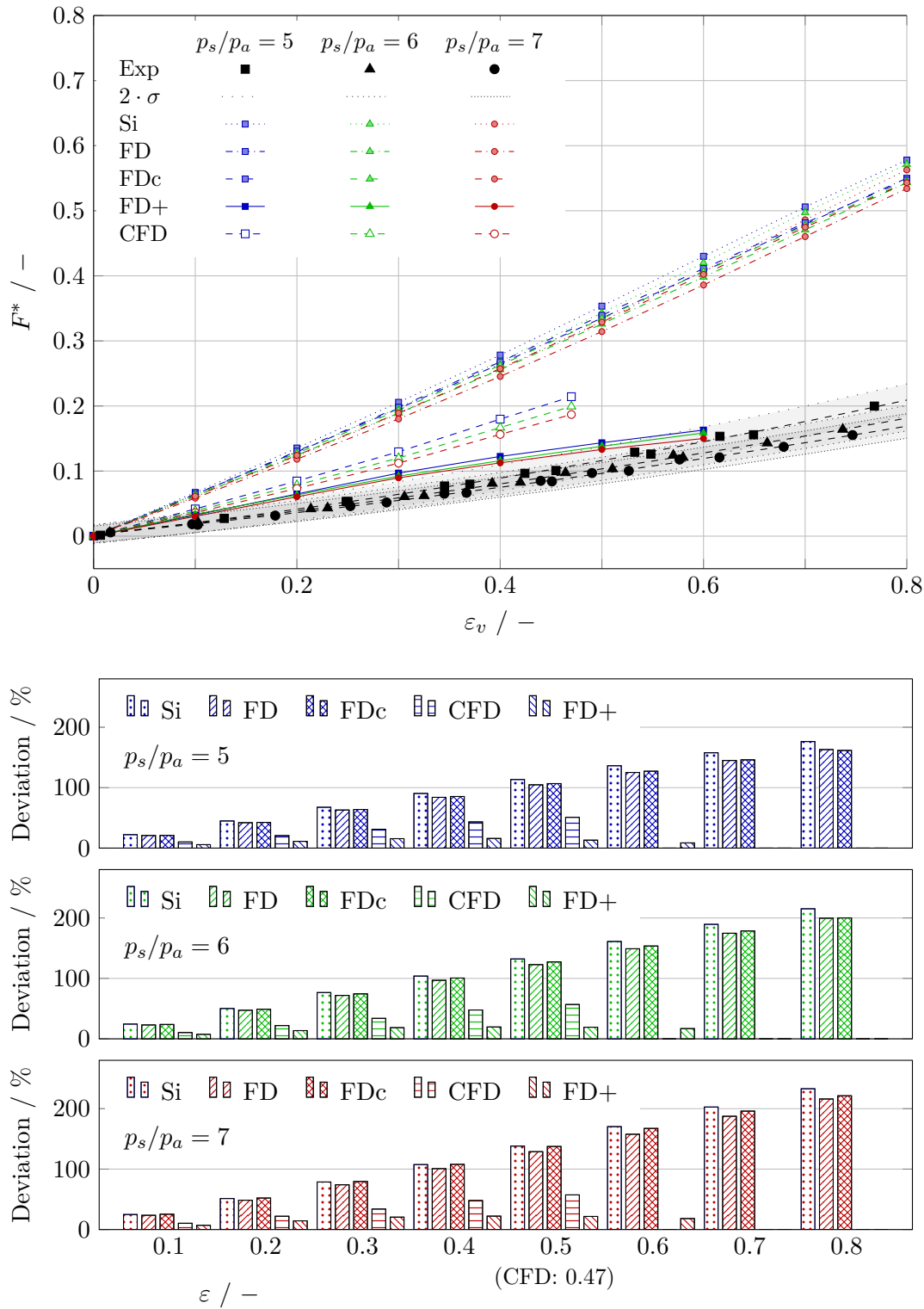


Figure 6.18: Validation of numerical results on the basis of static load-carrying capacity at $n = 8000$ rpm

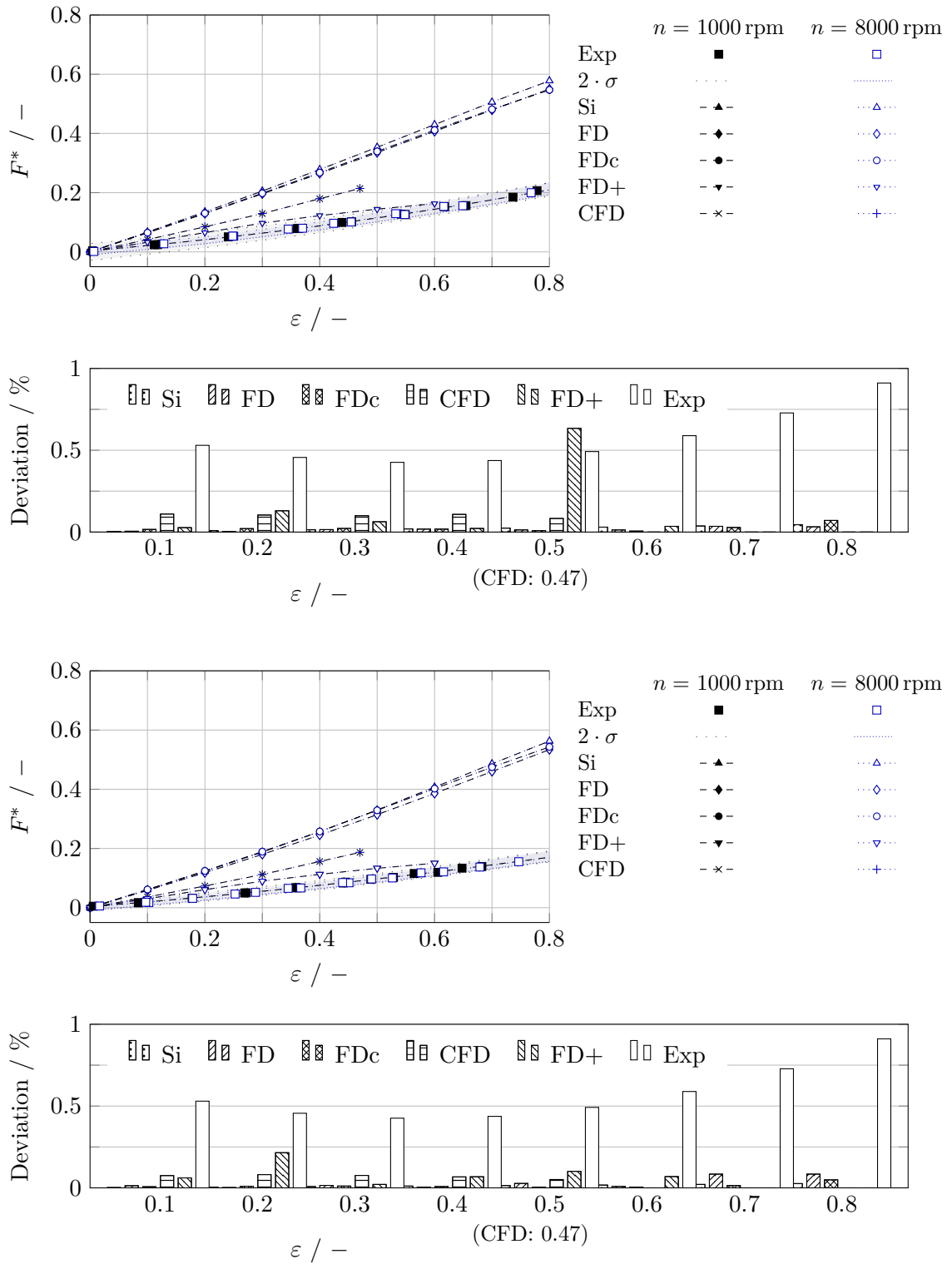


Figure 6.19: Impact of rotational speed on static load capacity at a pressure ratio of $p_s/p_a = 5$ (top) and $p_s/p_a = 7$ (bottom)

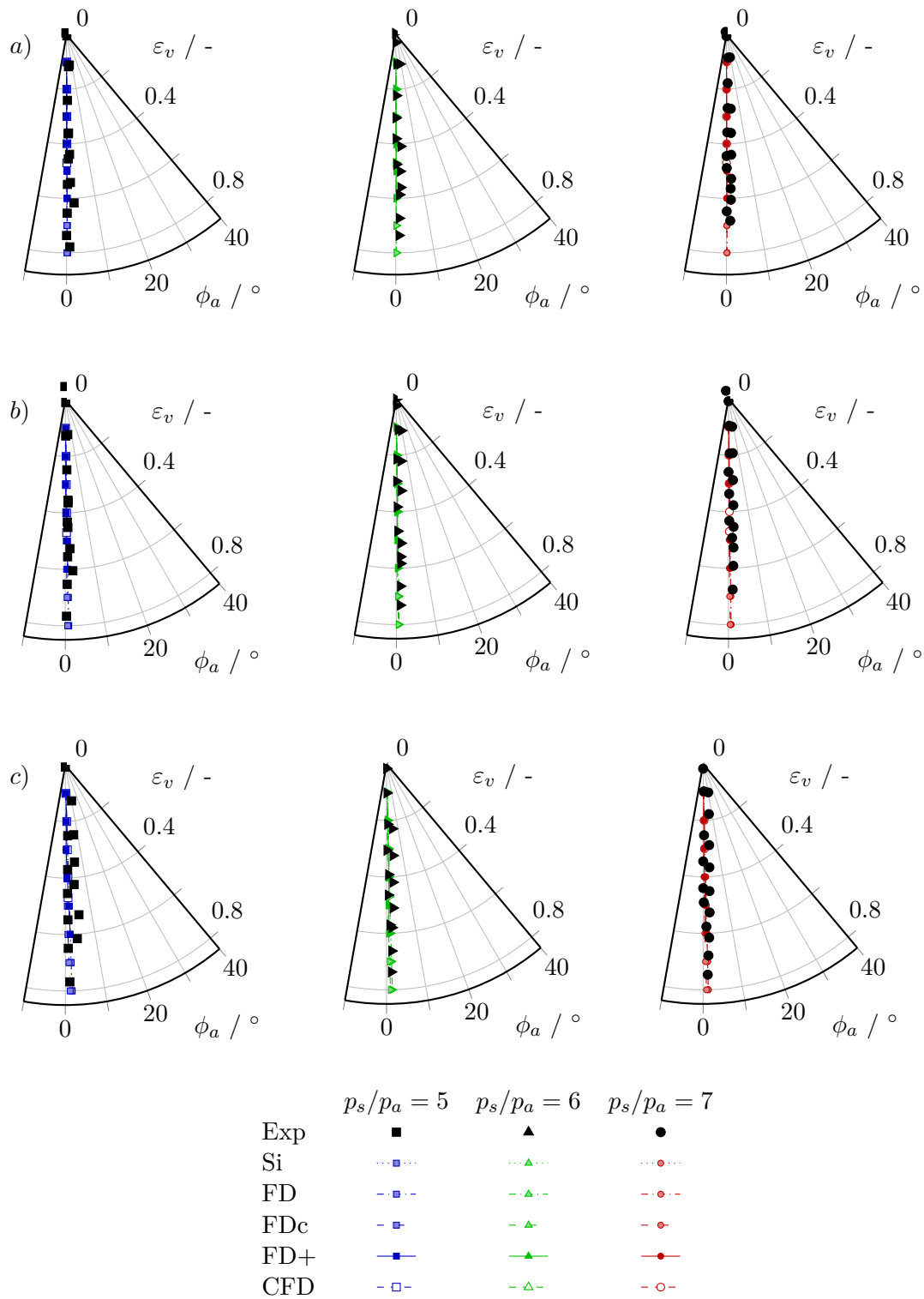


Figure 6.20: Validation of numerical results on the basis of the attitude angle:
a) $n = 1000$ rpm, b) $n = 4000$ rpm, c) $n = 8000$ rpm

deviations of less than 0.25 %. The deviations in the experiments were between 0.4 % and 0.9 % and within the error tolerance range. Consequently, the numerical and experimental results had a deviation of less than 1 % and showed no significant dependence in the speed range up to $n = 8000$ rpm..

The attitude angle of the investigated parameters are shown in Figure 6.20. The numerical results of the SI, FD, FDc, FD+ and the CFD models point to a high agreement of the angle, with a deviation of less than 1 %. The attitude angle of the numerical results is approximately 0° at $n = 1000$ rpm and approximately 1° to 2° at $n = 8000$ rpm.

The experimental values also tended to low attitude angles. The experimental results show varying degrees of scatter, depending on the rotational speed and pressure ratio. The highest observed attitude angles of up to approximately 10° were determined at $n = 1000$ rpm and $p_s/p_a = 4$.

Table 6.10: Maximum deviation for calculating an aerostatic porous bearing made of orthotropic layered C/C with respect to the pressure ratio p_s/p_a

	Si	FD	FDc	CFD	FD+
<hr/>					
$p_s/p_a = 5$					
max. δ_{F^*}	175.4 %	162.1 %	160.6 %	51.4 %	16.5 %
<hr/>					
$p_s/p_a = 6$					
max. δ_{F^*}	214.1 %	198.6 %	198.9 %	56.6 %	19.6 %
<hr/>					
$p_s/p_a = 7$					
max. δ_{F^*}	229.9 %	212.9 %	218.3%	56.3 %	21.6 %
<hr/>					

6.3.2 Gas Consumption

The gas consumption was expressed by the standardized volume flow rate q_n . It was calculated by standard conditions according to DIN 1343 [36] ($T_N = 273.15$ K and $p_N = 101\,325$ Pa) and expressed as follows:

$$q_n = \dot{m} \cdot \frac{T_n \cdot R_g}{p_n} \quad (6.11)$$

The comparison of the gas consumption q_n versus the dimensionless eccentricity for $n = 1000$ rpm is shown in Figure 6.21. The deviation of the numerical models was determined in relation to the measurement results.

The Si and FD models underestimated the gas consumption. The models showed nearly constant gas consumption over the eccentricity range. The maximum deviation of the Si from the experimental results is 87.6 % and, of the FD model, 87.3 %. An almost constant gas consumption versus eccentricity can also be observed in the FDc and the CFD models.

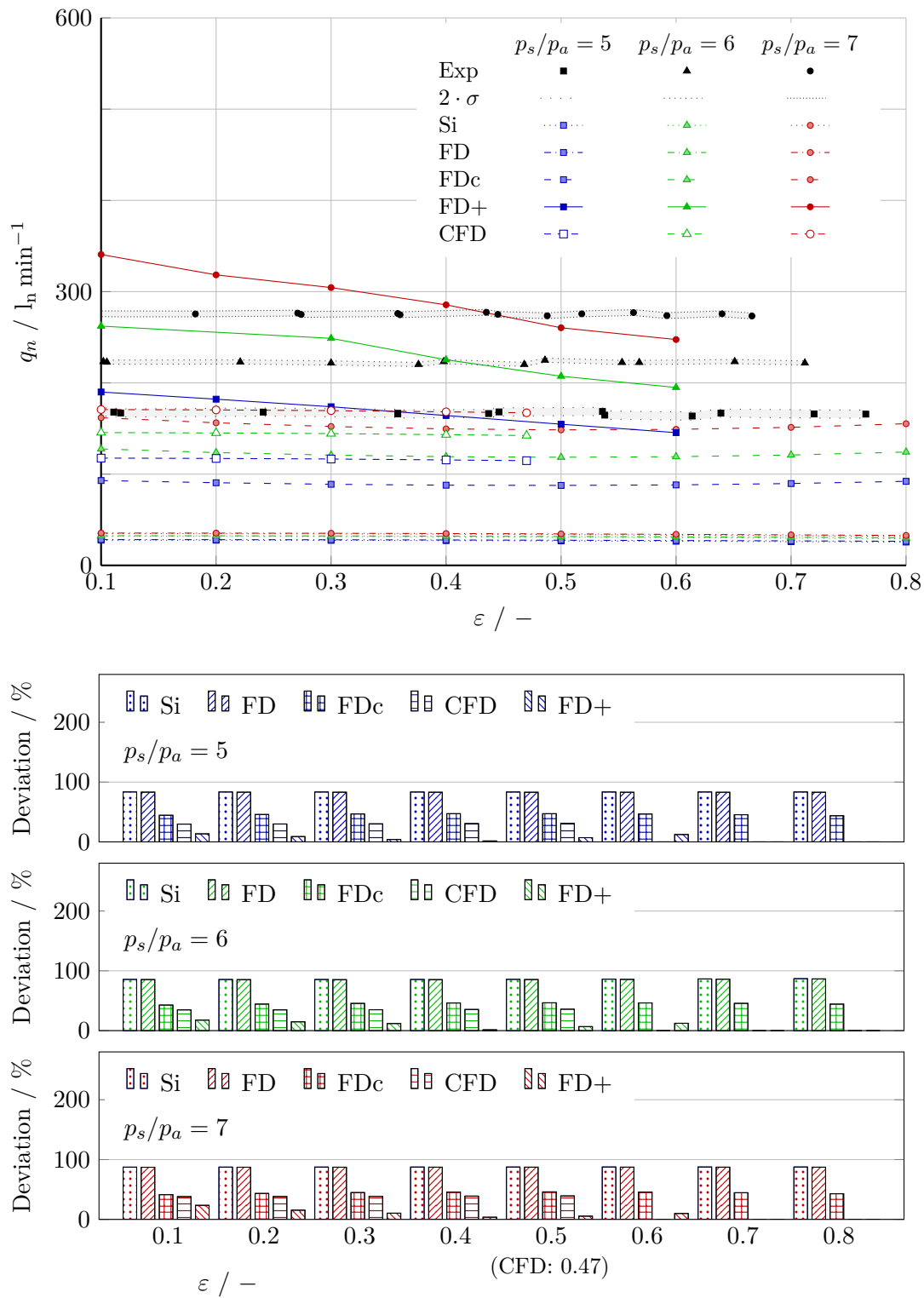


Figure 6.21: Validation of numerical results on the basis of norm flow rate at $n = 1000 \text{ rpm}$

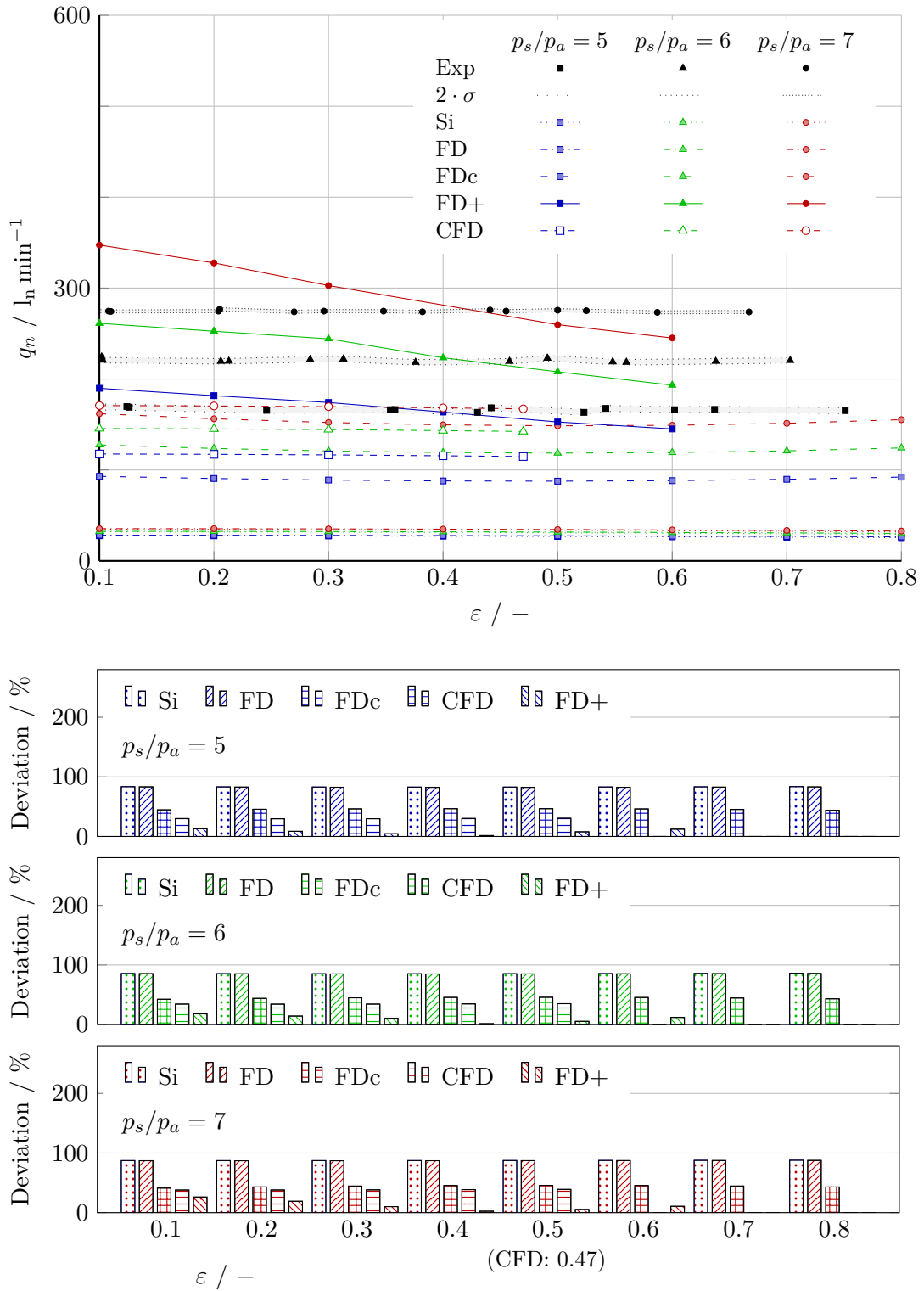


Figure 6.22: Validation of numerical results on the basis of norm flow rate at $n = 4000 \text{ rpm}$

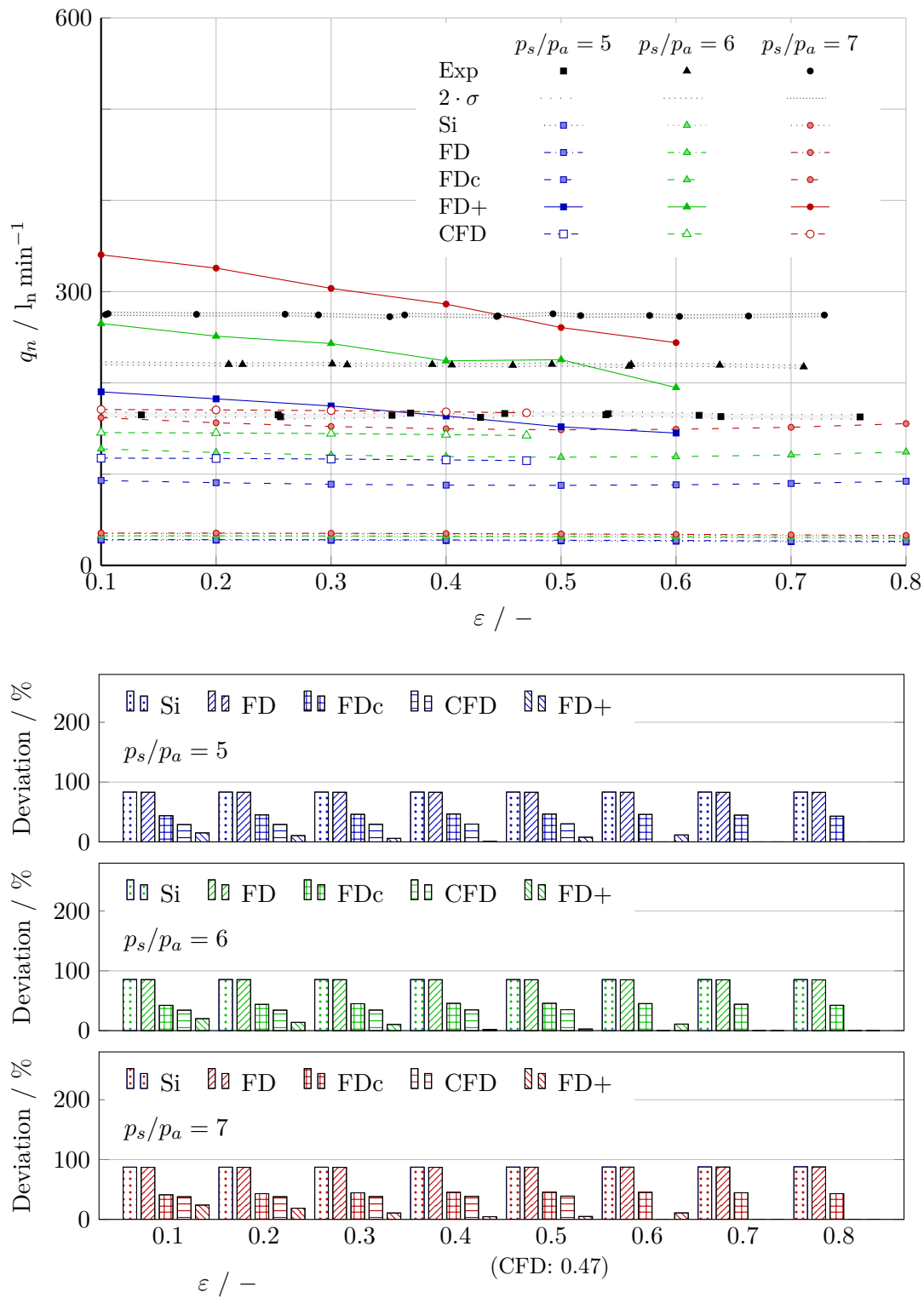


Figure 6.23: Validation of numerical results on the basis of norm flow rate at $n = 8000$ rpm

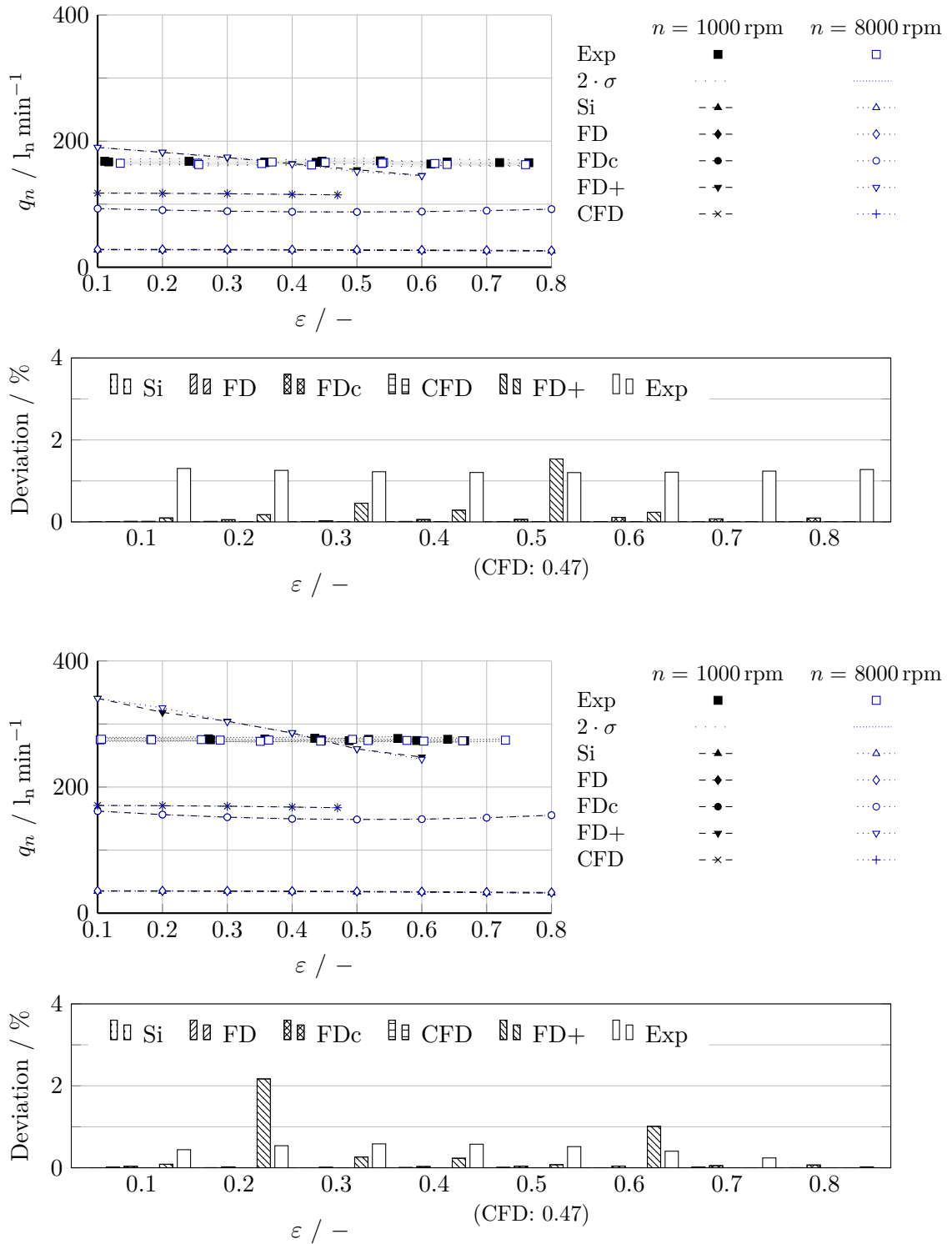


Figure 6.24: Impact of rotational speed on gas consumption at a pressure ratio of $p_s/p_a = 5$ (top) and $p_s/p_a = 7$ (bottom)

The FDc model showed a slight influence of the pressure ratio (approximately 1%). The maximum deviation of the CFD model increased with an increase in the pressure ratio. The FDc model showed a maximum deviation of 47.1% and the CFD model 46.0%.

The FD+ model showed a reduction in gas consumption with an increase in eccentricity. Furthermore, the deviation increased with an increase in the pressure ratio. The FD+ model showed a maximum deviation of 23.5%.

The effect of rotational speed up to 8000 rpm on gas consumption is presented in Figure 6.24. The analysis included the supply pressures $p_s/p_a = 5$ to 7 and the numerical as well as the experimental results. The results of the numerical models Si, FD, FDc and the CFD model showed a high agreement with $n = 1000$ and 8000 rpm. Deviations were well below 1%. A deviation of less than one 1% was widely observed for the FD+ model. There were individual outliers with a deviation of approximately 2% in the FD+ model. The experimental investigations showed a largely constant deviation in the eccentricity range up to 0.8. The constant deviations correspond approximately to 1% and are within the error tolerance.

Table 6.11: Maximum deviation for calculating an aerostatic porous bearing made of orthotropic layered C/C with respect to the pressure ratio p_s/p_a

	Si	FD	FDc	CFD	FD+
<hr/>					
$p_s/p_a = 5$					
max. δ_{q_n}	83.5 %	83.2 %	47.1 %	31.0 %	13.4 %
<hr/>					
$p_s/p_a = 6$					
max. δ_{q_n}	86.9 %	86.5 %	46.5 %	35.8 %	17.6 %
<hr/>					
$p_s/p_a = 7$					
max. δ_{q_n}	87.6 %	87.3 %	46.0 %	39.2 %	23.5 %
<hr/>					

6.3.3 Analysis of the Pressure Distribution

Qualitative pressure profiles of the lubricant film or in the porous bushing enable direct comparison of the models. The planes from Figure 6.25 include the lubricant film, a cross-section of the bushing in axial length (r - φ plane, $z = 15$ mm) and two longitudinal sections. The longitudinal cuts are in the region of the smallest (r - z plane, $\varphi = 0^\circ$) and the largest lubricant film width (r - z plane, $\varphi = 180^\circ$), respectively. In the following, the influence of the models on the pressure profiles is analyzed with the parameters: $c = 30 \mu\text{m}$, $\varepsilon = 0.4$, $p_s/p_a = 5$, $n = 1000$ rpm.

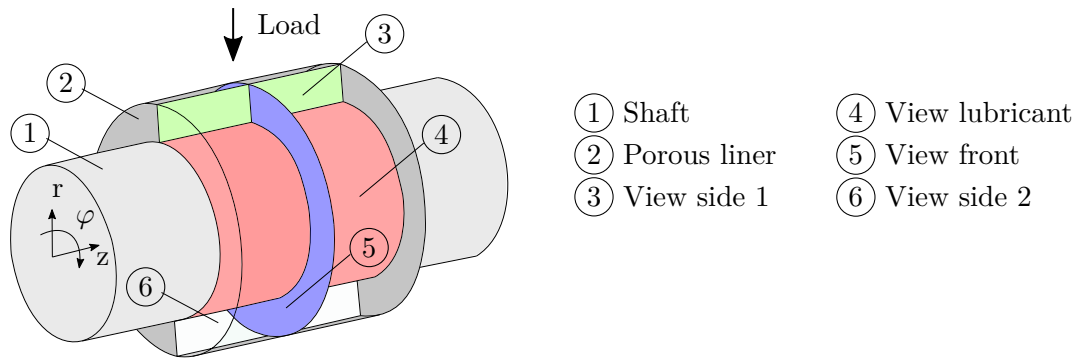


Figure 6.25: Overview planes

Gap Width

The lubrication gap height influences the pressure distribution of the lubricant film and the pressure distribution in the porous bushing. The lubricating film width profile is shown in Figure 6.26.

The Si, FD and CFD models used the same lubrication film width modeling approach. An ideal increase in the eccentricity without shaft misalignment was assumed. The narrowest lubricant film width at $\varphi = 0^\circ$ was constant in the axial direction. With an increase in eccentricity, the gradient in the film width increased in the circumferential direction. By negating the misalignment, the gradient of the lubricant film width in z direction equaled zero.

The FDc model included the shaft misalignment. The film width distribution of the FDc had a point-wise minimal lubrication clearance at $z = 0$ mm, $\varphi = 0^\circ$ due to the shaft misalignment. In comparison with the preceding model, the misalignment resulted in a greater difference between the minimum and maximum lubricant film widths. The FD+ model included, in addition to the shaft misalignment, the surface contour of the bushing. The layered design resulted in grooves. In the FD+ model, these grooves were modeled by gradations in the z direction. The measurement of the grooves is described in Chapter 2.3. In Chapter 4.3.3, the generation of the mean groove contour and the formula for the calculation of the lubricant film width are described. The groove contour was imposed on the lubricant film distribution with consideration of the shaft misalignment and resulted in a serrated course with strong increases in the lubrication gap. The misalignment of the shaft and the position of the narrowest lubricant film width correspond to the FDc model.

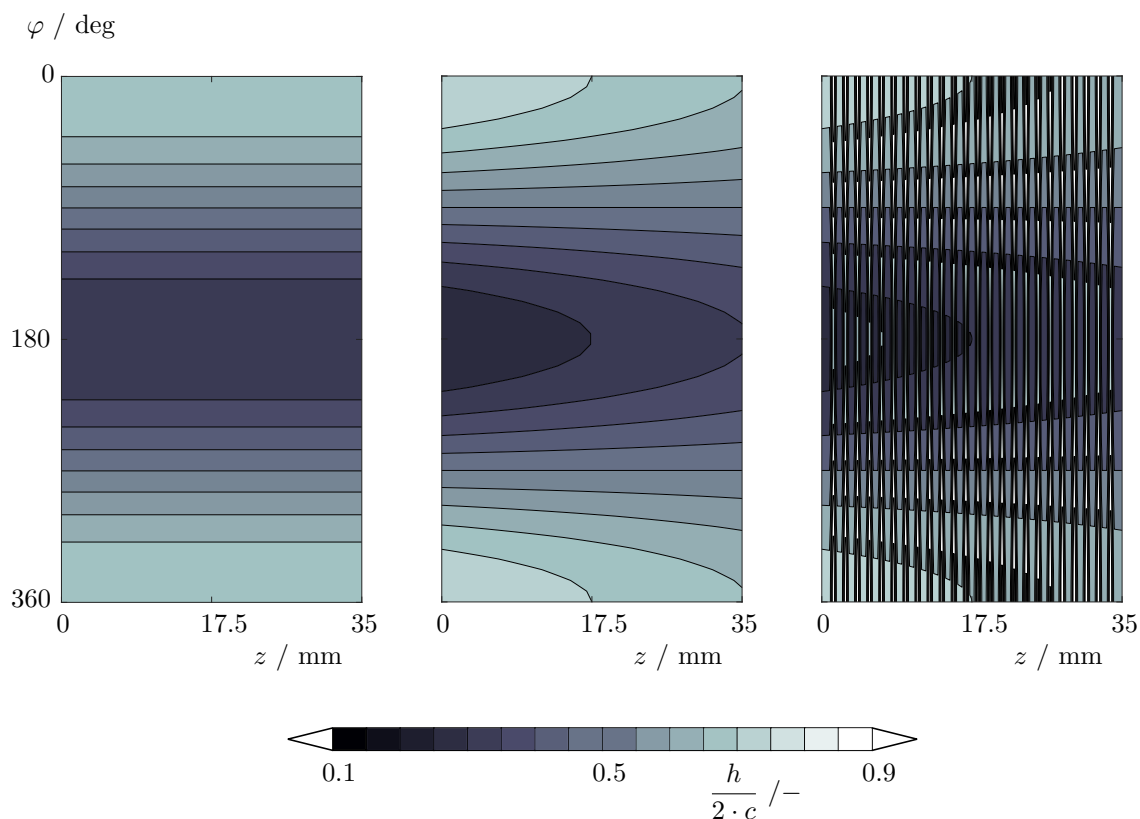


Figure 6.26: Film height distribution: No misalignment (left), vertical misalignment (middle), vertical misalignment plus texture (right)

Lubricant

The pressure distribution in the lubricant film of the respective models, which is dimensioned with the supply pressure, is shown in Figure 6.27. These are the pressure profiles with a pressure ratio $p_s/p_a = 4$ and a rotational speed of $n = 1000$ rpm.

The SI and FD models had a pressure maximum in the axial center due to the assumption of an axially uniform shaft misalignment. The shaft misalignment in the FDc model led to a shift in the pressure maximum in the axial direction. The FD+ model included the groove contour of the bushing in addition to the misalignment of the shaft. The groove contour led to serrated pressure isolines. The axial displacement of the pressure maximum was less pronounced compared to the FDc. The CFD model did not assume any shaft misalignment and led to a position of the pressure maxima in a central axial position. The pressure gradient in the radial direction was lower than in the SI, FD and FDc models and caused a lower load-carrying capacity.

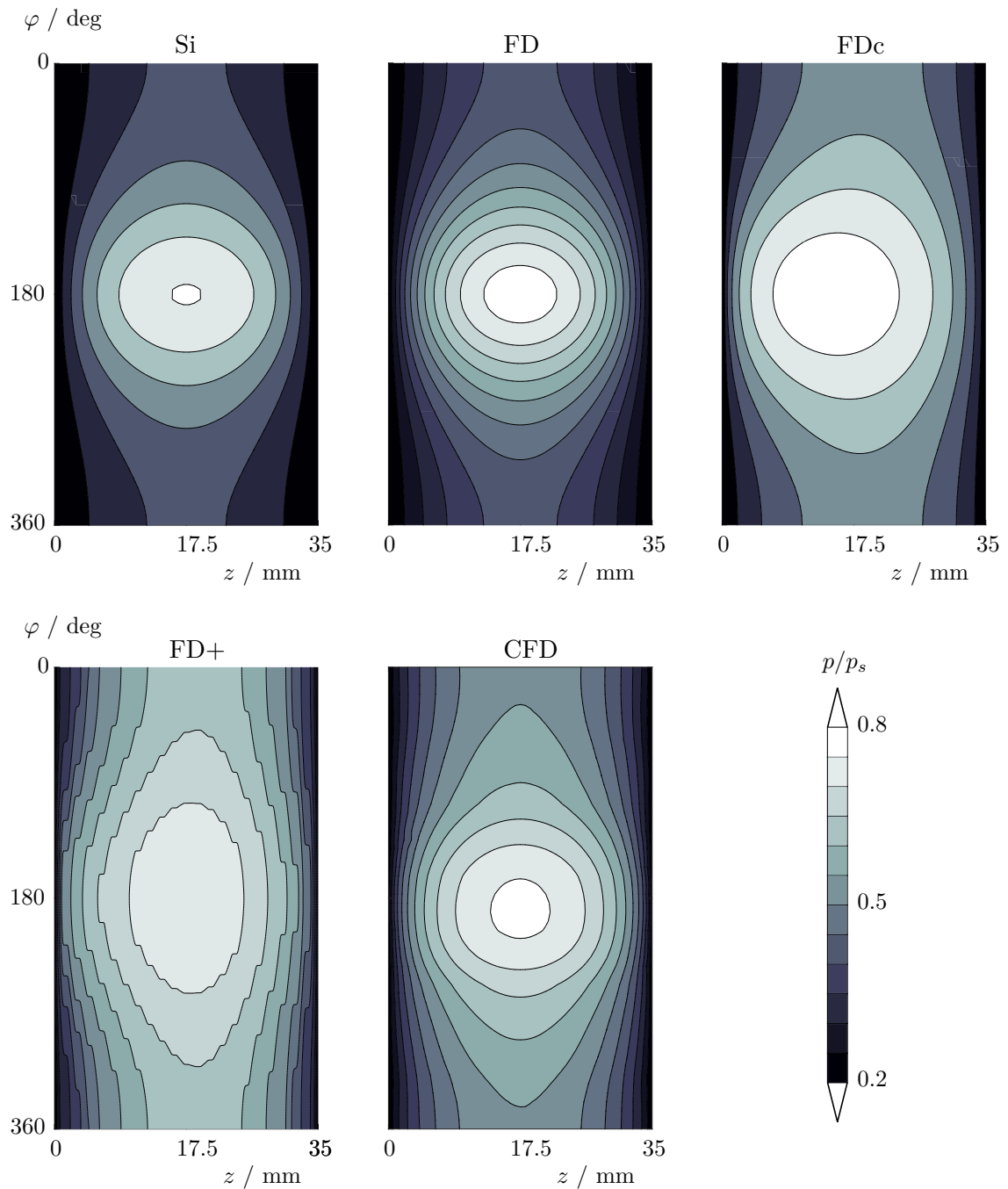


Figure 6.27: Pressure distribution lubricant view: $p_s/p_a = 5$, $\varepsilon = 0.4$, $n = 1000\text{rpm}$

Porous Liner - Front View

The front view of the numerical results is shown in Figure 6.28. This view represents the pressure profile in the cross-section of the porous bushing. The cross section was taken at the mean axial length ($z = 15 \text{ mm}$). The supply pressure p_s was applied at the outer diameter and the lubricant film was calculated at the inner diameter. The lowest

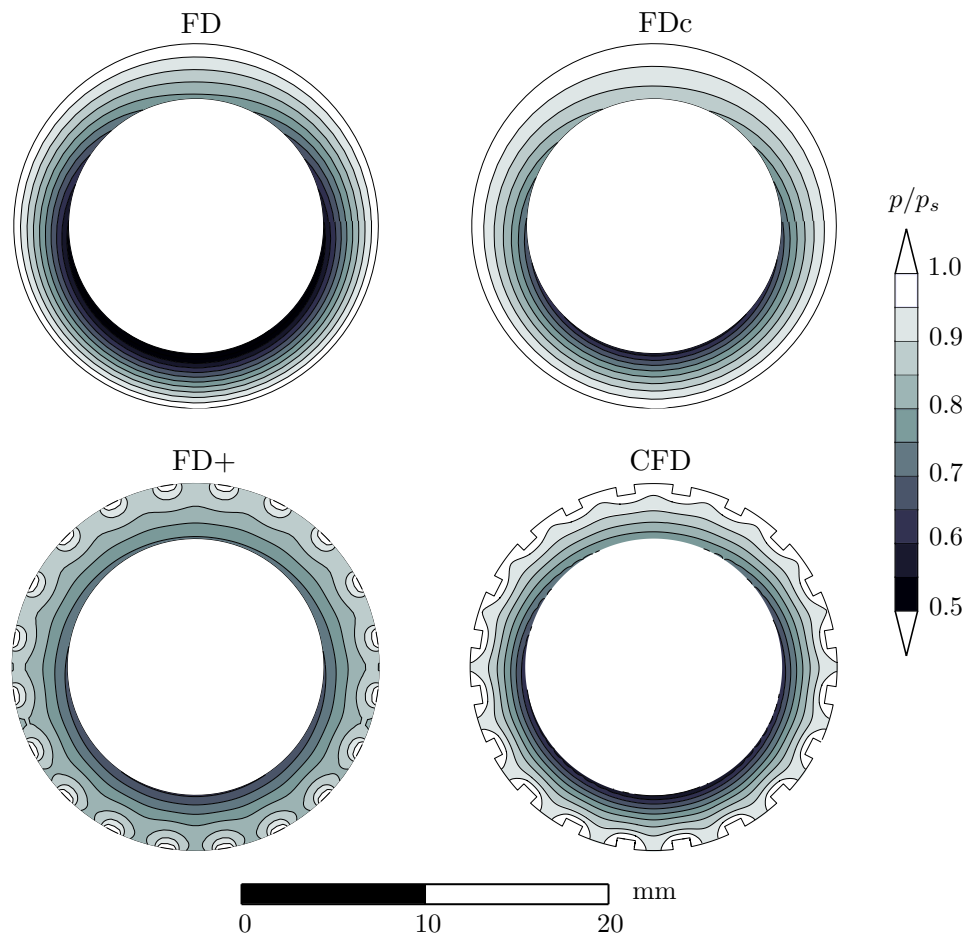


Figure 6.28: Pressure distribution front view: $p_s/p_a = 5$, $\varepsilon = 0.4$, $n = 1000\text{rpm}$

lubrication film width was at $\varphi = 0^\circ$.

The influence of the boundary condition at the outer diameter $r = 20\text{ mm}$ is evident on the contour plots. The Si, FD and FDc models used a continuous Dirichlet boundary condition at the outer diameter ($p_s = 5\text{ bar}$). This led to a pressure gradient primarily in the radial direction from the outer diameter to the inner diameter.

The CFD model additionally modeled the supply line and the air chambers to the porous bushing, for which an interface between the air domain and the porous domain was used. Based on the 20 chambers, the supply pressure was distributed in the porous bushing. The FD+ model also incorporated the influence of the chambers. Dirichlet boundary conditions were applied to the outer diameter and Neumann boundary conditions to the wall.

At the outer diameter, the CFD and FD+ models demonstrated circumferential pressure gradients, which were located between the air supply chambers. Downstream to the inner surface of the bushing, the circumferential pressure gradients decreased again rapidly.

Porous Liner - Side View

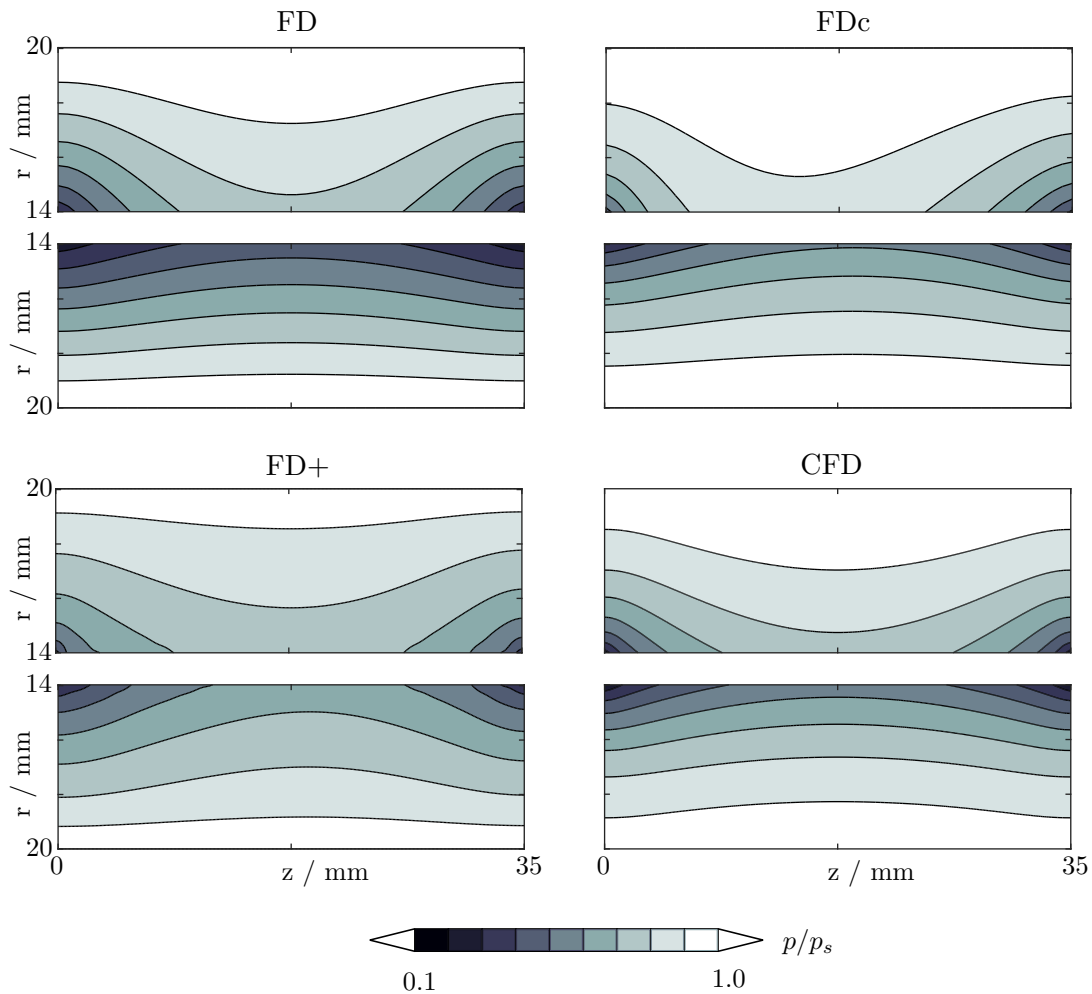


Figure 6.29: Pressure distribution side view: $p_s/p_a = 5$, $\varepsilon = 0.4$, $n = 1000\text{rpm}$

Figure 6.29 shows the pressure profile in the axial sectional view of the porous bushing. Views 1 and 2 show r - z planes intersecting the bushing in the lowest ($\varphi = 0^\circ$) and the highest film width ($\varphi = 180^\circ$), respectively.

The Dirichlet boundary conditions at the axial ends of the fluid-film significantly influenced the pressure profile in the porous bushing. For both views 1 and 2, at $z = 0\text{ mm}$, $r = 14\text{ mm}$ and $z = 35\text{ mm}$, $r = 14\text{ mm}$, are the respective bushing pressure minima. This was consistent in the four numerical models.

The shaft misalignment is shown in the sectional view of the pressure distribution in the porous bushing. The pressure maximum moves in the axial direction in the FDc and FD+ models. In the FD+ model, the axial offset was less significant relative the FDc model.

6.4 Discussion regarding the Validity of the Models

6.4.1 Dynamic Bearing with Oil Lubrication

The experiments conducted by Mokthar et al. [84] involved a dynamic porous bearing lubricated with oil. Measurements were taken for radial clearances of $32.0\ \mu\text{m}$ and $85.5\ \mu\text{m}$. Experiments with a higher lubricant film width had already been conducted by Elsharkawy et al. [46] to validate their numerical model. The results obtained by Mokthar et al. and Elsharkawy et al. were used for numerical comparison of the SI and FD models developed in this study.

The comparison showed that the deviations of the SI and FD models from the experimental results were dependent on the radial clearance and eccentricity. For a radial clearance of $32\ \mu\text{m}$, the maximum deviations of the Si and FD models were 46.8% and 47.3%, respectively. The higher radial clearance of $85.5\ \mu\text{m}$ resulted in lower deviations in the SI model, with 5.7%, and the FD model, with 4.1%. In addition, high eccentricities resulted in a rapid increase in deviations between the numerical and experimental results. The differences could be attributed to the numerical assumption of pure fluid-film lubrication. This approach can lead to good matches in a larger eccentricity range with larger radial clearances. In the series of tests with a small gap width of $32.0\ \mu\text{m}$, mixed friction may have already been present at low eccentricities due to the comparatively high viscosity of the oil, compared to air. A rapid increase in load was observed at high eccentricities in both series of tests, which could be attributed to a transition to contact friction. As a result of high eccentricity, contact occurs between the shaft and the bushing, causing a rapid increase in load.

The SI and FD models in this study were originally developed for air bearings, which have a lower dynamic viscosity than oil. In addition, the C/C experiments were conducted in a comparatively lower eccentricity ratio range of less than 0.80.

The agreement between the Si and the FD models was high in both series of measurements. The model developed by Elsharkawy et al. showed a tendency towards better agreement with the experimental results.

The deviations are due to the numerical assumptions. The three models use different kinds of interfaces between the porous bushing and the lubricating film. The simple model assumes a purely radial inflow from the porous bushing, and the FD model assumes a three-dimensional flow. In contrast, the model of Elsharkawy et al. includes the additional influence of viscous shear stress forces through the Darcy-Brinkman approach.

Another difference between the models refers to the cavitation model, for which Elsharkawy used the Elrod model that considers conservation of mass. The Si and FD models, on the other hand, adopted the simplified Gumbel approach.

6.4.2 Aerostatic Bearing made of Sintered Metal

Castelli's tests and simulations were used to validate the models with a pressurized porous bearing with a relatively low roughness of the inner surface of $1.6 \mu\text{m}$.

The Si, FD and FDc models showed strong agreement with the tests with the numerical model of Castelli with a stationary shaft, with max. $\delta_{F^*} = 5.6\%$, 8.2% and 6.6% . With an increase in the rotational speed to 6000 rpm, the difference between the simulations and the tests increased by up to 28% .

The reason for the discrepancy could not be clearly identified. One possible cause, already mentioned by Castelli, is that the dynamic effect may not occur in the numerical models at low speeds, unlike in the tests. Indeed, the four numerical models showed negligible influence from the rotational speed on the load-carrying capacity, with deviations of below 1% .

A further cause could be related to the repeatability of the measurements. The increase in rotational speed increases the fluctuation of the tested load-carrying capacities. Discrepancies between individual measured values are partially higher than the deviations of the numerical results. There is no indication of the error tolerance or the standard deviations of the measurements. Therefore, a conclusion cannot be reached as to whether the calculated load-carrying capacities were within the permissible error limits of the measuring instruments.

6.4.3 Aerostatic Bearing made of Sintered Graphite

Heidler's investigations with a porous bearing made of graphite with a relatively smooth inner surface ($R_a < 0.085 \mu\text{m}$) were used for validation. Both the experimental and numerical results of load-carrying capacity were used. The numerical computation includes Heidler's simplified model and commercial FEM software.

In the determination of the load-carrying capacity for Heidler's test cases, the FDc model, with max. $\delta_{F^*} = 20.6\%$, showed better agreement with the tests than the Si (max. 31.6%), FD (max. 29.3%) and the simplified Heidler (max. 41.6%) models. The maximum deviation of the FDc model was even 12.6% at a pressure ratio of 3.

The FDc model is based on the FD model, with the possibility to implement information regarding the misalignment of the shaft and a non-constant assumption of density and viscosity. In the present case, no misalignment of the shaft was experimentally determined; consequently, the positive effect can be attributed to the consideration of compressibility. Heidler's simplified model obtained deviations of approximately 40% in the experiments for the calculation of the load-carrying capacities.

Heidler attributes this to the simplifications in the model and the non-uniform permeability of the bushing as well as the cylindricity deviations in the elements. Differences in the Si, FD and FDc models can be justified by the numerical assumptions. The calculation of the lubricating film is based on a Poiseuille flow (see Heidler [61]). The model neglects the flow in circumferential direction. The Si, FD and FDc models were based on the GREL

model and take into account the velocities in the circumferential direction. In the simplified Heidler model, the porous bushing is not discretized. As in the SI model, a purely radial flow through the porous bushing is assumed. In contrast to the previous numerical models, the simplified Heidler model distinguishes between a continuum flow and a Knudsen flow in the lubricant film. This leads to a distinction where, for a Knudsen flow, a slip on the surface of the rotating shaft is assumed and, for a continuum flow, a no-slip boundary condition is assumed. For the Si, FD, and FDc models, a consistent no-slip boundary condition was assumed on the rotating wall.

The FEM model achieved a maximum deviation of 20.4% from the experimental load-carrying capacities, which is less than Heidler's simplified model.

In contrast to the simplified model, the FEM model discretizes the porous bushing and includes the circumferential components of the velocity. Nevertheless, a pure continuum flow is assumed in the FEM model.

The discrepancy in the numerical models may additionally be due to the experimentally determined permeability as well as the non-uniform permeability of the bushing (see Heidler [61]). In conclusion, the porous bushing restricts the flow and has a significant effect on the gas consumption.

6.4.4 Aerostatic Bearing made of Orthotropic Layered C/C

The Si, FD, FDc, FD+ models and commercial CFD software were used to validate the experiments with an orthotropic layered C/C bearing.

Regarding the static load-carrying capacity F^* , a higher agreement between numerical and experimental results was obtained through an increase in the model complexity. The maximum deviation of the models was 229.9% for Si, 212.9% for FD, 218.3% for FDc, 56.3% for CFD and 21.6% for FD+.

Thus, the SI, FD, and FDc models had the highest deviation in load-carrying capacity of the C/C bearing. The compressible modeling of the medium and the discretization of the porous bushing in the FDc model resulted in an approximate 10% improvement compared to the Si model. However, the maximum deviation in the experiments still exceeds 200%. However, the experimental and numerical results of the external validation of the Si, FD and FDc models showed significantly higher agreement with the simulations of dynamic oil bearings and aerostatic air bearings made of sintered metal and graphite. The main difference between the bearings is in the structure of the porous bushing. The sintered metal and graphite aerostatic bearings had a mean roughness of $1.6 \mu\text{m}$ and, in the case of the graphite bearing, a value below $0.1 \mu\text{m}$ was even reported. In contrast, the C/C bushing was manufactured by pyrolysis and the structure of the orthotropic layers resulted in the characteristic groove structure of the inner surface of the bushing. The grooves are considerably more significant (up to $120 \mu\text{m}$) than the roughness of the bushings examined in the external studies. Based on the measurement of the contour of the C/C bushing, a mean groove structure was generated and implemented in the computation of the lubricant

film thickness. In addition, the geometry of the pressure chambers was included in the simulation. In the previous models (Si, FD and FDc), an ideal pressure supply of the entire outer surface of the porous bushings was assumed. The resulting FD+ model achieved a maximum deviation of 21.6 %, while the commercial CFD achieved a maximum deviation of 56.3 %. In common with the FD+ model, the CFD models the pressure supply to the bearing. A key difference is that the FD+ model takes into account the groove contour of the porous bushing, which means that the structure can be assumed to have a significant influence on bearing performance.

The experimental results reported by Mokthar and Heidler showed F^* values in excess of 0.3, whereas the F^* values obtained from C/C measurements at comparable eccentricities were reported to be around 0.2. This discrepancy can be attributed to the presence of a groove contour which reduces the contact area available for the formation of a load-carrying lubricant film and consequently the load-carrying capacity of the bearing. It is noteworthy that the inclusion of the groove contour in the FD+ model resulted in a significant reduction in the calculated F^* values, thereby improving the model's approximation to the experimental results.

With regards to the gas consumption q_n , a higher agreement between the numerical and experimental results was also achieved by increasing the model complexity. The maximum deviation of the Si was 87.6 %, the FD 87.3 %, the FDc 47.1 %, the CFD 39.2 % and the FD+ 23.5 %.

The use of a compressible approach and consideration of shaft misalignment in the FDc model have resulted in an improvement of approximately 40 % compared to the SI and FD models. We are able to obtain higher agreement with the numerical CFD model. Additionally, consideration of the bearing structure has led to the lowest discrepancies in the FD+ model, with a maximum deviation of 23.5 %.

A rotational speed independence of up to 8000 rpm was observed for the load-carrying capacity and the gas consumption. The attitude angle of the simulations and the experiments showed a mainly vertical component. Furthermore, the comparison of the parameters with the lowest and highest rotational speed resulted in deviations of mostly below 1 %. A few outliers were observed in the FD+ model. The deviation in the experimental results with a rotational speed of 1000 to 8000 rpm is approximately 1 %, which is within the range of the double standard deviation.

The contour plots of the numerical models show the influence of the groove structure on the pressure distribution. It also shows that the groove structure partially negates the influence of the shaft misalignment. The axial offset of the pressure maximum of the FD+ model was less pronounced than in the comparable FDc model. Thus, the comparatively low misalignment was additionally reduced. The contour plots of the FD+ and CFD models also show that 20 pressure slots in the C/C bearing lead to a uniform pressure distribution.

7 Conclusion

This work involves the design of an aerostatic bearing made of an orthotropic layered porous CMC material. The preliminary tests included the determination of the permeability and the acquisition of the layered structure, and the findings from these tests were implemented in the development of the models. The models were extended stepwise to simulate the bearing more realistically and were compared in parallel with external studies. The FD+ model was validated with experiments with a developed air bearing test rig. The following main findings were obtained:

- **The experiments demonstrate the suitability of the material for aerostatic bearings.** No occurrence of pneumatic hammering was noted in the measurements. Temporary loads below 90 N with eccentricity ratios below 0.8 do not cause significant wear.
- **The influence of rotational speed on the performance of the bearing was negligible up to 8000 rpm.** The experimental results and the numerical calculations showed deviations of less than 1 % percent in this rotational speed range. Furthermore, small attitude angles were determined. The mainly vertical displacement indicates aerostatic operation mode.
- **Hydrodynamic validation.** For hydrodynamic validation, the Si and FD models showed a good deviation of up to 6 % from the experimental results, depending on the radial clearance. A reduction in the radial clearance showed a significant increase in the deviation to approximately 47 %. An improvement in the Si and FD models is achievable with regards to the cavitation model and with consideration of mixed as well as contact friction.

Table 7.1: Hydrodynamic evaluation of numerical models:
max. deviation to experimental results

	Si	FD	External
Metal mixture			
$c = 85.5 \mu\text{m}$: max. $\delta_{F\sim} / \%$	5.7	4.1	1.2 *
$c = 32.0 \mu\text{m}$: max. $\delta_{F\sim} / \%$	46.8	47.3	-

* Elsharkawy et al. [46]

- **The influence of the orthotropic layered structure is significant.** In the development of a numerical model for the calculation of the C/C bearing, the models were gradually extended, with consideration of the discretization of the porous bushing,

the shaft misalignment and the compressibility of the gas. The corresponding Si, FD and FDc models were validated with external studies and showed reasonable results. With a maximum deviation of approximately 20 - 24 %, the FDc model showed the best results and corresponded to the degree of accuracy of the external models. However, significant deviations were found with the orthotropic layered C/C specimen. The extension of the FD+ model, with consideration of the surface structure, led to a significant improvement in the resulting deviations of max. 21.6 %.

Table 7.2: Aerostatic evaluation of numerical models:
max. deviation to experimental results

	Si	FD	FDc	FD+	External
<hr/> Metal mixture <hr/>					
max. δ_{F^*} / %	25.1	27.8	23.7	-	22.2 *
<hr/> Graphit <hr/>					
max. δ_{F^*} / %	31.6	29.3	20.6	-	20.4 **
<hr/> C/C <hr/>					
max. δ_{F^*} / %	229.9	212.9	218.3	21.6	

* Castelli [25]

** Heidler [61]

- **Validation results of the FD+ model.** The maximum deviation in the simulated results from the tests corresponded to 21.6 % for the load-carrying capacity and 23.5 % for gas consumption.

8 Perspectives

- The tactile measurements revealed extensive grooves in the inner surfaces of the bearing. Further machining of the inner surface of the bushing could reduce the influence of the structure. However, a prerequisite for the re-machining is to avoid clogging the pores.
- The permeability investigations included the determination of the flow coefficient in one direction and an assumption of an isotropic material was made. The structure of the layered structure could cause different flow coefficients, depending on the flow direction. The anisotropic assumption and the determination of the corresponding permeabilities provides an approach to further improve the modeling.
- For dynamic bearing modelling, Hirs [62] has done pioneering work in turbulence modelling. In the case of static, porous or orifice bearings, the investigation and modelling of the transition would be a further improvement for bearing design.
- The bearings can potentially be used in demanding applications due to the use of the resistant material.

Extensive documentation of experiments performed with supercritical carbon dioxide (sCO_2) has been provided by White [121] and shows that a corresponding bearing design still has significant challenges. Magnetic bearings require a high auxiliary-systems effort [57] or can lead to instabilities [67]. Grease-lubricated bearings also have limited serviceability under sCO_2 conditions [58]. A pressurized fluid-film bearing constructed of a CMC material could be a promising alternative.

Turbopumps in liquid fuel engines are another possible area of application for fluid-film bearings. Ball bearings are mainly used in the aerospace sector (see, among others, in Rachuk et al. [95] or Caisso [22]). The high demands on the bearings with the high rotational speed and high temperatures cause a significant degree of wear on the components. Alternative bearing approaches for turbopumps were presented in 2020 by Xu et al. [125]. Inter alia, fluid-film bearings were mentioned as a promising alternative. As early as 1981, a NASA report [87] called for innovative new approaches to turbopump bearings, and fluid-film bearings were proposed as a possible approach.

During preliminary investigations, a porous C/C bushing was lubricated with liquid nitrogen [103], which has provided initial information on the possibility of use under cryogenic conditions.

Bibliography

- [1] G. L. Agrawal. Foil Air/Gas Bearing Technology - An Overview. *Proceedings of the ASME Turbo Expo*, 1, 1997.
- [2] F. Al-Bender. *Air Bearings: Theory, Design and Applications*. Wiley, 2021.
- [3] S. Altmeyer. Ferrofluidic Taylor Couette Flow in between Finite Length Porous Cylinders with Radial Through-Flow. *Journal of Magnetism and Magnetic Materials*, 500:166363, 2020.
- [4] Ansys® CFX 2020 R1. CFX Documentation, ANSYS, Inc., 2020.
- [5] Ansys® ICEM 2020 R1. ICEM Documentation, ANSYS, Inc., 2020.
- [6] Ansys® Workbench 2020 R1. Workbench Documentation, ANSYS, Inc., 2020.
- [7] K. Avila, D. Moxey, A. D. Lozar, M. Avila, D. Barkley, and B. Hof. The Onset of Turbulence in Pipe Flow. *Science*, 333(6039):192 – 196, 2011.
- [8] M. A. Barnett and A. Silver. Application of Air Bearings to High-Speed Turbomachinery. In *Combined National Farm, Construction and Industrial Machinery and Powerplant Meetings, Milwaukee, Wis., 14. - 17. September 1970*, 1970. 700720.
- [9] R. Bassani and B. Piccigallo. *Hydrostatic Lubrication*. Tribology series. Elsevier Science, 1992.
- [10] J. Bear. *Dynamics of Fluids in Porous Media (Dover Civil and Mechanical Engineering)*. Dover Publications, Inc., 1972.
- [11] G. Beaudoin and M. Y. Jaffrin. Plasma Filtration in Couette Flow Membrane Devices. *Artificial Organs*, 13(1):43–51, 1989.
- [12] G. Belforte, T. Raparelli, V. Viktorov, and A. Trivella. Discharge Coefficients of Orifice-Type Restrictor for Aerostatic Bearings. *Tribology International*, 40(3):512–521, 2007.
- [13] G. Belforte, T. Raparelli, V. Viktorov, and A. Trivella. Permeability and Inertial Coefficients of Porous Media for Air Bearing Feeding Systems. *Journal of Tribology*, 129(4):705–711, 2007.
- [14] I. H. Bell, J. Wronski, S. Quoilin, and V. Lemort. Pure and Pseudo-pure Fluid Thermophysical Property Evaluation and the Open-Source Thermophysical Property Library CoolProp. *Industrial & Engineering Chemistry Research*, 53(6):2498–2508, 2014.

- [15] K. E. Beschorner, C. F. Higgs, and M. R. Lovell. Derivation of Reynolds Equation in Cylindrical Coordinates Applicable to Pin-on-Disk and CMP. In *Proceedings of the STLE/ASME International Joint Tribology Conference, Miami, Florida, USA, 20. - 22. October 2008*, 2008. IJTC2008-71245.
- [16] M. Böhle. Numerical Investigation of the Flow in Hydrostatic Journal Bearings With Porous Material. In *Proceedings of ASME 2018 Fluids Engineering Divisions Summer Meeting, Montreal, USA, 15. - 20. July 2018*, volume 3, 07 2018. FEDSM2018-83437.
- [17] M. Böhle, Y. Gu, and A. Schimpf. Two Flow Models for Designing Hydrostatic Bearings With Porous Material. In *Fluids Engineering Division Summer Meeting, San Francisco, USA, 28. July - 01. August 2019*, 07 2019. AJKFLUIDS2019-4657.
- [18] P. T. Bobrowsky and B. Marker. *Encyclopedia of Engineering Geology*. Springer, 2017.
- [19] P. Bonello and H. Pham. The Efficient Computation of the Nonlinear Dynamic Response of a Foil–Air Bearing Rotor System. *Journal of Sound and Vibration*, 333(15):3459–3478, 2014.
- [20] J. Bouyer and M. Fillon. Influence of Deformation Effects on a Misaligned Plain Journal Bearing. In *Proceedings of WTC 2005, World Tribology Congress III, Washington, D.C., USA, 12. - 16. September 2005*, 2005. WTC2005-63680.
- [21] S. v. Buuren. *Modeling and Simulation of Porous Journal Bearings in Multibody Systems*. Phd thesis, Karlsruher Institut für Technologie (KIT), 2013.
- [22] P. Caisso, J. Barton, M. Illig, and T. Margat. Development Status of the Vulcain 2 Engine. In *36th AIAA/ASME/SAE/ASEE Joint Propulsion Conference and Exhibit, Las Vegas, NV, U.S.A., 24. - 28. July 2000*, 2000. AIAA 2000-3781.
- [23] V. Castelli and J. T. McCabe. Transient Dynamics of a Tilting Pad Gas Bearing System. *Journal of Lubrication Technology*, 89(4):499–507, 1967.
- [24] V. Castelli and J. Pirvics. Review of Numerical Methods in Gas Bearing Film Analysis. *Journal of Lubrication Technology*, 90(4):777–790, 1968.
- [25] V. P. Castelli. Experimental and Theoretical Analysis of the Gas-Lubricated Porous Rotating Journal Bearing. *A S L E Transactions*, 22(4):382–388, 1979.
- [26] S.-Y. Chien, M. Cramer, and A. Untaroiu. A Compressible Thermohydrodynamic Analysis of Journal Bearings Lubricated With Supercritical CO₂. In *Proceedings of the ASME 2017 Fluids Engineering Division Summer Meeting, Waikoloa, Hawaii, USA, 30. July - 3. August 2017*, 2017. FEDSM2017-69310.

- [27] D. Childs, H. Moes, and H. van Leeuwen. Journal Bearing Impedance Descriptions for Rotordynamic Applications. *Journal of Lubrication Technology*, 99(2):198–210, 1977.
- [28] K. Cieslicki. Investigations of the Effect of Inertia on Flow of Air through Porous Bearing Sleeves. *Wear*, 172:73–78, 1994.
- [29] J. A. Cole. Taylor Vortices with Eccentric Rotating Cylinders. *Nature*, 216:1200–1202, 1967.
- [30] S. M. Coleman. High Capacity Aerodynamic Air Bearing (HCAB) for Laser Scanning applications. *Optical Scanning 2005*, 5873:56–64, 2005.
- [31] H. Cui, H. Xia, D. Lei, X. Zhang, and Z. Jiang. A Calculation Method to Investigate the Effects of Geometric Parameters and Operational Conditions on the Static Characteristics of Aerostatic Spherical Bearings. *Journal of Tribology*, 141(2):021101, 2018.
- [32] K. Czolczynski. *Rotordynamics of Gas-Lubricated Journal Bearing Systems*. Springer, 1999.
- [33] A. Dal and T. Karavaş. Pneumatic Hammer Instability in the Aerostatic Journal Bearing–Rotor System: A Theoretical and Experimental Analyses. *Proceedings of the Institution of Mechanical Engineers, Part J: Journal of Engineering Tribology*, 235(3):524 – 543, 2021.
- [34] A. G. Darbyshire and T. Mullin. Transition to Turbulence in Constant-Mass-Flux Pipe Flow. *Journal of Fluid Mechanics*, 289:83–114, 1995.
- [35] C. Dellacorte, V. Lukaszewicz, M. J. Valco, K. C. Radil, and H. Heshmat. Performance and Durability of High Temperature Foil Air Bearings for Oil-Free Turbomachinery. *Tribology Transactions*, 43, 2000.
- [36] DIN 1343:1990-01. Referenzzustand, Normzustand, Normvolumen; Begriffe und Werte. Standard, DIN Deutsches Institut für Normung e.V., 1990.
- [37] DIN EN 60751:2008. Industrielle Platin-Widerstandsthermometer und Platin-Temperatursensoren. Standard, DKE Deutsche Kommission Elektrotechnik Elektronik Informationstechnik im DIN und VDE, 2008.
- [38] DIN EN ISO 4022:2018-12. Durchlässige Sintermetallwerkstoffe – Bestimmung der Flüssigkeitsdurchlässigkeit. Standard, DIN-Normenausschuss Werkstofftechnologie (NWT), 2018.
- [39] C. Dittert and M. Küttemeyer. Octra-Optimized Ceramic for Hypersonic Application with Transpiration Cooling. *Advances in High Temperature Ceramic Matrix Composites and Materials for Sustainable Development*, 263:389–399, 2017.

- [40] M. Dogigli, H. Weihs, K. Wildenrotter, and H. Lange. New High-Temperature Ceramic Bearing for Space Vehicles. In *51st Int. Astronautical Congress, Rio de Janeiro, Brazilien, 2. - 6. October 2000*, 2000.
- [41] D. Dowson. A Generalized Reynolds Equation for Fluid-Film Lubrication. *International Journal of Mechanical Sciences*, 4(2):159 – 170, 1962.
- [42] J. E. Dyson and B. W. Darvell. Aspects of the Design of Modern Dental Air Turbine Handpieces. *Australian Dental Journal*, 38:456–470, 1993.
- [43] B. Eckhardt. Introduction. Turbulence Transition in Pipe Flow: 125th Anniversary of the Publication of Reynolds' Paper. *Philosophical Transactions of the Royal Society A: Mathematical, Physical and Engineering Sciences*, 367:449–455, 2009.
- [44] H. G. Elrod. A General Theory for Laminar Lubrication With Reynolds Roughness. *Journal of Lubrication Technology*, 101(1):8–14, 1979.
- [45] H. G. Elrod. A Cavitation Algorithm. *Journal of Lubrication Technology*, 103(3):350–354, 1981.
- [46] A. A. Elsharkawy and L. H. Guedouar. Hydrodynamic Lubrication of Porous Journal Bearings using a Modified Brinkman-Extended Darcy Model. *Tribology International*, 34(11):767–777, 2001.
- [47] J. H. Ferziger, M. Perić, and R. L. Street. *Numerische Strömungsmechanik*, volume 1. Springer, 2008.
- [48] S. Fleder, B. Gwiasda, M. Appel, M. Böhle, M. Ortelt, and H. Hald. Design and Testing of Radial Gas Bearings with Porous Media, using Fiber-Reinforced C/C Composites. In *3rd International Rotating Equipment Conference (IREC), Pumps, Compressors and Vacuum Technology, Düsseldorf, 14 – 15 September 2016*, 2016.
- [49] J. Frêne and M. Godet. Transition from Laminar to Taylor Vortex Flow in Journal Bearings. *Tribology*, 4(4):216–217, 1971.
- [50] J. Frêne, D. Nicolas, B. Degueurce, D. Berthe, and M. Godet. Chapter 11 - Superlaminar Flow Regimes. In *Hydrodynamic Lubrication*, volume 33 of *Tribology Series*, pages 347–386. Elsevier, 1990.
- [51] S. Fujita, K. Minagawa, G. Tanaka, and H. Shimosaka. Intelligent Seismic Isolation System Using Air Bearings and Earthquake Early Warning. *Soil Dynamics and Earthquake Engineering*, 31(2):223–230, 2011.
- [52] K. Gaffal, A. K. Usbeck, and W. Prechtl. Neue Werkstoffe ermöglichen innovative Pumpenkonzepte für die Speisewasserförderung in Kesselanlagen. *VDI-Berichte*, 1331:275–289, 1997.

- [53] M. J. Gray, N. Kumar, R. O'Connor, M. Hoek, E. Sheridan, M. C. Doyle, M. L. Romanelli, G. B. Osterhoudt, Y. Wang, V. Plisson, S. Lei, R. Zhong, B. Rachmilowitz, H. Zhao, H. Kitadai, S. Shepard, L. M. Schoop, G. D. Gu, I. Zeljkovic, X. Ling, and K. S. Burch. A Cleanroom in a Glovebox. *Review of Scientific Instruments*, 91:073909, 2020.
- [54] D. Greenberg and E. Weger. An Investigation of the Viscous and Inertial Coefficients for the Flow of Gases Through Porous Sintered Metals with High Pressure Gradients. *Chemical Engineering Science*, 12(1):8–19, 1960.
- [55] D. Greuel. *Untersuchungen zum Impuls- und Stofftransport in effusiv gekühlten faserkeramischen Raketebrennkammerwänden*. Phd thesis, Rheinisch-Westfälische Technische Hochschule Aachen, 2013.
- [56] D. Gropper, L. Wang, and T. J. Harvey. Hydrodynamic Lubrication of Textured Surfaces: A Review of Modeling Techniques and Key Findings. *Tribology International*, 94:509–529, 2016.
- [57] A. Hacks, S. Schuster, H. J. Dohmen, F.-K. Benra, and D. Brillert. Turbomachine Design for Supercritical Carbon Dioxide Within the sCO₂-HeRo.eu Project. *Journal of Engineering for Gas Turbines and Power*, 140(12), 2018. 121017.
- [58] A. J. Hacks, A. Vojacek, H. J. Dohmen, and D. Brillert. Experimental Investigation of the sCO₂-HeRo Compressor. In *2nd European sCO₂ Conference, Essen, Germany, 30. - 31. August 2018*, 2018. 2018-sCO₂.eu-115.
- [59] H. Hald, M. Ortelt, I. Fischer, and D. Greuel. CMC Rocket Combustion Chamber with Effusion Cooling. In *54th International Astronautical Congress of the International Astronautical Federation, 29. September - 3. October 2003*, 01 2003. IAC-03-S.P.22.
- [60] B. J. Hamrock, S. R. Schmid, and B. O. Jacobson. *Fundamentals of Fluid Film Lubrication*. CRC Press, 2004.
- [61] N. Heidler. *Untersuchungen zylindrischer Gasführungselemente für Hochvakuumanwendungen*. Phd thesis, TU Ilmenau, 2016.
- [62] G. G. Hirs. A Bulk-Flow Theory for Turbulence in Lubricant Films. *Journal of Lubrication Technology*, 95(2):137–145, 1973.
- [63] Y.-Z. Hu and D. Zhu. A Full Numerical Solution to the Mixed Lubrication in Point Contacts. *Journal of Tribology*, 122(1):1–9, 1999.
- [64] K. Ilin and A. Morgulis. On the Stability of the Couette–Taylor Flow between Rotating Porous Cylinders with Radial Flow. *European Journal of Mechanics - B/Fluids*, 80:174–186, 2020.

- [65] JCGM 100:2008. Evaluation of Measurement Data — Guide to the Expression of Uncertainty in Measurement. Standard, Joint Committee for Guides in Metrology, 2008.
- [66] E. C. Johnson and R. M. Lueptow. Hydrodynamic Stability of Flow between Rotating Porous Cylinders with Radial and Axial Flow. *Physics of Fluids*, 9(12):3687–3696, 1997.
- [67] D. Kim, S. Baik, and J. I. Lee. Instability Study of Magnetic Journal Bearing under S-CO₂ Condition. *Applied Sciences (Switzerland)*, 11:3491, 2021.
- [68] D. Kim, B. Nicholson, L. Rosado, and G. Givan. Rotordynamics Performance of Hybrid Foil Bearing Under Forced Vibration Input. *Journal of Engineering for Gas Turbines and Power*, 140(1):012507, 2017.
- [69] D. Kim and G. Zimbru. Start-Stop Characteristics and Thermal Behavior of a Large Hybrid Airfoil Bearing for Aero-Propulsion Applications. *Journal of Engineering for Gas Turbines and Power*, 134(3):032502, 2012.
- [70] L. Klinkenberg. The Permeability of Porous Media to Liquids and Gases. *Am. Petrol. Inst., Drilling and Production Practice*, 2:200–213, 1941.
- [71] W. Kochanowski and P. Tillack. New Pump Bearing Materials Prevent Damage to Tubular Casing Pumps. *VDI-Berichte*, 1421:227–242, 1998.
- [72] A. Korenaga, H. Mano, A. Omura, T. Ohana, S. Aso, K. Sadakata, S. Tanabe, Y. Akiyama, and F. Habuki. Friction Reduction of Oil-Impregnated Sintered Bearings by Surface Texturing. *Journal of Tribology*, 142(9):091801, 2020.
- [73] A. Kumar and S. C. Sharma. Ferrofluid Lubrication of Optimized Spiral-Grooved Conical Hybrid Journal Bearing Using Current-Carrying Wire Model. *Journal of Tribology*, 144(4):041801, 2021.
- [74] Y. B. P. Kwan and J. Corbett. Porous Aerostatic Bearings – an Updated Review. *Wear*, 222:69–73, 1998.
- [75] D. Lee, H. Lim, B. Choi, B. Kim, J. Park, and J. Bang. Thermal Behavior of Radial Foil Bearings Supporting an Oil-Free Gas Turbine: Design of the Cooling Flow Passage and Modeling of the Thermal System. *Journal of Engineering for Gas Turbines and Power*, 139(6):061902, 2017.
- [76] M. Leuchs and A. Mühlratzer. Ceramic Matrix Composite Material in Highly Loaded Journal Bearings. In *Proceedings of ASME TURBO EXPO 2002*, volume 4, pages 29–38, 06 2002.

- [77] W. Li, S. Wang, Z. Zhao, K. Zhang, K. Feng, and W. Hou. Numerical and Experimental Investigation on the Performance of Hybrid Porous Gas Journal Bearings. *Lubrication Science*, 33(2):60–78, 2021.
- [78] W.-L. Li. Derivation of Modified Reynolds Equation—A Porous Media Model. *Journal of Tribology*, 121(4):823–829, 1999.
- [79] Y. Li, K. Zhou, and Z. Zhang. A Flow-Difference Feedback Iteration Method and its Application to High-Speed Aerostatic Journal Bearings. *Tribology International*, 84:132–141, 2015.
- [80] E. Maleki, H. Sadrhosseini, and A. Ghiami. Investigation of Artificial Neural Networks Capability to Predict Viscosity of Lubricants used in Journal Bearings. In *Proceedings of the The International Conference on Engineering & MIS 2015, Istanbul, Turkey, 24. - 26. September 2015, ICEMIS '15*, New York, NY, USA, 2015.
- [81] P. H. Markho, S. S. Grewal, and T. B. Stowell. An Experimental Investigation of the Effect of Misalignment and Directionality on the Performance of an Externally-Pressurized, Orifice-Compensated Air Journal Bearing. *Journal of Lubrication Technology*, 101(1):28–37, 1979.
- [82] D. Martinand, E. Serre, and R. M. Lueptow. Absolute and Convective Instability of Cylindrical Couette Flow with Axial and Radial Flows. *Physics of Fluids*, 21(10):104102, 2009.
- [83] K. Min and R. Lueptow. Circular Couette Flow with Pressure-Driven Axial Flow and a Porous Inner Cylinder. *Experiments in fluids*, 17(3):190–197, 1994.
- [84] M. Mokhtar, M. Rafaat, and G. Shawki. Experimental Investigations into the Performance of Porous Journal Bearings. In *International Congress & Exposition, Detroit, Michigan, 27. February - 2. March 1984*, 02 1984. 840097.
- [85] D. J. Munk, M. Selzer, H. Seiler, M. Ortelt, and G. A. Vio. Analysis of a Transpiration Cooled LOX/CH₄ Rocket Thrust Chamber. *International Journal of Heat and Mass Transfer*, 182:121986, 2022.
- [86] M. Naeem, S. Lock, P. Collins, and G. Hooley. Electron Beam Welding vs. Laser Beam Welding for Air Bearing Shaft. In *ICALEO 2005 Congress Proceedings*, pages 144–151. Laser Institute of America, 2005.
- [87] National Research Council. Liquid Rocket Propulsion Technology: An Evaluation of NASA's Program . *Washington, DC: The National Academies Press.*, 1981.
- [88] H. Oertel, M. Böhle, and T. Reviol. *Strömungsmechanik: Grundlagen-Grundgleichungen-Lösungsmethoden-Softwarebeispiele*. Springer-Verlag, 2011.

- [89] M. Ortelt, H. Hald, and A. Herbertz. Investigations on Fibre Reinforced Combustion Chamber Structures under Effusion Cooled LOX/LH2 Operation. In *45th AIAA/ASME/SAE/ASEE Joint Propulsion Conference & Exhibit, Denver, Colorado, 2. - 5. August 2009*, 2009. AIAA 2009-5475.
- [90] N. Patir and M. S. Cheng. Application of Average Flow Model to Lubrication between Rough Sliding Surfaces. *Journal of Tribology*, 101(2):220–229, 1979.
- [91] B. T. Paulsen, S. Morosi, and I. F. Santos. Static, Dynamic, and Thermal Properties of Compressible Fluid Film Journal Bearings. *Tribology Transactions*, 54(2):282–299, 2011.
- [92] I. Pierre, J. Bouyer, and M. Fillon. Thermohydrodynamic Behavior of Misaligned Plain Journal Bearings: Theoretical and Experimental Approaches. *Tribology Transactions*, 47(4):594–604, 2004.
- [93] M. Pourjafar, A. Hejri, S. Bazargan, and K. Sadeghy. On the Use of a Fluid’s Elasticity for Deliberate Rise of Taylor Cells in a Rotating Micro-Filter Separator. *Physics of Fluids*, 30(11):114106, 2018.
- [94] B. S. Prabhu. An Experimental Investigation on the Misalignment Effects in Journal Bearings. *Tribology Transactions*, 40(2):235–242, 1997.
- [95] V. S. Rachuk, A. I. Dmitrenko, M. Buser, and A. Minick. Single Shaft Turbopump Expands Capabilities of Upper Stage Liquid Propulsion. In *44th AIAA/ASME/SAE/ASEE Joint Propulsion Conference and Exhibit, Hartford, CT, 21. - 23. July 2008*, 2008. AIAA 2008-4946.
- [96] K. Radil, C. Dellacorte, and M. Zeszotek. Thermal Management Techniques for Oil-Free Turbomachinery Systems. *Tribology Transactions*, 50(3):319–327, 2007.
- [97] O. Reynolds. IV. On the Theory of Lubrication and its Application to Mr. Beauchamp Tower’s Experiments, Including an Experimental Determination of the Viscosity of Olive Oil. *Philosophical transactions of the Royal Society of London*, 177:157–234, 1886.
- [98] O. Reynolds. IV. On the Dynamical Theory of Incompressible Viscous Fluids and the Determination of the Criterion. *Philosophical Transactions of the Royal Society of London. (A.)*, 186, 1895.
- [99] K. Ryu and L. San Andrés. On the Failure of a Gas Foil Bearing: High Temperature Operation Without Cooling Flow. *Journal of Engineering for Gas Turbines and Power*, 135:112506, 2013.
- [100] L. San Andrés. Hybrid Flexure Pivot-Tilting Pad Gas Bearings: Analysis and Experimental Validation. *Journal of Tribology*, 128(3):551–558, 03 2006.

- [101] A. Schimpf, Y. Gu, and M. Böhle. Analysis of Flow Models for Aerostatic Thrust Bearings with Porous Material. *Journal of Physics: Conference Series*, 1909:012039, 2021.
- [102] A. Schimpf, M. Ortelt, H. Seiler, Y. Gu, A. Schwarzwälder, and M. Böhle. Experimental Investigation of Aerostatic Journal Bearings Made of Carbon Fiber-Reinforced Carbon Composites. *Journal of Tribology*, 144(4):041806, 2022.
- [103] A. Schimpf, H. Seiler, M. Ortelt, D. Gudi, and M. Böhle. Static Performance Analysis of a Porous Journal Bearing for Cryogenic Applications. In *23rd International Colloquium Tribology: Industrial and Automotive Lubrication, TAE, Technische Akademie Esslingen, 25. – 27. January 2022*, page 259, 01 2022.
- [104] H. Seiler, M. Ortelt, and M. Böhle. Development of a Hydrostatic Journal Bearing with Micro Porous CMC Material. In *AIAA Propulsion and Energy Forum, Indianapolis, USA, 19. - 22. August 2019*, 2019. AIAA 2019-4434.
- [105] Y. Sha, J. Fritz, T. Klemm, and S. Ripperger. Untersuchung der Strömung im Taylor-Couette-System bei geringen Spaltbreiten. *Chemie Ingenieur Technik*, 88(5):640–647, 2016.
- [106] J. Shi, H. Cao, and X. Chen. Effect of Angular Misalignment on the Dynamic Characteristics of Externally Pressurized Air Journal Bearing. *Proceedings of the Institution of Mechanical Engineers, Part J: Journal of Engineering Tribology*, 234(2):205–228, 2020.
- [107] K. Sim, Y. B. Lee, J. W. Song, and T. H. Kim. Effect of Cooling Flow on Thermal Performance of a Gas Foil Bearing Floating on a Hot Rotor. *Journal of Mechanical Science and Technology*, 32:1939–1954, 2018.
- [108] H. J. Sneek and R. C. Elwell. The Externally Pressurized, Porous Wall, Gas-Lubricated Journal Bearing. II. *A S L E Transactions*, 8(4):339–345, 1965.
- [109] T. Someya. *Journal-Bearing Databook*. Springer-Verlag, Berlin, Heidelberg, 1989.
- [110] L. Song, G. Yuan, H. Zhang, Y. Ding, and K. Cheng. The Stability of Spiral-Grooved Air Journal Bearings in Ultrahigh Speeds. *Materials*, 15:1759, 2022.
- [111] R. Span. *Multiparameter Equations of State- An Accurate Source of Thermodynamic Property Data*. Springer Berlin, Heidelberg, 2010.
- [112] T. A. Stolarski. Running Characteristics of Aerodynamic Bearing with Self-Lifting Capability at Low Rotational Speed. *Advances in Tribology*, 2011:1 – 10, 2011.
- [113] I. Takahashi, T. Koganezawa, G. Su, and K. Oyama. A Super High Speed PM Motor Drive System by a Quasi-Current Source Inverter. In *Conference Record of the 1993*

- IEEE Industry Applications Conference Twenty-Eight IAS Annual Meeting*, volume 1, pages 657–662, 1993.
- [114] G. I. Taylor. VIII. Stability of a Viscous Liquid Contained Between Two Rotating Cylinders. *Philosophical Transactions of the Royal Society of London. Series A, Containing Papers of a Mathematical or Physical Character*, 223(605-615):289–343, 1923.
- [115] R. Taylor and G. K. Lewis. Experience Relating to the Steady Performance of Aerostatic Porous Thrust Bearings. *Proceedings of the Institution of Mechanical Engineers*, 189(1):383–390, 1975.
- [116] E. Uhlmann and C. Neumann. Air Bearings Based on Porous Ceramic Composites. In *Intelligent Production Machines and Systems*, pages 211–216. Elsevier Science Ltd, 2006.
- [117] J. M. Vance. *Rotordynamics of Turbomachinery*. Wiley and Sons Inc., New Delhi, India, 1988.
- [118] J. H. Vohr. An Experimental Study of Taylor Vortices and Turbulence in Flow Between Eccentric Rotating Cylinders. *Journal of Lubrication Technology*, 90(1):285–296, 1968.
- [119] B. Wei, Y. Jiao, and X. Wu. Numerical Calculation of Fluid Film Force on Journal Bearings Based on a Biconjugate Gradient-Stabilized Algorithm. *Journal of Tribology*, 144(11), 2022. 114502.
- [120] S. Whitaker. The Forchheimer Equation: A Theoretical Development. *Transport in Porous Media*, 25:27–61, 1996.
- [121] M. T. White, G. Bianchi, L. Chai, S. A. Tassou, and A. I. Sayma. Review of Supercritical CO₂ Technologies and Systems for Power Generation. *Applied Thermal Engineering*, 185:116447, 2021.
- [122] E.-R. Wu. Gas-Lubricated Porous Bearings of Finite Length—Self-Acting Journal Bearings. *Journal of Lubrication Technology*, 101(3):338–347, 07 1979.
- [123] W. Xiao, Y. Bernabé, B. Evans, U. Mok, J. Zhao, X. Ren, and M. Chen. Klinkenberg Effect and Effective Pressure for Gas Permeability of Tight Sandstones. *Journal of Geophysical Research: Solid Earth*, 124(2):1412–1429, 2019.
- [124] G. Xu, J. Zhou, H. Geng, M. Lu, L. Yang, and L. Yu. Research on the Static and Dynamic Characteristics of Misaligned Journal Bearing Considering the Turbulent and Thermohydrodynamic Effects. *Journal of Tribology*, 137(2):024504, 2015.

-
- [125] J. Xu, C. Li, X. Miao, C. Zhang, and X. Yuan. An Overview of Bearing Candidates for the Next Generation of Reusable Liquid Rocket Turbopumps. *Chinese Journal of Mechanical Engineering*, 33(1):1–13, 2020.
- [126] Y. Yu, G. Pu, T. Jiang, and K. Jiang. Optimization of Herringbone Grooved Thrust Air Bearings for Maximum Load Capacity. *Journal of Tribology*, 143(12):121805, 2021.
- [127] J. Zhang, F. Yu, D. Zou, N. Ta, and Z. Rao. Comparison of the Characteristics of Aerostatic Journal Bearings Considering Misalignment under Pure-Static and Hybrid Condition. *Proceedings of the Institution of Mechanical Engineers, Part J: Journal of Engineering Tribology*, 233(5):769–781, 2019.
- [128] W. Zhong, X. Ji, C. Li, J. Fang, and F. Liu. Determination of Permeability and Inertial Coefficients of Sintered Metal Porous Media using an Isothermal Chamber. *Applied Sciences (Switzerland)*, 8(9):1670, 2018.

List of Figures

1.1	Types of fluid-film bearings	2
1.2	Schematic concept of the orthotropic layered structure [102]	4
2.1	Top: C/C and aluminum liner, bottom: dimensions of the C/C liner [102]	6
2.2	Top: shaft after the performed experiments, bottom: dimensions of the shaft [102]	7
2.3	C/C bearing housing	8
2.4	Seals of the aluminium liner	9
2.5	Assembly of the bearing test housing	9
2.6	Porous C/C sample for permeability measurements	10
2.7	Concept of the permeability measurement	11
2.8	Instruments for determining the flow coefficients	12
2.9	Experimental results of permeability measurements	13
2.10	Applicability of Darcy's law	14
2.11	SEM image of a C/C sample made by PIP [59]	15
2.12	Determination of fluid permeability coefficients according standard DIN EN ISO 4022:2018 [38]	16
2.13	Klinkenberg effect	17
2.14	Experimental setup for determining the inner surface texture of the porous liner	17
2.15	Inner surface texture of the porous liner	18
3.1	Concept of the test bench for journal gas bearings	21
3.2	Test bench for journal gas bearings	22
3.3	Nomenclature of the eccentricity measurement	25
3.4	Hysteresis at $n = 1000$ rpm	26
3.5	Hysteresis at $n = 4000$ (top) and 8000 rpm (bottom)	27
3.6	Experimental results: load-carrying capacity and vertical misalignment	29
3.7	Experimental results: mass flow rate	30
3.8	Orbit of the shaft	31
3.9	Nomenclature of a misaligned shaft	32
3.10	Absolute vertical displacement V_{S1} and V_{S2}	35
3.11	Absolute vertical displacement of shaft at 1000 rpm	36
3.12	Absolute vertical displacement of shaft at 4000 rpm	37
3.13	Absolute vertical displacement of shaft at 8000 rpm	38
3.14	Vertical misalignment ratio based on shaft inclination	39
4.1	Nomenclature of a porous journal bearing (overscaled visualization of the lubricant film width)	43

4.2	Schematic representantation of an axially uniform lubricant film thickness in cylindrical coordinates (overscaled visualization of the lubricant film width)	50
4.3	Schematic representation of the lubricant film width under consideration of the shaft misalignment in cylindrical coordinates (overscaled visualization of the lubricant film width)	51
4.4	Schematic representation of the lubricant film width under consideration of the shaft misalignment and surface structure in cylindrical coordinates (overscaled visualization of the lubricant film width)	52
4.5	Generating the average groove profile: i) Set offset, ii) Detection of grooves	54
4.6	Groove profile h_{tex}	55
4.7	External experiments and calculations to determine the transition of a laminar flow to a laminar flow with Taylor vortices	58
4.8	Schematic concepts of flow configurations - a) Taylor-Couette flow [114]: Rotating inner cylinder, b) Pourjafar et al. [93]: Rotating inner cylinder, radial throughflow c) Johnson and Lueptow [66]: Rotating inner cylinder, radial throughflow, axial flow, d) Altmeyer [3]: Rotating inner cylinder, radial throughflow, magnetic field, e) external pressurized porous journal bearing: Rotating inner cylinder, radial inflow at outer cylinder, axial outflow at annulus	59
4.9	A schematic representation of a porous liner	60
4.10	Si: numerical grid of the lubricant film	62
4.11	Si: flowchart	63
4.12	FD: numerical mesh for the porous bushing	64
4.13	FD: flowchart	67
4.14	FDc - numerical mesh for the porous bushing	68
4.15	FDc: numerical grid of the lubricating film	70
4.16	FDc: flowchart	71
4.17	FD+: schematic concept of the inlet flow	73
4.18	FD+: numerical mesh for the porous bushing	73
4.19	FD+: numerical grid of the lubricating film	75
4.20	FD+: flowchart	76
5.1	Overview of the CFD bearing model	77
5.2	CFD setup	78
5.3	CFD: numerical grid	79
6.1	Mesh independency - Si	82
6.2	Pressure distribution - Si ($N\varphi \times Nz$): a) 21 x 20, b) 51 x 50, c) 81 x 80	83
6.3	Mesh independency - FD	84
6.4	Pressure distribution on FD grids at $z = 17.5$ mm ($Nr \times N\varphi \times Nz$): a) 51 x 50 x 10, b) 51 x 50 x 40, c) 51 x 50 x 50	85

6.5	Mesh independency - FDc	86
6.6	Pressure distribution on FDc grids ($Nr \times N\varphi \times Nz$): a) $10 \times 51 \times 50$, b) $40 \times 51 \times 50$, c) $51 \times 50 \times 60$	87
6.7	Average groove pattern	88
6.8	Mesh independency - FD+	89
6.9	Pressure distribution on FD+ (sectional view through the porous bushing, $Nr \times N\varphi \times Nz$): a) $40 \times 61 \times 286$, b) $40 \times 181 \times 350$	90
6.10	Lubricant pressure distribution on FD+ grids ($Nr \times N\varphi \times Nz$): a) $40 \times 61 \times 286$, b) $40 \times 181 \times 350$	91
6.11	Numerical meshes of the CFD: a) Coarse mesh, b) Fine mesh	93
6.12	Mesh independency - CFD	93
6.13	Validation and deviation of Si and FD with a hydrodynamic porous bearing	97
6.14	Validation of Si, FD and FDc with an aerostatic porous bearing made of sintered iron	100
6.15	Validation and deviation of Si, FD and FDc with an aerostatic porous bearing made of sintered graphite based on F^*	102
6.16	Validation of numerical results on the basis of static load-carrying capacity at $n = 1000$ rpm	105
6.17	Validation of numerical results on the basis of static load-carrying capacity at $n = 4000$ rpm	106
6.18	Validation of numerical results on the basis of static load-carrying capacity at $n = 8000$ rpm	107
6.19	Impact of rotational speed on static load capacity at a pressure ratio of $p_s/p_a = 5$ (top) and $p_s/p_a = 7$ (bottom)	108
6.20	Validation of numerical results on the basis of the attitude angle: a) $n = 1000$ rpm, b) $n = 4000$ rpm, c) $n = 8000$ rpm	109
6.21	Validation of numerical results on the basis of norm flow rate at $n = 1000$ rpm	111
6.22	Validation of numerical results on the basis of norm flow rate at $n = 4000$ rpm	112
6.23	Validation of numerical results on the basis of norm flow rate at $n = 8000$ rpm	113
6.24	Impact of rotational speed on gas consumption at a pressure ratio of $p_s/p_a = 5$ (top) and $p_s/p_a = 7$ (bottom)	114
6.25	Overview planes	116
6.26	Film height distribution: No misalignment (left), vertical misalignment (middle), vertical misalignment plus texture (right)	117
6.27	Pressure distribution lubricant view: $p_s/p_a = 5, \varepsilon = 0.4, n = 1000rpm$	118
6.28	Pressure distribution front view: $p_s/p_a = 5, \varepsilon = 0.4, n = 1000rpm$	119
6.29	Pressure distribution side view: $p_s/p_a = 5, \varepsilon = 0.4, n = 1000rpm$	120

List of Tables

4.1	Assumptions underlying the models	42
4.2	Parameters of the studies by Paulsen and Santos [91] and Zhang et al. [127]	56
4.3	Ta of the C/C experiments: $R_1 = 14.03$ mm, $c = 0.03$ mm, $c \cdot R_1^{-1} = 0.0021$	57
6.1	Absolute values - Si	83
6.2	Absolute values - FD	85
6.3	Absolute values - FDc	86
6.4	Absolute values - FD+	92
6.5	Absolute values - CFD	92
6.6	Overview of the external studies for the validation of the numerical models	95
6.7	Maximum deviation for calculating a hydrodynamic bearing with respect to the radial clearance c and permeability parameter Ψ	98
6.8	Maximum deviation for calculating an aerostatic porous bearing made of sintered iron with respect to the rotational speed n	99
6.9	Maximum deviation for calculating an aerostatic porous bearing made of sintered graphite with respect to the pressure ratio p_s/p_a	103
6.10	Maximum deviation for calculating an aerostatic porous bearing made of orthotropic layered C/C with respect to the pressure ratio p_s/p_a	110
6.11	Maximum deviation for calculating an aerostatic porous bearing made of orthotropic layered C/C with respect to the pressure ratio p_s/p_a	115
7.1	Hydrodynamic evaluation of numerical models: max. deviation to experimental results	125
7.2	Aerostatic evaluation of numerical models: max. deviation to experimental results	126

Publications and Conferences

- **A. Schimpf**, H. Seiler, M. Ortelt, D. Gudi, and M. Böhle. Static Performance Analysis of a Porous Journal Bearing for Cryogenic Applications. In 23rd International Colloquium Tribology: Industrial and Automotive Lubrication, TAE, Technische Akademie Esslingen, 25. – 27. January 2022, page 259, 01 2022.
- **A. Schimpf**, M. Ortelt, H. Seiler, Y. Gu, A. Schwarzwälder, and M. Böhle. Experimental Investigation of Aerostatic Journal Bearings Made of Carbon Fiber-Reinforced Carbon Composites. *Journal of Tribology*, 144(4):041806, 2022.
- **A. Schimpf**, Y. Gu, and M. Böhle. Analysis of Flow Models for Aerostatic Thrust Bearings with Porous Material. *Journal of Physics: Conference Series*, 1909:012039, 2021.
- M. Böhle, Y. Gu, and **A. Schimpf**. Two Flow Models for Designing Hydrostatic Bearings With Porous Material. In Fluids Engineering Division Summer Meeting, San Francisco, USA, 28. July - 01. August 2019, 07 2019. AJKFLUIDS2019-4657.

List of Supervised Student Thesis

T. Schwarz	Numerische Untersuchung des Einflusses von Radialspalt und Massenstrom auf den Verlustbeiwert einer Mikrodüse hinsichtlich der Anwendung in aerostatischen Lagern	PA 2023
S. Hammes	Entwicklung einer Applikation zur optischen Bestimmung des Innendurchmessers und der Rauheit von Graphithülsen	SA 2023
S. Kottas	Numerische Modellierung und Beurteilung der Schubeinbringung eines Strahllüfterkonzepts zur Tunnelbelüftung	DA 2021
D. Gudi	Konstruktion eines Prüfstandes zur optischen Messung von Innendurchmessern und Oberflächengüte	SA 2021
L. Schädler	Numerische Untersuchung von aerostatischen Axiallagern mit porösem Medium anhand von CFD-Simulationen und Validierung des SAM CODE	SA 2020
M. M. Raase	Konstruktion und Untersuchung einer Kennlinienstabilisierungseinheit am Gitterwindkanal	BA 2020
P. Metzler	Conical Journal Bearings - Development and Implementation of a Numerical Model for Static Characteristic Performance	PA 2020
A. Schwarzwälder	Auslegung und numerische Untersuchung von gesichelten Ventilatorlaufrädern für industrielle Kühltürme (CTF)	PA 2020
M. Brandauer	Experimentelle Bestimmung der Permeabilität von porösen Medien mit Bezug auf die Einsatzmöglichkeit in aerostatischen Lagerungen	BA 2019
R. Will	Konstruktion und Schwingungsanalyse eines Hochgeschwindigkeitsprüfstandes für radiale Luftlager	BA 2019

Curriculum Vitae

Personal Data

Name: Artur Schimpf
E-Mail: schimpf@mv.uni-kl.de

Education

04/2011 - 05/2018 Diploma in Mechanical Engineering
Technical University Kaiserslautern
05/2015 - 11/2015 Semester Abroad
Jiangnan University, Wuhan (China)
07/2010 - 12/2010 Obligatory Military Service
5. Gebirgsfernmeldebataillon 210, Bad Reichenhall
04/2000 - 04/2010 General Qualification for University Entrance
IGS Rockenhausen

Work Experience

05/2018 - Present Research Assistant
Institute of Fluid Mechanics and Fluid Machinery
Technical University Kaiserslautern
05/2017 - 04/2018 Student Assistant
Institute of Fluid Mechanics and Fluid Machinery
Technical University Kaiserslautern
10/2016 - 04/2017 Internship
MAN Diesel & Turbo, Augsburg
01/2016 - 09/2016 Student Assistant
Institute of Fluid Mechanics and Fluid Machinery
Technical University Kaiserslautern